Journal of Experimental and Theoretical Physics, Vol. 95, No. 6, 2002, pp. 1006–1032.
Translated from Zhurnal Éksperimental'noĭ i Teoreticheskoĭ Fiziki, Vol. 122, No. 6, 2002, pp. 1168–1197.

NUCLEI, PARTICLES, AND THEIR INTERACTION

Two-Photon Bremsstrahlung Processes in Atoms: Polarization Effects and Analytic Results for the Coulomb Potential

A. A. Krylovetskiĭ[a], N. L. Manakov[a, *], S. I. Marmo[a], and A. F. Starace[b]

[a]*Voronezh State University, Universitetskaya pl. 1, Voronezh, 394006 Russia*
[b]*Department of Physics and Astronomy, University of Nebraska, Lincoln NE 68588-0111, USA*
**e-mail: manakov@thp.vsu.ru*

Received June 7, 2002

Abstract—The partial wave analysis of two-photon free–free (bremsstrahlung) electron transition cross sections during scattering by a static potential $U(r)$, as well as by an atom with a nonzero angular momentum, is carried out. The dipole interaction with radiation is taken into account in the second order of perturbation theory for the general case of elliptic polarization of photons. The polarization and angular dependences of the two-photon potential scattering amplitude is presented as a combination of the scalar product of electron momenta and photon polarization vectors and five atomic parameters containing Legendre polynomials of the scattering angle as well as radial matrix elements depending on the initial (E) and final (E') electron energies. The results are applicable both for spontaneous double bremsstrahlung at nonrelativistic energies and for induced absorption and emission in the field of a light wave. Specific polarization effects (circular and elliptic dichroism) are analyzed for two-photon bremsstrahlung processes associated with the interference of the Hermite and anti-Hermite parts of the amplitude and depending on the sign of photon helicity. The limiting cases of high and low photon frequencies are investigated analytically, and the asymptotic forms of radial matrix elements and amplitudes for the general form of the $U(r)$ potential are determined. Closed analytic expressions are derived for the radial matrix elements of the Coulomb potential in the form of integrals of hypergeometric function, and singularities are singled out in explicit form for $E' \longrightarrow E$. The methods of approximate calculation of the radial matrix elements are discussed, and the results of their exact numerical calculation, as well as angular distributions and the cross sections of induced one- and two-photon emission and absorption, are given for the case of the Coulomb potential. The numerical results show that dichroism effects are quite accessible for experimental observations. © *2002 MAIK "Nauka/Interperiodica".*

1. INTRODUCTION

Electron scattering by atoms and ions accompanied by emission and absorption of photons constitutes a significant branch in atomic physics. A quantum-mechanical description of such processes originates from the experiments on spontaneous bremsstrahlung (BrS) carried out in 1931 by Sommerfeld, who studied electron scattering by a Coulomb center [1]. In the nonrelativistic dipole approximation, the BrS cross section with the emission of a photon of frequency ω and polarization vector $\mathbf{e}$ in direction $\mathbf{k}$,

$$\frac{d\sigma}{d\omega d\Omega_{\mathbf{p}'} d\Omega_{\mathbf{k}}} = \frac{e^2\hbar^5}{(2\pi)^4 c^3}\frac{p'}{p}\omega|\mathcal{M}|^2, \quad (1)$$

is determined by the matrix element (ME)

$$\mathcal{M} = \left\langle \psi_{\mathbf{p}'}^{(-)} \middle| \mathbf{e}^* \cdot \nabla \middle| \psi_{\mathbf{p}}^{(+)} \right\rangle \quad (2)$$

of the transition between the states $\psi_{\mathbf{p}}^{(+)}$ and $\psi_{\mathbf{p}'}^{(-)}$ of the continuous electron spectrum in the static atomic potential $U(r)$. For scattering by a Coulomb center, the 3D ME $\mathcal{M}$ can be calculated in terms of hypergeometric functions ${}_2F_1(a, b; c; x)$ [1, 2]. Moreover, it is possible in this case to analytically integrate cross section (1) over the directions of scattered electron and to express the BrS spectral distribution $d\sigma/d\omega$ in closed form in terms of the derivative of the squared modulus of function ${}_2F_1$ with respect to the argument (Sommerfeld formula [1, 3]). The calculation of cross section (1) for the general form of potential $U(r)$ is based on the use of multipole expansion of function $\psi_{\mathbf{p}}^{(\pm)}$ (see formula (15) below). In this case, the partial expansion of amplitude $\mathcal{M}$, which is convenient for analysis of the polarization-angular dependence of the cross section, has the form [4]

$$\mathcal{M} = Q(p, p', \theta)(\mathbf{e}^* \cdot \mathbf{p}) + Q(p', p, \theta)(\mathbf{e}^* \cdot \mathbf{p}'), \quad (3)$$

$$Q(p, p', \theta) = i\frac{2\pi^2}{m\sqrt{p^3 p'}}\sum_{l=1}^{\infty}[\exp(i\Delta_{l-})d_{l-1\,l}(E', E) + \exp(i\Delta_{l+})d_{l+1\,l}(E', E)]P_l^{(1)}(\cos\theta). \quad (4)$$

Here, $\Delta_{l\pm} = \delta_{l\pm1}(p') + \delta_l(p)$, $\delta_l(p)$ are the phases of scattering at potential $U(r)$, $P_l^{(1)}(x) = (d/dx)P_l(x)$ is the derivative of the Legendre polynomial $P_l(x)$, $E' = p'^2/2m = E - \hbar\omega$, and $\delta_{l'\,l}(E', E)$ are the radial MEs of

the momentum operator (see formula (37)). The spectral distribution $d\sigma/d\omega$ can also be written in the form of a partial series:

$$\frac{d\sigma}{d\omega} = \frac{8\pi^2 e^2 \hbar^5}{3m^2 c^3}\frac{\omega}{p^2} \times \sum_{l=1}^{\infty} l[|d_{l\,l-1}(E', E)|^2 + |d_{l-1\,l}(E', E)|^2]. \quad (5)$$

In the case of a Coulomb potential, this series can be summed directly (see [5], where the sum of series (5) written using the interaction operator in the "form of acceleration" is calculated analytically) and the Sommerfeld formula can be reproduced. Although such an approach is of rather methodical interest for Coulomb-type BrS, the partial wave analysis for a $U(r)$ potential of the general form is the only method of simplifying general formulas (1) and (2) without using additional approximations.

Apart from conventional BrS, the scattering of an electron at a force center can be accompanied by simultaneous emission of two spontaneous photons (double bremsstrahlung, 2BrS), which was considered for the first time in the general form by Heitler and Nordheim in 1934 [6] as a radiation correction to conventional BrS. In 1985, spontaneous 2BrS was detected experimentally (see [7] and subsequent publications [8], where the differential cross sections of emission of two bremsstrahlung photons during scattering of electrons with an energy of about 70 keV by thin targets were measured by the coincidence method). In experiments [9], spontaneous 2BrS was observed for electrons with energy of the order of 10 keV. The first theoretical calculations of the 2BrS cross section for electron scattering by a nucleus were made in the framework of the relativistic Born approximation [10]. The action of the Coulomb field on the electron in a 2BrS process can be taken into account exactly in the nonrelativistic dipole approximation. Using the Coulomb Green function, the 2BrS amplitude can be presented in the form of integrals of the hypergeometric function ${}_2F_1$ (a two-photon analog of the results obtained in [1, 2] for $\mathcal{M}$ in Eq. (2)). Different methods of calculation of two-photon amplitudes (with different representations of the Coulomb Green function) used by different authors lead to quantitatively equivalent expressions, but having different forms [11–13]. In particular, the integrated ("Born") terms were singled out in the amplitude in [13], which considerably simplifies analysis of the limiting cases. It is worth mentioning the effective approximate method of calculation of the 2BrS amplitude proposed by Korol [14] by taking into account only the contribution for δ-shaped singularities emerging for $E_2 \longrightarrow E_1$ in the single-photon MMs $d_{l_2 l_1}(E_2, E_1)$ appearing in the compound ME of the two-photon transition. This method was subsequently extended to nondipole calculations [15] and to the relativistic case [16]. Exact analytic expressions for the nonrelativistic 2BrS amplitude taking into account delay effects were obtained in [17, 18]. In addition to the above results obtained for the Coulomb potential, numerical calculations of spontaneous 2BrS were also made for electron scattering by neutral atoms both in the model of potential scattering [19] and in the model taking into account the polarization bremsstrahlung emitted by an atomic core [20].

In addition to spontaneous emission, considerable interest in multiquanta bremsstrahlung processes was stimulated by laser experiments, which made it possible to observe induced multiphoton bremsstrahlung emission and absorption in the optical frequency range. The first measurements of the cross sections of free–free electron transitions in the presence of a high-intensity laser wave were made in [21, 22]. Such experiments were subsequently repeated more than once with different atomic targets for different electron beam energies and experimental geometries (see, for example, [23] and review [24]). Quite general results could be obtained in the theoretical description of multiphoton transitions in the continuous spectrum in the Born and low-frequency approximations. In the Born case, the cross section $d\sigma^n$ of the n-photon induced emission ($n < 0$) and absorption ($n > 0$) in a laser field with amplitude F, polarization vector $\mathbf{e}$, and frequency ω has a simple form (the Bunkin–Fedorov formula [25]; see also [26]):

$$d\sigma^n = \frac{p'_n}{p} J_n^2\left(\frac{eF|\mathbf{e}\cdot(\mathbf{p}-\mathbf{p}'_n)|}{m\hbar\omega^2}\right) d\sigma_B, \quad (6)$$

where J_n is the Bessel function, $d\sigma_B$ is the Born elastic scattering cross section in the absence of a light wave, and momenta p and p'_n in the initial and final states are associated with the energy conservation law: $(p'^2_n - p^2)/2m = n\hbar\omega$. It was shown in [27] that the Born series can be summed exactly in the low-frequency limit ($\omega \longrightarrow 0$) so that cross section $d\sigma^n$ also has factorized form (6) in which $d\sigma_B$ is replaced by the exact elastic scattering cross section $d\sigma_0$ in zero light field even for slow electrons for which $\hbar\omega \ll E$. It should be noted that, although various versions were proposed for deriving the low-frequency asymptotic form (see, for example, [28, 29]), the limits of applicability of the Kroll–Watson approximation [27] disregarding the action of the laser field on the dynamics of interaction between a slow electron and the atomic potential are still a subject of discussions [30–33]. In [34], the expression for $d\sigma^n$ was derived in the approximation in which the motion of an electron is described classically and the emission and absorption processes are described quantum-mechanically. Various versions of generalization of the results obtained in [25, 27] taking into account the effects of a strong laser field are given, for example, in review [35]; however, the scattering potential can be taken into account exactly only in per-

turbation theory in the field of the wave. In particular, such calculations for the Coulomb-type double bremsstrahlung emission and absorption is completely identical to the case of spontaneous 2BrS [11–13]. However, a special situation emerges in the case of elastic reemission of photons: both MEs determining the transition amplitude are diverging; consequently, we must eliminate the divergence to obtain a finite result [13, 36]. In addition to purely stimulated transitions induced by a high-intensity laser field, the latter may modify spontaneous BrS also. This question was investigated in [37] in the Born approximation. A more detailed inclusion of the effects of an atomic (Coulomb) potential was carried out in [38, 39]. It is also appropriate to mention publications [40, 41], in which "combined" Compton-type bremsstrahlung processes (absorption of a laser photon by an electron followed by spontaneous BrS in the field of the nucleus) were considered.

In view of the difficulties encountered in the experimental determination of the polarization characteristics of spontaneous BrS, the energy and angular dependences of cross sections have been mainly analyzed in publications devoted to spontaneous bremsstrahlung processes. On the contrary, in the case of induced processes, the possibility of controllable variation of laser polarization opens new prospects for studying the free–free transitions, which stimulates an analysis of polarization effects in bremsstrahlung processes. A generalization of the results obtained by Kroll and Watson [27] to the case of elliptic polarization of laser radiation is considered in [31, 42]. A considerable difference in the one- and two-photon scattering cross sections in the cases of linear and circular laser polarizations for electrons scattered by hydrogen [43] and helium [44] atoms is demonstrated in [43, 44]. However, the most impressive polarization effect is the dichroism manifested in the difference in the cross sections for the opposite polarities of the degree of circular polarization of photons. It was found [4] that the differential cross section of single-photon BrS for electron scattering by a nucleus differs significantly for photons with right and left circular polarizations (circular dichroism, CD). A general analysis of the CD in bremsstrahlung in the case when an electron is scattered by an atom with a nonzero angular momentum was carried out in [45]. The polarization dependence of corrections to the Coulomb scattering, which are associated with the effect of the light wave, was studied in [13, 36]. The CD effect is sensitive to the electron energy and the photon frequency and vanishes in the Born limit as well as in the low-frequency limit and for small scattering angles. Outside these regions, CD has a noticeable magnitude and is quite accessible for experimental observation. It should be noted that CD in photoprocesses with nonpolarized atomic targets is an essentially quantum-mechanical interference effect, which is absent, in particular, in the classical analysis of BrS in a strong laser field [46]. At the same time, numerical quantum calculations of single-photon Coulomb BrS, which are not confined to perturbation theory in the laser field [47] indicate significant CD. Electron scattering by a hydrogen atom in the presence of two fields with linear and circular polarizations is considered in [48]. The emergence of dichroism effects in the presence of the two fields is quite obvious; in this case, CD differs from zero for certain geometries of the fields for fast (Born) electrons also and in the total cross section.

It was noted above that the first Born approximation is insufficient for correctly describing the polarization effect, and the interaction of an electron with the target must be taken into account more exactly; this involves considerable difficulties for processes with two or more photons even in the framework of perturbation theory in the electron interaction with radiation. Since the problem has several vector parameters, the separation of dynamic (depending on the energy and structure of the potential) and kinematic (depending on the photon polarization and the geometry of the problem) factors in the general expressions for cross sections is of prime importance. We will carry out partial-wave analysis of two-photon free–free transitions as applied to potential scattering $U(r)$ both in the field and by atoms with nonzero angular momentum. General results are illustrated by analytic and numerical calculations for scattering by a Coulomb potential. In Section 2, the analytic expression for the amplitude of two-photon dipole transitions is simplified to the maximum possible extent for the case of a central potential $U(r)$, which generalizes results (3) and (4) to the case of single-photon BrS. In contrast to binomial expression (3), the two-photon amplitude in the general case of different photons can be written in the form of five products of invariant (independent of photon polarizations) atomic parameters Q_i and the scalar products of photon polarization vectors by the initial and final electron momenta. By analogy with Eq. (4), parameters Q_i are presented in the form of a series of products of the second-order radial MEs $M_{l'l}^{L=l\pm1}$ between the states of the continuum with fixed values of the orbital angular momenta l and l' and the Legendre polynomials in the scattering angle θ. Such a form of representing the amplitude makes it possible to obtain explicit expressions for the atomic parameters that describe dichroic polarization effects depending on the sign of the photon helicity (Subsection 2.3) and to demonstrate, in particular, a new dichroic effect, viz., elliptic dichroism (ED), which emerges in induced two-photon processes along with CD and vanishes in the case of a purely circular laser field polarization. The optimal conditions for the observation of CD and ED are analyzed. Closed analytic expressions for the Coulomb MEs $M_{l'l}^{L}$ are obtained in Section 3 (see also Appendix B) in the form of the sum of the MEs $d_{l_2l_1}(E', E)$ for conventional bremsstrahlung and a single integral of the function ${}_2F_1$. In Section 4, elastic two-photon transitions are considered and it is

shown that singularities appearing in $M^L_{l'l}$ in the case when the energy difference between the initial and final states becomes insignificant ($E' \longrightarrow E$) are compensated in the calculation of the invariant parameters Q_i^{el}, for which explicit analytic expressions are derived in the case of Coulomb scattering. The limiting ranges of low and high photon frequencies are investigated, and simple asymptotic forms of inelastic scattering amplitudes are obtained for the central field $U(r)$ in Section 5. The frequency and energy dependences of the Coulomb radial MEs and the accuracy of approximate methods of computation are discussed in Subsection 6.1. The results for the angular distributions and the polarization dependence of induced two-photon emission and absorption are given in Subsection 6.2, where the numerical values of the cross sections of one- and two-photon bremsstrahlung transitions are compared. The analytic formulas derived by us for the Coulomb MEs $M^L_{l'l}$ are the most general expressions for the amplitudes of two-photon transitions in the Coulomb field between the states with fixed orbital angular momenta l and l'. It is shown in Appendix B that the well-known results for the case when both states or one state belong to the discrete spectrum can be obtained from these formulas by the analytic continuation in energy ($p \longrightarrow imZe^2/n\hbar$ and/or $p' \longrightarrow imZe^2/n'\hbar$) [49].

In the subsequent analysis, we will use the atomic system of units.

2. POLARIZATION–ANGULAR STRUCTURE OF CROSS SECTIONS OF TWO-PHOTON BREMSSTRAHLUNG PROCESSES

2.1. General Formulas

The amplitude of a two-photon electron transition between two scattering states with asymptotic momenta $\mathbf{p}_i \equiv \mathbf{p}$ and $\mathbf{p}_f \equiv \mathbf{p}'$ in potential $U(r)$ is determined by the second-order ME in perturbation theory (cf. Eq. (2)):

$$M(\mathbf{e}_2, \mathbf{e}_1, \mathscr{E}) = -\left\langle \psi^{(-)}_{\mathbf{p}'} \middle| (\mathbf{e}_2 \cdot \nabla') G_{\mathscr{E}}(\mathbf{r}', \mathbf{r}) (\mathbf{e}_1 \cdot \nabla) \middle| \psi^{(+)}_{\mathbf{p}} \right\rangle, \tag{7}$$

where $\psi^{(-)}_{\mathbf{p}'}(\mathbf{r})$ and $\psi^{(+)}_{\mathbf{p}}(\mathbf{r})$ are the wave functions of the continuum with the asymptotic forms of converging (–) and diverging (+) waves, normalized by the condition

$$\langle \psi^{(\pm)}_{\mathbf{p}'} | \psi^{(\pm)}_{\mathbf{p}} \rangle = (2\pi)^3 \delta(\mathbf{p}' - \mathbf{p}),$$

and $G_{\mathscr{E}}$ is Green's function of the Hamiltonian with potential $U(r)$ and with the asymptotic form for diverging waves for $\mathscr{E} > 0$. The differential cross section of a spontaneous 2BrS with the photon emission in directions $\mathbf{k}_1$ and $\mathbf{k}_2$ ($|\mathbf{k}_i| = 1$, $\mathbf{e}_i \cdot \mathbf{e}_i^* = 1, i = 1, 2$) has the form

$$\frac{d\sigma^5}{d\Omega_{\mathbf{p}'} d\Omega_{\mathbf{k}_1} d\Omega_{\mathbf{k}_2} d\omega_1 d\omega_2} = \frac{\alpha^6}{(2\pi)^6} \frac{p'}{p} \omega_1 \omega_2 \times \left| M(\mathbf{e}_2^*, \mathbf{e}_1^*, E - \omega_1) + M(\mathbf{e}_1^*, \mathbf{e}_2^*, E - \omega_2) \right|^2. \tag{8}$$

For an electron scattered by a force center $U(r)$ in the presence of a high-intensity light wave whose electric vector is written in the form

$$\mathbf{F}(t) = F \mathrm{Re}\{\mathbf{e} \exp(-i\omega t)\}, \quad \mathbf{e} \cdot \mathbf{e}^* = 1,$$

induced multiphoton processes are of prime importance. Induced two-photon transitions determine double bremsstrahlung emission and absorption as well as the correction to the elastic scattering cross section, which is linear in the wave intensity $I = cF^2/4\pi$. The cross sections of the above-mentioned processes are also determined by ME (7). For example, the differential (with respect to the angles of a scattered electron) induced 2BrS cross section has the form

$$\frac{d\sigma}{d\Omega_{\mathbf{p}'}} = \frac{1}{4\pi^2} \left(\frac{F}{2\omega} \right)^4 \frac{p'}{p} |M(\mathbf{e}^*, \mathbf{e}^*, \mathscr{E})|^2, \tag{9}$$

where the electron energy $\mathscr{E}$ in the intermediate state is connected to the energies in the initial ($E = p^2/2$) and final ($E' = p'^2/2$) states through the relation $\mathscr{E} = E - \omega = E' + \omega$. Similarly, the double bremsstrahlung absorption cross section is given by

$$\frac{d\sigma}{d\Omega_{\mathbf{p}'}} = \frac{1}{4\pi^2} \left(\frac{F}{2\omega} \right)^4 \frac{p'}{p} |M(\mathbf{e}, \mathbf{e}, \mathscr{E})|^2, \tag{10}$$

where $\mathscr{E} = E + \omega = E' - \omega$.

In the case of elastic scattering ($E' = E$), the inclusion of the interaction with the light wave in the lowest (second) order of perturbation theory gives a correction to the amplitude linear in wave intensity,

$$f = f_0 + f_2, \tag{11}$$

where f_0 is the amplitude of elastic scattering by potential $U(r)$ in the absence of a light wave, while

$$f_2 = \frac{1}{2\pi} \left(\frac{F}{2\omega} \right)^2 \times [M(\mathbf{e}, \mathbf{e}^*, E - \omega) + M(\mathbf{e}^*, \mathbf{e}, E + \omega)] \tag{12}$$

is the correction associated with the two-photon transition induced by the wave (reemission of a photon by an electron during scattering, Fig. 1). A correction on the order of F^2 to the elastic scattering cross section is determined by the interference of amplitudes f_0 and f_2:

$$\frac{d\sigma}{d\Omega_{\mathbf{p}'}} = |f_0|^2 + 2\mathrm{Re}(f_0^* f_2). \tag{13}$$

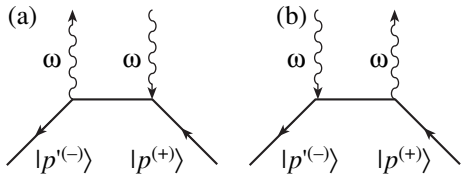

Fig. 1. Feynman diagrams for reemission of a photon by an electron in the continuum.

2.2. Partial-Wave Expansion of the Amplitude

Since $\mathbf{e}_1$ and $\mathbf{e}_2$ appear linearly in Eq. (7), ME $M(\mathbf{e}_2, \mathbf{e}_1, \mathscr{E})$ can be presented as the sum of the products of linearly independent combinations of vectors $\mathbf{e}_1$, $\mathbf{e}_2$ and $\mathbf{n}$, $\mathbf{n}'$ (where $\mathbf{n} = \mathbf{p}/p$ and $\mathbf{n}' = \mathbf{p}'/p'$) and the invariant amplitudes $\mathscr{P}_i$ depending only on p, p', $\mathscr{E}$, and the angle θ between $\mathbf{n}$ and $\mathbf{n}'$. There are five linearly independent combinations $\mathbf{e}_1$, $\mathbf{e}_2$ and $\mathbf{n}$, $\mathbf{n}'$; choosing these combinations appropriately, we can write $M(\mathbf{e}_2, \mathbf{e}_1, \mathscr{E})$ in the form

$$\begin{aligned} M(\mathbf{e}_2, \mathbf{e}_1, \mathscr{E}) &= \mathscr{P}_1(\mathbf{e}_2 \cdot \mathbf{n})(\mathbf{e}_1 \cdot \mathbf{n}) \\ &+ \mathscr{P}_2(\mathbf{e}_2 \cdot \mathbf{n}')(\mathbf{e}_1 \cdot \mathbf{n}') + \mathscr{P}_3(\mathbf{e}_2 \cdot \mathbf{n})(\mathbf{e}_1 \cdot \mathbf{n}') \\ &+ \mathscr{P}_4(\mathbf{e}_2 \cdot \mathbf{n}')(\mathbf{e}_1 \cdot \mathbf{n}) + \mathscr{P}_5(\mathbf{e}_2 \cdot \mathbf{e}_1). \end{aligned} \tag{14}$$

It should be noted that the analytic expressions for the amplitude of two-photon transitions in the Coulomb field, derived in [11–13] without using partial expansions, have exactly the same structure. The explicit form of the amplitudes $\mathscr{P}_i = \mathscr{P}_i(p, p', \theta, \mathscr{E})$ for an arbitrary potential $U(r)$ can be obtained only by specific calculations of ME (7). A general method for simplifying expressions of form (7) is the use of multipole expansions of the wave functions and operators appearing in Eq. (7), followed by integration with respect to angular variables by the methods of quantum theory for angular momentum [50]. Let us write the wave functions and Green's function in Eq. (7) in the form of expansions in spherical functions:

$$\begin{aligned} \psi_{\mathbf{p}}^{(\pm)}(\mathbf{r}) &= \frac{(2\pi)^{3/2}}{\sqrt{p}} \\ &\times \sum_{lm} i^l \exp(\pm i\delta_l(p)) R_{El}(r) Y_{lm}\left(\frac{\mathbf{r}}{r}\right) Y_{lm}^*(\mathbf{n}), \end{aligned} \tag{15}$$

$$G_{\mathscr{E}}(\mathbf{r}, \mathbf{r}') = \sum_{LM} g_L(r, r', \mathscr{E}) Y_{LM}\left(\frac{\mathbf{r}}{r}\right) Y_{LM}^*\left(\frac{\mathbf{r}'}{r'}\right),$$

where $R_{El}(r)$ are the radial functions of the continuum in potential $U(r)$, normalized to energy, and $\delta_l(p)$ are scattering phases. Substituting expressions (15) into Eq. (7), integrating with respect to angles, and carrying out summation over the angular momenta components, we obtain

$$\begin{aligned} M(\mathbf{e}_2, \mathbf{e}_1, \mathscr{E}) &= -\frac{(2\pi)^3}{\sqrt{pp'}} \\ &\times \sum_{c=0}^{2} \sum_{ll'L} i^{l+l'} \exp[i(\delta_{l'}(p') + \delta_l(p))] \\ &\times \begin{Bmatrix} 1 & 1 & c \\ l' & l & L \end{Bmatrix} \langle R_{E'l'} \| \nabla g_L \nabla \| R_{El} \rangle \\ &\times (\{\mathbf{e}_2 \otimes \mathbf{e}_1\}_c \cdot \{Y_{l'}(\mathbf{n}') \otimes Y_l(\mathbf{n})\}_c) \end{aligned} \tag{16}$$

(we will use below the standard notation in the quantum theory of angular momentum [50]).

Expressions of type (16) are usually considered as the final result of analytic transformations of the "geometrical" part of the amplitudes by the methods of quantum theory of angular momentum, and subsequent calculations are based on numerical computations of tensor constructions in Eq. (16) in an appropriately chosen system of coordinates (see, for example, the publications [30] on the induced one- and two-photon emission and absorption in a linearly polarized field; it should be noted that the function $\psi_{\mathbf{p}'}^{(\pm)}(\mathbf{r})$ with the asymptotic form for diverging waves is groundlessly used by the author of [30] as the final state of ME (2) and (7)). A special technique for simplifying tensor products of the spherical functions $Y_{lm}(\mathbf{n})$ based on the reduced formula for bipolar harmonics $Y_{LM}^{l'l}(\mathbf{n}', \mathbf{n})$ defined as

$$\begin{aligned} Y_{LM}^{l'l}(\mathbf{n}', \mathbf{n}) &= \{Y_{l'}(\mathbf{n}') \otimes Y_l(\mathbf{n})\}_{LM} \\ &= \sum_{mm'} C_{l'm'lm}^{LM} Y_{l'm'}(\mathbf{n}') Y_{lm}(\mathbf{n}) \end{aligned} \tag{17}$$

was developed in [45] (see also [51]). This technique makes it possible to present $Y_{LM}^{k,L-k}(\mathbf{n}', \mathbf{n})$ with arbitrary values of l, $l' > L$ in the form of a finite sum of "minimal" harmonics $Y_{LM}^{k,L-k}(\mathbf{n}', \mathbf{n})$ with $0 \le k \le L$ and Legendre polynomials. For example, for the bipolar harmonic $Y_{2m}^{ll}(\mathbf{n}', \mathbf{n})$, we have [45]

$$\begin{aligned} Y_{2m}^{ll}(\mathbf{n}', \mathbf{n}) &= \frac{(-1)^{l-1}}{4\pi}\left[\frac{30(2l+1)}{(2l-1)l(l+1)(2l+3)}\right]^{1/2} \\ &\times (P_l^{(1)}(x)\{\mathbf{n}' \otimes \mathbf{n}\}_{2m} \\ &+ P_l^{(2)}(x)\{[\mathbf{n}' \times \mathbf{n}] \otimes [\mathbf{n}' \times \mathbf{n}]\}_{2m}), \end{aligned} \tag{18}$$

where $x = \mathbf{n} \cdot \mathbf{n}' = \cos\theta$ and $P_l^{(k)}(x) = (d/dx)^k P_l(x)$. The expressions for the remaining bipolar harmonics $Y_{cm}^{l'l}(\mathbf{n}', \mathbf{n})$ with $c = 0, 1, 2$, which appear in Eq. (16), are also given in [45]. Using these expressions and writing the appearing tensor constructions in the form ($\{\mathbf{e}_2 \otimes$

$\mathbf{e}_1\}_c \cdot \{\mathbf{n}' \otimes \mathbf{n}\}_c$) in terms of the scalar products of vectors $\mathbf{e}_1$, $\mathbf{e}_2$, and $\mathbf{n}$, $\mathbf{n}'$ (Section 3 in [50]), we can reduce expression (16) for $M(\mathbf{e}_2, \mathbf{e}_1, \mathscr{E})$ to the form (14). It is convenient to write the final result in the form

$$\begin{aligned} M(\mathbf{e}_2, \mathbf{e}_1, \mathscr{E}) &= Q_1\Big[(\mathbf{e}_2\cdot\mathbf{n})(\mathbf{e}_1\cdot\mathbf{n}) - \frac{1}{3}(\mathbf{e}_2\cdot\mathbf{e}_1)\Big] \\ &+ Q_2\Big[(\mathbf{e}_2\cdot\mathbf{n}')(\mathbf{e}_1\cdot\mathbf{n}') - \frac{1}{3}(\mathbf{e}_2\cdot\mathbf{e}_1)\Big] \\ &+ \frac{1}{2}Q_3\Big[(\mathbf{e}_2\cdot\mathbf{n}')(\mathbf{e}_1\cdot\mathbf{n}) + (\mathbf{e}_2\cdot\mathbf{n})(\mathbf{e}_1\cdot\mathbf{n}') \\ &- \frac{2}{3}(\mathbf{n}\cdot\mathbf{n}')(\mathbf{e}_2\cdot\mathbf{e}_1)\Big] \\ &+ Q_4[(\mathbf{e}_2\cdot\mathbf{n}')(\mathbf{e}_1\cdot\mathbf{n}) - (\mathbf{e}_2\cdot\mathbf{n})(\mathbf{e}_1\cdot\mathbf{n}')] + Q_5(\mathbf{e}_2\cdot\mathbf{e}_1), \end{aligned} \tag{19}$$

where

$$\begin{aligned} Q_1 &= -\sum_{l=2}^{\infty}\Big[\frac{1}{2l+3}(\mathcal{M}_{ll}^{l+1} + \mathcal{M}_{l+2\,l}^{l+1}) \\ &+ \frac{1}{2l-1}(\mathcal{M}_{ll}^{l-1} + \mathcal{M}_{l-2\,l}^{l-1})\Big]P_l^{(2)}(x), \\ Q_2 &= -\sum_{l=2}^{\infty}\Big[\frac{1}{2l+3}(\mathcal{M}_{ll}^{l+1} + \mathcal{M}_{l\,l+2}^{l+1}) \\ &+ \frac{1}{2l-1}(\mathcal{M}_{ll}^{l-1} + \mathcal{M}_{l\,l-2}^{l-1})\Big]P_l^{(2)}(x), \\ Q_3 &= \sum_{l=1}^{\infty}\Big[\frac{1}{2l-1}\mathcal{M}_{l\,l}^{l-1} + \frac{1}{2l+3}M_{l\,l}^{l+1}\Big]P_l^{(1)}(x) \\ &+ 2\sum_{l=2}^{\infty}\Big[\Big(\frac{1}{2l-1}\mathcal{M}_{l\,l}^{l-1} + \frac{1}{2l+3}\mathcal{M}_{l\,l}^{l+1}\Big)x \\ &+ \frac{1}{2l+1}(\mathcal{M}_{l-1\,l+1}^{l} + \mathcal{M}_{l+1\,l-1}^{l})\Big]P_l^{(2)}(x), \\ Q_4 &= \frac{1}{2}\sum_{l=1}^{\infty}[\mathcal{M}_{l\,l}^{l-1} - \mathcal{M}_{l\,l}^{l+1}]P_l^{(1)}(x), \\ Q_5 &= \frac{1}{3}\sum_{l=0}^{\infty}[l\mathcal{M}_{l\,l}^{l-1} + (l+1)\mathcal{M}_{l\,l}^{l+1}]P_l(x). \end{aligned} \tag{20}$$

Radial MEs $M_{l'\,l}^{L}$ contain the phase factors from relations (15):

$$\begin{aligned} \mathcal{M}_{l'\,l}^{L} &= (2\pi^2/\sqrt{pp'}) \\ &\times \exp[i(\delta_{l'}(p') + \delta_l(p))]M_{l'\,l}^{L}(E', E, \mathscr{E}), \\ M_{l'\,l}^{L}(E', E, \mathscr{E}) &= \langle D(L, l')R_{E'l'}|g_L(\mathscr{E})|D(L, l)R_{El}\rangle, \\ D(l_1, l_2) &= \frac{d}{dr} + \frac{\mathrm{sgn}(l_2 - l_1)\max(l_1, l_2) + 1}{r}. \end{aligned} \tag{21, 22}$$

Formulas (20) give five invariant parameters Q_i (which are obviously associated with $\mathscr{P}_i$ in Eq. (14)) in explicit form in terms of radial MEs. Relations (20) directly demonstrate the symmetry properties,

$$Q_1(p, p') = Q_2(p', p), \quad Q_{3,4,5}(p', p) = Q_{3,4,5}(p, p').$$

2.3. Effects of Circular and Elliptic Dichroism in free–free Transitions

Parametrization of the amplitude in the form (19) and (20) makes it possible to completely analyze the polarization and angular dependences both in spontaneous 2BrS (with different polarizations $\mathbf{e}_1$ and $\mathbf{e}_2$) and for induced processes (with $\mathbf{e}_1 = \mathbf{e}_2$). Let us first consider induced 2BrS (the results for double bremsstrahlung absorption follow from the formulas given below with the substitution $\mathbf{e}, \omega \longrightarrow \mathbf{e}^*, -\omega$). Assuming that $\mathbf{e}_1 = \mathbf{e}_2 = \mathbf{e}^*$ in Eq. (19), we see that parameter Q_4 for induced processes is omitted and the expression for M has the form

$$\begin{aligned} M &= Q_1(\mathbf{e}^*\cdot\mathbf{n})^2 + Q_2(\mathbf{e}^*\cdot\mathbf{n}')^2 \\ &+ Q_3(\mathbf{e}^*\cdot\mathbf{n})(\mathbf{e}^*\cdot\mathbf{n}') + \mathcal{Q}(\mathbf{e}^*\cdot\mathbf{e}^*), \\ \mathcal{Q} &= Q_5 - \frac{1}{3}(Q_1 + Q_2 + xQ_3). \end{aligned} \tag{23}$$

As a result, cross section (9) assumes the form

$$\frac{d\sigma}{d\Omega_{\mathbf{p}'}} = \frac{1}{4\pi^2}\Big(\frac{F}{2\omega}\Big)^4\frac{p'}{p}(f_{\mathrm{reg}} + \Delta_{\mathrm{CD}} + \Delta_{\mathrm{ED}}), \tag{24}$$

where

$$\begin{aligned} f_{\mathrm{reg}} &= |Q_1|^2|\mathbf{e}\cdot\mathbf{n}|^4 + |Q_2|^2|\mathbf{e}\cdot\mathbf{n}'|^4 + |Q_3|^2|\mathbf{e}\cdot\mathbf{n}|^2|\mathbf{e}\cdot\mathbf{n}'|^2 \\ &+ l^2|\mathcal{Q}|^2 + 2\mathrm{Re}(Q_1^*Q_2)\mathrm{Re}\{(\mathbf{e}\cdot\mathbf{n})^2(\mathbf{e}^*\cdot\mathbf{n}')^2\} \\ &+ 2\mathrm{Re}(Q_1^*Q_3)|\mathbf{e}\cdot\mathbf{n}|^2\mathrm{Re}\{(\mathbf{e}\cdot\mathbf{n})(\mathbf{e}^*\cdot\mathbf{n}')\} \\ &+ 2l\mathrm{Re}(Q_1^*\mathcal{Q})\mathrm{Re}\{(\mathbf{e}\cdot\mathbf{n})^2\} \\ &+ 2\mathrm{Re}(Q_2^*Q_3)|\mathbf{e}\cdot\mathbf{n}'|^2\mathrm{Re}\{(\mathbf{e}\cdot\mathbf{n}')(\mathbf{e}^*\cdot\mathbf{n})\} \\ &+ 2l\mathrm{Re}(Q_2^*\mathcal{Q})\mathrm{Re}\{(\mathbf{e}\cdot\mathbf{n}')^2\} \\ &+ 2l\mathrm{Re}(Q_3^*\mathcal{Q})\mathrm{Re}\{(\mathbf{e}\cdot\mathbf{n})(\mathbf{e}\cdot\mathbf{n}')\}, \end{aligned} \tag{25}$$

$$\Delta_{CD} = 2\mathrm{Im}\{(\mathbf{e}\cdot\mathbf{n})(\mathbf{e}^*\cdot\mathbf{n}')\}(\mathrm{Im}(Q_2^*Q_3)|\mathbf{e}\cdot\mathbf{n}'|^2 \quad (26)$$
$$-2\mathrm{Im}(Q_1^*Q_2)\mathrm{Re}\{(\mathbf{e}\cdot\mathbf{n})(\mathbf{e}^*\cdot\mathbf{n}')\} - \mathrm{Im}(Q_1^*Q_3)|\mathbf{e}\cdot\mathbf{n}|^2),$$

$$\Delta_{ED} = -2l(\mathrm{Im}(Q_1^*\mathcal{Q})\mathrm{Im}\{(\mathbf{e}\cdot\mathbf{n})^2\} + \mathrm{Im}(Q_2^*\mathcal{Q})\mathrm{Im}\{(\mathbf{e}\cdot\mathbf{n}')^2\} + \mathrm{Im}(Q_3^*\mathcal{Q})\mathrm{Im}\{(\mathbf{e}\cdot\mathbf{n})(\mathbf{e}\cdot\mathbf{n}')\}). \quad (27)$$

Obviously, f_{reg} remains unchanged upon the substitution $\mathbf{e} \rightleftarrows \mathbf{e}^*$, i.e., is independent of the sign of photon helicity. In order to analyze Δ_{CD} and Δ_{ED}, it is convenient to write the unit complex polarization vector in an invariant (relative to the choice of the coordinate system) form,

$$\mathbf{e} = \frac{\boldsymbol{\epsilon} + i\eta[\mathbf{k}\times\boldsymbol{\epsilon}]}{\sqrt{1+\eta^2}}, \quad -1 \le \eta \le 1, \quad (28)$$

where the unit vectors $\boldsymbol{\epsilon}$ and $\mathbf{k}$ define the directions of the principal axis of the polarization ellipse and of the propagation of waves, while ellipticity η is connected to the degrees of linear (l) and circular (ξ) polarizations, which we define as in [3]:

$$l = \frac{1-\eta^2}{1+\eta^2} = \mathbf{e}\cdot\mathbf{e} = \mathbf{e}^*\cdot\mathbf{e}^*,$$
$$\xi = \frac{2\eta}{1+\eta^2} = i\mathbf{k}\cdot[\mathbf{e}^*\times\mathbf{e}].$$

Using relations (28), we can easily find that

$$2\mathrm{Im}\{(\mathbf{e}^*\cdot\mathbf{n})(\mathbf{e}\cdot\mathbf{n}')\} = \xi(\mathbf{k}\cdot[\mathbf{n}\times\mathbf{n}']),$$
$$2\mathrm{Im}\{(\mathbf{e}\cdot\mathbf{n})(\mathbf{e}\cdot\mathbf{n}')\} = \xi\{(\boldsymbol{\epsilon}\cdot\mathbf{n})([\mathbf{k}\times\boldsymbol{\epsilon}]\cdot\mathbf{n}') + (\boldsymbol{\epsilon}\cdot\mathbf{n}')([\mathbf{k}\times\boldsymbol{\epsilon}]\cdot\mathbf{n})\}, \quad (29)$$

so that

$$\Delta_{CD} \sim \xi, \quad \Delta_{ED} \sim \xi l. \quad (30)$$

Relations (30) show that the last two terms in Eq. (24) lead to a dependence of the cross section on the sign of ξ and describe the CD and ED effects. The value of Δ_{ED} vanishes for purely circular polarization ($\xi = \pm 1$, $l = 0$), while the CD term Δ_{CD} attains its maximum value in this case. Although the quantitative results for CD and ED can be obtained only from numerical calculations, the distinguishing features of these effects can be seen even from general formulas (24)–(27). In particular, the CD and ED terms in Eq. (24) exhibit essentially different dependences not only on the polarization parameters of the waves, but also on the geometry of the process. For example, the term Δ_{CD} contains the common polarization-angular factor $\xi(\mathbf{k}\cdot[\mathbf{n}\times\mathbf{n}'])$ (see relations (29)) and attains the "geometrical" maximum for a light wave propagating orthogonally to the plane of electron scattering: $\mathbf{k} \parallel \pm[\mathbf{n}\mathbf{n}']$. In this case, the term Δ_{CD} has the form

$$\Delta_{CD} = \xi\sin\theta \times [2\mathrm{Im}(Q_1^*Q_2)\cos\theta + \mathrm{Im}(Q_1^*Q_3) - \mathrm{Im}(Q_2^*Q_3)]. \quad (31)$$

If, however, the initial electron momentum is collinear to the direction of wave propagation ($\mathbf{n}\times\mathbf{k} = 0$), CD vanishes in the same way as in the case of forward and backward scattering, $\mathbf{n}' = \pm\mathbf{n}$. It should be noted that the kinematic factor $\xi(\mathbf{k}\cdot[\mathbf{a}\times\mathbf{b}])$ determining Δ_{CD} is universal by nature and describes CD in various single-phonon processes with nonpolarized atoms in the presence of two polar vectors, **a** and **b**, say, in the case of conventional and induced single-photon BrS [4] and two-electron ionization of an atom by a hard photon [45, 52]. ED is possible only in processes with two or more identical photons and is less sensitive to the process geometry; in accordance with Eq. (27), the necessary condition for vanishing Δ_{CD} is simultaneous fulfillment of the conditions $\mathbf{e}\cdot\mathbf{n} = 0$ and $\mathbf{e}\cdot\mathbf{n}' = 0$. The ED effect is manifested in "pure form" (without CD accompanying it) in the angular distribution of scattered electrons, when the initial momentum **p** is collinear to the light beam, $[\mathbf{k}\times\mathbf{n}] = 0$. In this case, only the terms with $\mathcal{Q}$ and Q_2 remain in relation (23) and Δ_{ED} has the simple form

$$\Delta_{ED} = -2l\mathrm{Im}(Q_2^*\mathcal{Q})\mathrm{Im}\{(\mathbf{e}\cdot\mathbf{n}')^2\} = -2l\xi\mathrm{Im}(Q_2^*\mathcal{Q})(\boldsymbol{\epsilon}\cdot\mathbf{n}')(\mathbf{k}\cdot[\boldsymbol{\epsilon}\times\mathbf{n}']) \quad (32)$$

and attains its maximum value for scattering at right angles (i.e., in the polarization plane) in the directions forming the angles $\pm\pi/4$ and $\pm 3\pi/4$ with the direction of the principal axis of the polarization ellipse.

In contrast to CD, the ED effect persists in the cross section of the induced 2BrS (or double bremsstrahlung absorption), integrated over the directions $\mathbf{n}'$ of a scattered electron momentum. In this case, the cross section depends only on vectors **e** and **n** and has the following structure:

$$\sigma = \frac{1}{4\pi^2}\left(\frac{F}{2\omega}\right)^4\frac{p'}{p}(A_1 + A_2l^2 + A_3l\mathrm{Re}\{(\mathbf{e}\cdot\mathbf{n})^2\} + A_4l\xi(\boldsymbol{\epsilon}\cdot\mathbf{n})(\boldsymbol{\epsilon}\cdot[\mathbf{n}\times\mathbf{k}]) + A_5|\mathbf{e}\cdot\mathbf{n}|^2 + A_6|\mathbf{e}\cdot\mathbf{n}|^4). \quad (33)$$

It can be seen that the ED term in the expression for σ attains its maximum value when the initial electron momentum **p** is orthogonal to the direction of the light beam and forms an angle of $\pi/4$ with principal axis of the polarization ellipse. It should be noted that expression (33) is completely identical kinematically to the angular distribution of photoelectrons in the case of two-photon ionization of an atom with a nonzero orbital angular momentum in an elliptically polarized

field (polarization effects and ED in this problem were analyzed in [53]). We can derive explicit expressions for dynamic parameters A_i in relation (33) in terms of radial MEs (21) by integrating the squared modulus of amplitude (16) with respect to $\mathbf{n}'$. By way of an example, we consider only the expression for the "dichroic parameter" A_4:

$$A_4 = \frac{16\pi^5}{pp'}\sum_{l=0}^{\infty}\mathrm{Im}\left\{\frac{l(l+1)}{(2l-1)(2l+3)}M_{ll}^{l-1}M_{ll}^{l+1*}\right.$$
$$+ (lM_{ll}^{l-1} + (l+1)M_{ll}^{l+1})$$
$$\times\left[\frac{(l+1)(l+2)}{(2l+1)(2l+3)}e^{i(\delta_l(p)-\delta_{l+2}(p))}M_{l\,l+2}^{l+1*}\right.$$
$$\left.\left.+\frac{l(l-1)}{(2l-1)(2l+1)}e^{i(\delta_l(p)-\delta_{l-2}(p))}M_{l\,l-2}^{l-1*}\right]\right\}.$$

In all investigated cases, the numerical values of dichroic parameters (Δ_{CD}, Δ_{ED}, and A_4) in the cross sections is determined in the long run by the relation between the real and imaginary parts of the radial ME $\mathcal{M}_{l'\,l}^{L}$, i.e., by the interference of Hermite and anti-Hermite parts of the process amplitude. Consequently, dichroism effects disappear in the Born electron energy range E and E' as well as in the low-frequency limit (see Section 5 below, where it is proved that the parameters Q_i differ in this limit differ only in the real multipliers so that $\mathrm{Im}(Q_i^*Q_j) = 0$). In the remaining cases, the dichroic terms in the cross section have no smallness parameter symbols and the relative magnitude of the dichroism effects (in a favorable geometry of the process) may be as high as 100%. Thus, in contrast to single-photon bremsstrahlung processes in which only the CD effect can take place and the cross section of elliptical polarization can be reconstructed from experimental data for linear and circular polarizations, the fullest information on the process in the case of double-photon bremsstrahlung emission and absorption can be obtained only from a light wave with an elliptical polarization.

It should be borne in mind in an analysis of polarization effects in elastic scattering that $Q_1 = Q_2$ for $E' = E$, and, hence, the correction to the elastic cross section in Eq. (13) contains four invariant parameters Q_i^{el}:

$$\frac{d\sigma}{d\Omega_{\mathbf{p}'}} = |f_0|^2 + \frac{1}{\pi}\left(\frac{F}{2\omega}\right)^2$$
$$\times\{\mathrm{Re}(f_0^*Q_1^{\mathrm{el}})(|\mathbf{e}\cdot\mathbf{n}|^2 + |\mathbf{e}\cdot\mathbf{n}'|^2 - 2/3)$$
$$+ \mathrm{Re}(f_0^*Q_2^{\mathrm{el}})(\mathrm{Re}\{(\mathbf{e}^*\cdot\mathbf{n})(\mathbf{e}\cdot\mathbf{n}')\} - (1/3)\cos\theta) \quad (34)$$
$$+ \mathrm{Re}(f_0^*Q_4^{\mathrm{el}}) + \mathrm{Im}(f_0^*Q_3^{\mathrm{el}})\xi(\mathbf{k}\cdot[\mathbf{n}\times\mathbf{n}'])\}.$$

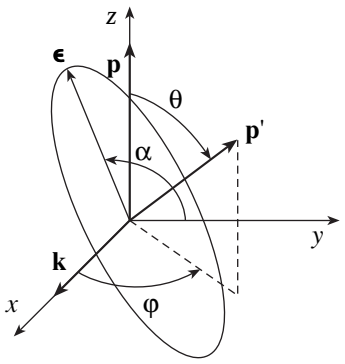

Fig. 2. Geometry of induced bremsstrahlung emission and absorption: θ and φ are the spherical angles of the momentum vector $\mathbf{p}'$ of a scattered electron in the coordinate system with the polar axis along vector $\mathbf{p}$ and the x axis along the direction $\mathbf{k}$ of the laser beam; angle α defines the orientation of the polarization ellipse in the yz plane.

Thus, elastic scattering of an electron in a light field gives rise only to the CD effect, which is described by the term containing Q_3^{el} and characterized by the same interference nature and the kinematic dependence as CD in inelastic processes as well as in the case of single-photon scattering [4]. Explicit expressions for the parameters Q_i^{el} similar to expressions (20) will be given below (see Eqs. (48)).

In view of the presence of several vector parameters in the problem, the symmetry properties of angular distributions of scattered electrons in the general case of elliptic photon polarization can be established only for the simplest initial configurations of the electron and laser beams. The most informative and convenient experimental configuration is the "orthogonal" geometry, in which the initial electron momentum $\mathbf{p}$ (z axis) is orthogonal to the direction of the light beam (x axis), while the principal axis of the polarization ellipse forms angle α with the y axis (Fig. 2). In this case, the yz (polarization) plane is the symmetry plane of the angular distribution in the general case of elliptic polarization. Since in the case of circular polarization the results are independent of angle α, the angular distribution in the absence of CD would also possess a symmetry relative to the xz plane, i.e., to the substitution $\varphi \longrightarrow -\varphi$. The CD terms break this symmetry since $\xi(\mathbf{k}\cdot[\mathbf{n}\times\mathbf{n}']) = -\xi\sin\theta\sin\varphi$. Nevertheless, this relation shows that the angular distributions in a circular field are transformed into one another for $\xi = 1$ and $\xi = -1$ upon reflection by the xz plane (or rotation through 180° about the z axis); i.e., the cross section $d\sigma/d\Omega$ is invariant relative to the substitutions $\xi \longrightarrow -\xi$ and $\varphi \longrightarrow -\varphi$. In an elliptic field, symmetry is lowered and the above invariance is preserved only for values of α multiple to π/2.

For spontaneous 2BrS, the cross section integrated over the directions $\mathbf{n}'$ of a scattered electron is of experimental interest. The general form of the polarization–

angular dependence of cross sections for this case follows from Eqs. (8) and (19) (cf. Eq. (33)):

$$\frac{d\sigma^4}{d\Omega_{\mathbf{k}_1}d\Omega_{\mathbf{k}_2}d\omega_1 d\omega_2} = a_1 + a_2|\mathbf{e}_1\cdot\mathbf{e}_2|^2 + a_3|\mathbf{e}_1\cdot\mathbf{e}_2^*|^2 + a_4|\mathbf{e}_1\cdot\mathbf{n}|^2 + a_5|\mathbf{e}_2\cdot\mathbf{n}|^2 + a_6|\mathbf{e}_1\cdot\mathbf{n}|^2|\mathbf{e}_2\cdot\mathbf{n}|^2 + a_7\mathrm{Re}I_1 + a_8\mathrm{Re}I_2 + a_9\mathrm{Im}I_1 + a_{10}\mathrm{Im}I_2, \quad (35)$$

where

$$I_1 = (\mathbf{e}_1\cdot\mathbf{n})(\mathbf{e}_2\cdot\mathbf{n})(\mathbf{e}_1^*\cdot\mathbf{e}_2^*),$$

$$I_2 = (\mathbf{e}_1\cdot\mathbf{n})(\mathbf{e}_2^*\cdot\mathbf{n})(\mathbf{e}_1^*\cdot\mathbf{e}_2).$$

Omitting cumbersome expressions for coefficients a_i in terms of radial ME, we note that factors $\mathrm{Im}I_1$ and $\mathrm{Im}I_2$ in the last two terms in Eq. (35) change their sign upon the simultaneous replacement of the polarization vectors by their complex conjugate, $\mathbf{e}_1 \rightleftharpoons \mathbf{e}_1^*$ and $\mathbf{e}_2 \rightleftharpoons \mathbf{e}_2^*$; for this reason, the cross section contains terms linear in ξ_1 and ξ_2 and depends on the sign of the degree of circular polarization of photons. Thus, the CD effect in spontaneous 2BrS is also preserved in the integration over $\mathbf{n}'$. The complex quantities I_1 and I_2 can be expressed in terms of the real vectors $\boldsymbol{\epsilon}_i$ and $\mathbf{k}_i$ for any polarizations $\mathbf{e}_1$ and $\mathbf{e}_2$ (such expressions can be found in [54]); however, the case when one of the photons is polarized linearly (say, $\mathbf{e}_2 = \mathbf{e}_2^* \equiv \boldsymbol{\epsilon}_2$) is most interesting for CD observation. In this case, $I_1 = I_2 \equiv I$, and the kinematic dependence of the CD term in Eq. (35) is given by

$$2\mathrm{Im}I = \xi_1(\boldsymbol{\epsilon}_2\cdot\mathbf{n})(\boldsymbol{\epsilon}_2\cdot[\mathbf{n}\times\mathbf{k}_1]).$$

This expression has a maximum in the orthogonal geometry ($\mathbf{k}_1 \perp \mathbf{n}$, $\mathbf{k}_2 = -\mathbf{k}_1$) used in experiments [8], when bremsstrahlung photons are detected in the opposite direction at right angles to the incident electron beam. Using polarization-sensitive detectors, the CD effect can be observed in these experiments by measuring the difference in the yields of photons with right and left circular polarizations for a fixed linear polarization of the second photon at an angle of $\pi/4$ to the plane of vectors $\mathbf{n}$, $\mathbf{k}_1$, and $\mathbf{k}_2$.

When an electron is scattered by a freely oriented atom with a nonzero total angular momentum, the polarization structure of the cross section of two-photon bremsstrahlung processes is much more complicated. Indeed, in this case only the cross section (and not the amplitude) of the process is a scalar that can be presented as a combination of scalar and mixed products of photon polarization vectors and electron momenta $\mathbf{p}$ and $\mathbf{p}'$. Accordingly, the number of terms in the expression for the cross section, which are determined by linearly independent polarization-angular factors, increases considerably. Nevertheless, the general expression for the cross section in vector form, as well as explicit expressions for dichroic terms represented in terms of reduced MEs of the momentum operator, can be obtained in analogy to the case of potential scattering.

3. COULOMB TWO-PHOTON RADIAL MATRIX ELEMENTS

Formulas (20) express parameters Q_i in terms of the radial MEs $M^L_{l'\,l}(E', E, \mathscr{E})$ (21) of transitions between the states of the continuum with fixed values of the orbital angular momentum in potential $U(r)$. In accordance with the dipole selection rules, MEs of the following four types appear in expressions (20):

$$M^{l+1}_{l\,l}(E', E, \mathscr{E}) = \langle D(l+1, l)R_{E'l}|g_{l+1}(\mathscr{E})|D(l+1, l)R_{El}\rangle,$$

$$M^{l+1}_{l+2\,l+2}(E', E, \mathscr{E}) = \langle D(l+1, l+2)R_{E'l+2}|g_{l+1}(\mathscr{E})|D(l+1, l+2)R_{El+2}\rangle,$$

$$M^{l+1}_{l+2\,l}(E', E, \mathscr{E}) = \langle D(l+1, l+2)R_{E'l+2}|g_{l+1}(\mathscr{E})|D(l+1, l)R_{El}\rangle, \quad (36)$$

$$M^{l+1}_{l\,l+2}(E', E, \mathscr{E}) = \langle D(l+1, l)R_{E'l}|g_{l+1}(\mathscr{E})|D(l+1, l+2)R_{El+2}\rangle.$$

It can be seen from the definition that $M^{l+1}_{l\,l+2}(E', E, \mathscr{E}) = M^{l+1}_{l+2\,l}(E, E', \mathscr{E})$; consequently, it is sufficient to calculate $M^{l+1}_{l\,l}$, $M^{l+1}_{l+2\,l+2}$, and $M^{l+1}_{l+2\,l}$ only.

In the case of the Coulomb potential $U(r) = -Z/r$, the MEs $M^L_{l'\,l}$ can be calculated in closed analytic form. It is shown in Appendix A that each ME from $M^L_{l'\,l}$ can be presented as a sum of six terms of which two contain first-order dipole MEs,

$$d_{l'\,l}(E', E) = \langle R_{E'l'}|D(l', l)|R_{El}\rangle, \quad l' = l \pm 1, \quad (37)$$

while the remaining four terms include the integrated terms $J^{mm'}$ (A.4) with $m, m' = 0, 1$:

$$M^{l+1}_{ll}(E', E, \mathscr{E}) = \frac{p}{E-\mathscr{E}}\frac{l+1-ia}{|l+1-ia|}d_{l\,l+1}(E', E) - \frac{p'}{E'-\mathscr{E}}\frac{l+1-ia'}{|l+1-ia'|}d_{l+1\,l}(E', E) + \frac{2^{2l+2}Z^2(pp')^l}{[(2l+3)!]^2}C_{El}C_{E'l}[(l+2+ia')(l+2+ia)J^{00} + (l+2+ia')(l+1-ia)J^{01} + (l+1-ia')(l+2+ia)J^{10} \quad (38)$$

$$+ (l+1-ia')(l+1-ia)J^{11}],$$

$$M^{l+1}_{l+2\,l+2}(E', E, \mathscr{E}) = -\frac{p}{E-\mathscr{E}}\frac{|l+2-ia|}{l+2-ia}d_{l+2l+1}(E', E) + \frac{p'}{E'-\mathscr{E}}\frac{|l+2-ia'|}{l+2-ia'}d_{l+1l+2}(E', E) + \frac{2^{2l+2}Z^2(pp')^l}{[(2l+3)!]^2(l+2-ia)(l+2-ia')} \times C_{El+2}C_{E'l+2}[J^{00}-J^{01}-J^{10}+J^{11}], \quad (39)$$

$$M^{l+1}_{l+2l}(E', E, \mathscr{E}) = \frac{p}{E-\mathscr{E}}\frac{l+1-ia}{|l+1-ia|}d_{l+2l+1}(E', E) + \frac{p'}{E'-\mathscr{E}}\frac{|l+2-ia'|}{l+2-ia'}d_{l+1l}(E', E) + \frac{2^{2l+2}Z^2(pp')^l}{[(2l+3)!]^2(l+2-ia')} \times C_{El}C_{E'l+2}[(l+2+ia)J^{00}+(l+1-ia)J^{01} - (l+2+ia)J^{10}-(l+1-ia)J^{11}]. \quad (40)$$

Here, $a = Z/p$ is the standard Coulomb parameter, and C_{El} is the normalization factor for the continuum state $R_{El}(r)$:

$$C_{El} = \sqrt{\frac{2p}{\pi}}\exp(\pi a/2)|\Gamma(l+1-ia)|.$$

The MEs $d_{ll'}$ satisfy the symmetry relations

$$d_{ll+1}(E', E) = -d_{l+1l}(E, E'),$$
$$d_{l+2l+1}(E', E) = -d_{l+1l+2}(E, E')$$

and can be expressed explicitly (see Appendix A) in terms of the functions ${}_2F_1$ (cf. the expression for the ME for a single-photon transition with the interaction operator in the "form of length" [55]):

$$d_{l+1l}(E', E) = -\frac{2^{2l+2}Zp'^{l+1}p^l}{[(2l+3)!]^2} \times C_{E'l+1}C_{El}[(l+2+ia)I^{10}+(l+1-ia)I^{11}], \quad (41)$$

$$d_{l+1l+2}(E', E) = -\frac{2^{2l+2}Zp'^{l+1}p^l}{[(2l+3)!]^2(l+2-ia)} \times C_{E'l+1}C_{El+2}(I^{10}-I^{11}).$$

Here,

$$I^{m'm}(E', E) = (-1)^l(2l+3)! \times \frac{(p-p'+i0)^{-l-1-m'+ia'}(p'-p+i0)^{-l-1-m+ia}}{(p+p')^{2+ia'+ia-m'-m}} \times {}_2F_1(l+1+m'-ia', l+1+m-ia, 2l+4, \lambda_0), \quad (42)$$

where $\lambda_0 = -4pp'/(p-p')^2$.

Expression (A.4) for $J^{mm'}$ can be written only in the form of a one-dimensional integral of the function ${}_2F_1$ with the same parameters as in Eq. (42):

$$J^{m'm}(E', E, \mathscr{E}) = 2^{2l+4}(2l+3)!\nu^{2l+5}\int_0^1 dt \times \frac{t^{l+1-Z\nu}\,{}_2F_1(l+1+m'-ia', l+1+m-ia, 2l+4; \lambda)}{A^{l+1+m-ia}B^{l+1+m'-ia'}C^{2-m'-m+ia'+ia}}, \quad (43)$$

where $\nu = 1/\sqrt{-2\mathscr{E}}$, $\lambda = (16pp'|\nu|^2t)/AB$, and

$$A = (1-p|\nu|+i0)(1+p'|\nu|+i0) - t(1+p|\nu|-i0)(1-p'|\nu|-i0),$$
$$B = (1+p|\nu|+i0)(1-p'|\nu|+i0) - t(1-p|\nu|-i0)(1+p'|\nu|-i0), \quad (44)$$
$$C = (1+p|\nu|+i0)(1+p'|\nu|+i0) - t(1-p|\nu|-i0)(1-p'|\nu|-i0).$$

Formulas (43) and (44) are written under the assumption that the energy of the intermediate state is positive: $\mathscr{E} > 0$. If $\mathscr{E} < 0$ (this case is realized in elastic scattering with reemission of a photon with $\omega > E$), the parameter $\nu = 1/\sqrt{-2\mathscr{E}}$ is real-valued and the substitution $|\nu| \longrightarrow -i\nu$ must be carried out in Eqs. (43) and (44). Infinitely small corrections $\pm i0$ in Eqs. (42) and (44), which determine the rules for raising negative quantities to a power, appear as a result of regularization of integrals (A.3) and (A.4) with oscillating functions. It can be seen that expressions (38)–(40) contain two types of terms: the hypergeometric functions ${}_2F_1$ and integrals of ${}_2F_1$. Relatively simple "integrated" terms make a dominating contribution to $M^L_{l'l}(E', E, \mathscr{E})$ in the domain of the variables (see Section 5) and contain, in particular, the Born limit since the terms with integrals $J^{m'm}$ have an extra factor Z.

In spite of the cumbersome form typical of analytic calculations with Coulomb functions of the continuum, formulas (38)–(40) and (43) cannot apparently be sim-

plified further and are the simplest expressions generalizing Coulomb matrix elements of the type (41), (42) for single-photon bremsstrahlung processes to the case of two-photon free–free transitions. At the same time, the analytic expressions for the MEs for bound–bound and bound–free transitions following from them for analytic continuations in E and E' can be simplified and reduced to two-photon Gordon formulas [49], which are free of integrations. The corresponding transformations can be found in Appendix B.

4. ELIMINATION OF SINGULARITIES IN THE AMPLITUDE OF ELASTIC TWO-PHOTON TRANSITIONS

Elastic two-photon transitions in the continuous spectrum require special analysis in view of the convergence of the radial MEs of dipole transitions between the states of the continuum with identical energies even in the single-photon case. The situation in two-photon transitions is analogous: it can be seen from expressions (42) and (43) that all MEs $M^L_{l'l}$ diverge for $E' \longrightarrow E$ ($p' \longrightarrow p$). The reason for the divergence can be easily grasped if we consider the asymptotic form of the radial Coulomb Green function integrated with the wave function of the continuum:

$$\int_0^\infty dr' r'^2 g_L(\mathscr{E}; r, r')\left(\frac{d}{dr'} + \frac{A}{r'}\right)R_{El}(r') \xrightarrow[r\to\infty]{} C_1 r^{Z\nu-1}e^{-r/\nu}$$

$$+ \frac{C_2}{r}\cos\left(pr + \frac{Z}{p}\ln(2pr) - \frac{\pi}{2}l + \delta_l(p)\right),$$

where A, C_1, and C_2 are constants. The presence of the second term oscillating with the same frequency as the wave function $R_{El}(r)$ in the asymptotic form is responsible for the divergence of $M^L_{l'l}(E', E, \mathscr{E})$ for $E' \longrightarrow E$ both in the case of the Coulomb potential and for $Z = 0$. Since the cross sections of elastic processes are finite, the singularities in $M^L_{l'l}$ must be compensated in the calculation of the limit $E' \longrightarrow E$ in the sum

$$M(\mathbf{e}^*, \mathbf{e}, E + \omega) + M(\mathbf{e}, \mathbf{e}^*, E - \omega'), \qquad (45)$$

defining the total amplitude f_2 of the transition in relation (12). The first term in expression (45) corresponds to the absorption of a photon followed by its emission (see Fig. 1a), while the second term corresponds to the reverse process (see Fig. 1b). The quantities ω and ω' in sum (45) are connected through the relation $\omega - \omega' = E' - E$.

It follows from expression (19) for $M(\mathbf{e}^*, \mathbf{e}, \mathscr{E})$ that the polarization-angular parameter Q_4 reverses its sign upon the transposition of $\mathbf{e}$ and $\mathbf{e}^*$, while the signs of the remaining Q_i remain unchanged. It follows hence that singularities for $E' \longrightarrow E$ must be compensated in the combinations of MEs,

$$S^L_{l'l} = \lim_{E'\to E}[M^L_{l'l}(E', E, E + \omega) + M^L_{l'l}(E', E, E - \omega')], \qquad (46)$$

$$R_l(\mathscr{E}) = \lim_{E'\to E}[M^{l-1}_{ll}(E', E, \mathscr{E}) - M^{l+1}_{ll}(E', E, \mathscr{E})], \qquad (47)$$

through which we can express the parameters Q^{el}_i of elastic transition in formula (34):

$$Q^{\mathrm{el}}_1 = -\sum_{l=2}^{\infty}\left[\frac{1}{2l+3}(\mathscr{S}^{l+1}_{ll} + \mathscr{S}^{l+1}_{l+2l}) + \frac{1}{2l-1}(\mathscr{S}^{l-1}_{ll} + \mathscr{S}^{l-1}_{l-2l})\right]P^{(2)}_l(x),$$

$$Q^{\mathrm{el}}_2 = \sum_{l=1}^{\infty}\left[\frac{1}{2l-1}\mathscr{S}^{l-1}_{ll} + \frac{1}{2l+3}\mathscr{S}^{l+1}_{ll}\right]P^{(1)}_l(x) + 2\sum_{l=2}^{\infty}\left[\left(\frac{1}{2l-1}\mathscr{S}^{l-1}_{ll} + \frac{1}{2l+3}\mathscr{S}^{l+1}_{ll}\right)x + \frac{1}{2l+1}(\mathscr{S}^{l}_{l-1\,l+1} + \mathscr{S}^{l}_{l+1\,l-1})\right]P^{(2)}_l(x), \qquad (48)$$

$$Q^{\mathrm{el}}_3 = \sum_{l=1}^{\infty}[\mathscr{R}_l(E + \omega) - \mathscr{R}_l(E - \omega)]P^{(1)}_l(x),$$

$$Q^{\mathrm{el}}_4 = \frac{1}{3}\sum_{l=0}^{\infty}[l\mathscr{S}^{l-1}_{ll} + (l+1)\mathscr{S}^{l+1}_{ll}]P_l(x),$$

where

$$\mathscr{S}^L_{l'l} = (2\pi^2/p)\exp[i(\delta_{l'}(p) + \delta_l(p))]\mathscr{S}^L_{l'l},$$

$$\mathscr{R}_l(\mathscr{E}) = (\pi^2/p)\exp[2i\delta_l(p)]R_l(\mathscr{E}).$$

In order to verify the compensation of the divergences and to find the limits of expressions (46) and (47), we must explicitly separate the diverging and finite parts of the ME $M^L_{l'l}$. We will illustrate the corresponding results using analytic expressions (38)–(40) for the Coulomb potential. This can easily be done for the integrated terms through the known asymptotic expansion of function ${}_2F_1$ in inverse powers of argument [56]. The separation of singularities from $J^{m'm}$ in expressions (38)–(40) requires more complex transformations. It should be noted above all (see Eq. (43)) that integrals J^{00} and J^{11} are finite for $E' = E$, while J^{01} and J^{10} diverge as $\ln(E' - E)$. The presence of the logarithmic singularity alone allows us to set $E' = E$ in the coefficients of the integrated terms in expressions (38)–(40)

everywhere except in factors A and B. Using the technique for separating singularities described in [13], we can present the diagonal MEs in the form

$$M^{l+1}_{l+2\,l+2}(E', E, \mathscr{E}) = -\frac{a}{\pi}\frac{1}{E-\mathscr{E}}\left(\ln\left(\frac{p-p'}{2p}\right)^2 - 2\psi(1)\right)$$
$$+\frac{1}{E-\mathscr{E}}\frac{a}{\pi(l+2-ia)}\left(\frac{2\mathscr{E}}{E-\mathscr{E}} + ia\psi(l+1-ia)\right.$$
$$+ia\psi(l+2-ia) + 2ia\psi(l+3+ia) \quad (49)$$
$$\left.-2(l+2+ia)\mathrm{Re}\psi(l+2-ia)\right)$$
$$+Z^2\frac{2^{2l+2}p^{2l}}{((2l+3)!)^2}\frac{C^2_{El+2}}{(l+2-ia)^2}[J^{00}+J^{11}-K],$$

$$M^{l+1}_{l\,l}(E', E, \mathscr{E}) = -\frac{a}{\pi}\frac{1}{E-\mathscr{E}}\left(\ln\left[\left(\frac{p-p'}{2p}\right)^2\right] - 2\psi(1)\right)$$
$$+\frac{1}{E-\mathscr{E}}\frac{a}{\pi(l+1+ia)}\left(-\frac{2\mathscr{E}}{E-\mathscr{E}} + \frac{ia}{l+1-ia}\right.$$
$$+\frac{ia}{l+2+ia} - ia\psi(l+1-ia) - ia\psi(l+2-ia) \quad (50)$$
$$\left.-2ia\psi(l+3+ia) - 2(l+1-ia)\mathrm{Re}\psi(l+2-ia)\right)$$
$$+Z^2\frac{2^{2l+2}p^{2l}}{((2l+3)!)^2}C^2_{El}[(l+2+ia)^2J^{00}$$
$$+(l+1-ia)^2J^{11} + (l+1-ia)(l+2+ia)K],$$

where K is the regular part of the sum $J^{01} + J^{10}$,

$$K = -\frac{2^{2l+4}(2l+3)!\nu^{2l+5}}{(1-p^2|\nu|^2)(l+1-ia)}\int_0^1 dt\frac{t^{l-Z\nu}}{A^{2l+2-2ia}C^{1+2ia}}$$
$$\times\left[\left(ia(1-p|\nu|) + \frac{t}{C}(1+2ia)(1-p|\nu|)^2\right)\right. \quad (51)$$
$$\times {}_2F_1(l+1-ia, l+1-ia, 2l+4, \lambda)$$
$$\left.+(l+1-ia){}_2F_1(l+1-ia, l+2-ia, 2l+4, \lambda)\right],$$

and $\psi(x) = (d/dx)\ln\Gamma(x)$ is the psi function. Integrals J^{mm} in expressions (49) and (50) are defined by formula (43) with $p' = p$. In this case,

$$A = B = (1-p^2|\nu|^2)(1-t) + i0,$$
$$C = (1+p|\nu|)^2 - t(1-p|\nu|)^2, \quad \lambda = \frac{16p^2|\nu|^2t}{A^2}. \quad (52)$$

Considering that $E - \mathscr{E} = -\omega$ for the diagram presented in Fig. 1a and $E - \mathscr{E} = \omega'$ for the diagram in Fig. 1b and that the singular terms in expressions (49) and (50) are identical and independent of l, we can easily see that the divergences in the calculation of $R_l(\mathscr{E})$ in expression (47) and in the diagonal elements $S^L_{l\,l}$ in expression (46) are compensated and the final results obviously follow from expressions (49) and (50).

The nondiagonal MEs contain, in addition to the logarithmic singularity, a power singularity; consequently, their singular part has the form

$$[M^{l+1}_{l+2\,l}(E', E, \mathscr{E})]_{\mathrm{sing}} = \frac{a}{\pi|l+1-ia||l+2+ia|}$$
$$\times\left(\frac{l+1-ia}{E-\mathscr{E}} + \frac{l+2+ia}{E'-\mathscr{E}}\right)\frac{p}{p-p'} \quad (53)$$
$$+\left(\frac{C(E,l)}{E-\mathscr{E}} + \frac{C(E',l)}{E'-\mathscr{E}}\right)\ln\left[\left(\frac{p-p'}{2p}\right)^2\right].$$

When we evaluate the limit $E' \longrightarrow E$ in sum (46) with $l' = l + 2$, the terms with the logarithmic singularities vanish, while the terms with the power singularities make a finite contribution. As a result, the final expression for $S^{l+1}_{l+2\,l}$ assumes the form

$$S^{l+1}_{l+2\,l} = \frac{Zp(1+2ia)}{\pi|l+1-ia||l+2+ia|}\frac{1}{\omega^2}$$
$$+\frac{Z^2 2^{2l+2}p^{2l}}{[(2l+3)!]^2(l+2-ia)}$$
$$\times[(l+2+ia)(J^{00}(E+\omega) + J^{00}(E-\omega)) \quad (54)$$
$$-(l+1-ia)(J^{11}(E+\omega) + J^{11}(E-\omega))$$
$$-(1/2+ia)(K(E+\omega) + K(E-\omega))].$$

The functions ${}_2F_1$ in the integrands of the integrals $J^{mm'}$ and K appearing in expressions (49), (50), and (54) have a branching point for $\lambda = 1$, lying on the integration contour. The choice of the required analytic branch is determined by the imaginary correction in expression (52) for A. Expressions (49), (50), and (54) completely determine the amplitude f_2 in expression (12) and the cross section (34) of elastic two-photon transition in the Coulomb field.

5. ASYMPTOTIC ANALYSIS OF THE AMPLITUDES OF INELASTIC TWO-PHOTON TRANSITIONS

The partial-wave approach leads to expressions for parameters $Q_i(p, p', \theta)$ only in the form of series in Legendre polynomials, and the radial MEs appearing in these series can be calculated analytically only in the Coulomb case. Nevertheless, we can derive quite simple closed expressions for Q_i and transition amplitudes

in potential $U(r)$ of the general form for the number of limiting ranges of the parameters of the problem, which will be considered below.

5.1. Low-Frequency Limit ($\omega/p^2 \ll 1$)

Let us first consider first-order MEs $d_{l'l}(E', E)$ (37). Since the oscillation frequencies of the wave functions of the initial and final states become close for $E' \longrightarrow E$, the radial integral in formula (37) diverges at infinity. Replacing the wave functions by their asymptotic expressions for $r \longrightarrow \infty$,

$$R_{El} \longrightarrow \sqrt{\frac{2p}{\pi}}\sin\left(pr - \frac{1}{2}\pi l + \delta_l(p)\right), \tag{55}$$

and retaining in expression (37) only the principal terms in $1/r$, we obtain

$$\begin{aligned} d_{l'l} &= -\frac{p}{\pi}\mathrm{Re}\left(\frac{\exp(-i\Delta_{l'l}(E))}{E' - E + i0}\right) \\ &= p\sin\Delta_{l'l}(E)\delta(E' - E) + \frac{p}{\pi}\frac{\cos\Delta_{l'l}(E)}{E' - E}, \end{aligned} \tag{56}$$

where $\Delta_{l'l}(E) = \delta_l(p) - \delta_{l'}(p) - (\pi/2)(l - l')$. The presence of the δ function in the MEs of the free–free transitions and the method of determining of their asymptotic form are well known (see Section 21 in [57]). In real single-photon transitions between the states of the continuum (with $E' \neq E$), the singular term is omitted; however, in compound MEs, integration is carried out with respect to the energies of virtual states and the δ term in $d_{l'l}$ plays a significant role. The problems associated with its inclusion in numerical and analytic calculations have been repeatedly discussed in the literature [14, 58–62].

Let us now consider the low-frequency limit of the second-order MEs $M^L_{l'l}(E', E, \mathscr{E})$ with $\mathscr{E} = E \pm \omega$ and $E' = \mathscr{E} \pm \omega'$. Using the spectral expansion for the Green function in relations (21), we can represent $M^L_{l'l}$ in the form

$$\begin{aligned} M^L_{l'l}(E', E, \mathscr{E}) &= -\sum_n \frac{d_{l'L}(E', E_n)d_{Ll}(E_n, E)}{E_n - \mathscr{E}} \\ &\quad - \int d\epsilon \frac{d_{l'L}(E', \epsilon)d_{Ll}(\epsilon, E)}{\epsilon - \mathscr{E} - i0}, \end{aligned} \tag{57}$$

where summation is carried out over the states of the discrete spectrum, while integration is carried out over the states of the continuous spectrum of the Hamiltonian with potential $U(r)$. In the low-frequency range, the two terms in Eq. (57) have different values; we can easily verify that the sum over the discrete spectrum gives a finite result for $\omega, \omega' \longrightarrow 0$, while the integral is of the order of $1/\omega\omega'$ in accordance with the general nature of the frequency dependence of the amplitude of scattering accompanied by the emission of soft photons [3]. It turns out that the main contribution to the integral in expression (57), leading to the above-mentioned singularity for $\omega, \omega' \longrightarrow 0$, is associated with δ-shaped terms in the integrand function, whose presence follows from relation (56) and from the well-known relation

$$\frac{1}{\epsilon - \mathscr{E} - i0} = \text{V.p.}\frac{1}{\epsilon - \mathscr{E}} + i\pi\delta(\epsilon - \mathscr{E}). \tag{58}$$

Omitting the sum over the discrete spectrum in expression (57) and taking into account only the contribution from the points $\epsilon = E, E', \mathscr{E}$ in the integral, we obtain the following intermediate expression for $M^L_{l'l}$:

$$\begin{aligned} M^L_{l'l} &= p'\sin\Delta_{l'L}(E')\frac{1}{E' - \mathscr{E}}d_{Ll}(E', E) \\ &\quad + p\sin\Delta_{Ll}(E)\frac{1}{E - \mathscr{E}}d_{l'L}(E', E) \\ &\quad - i\pi d_{l'L}(E', \mathscr{E})d_{Ll}(\mathscr{E}, E). \end{aligned} \tag{59}$$

Replacing the MEs $d_{l_2l_1}(E_2, E_1)$ by their limiting expressions for $E_2 \longrightarrow E_1$ (second term in Eq. (56)) and retaining only the principal term in the asymptotic form for $\omega, \omega' \longrightarrow 0$, we obtain

$$\begin{aligned} M^L_{l'l} &= \frac{p^2}{\pi}\frac{\sin\Delta_{l'L}(E)\cos\Delta_{Ll}(E)}{(E' - \mathscr{E})(E' - E)} \\ &\quad + \frac{p^2}{\pi}\frac{\cos\Delta_{l'L}(E)\sin\Delta_{Ll}(E)}{(E - \mathscr{E})(E' - E)} \\ &\quad - i\frac{p^2}{\pi}\frac{\cos\Delta_{l'L}(E)\cos\Delta_{Ll}(E)}{(E' - \mathscr{E})(\mathscr{E} - E)}. \end{aligned} \tag{60}$$

In the low-frequency limit, we cannot only simplify partial MEs, but also sum the series in relations (20) in the general form for parameters Q_i. Let us consider for definiteness the process of induced 2BrS: $\mathbf{e}_1 = \mathbf{e}_2 = \mathbf{e}^*$, $\mathscr{E} = E - \omega$, $E' = E - 2\omega$. Then relation (60) leads to the following expressions for $\mathscr{M}^{l''}_{l'l}$:

$$\begin{aligned} \mathscr{M}^{l+1}_{ll} &= \frac{\pi p}{i\omega^2}(e^{2i\delta_l(p)} - e^{2i\delta_{l+1}(p)}), \\ \mathscr{M}^{l-1}_{ll} &= \frac{\pi p}{i\omega^2}(e^{2i\delta_l(p)} - e^{2i\delta_{l-1}(p)}), \\ \mathscr{M}^{l+1}_{l+2l} &= \frac{\pi p}{2i\omega^2}(2e^{2i\delta_{l+1}(p)} - e^{2i\delta_{l+2}(p)} - e^{2i\delta_l(p)}). \end{aligned} \tag{61}$$

Substituting expressions (61) into (20) and using the recurrence relation for the derivatives of the Legendre polynomial [56], we present parameter Q_1 in the form

$$Q_1 = \frac{\pi p}{2i\omega^2}\sum_{l=0}^{\infty}(2l + 1)P_l(x)e^{2i\delta_l(p)}.$$

Taking now into account the well-known relation for the amplitude f_0 of elastic scattering in the field $U(r)$ [57],

$$f_0(\theta) = \frac{1}{2ip}\sum_l (2l+1)P_l(\cos\theta)e^{2i\delta_l(p)}, \qquad (62)$$

we express Q_1 in terms of f_0:

$$Q_1 = \frac{\pi p^2}{\omega^2} f_0.$$

Similarly, we can express the remaining parameters Q_i in relations (20) in terms of f_0 with the help of appropriate recurrence relations for $P_k^{(m)}(x)$ and find that

$$Q_2 = Q_1, \quad Q_3 = -2Q_1, \quad Q_5 = \frac{2}{3}(1-\cos\theta)Q_1.$$

As a result, we obtain the following expression for the 2BrS amplitude $M(\mathbf{e}^*, \mathbf{e}^*, E-\omega)$ in expression (19),

$$M = \frac{\pi p^2}{\omega^2} f_0(\mathbf{e}^* \cdot (\mathbf{n}-\mathbf{n}'))^2, \qquad (63)$$

and the low-frequency asymptotic form of the cross section (see Eq. (9)) has the form

$$d\sigma = \frac{F^4}{2^6\omega^8}|\mathbf{e}\cdot(\mathbf{p}-\mathbf{p}')|^4 d\sigma_0. \qquad (64)$$

The same result follows from the Kroll–Watson formula (expression (6) with $d\sigma_B \longrightarrow d\sigma_0 = |f_0|^2 d\Omega$) if we pass to a low field strength F in it.

Let us write for reference the low-frequency asymptotic expressions for 2BrS partial MEs (61) in the Coulomb field. In this case,

$$e^{i\delta_l(p)} = \frac{\Gamma(l+1-ia)}{|\Gamma(l+1-ia)|}, \qquad (65)$$

so that we obtain from relations (61)

$$\mathcal{M}_{l\,l}^{l+1} = \frac{Zp}{\pi\omega^2}\frac{l+1-ia}{(l+1)^2+a^2},$$

$$\mathcal{M}_{l+2\,l+2}^{l+1} = -\frac{Zp}{\pi\omega^2}\frac{l+2+ia}{(l+2)^2+a^2}, \qquad (66)$$

$$\mathcal{M}_{l+2\,l}^{l+1} = -\frac{Zp}{\pi\omega^2}\frac{1/2+ia}{|(l+1-ia)(l+2-ia)|}.$$

We considered above the arbitrary potential $U(r)$ (the general method of estimating ME in the low-frequency region was used earlier [62]); however, the behavior of Coulomb amplitudes in the low-frequency range can also be analyzed proceeding from exact expressions derived in Section 3. Expanding the functions ${}_2F_1$ in the expression for $M_{l'l}^L$ in inverse powers of the argument and retaining the principal term in $1/\omega$, we arrive at results exactly coinciding with relations (66). It turns out that the contribution to the main term of the asymptotic form comes only from the integrated terms. Formula (59), taking into account the contribution from the δ-type singularities in the compound ME only and appearing in our calculations as an intermediate expression, was derived in an analogous way by Korol [14] and was used for approximate evaluation of Coulomb amplitudes in the entire range of variables. A comparison with the available data from the literature [11, 12] shows that formula (59), which is simple for calculations, successfully reproduces the results of exact calculations of the spontaneous 2BrS cross section. The existence of exact analytic expressions for Coulomb amplitudes makes it possible to establish the source of such good agreement. Comparing relation (59) with (38)–(40) and taking into account relations (65), we can easily verify that the real part in Korol's formula (59) exactly coincides with the real part of the integrated terms in $M_{l'l}^L$. At the same time, the imaginary part in relation (59) is exact. Thus, formula (59) disregards only the real part of the integral terms in (38)–(40). It was mentioned above that the integrated terms make the main contribution to the amplitude in the Born and low-frequency region. The first term in the asymptotic form of the integral part of $M_{l'l}^L$ in the Born region, as well as in the low-frequency range, turns out to be purely imaginary so that correction appears in formula (59) only in the next order and has the relative value

$$\frac{a^2\omega^2}{E^2}\left[\ln^2\left(\frac{\omega}{E}\right) + C\ln\left(\frac{\omega}{E}\right) + C'\right], \qquad (67)$$

where C and C' are constants. This estimate determines the accuracy of approximation of formula (59) for the Coulomb field.

It should be noted that the low-frequency Kroll–Watson approximation is inapplicable for small scattering angles, when the inclusion of only the principal term of expression (60) of the asymptotic form of the ME $M_{l'l}^L$ for $\omega, \omega' \longrightarrow 0$ is insufficient for estimating amplitudes Q_i. Since the estimation of corrections to expression (60) for the field $U(r)$ of the general form is complicated, we will illustrate this statement for the Coulomb scattering. In this case, the low-frequency asymptotic form (64) is given by

$$\frac{d\sigma}{d\Omega} = \frac{1}{4\pi^2}\left(\frac{F}{2\omega}\right)^4\frac{p'}{p}f_{\text{reg}} = B|\mathbf{e}\cdot(\mathbf{n}-\mathbf{n}')|^4, \qquad (68)$$

where

$$B = \frac{F^4Z^2}{2^8\omega^8}\frac{1}{\sin^4(\theta/2)}.$$

Corrections of the next order in frequency are cumbersome and can be obtained from the exact formulas

obtained in Section 3. In particular, in the next order in ω, there appears the CD term

$$\frac{1}{4\pi^2}\left(\frac{F}{2\omega}\right)^4\frac{p'}{p}\Delta_{CD} = B\frac{2a\omega}{p^2}(\ln y + b)\xi(\mathbf{k}\cdot[\mathbf{n}\times\mathbf{n}'])|\mathbf{e}\cdot(\mathbf{n}-\mathbf{n}')|^2, \quad (69)$$

where

$$y = \frac{4pp'}{(p-p')^2}\sin^2\frac{\theta}{2}$$

and $b = b(a)$ is a smooth function of the momentum p. Obviously, the condition of applicability of the Kroll–Watson approximation is the fulfillment of the inequality

$$\frac{a\omega}{p^2}|(\mathbf{k}\cdot[\mathbf{n}\times\mathbf{n}'])| \ll |\mathbf{e}\cdot(\mathbf{n}-\mathbf{n}')|^2. \quad (70)$$

Since $|\mathbf{e}\cdot(\mathbf{n}-\mathbf{n}')|^2 \sim \theta^2$ and $|\mathbf{n}\times\mathbf{n}'| \sim \theta$ for $\theta \longrightarrow 0$, condition (70) is obviously violated for small scattering angles (the fulfillment of this condition naturally depends also on the azimuth angle). It should be noted that, since correction (69) depends on ξ, dichroism effects are significant in the 2BrS cross section even for small values of the ratio ω/p^2 in this range of angles (although the CD effect obviously vanishes for $\theta = 0$).

5.2. High-Frequency Limit ($Z/p \ll 1$, $\omega/E' \gg 1$, $\omega/E \sim 1$) and Born Approximation

Let a fast electron lose a considerable part of its energy during induced 2BrS so that the final state is not of the Born type. In this case, the replacement of the wave function of the initial state by the function of free motion,

$$R_{El}(r) \longrightarrow R^{(0)}_{El}(r), \quad R^{(0)}_{El} = \sqrt{\frac{2p}{\pi}}j_l(pr), \quad (71)$$

leads to the following results of the action of operators D on the wave function:

$$D(l+1, l)R^{(0)}_{El} = -pR^{(0)}_{El+1},$$
$$D(l+1, l+2)R^{(0)}_{El+2} = pR^{(0)}_{El+1}. \quad (72)$$

Substituting now Green's function for a free electron for Green's function g_L in relations (36) and using relations (72), we reduce $M^L_{l'l}$ to the form

$$M^L_{l'l} = (-1)^{(l-l')/2}\frac{2E}{E-\mathscr{E}}\left\langle R_{E'l'}\middle|R^{(0)}_{El'}\right\rangle. \quad (73)$$

Evaluating the overlap integral $\left\langle R_{E'l'}\middle|R^{(0)}_{El'}\right\rangle$ [63] and proceeding to the limit $E \longrightarrow \infty$, we obtain

$$M^L_{l'l} = (-1)^{(l-l')/2}2^{2l'+9/2}Z\frac{C_{E'l'}(l'+1)!\,p'^{l'}}{\sqrt{\pi}(2l'+2)!\,p^{l'+7/2}}. \quad (74)$$

Comparing relations (72) with (A.1) and (A.2), we can easily establish that expression (74) in the Coulomb case corresponds to the inclusion in relations (38)–(40) of only the integrated term with $d_{l'l+1}$ in which the wave function of the initial state is replaced by $R^{(0)}_{El'}$. A more detailed analysis of expressions (38)–(40) in the high-frequency range shows that the term with $d_{l'l+1}$ makes the main contribution to the asymptotic form of $M^L_{l'l}$ only for $L = l'+1$, while all the terms with $M^{l+1}_{l+2\,l}$ and $M^{l+1}_{l+2\,l+2}$ (including the real part of the integral terms) are of the same order of magnitude for $L = l'-1$. Thus, expression (74) is a correct high-frequency asymptotic form for the MEs M^{l+1}_{ll} and M^{l+1}_{ll+2} and differs from the correct result for $M^{l+1}_{l+2\,l}$ and $M^{l+1}_{l+2\,l+2}$ in the coefficient of $p^{-l'-7/2}$.

It is interesting to note that an analogous situation also emerges in an analysis of single-photon transitions: substitution (71) in the MEs of photoionization,

$$d_{l_fl_i}(E_f, E_{n_i}) = \left\langle R_{E_fl_f}|D(l_f, l_i)|R_{n_il_i}\right\rangle, \quad (75)$$

leads to a correct asymptotic form of MEs with $l_f = l_i + 1$ and gives an erroneous factor in the energy dependence for $l_f = l_i - 1$ (this fact is mentioned in the monograph [55], although its origin is not discussed). In order to clarify the reason for such results, we consider the formation of the high-frequency asymptotic form of the photoionization MEs in the Born approximation:

$$d^{(0)}_{l-1\,l}(E_f, E_{n_i}) = \left\langle R^{(0)}_{E_fl-1}\middle|\left(\frac{d}{dr}+\frac{l+1}{r}\right)\middle|R_{n_il}\right\rangle. \quad (76)$$

The integral in this relation contains the rapidly oscillating (for $E_f \longrightarrow \infty$) spherical Bessel function $j_{l_f}(pr)$; consequently, the main contribution comes from the neighborhood of point $r = 0$. Since $R_{n_il} \sim N_{n_il}r^l$ for small r, it follows from expression (76) that

$$d_{l-1\,l}(E_f, E_{n_i}) = (2l+1)N_{n_il}\int_0^\infty r^{l+1}R^{(0)}_{E_fl-1}(r)dr. \quad (77)$$

Using the well-known formula [63], we obtain the following expression for an integral of the form (77):

$$\int_0^\infty r^{l_1} R^0_{El_2}(r)\,dr = \frac{\Gamma\left(\frac{l_2+l_1+1}{2}\right)}{\Gamma\left(\frac{l_2-l_1+2}{2}\right)} 2^{l_1-1/2}(2E)^{-(2l_1+1)/4}. \quad (78)$$

For $l_1 = l + 1$ and $l_2 = l - 1$, the gamma function in the denominator of this expression becomes infinitely large; consequently, the principal term in the expansion of $R_{n_i l}$ in r does not contribute to the asymptotic form. In order to evaluate the first nonvanishing term of the high-frequency asymptotic form of $d_{l-1\,l}(E_f, E_{n_i})$, we must not only continue the expansion of $R_{n_i l_i}$ in r, but also take into account the next terms in the expansion of the wave function R_{El} in $1/E$, i.e., the correction to $R^{(0)}_{El}$ in expressions (71), as well as the Coulomb correction to Green's function of a free electron for the second-order MEs. We omit here these calculations and only note that the main contribution to the asymptotic form of the total ME $M(\mathbf{e}^*, \mathbf{e}^*, E - \omega)$ in relation (7) comes from the partial amplitudes with $l' = 0$, whose high-frequency asymptotic form is given by formula (74) (it should be recalled that all partial amplitudes in the low-frequency region had the same order of magnitude in ω).

In the Coulomb case, taking into account in relations (20) only the terms with $l' = 0$, which appear only in Q_1 and Q_5,

$$Q_1 = 3Q_5 = 2^5\pi Z e^{\pi a'/2}\Gamma(1 - ia')p^{-4}, \quad (79)$$

we arrive at the following expression for the total amplitude:

$$M(\mathbf{e}^*, \mathbf{e}^*, E - \omega) = 2^5\pi Z e^{\pi a'/2}\Gamma(1 - ia')p^{-4}(\mathbf{e}^* \cdot \mathbf{n})^2. \quad (80)$$

It should be noted that the quantitative agreement between the asymptotic and exact results is improved significantly if we calculate the asymptotic form retaining the exact normalization factor C_{El} in $M^L_{l'\,l}$, which corresponds to the substitution $\sqrt{2p/\pi} \longrightarrow C_{El}/l!$ in relations (71).

Since the high-frequency asymptotic form of $M^{l+1}_{l\,l}$ and $M^{l+1}_{l\,l+2}$ is determined by the integrated terms (see above), formula (59), taking into account these terms, exactly gives the correct limit (74) for these MEs in this region also. On the contrary, the high-frequency limit of formula (59) for $M^{l+1}_{l+2\,l+1}$ and $M^{l+1}_{l+2\,l+2}$ coincides with relation (74) and differs from the correct result.

If an electron remains fast in the final state also ($a' = Z/p' \ll 1$), we can apply the Born approximation. According to the results obtained by Bunkin and Fedorov [25] (see Eq. (6)), the induced 2BrS cross section in the Coulomb field in this case has the elementary form

$$\frac{d\sigma_B}{d\Omega} = \frac{F^4 Z^2}{2^4\omega^8}\frac{|\mathbf{e}\cdot(\mathbf{p}-\mathbf{p}')|^4}{(\mathbf{p}-\mathbf{p}')^4}\frac{p'}{p}, \quad p'^2 = p^2 - 4\omega. \quad (81)$$

This result can also be obtained directly from the exact results of partial-wave analysis. In the low-frequency region $\omega \ll p^2$ (although the frequency in this case may be significant as compared to the binding energy, $\omega \sim 1$), the partial Born series can be reduced to low-frequency series in which we must assume that $a \longrightarrow 0$ (see Subsection 5.1). For an arbitrary ω, partial Coulomb MEs $M^L_{l'\,l}$ are also simplified significantly in the Born region: first, the terms containing integrals in relations (38)–(40) are small for $a, a' \ll 1$ since these terms contain an extra factor Z/p; second, the parameters of functions ${}_2F_1$ become integral so that these function can be reduced to elementary functions. For example, the expression for $M^{l+1}_{l\,l}$ in the Born limit assumes the form

$$M^{l+1}_{l\,l} = Z\frac{(-1)^l 4^{l+1}(l!)^2}{(2l+3)!}\frac{(l+1)(pp')^{l+1/2}}{(p-p')^{2l+4}} \times\left[(l+2)\frac{p^2+p'^2}{\omega(p+p')}{}_2F_1(l+1, l+2, 2l+4; \lambda_0) + 4(l+1){}_2F_1(l+2, l+2, 2l+4; \lambda_0)\right],$$

where $\lambda_0 = -4pp'/(p-p')^2$. Moreover, assuming that $a = a' = 0$ in the integrand in formulas (38)–(40), we can calculate the second Born correction from the integrated terms in radial MEs in elementary form as well. However, the explicit expressions of these integrals and of functions ${}_2F_1$ with integral parameters in terms of elementary (power and logarithmic) functions turn out to be cumbersome and become more and more involved with increasing l, which complicates the summation of partial series in l in formulas (20). In the first Born approximation, such a summation can be carried out by using the expansion (see formulas (5.17.26) and (5.17.32) in [50])

$$\frac{1}{(\mathbf{p}-\mathbf{p}')^2} = \sum_{l=0}^{\infty} a_l(p, p')P_l(\cos\theta),$$

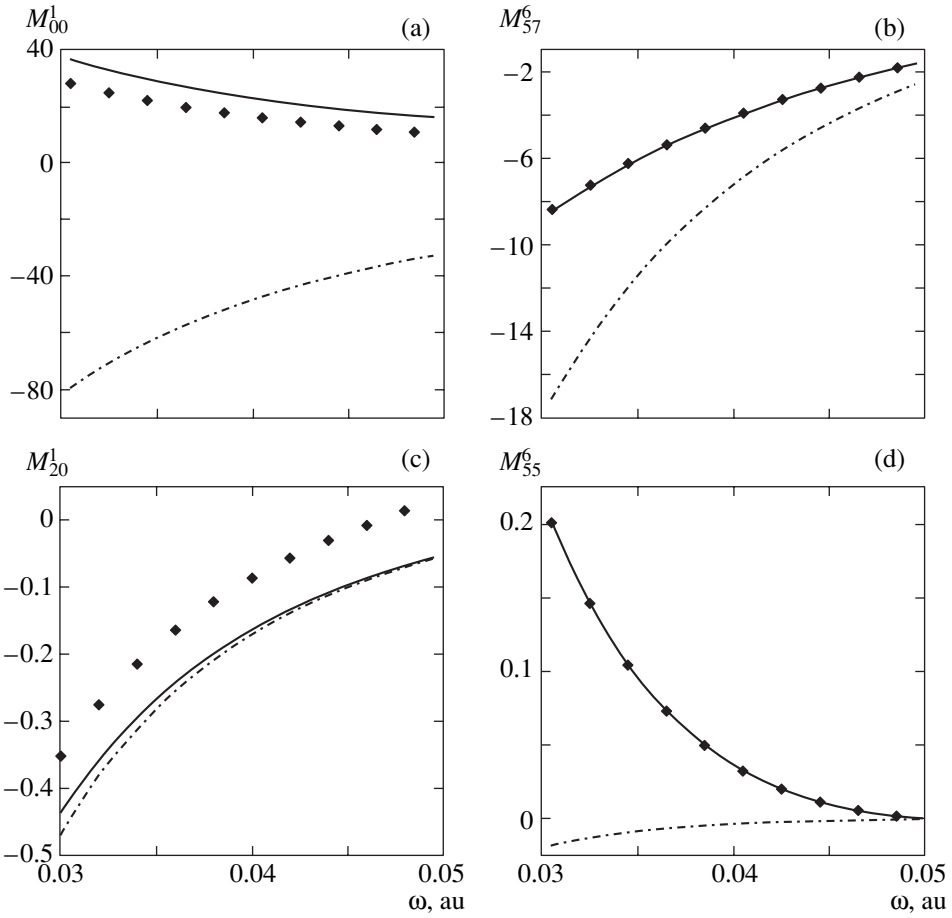

Fig. 3. Frequency dependences of the matrix elements of 2BrS for the initial electron energy $E = 0.1$ (a, b) and 1.0 (c, d). Solid curves correspond to ReM, dot-and-dash curves to ImM, and rhombs to ReM in approximation (59).

$$a_l(p, p') = \frac{l!(pp')^l}{(1/2)_l(p-p')^{2l+2}} \times {}_2F_1\left(l+1, l+1, 2l+2; -\frac{4pp'}{(p-p')^2}\right).$$

Using the recurrence relations for functions ${}_2F_1$ and Legendre polynomials, we can verify that the summation of partial series for the amplitude in the Born limit results in expression (81).

6. NUMERICAL RESULTS FOR THE COULOMB POTENTIAL AND DISCUSSION

6.1. Frequency and Energy Dependences of Radial Matrix Elements

Since the cross sections of two-photon bremsstrahlung processes remain multiparametric functions even for fixed experimental geometry and photon polarization, it would be interesting to analyze qualitatively the dependence of MEs $M^L_{l'l}(E', E, \mathscr{E})$ on the frequency of photons and on the electron energy for various values the orbital angular momenta l, L, and l'. The existence of exact formulas (38)–(40) for the Coulomb potential makes it possible to obtain quantitative results for MEs and cross sections in a wide range of these parameters since the problem is reduced to the evaluation of functions ${}_2F_1$ and their integrals, which can easily be carried out using standard computer programs. It was shown in [64] that single-photon Coulomb MEs $d_{l'l}(E', E)$ are positive monotonic functions of energy, which decrease monotonically with increasing E', say, for a fixed E and $E' > E$ and diverge for $E' \longrightarrow E$ (in the presence of a non-Coulomb part in potential $U(r)$, the MEs may change their sign in a certain energy range depending on the value of the non-Coulomb correction to scattering phases [65]). In the two-photon case, the situation is complicated significantly due to the presence of an additional parameter, viz., the photon frequency ω (or the energy of an electron $\mathscr{E} = E \pm \omega$ in the virtual state), and in view of the complex nature of the MEs $M^L_{l'l}$ (these matrix elements are real-valued only for $\mathscr{E} < 0$, which corresponds to the re-emission of a photon with $\omega > E$ in the course of elastic scattering (see Fig. 1b)).

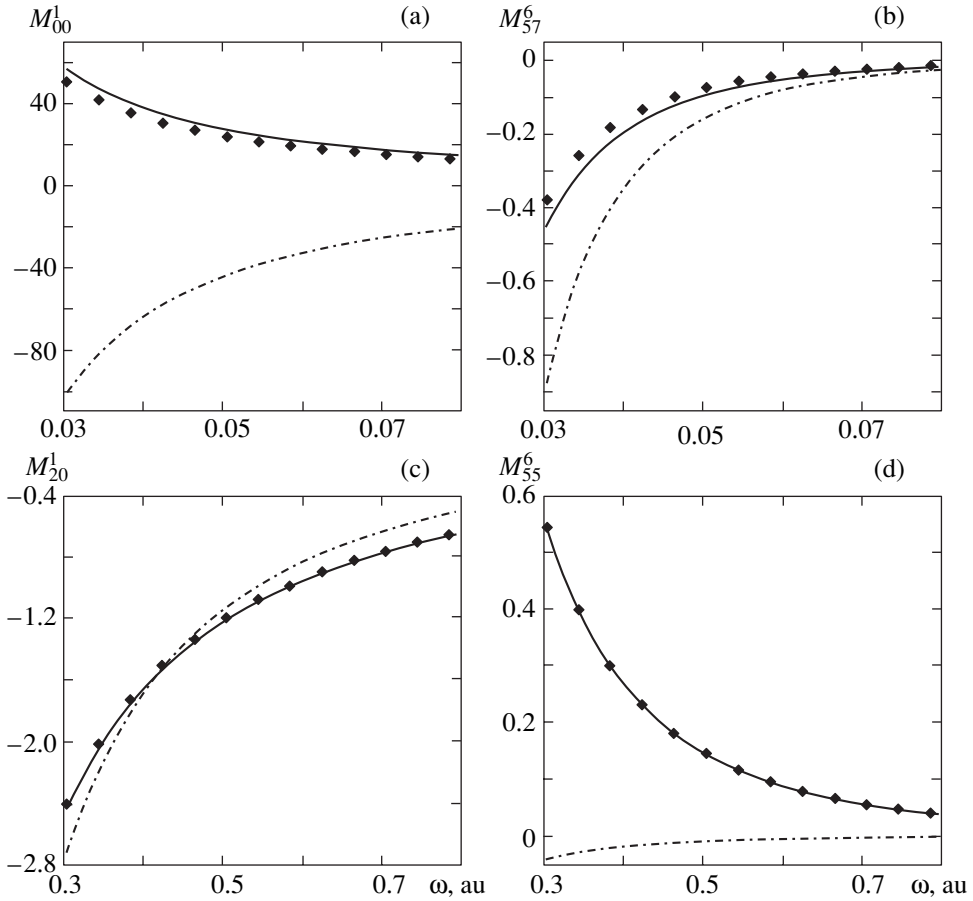

Fig. 4. The same as in Fig. 3 for the matrix elements of double bremsstrahlung absorption.

Since the imaginary parts of the MEs $M^L_{l'\,l}$ can be reduced to the simple product of single-photon MEs (see formula (59)), it becomes especially interesting to establish the range of the parameters, in which the imaginary part makes a dominating contribution to two-photon MEs in view of the obvious radical simplification of the results.

It was mentioned above that, for a fixed l, the contribution to two-photon cross sections comes from two "diagonal" ($M^{l+1}_{l\,l}$ and $M^{l}_{l+1\,l+1}$) and two "nondiagonal" ($M^{l+1}_{l\,l+2}$ and $M^{l+1}_{l+2\,l}$) radial MEs. According to the results of calculations made in a wide range of E, ω, and l, all these elements exhibit quite a universal behavior. The real and imaginary parts of all radial MEs (except $\mathrm{Re}\,M^{l+1}_{l\,l}$) are negative and decrease monotonically in absolute value with increasing frequency without reversing their signs (the imaginary part decreases at a higher rate than the real part). The signs of $\mathrm{Re}\,M^L_{l'\,l}$ and $\mathrm{Im}\,M^L_{l'\,l}$ are preserved upon a change in l. The absolute values of $\mathrm{Re}\,M^L_{l'\,l}$ and $\mathrm{Im}\,M^L_{l'\,l}$ for a given initial energy (outside the low-frequency region) decrease with increasing l (the imaginary part decreases at a higher rate than the real part in this case also), the rate of their decrease with increasing frequency increasing with l. Figure 3 illustrates some examples of numerical calculations of the frequency dependence of radial MEs with $l = 0$ and 5 for induced 2BrS ($\mathscr{E} = E - \omega$, $E' = E - 2\omega$) for small ($E = 0.1$) and intermediate ($E = 1.0$) values of the initial energy E. It should be noted that all MEs assume finite values at the threshold frequency $\omega = E/2$ ($E' = 0$).

Figure 4 shows the frequency dependence of radial MEs of double bremsstrahlung absorption ($\mathscr{E} = E + \omega$, $E' = E + 2\omega$) for the same values of E and l as in the case of 2BrS (see Fig. 3). It can be seen that the behavior of $M^L_{l'\,l}$ for emission and absorption processes is qualitatively the same (monotonic decrease of $\mathrm{Re}\,M^L_{l'\,l}$ and $\mathrm{Im}\,M^L_{l'\,l}$ upon an increase in ω and angular momentum l preserving fixed sign, and the rapid decrease in the imaginary part). The only difference is that there is no threshold limitation on frequency in the case of bremsstrahlung absorption, and the MEs decrease upon

an increase in ω, tending to an asymptotic form of type (74) (in a very far frequency range). For a given frequency ω, the "diagonal" MEs for absorption are considerably larger than the corresponding MEs for 2BrS, and $\left|M^{l+1}_{l\,l}\right| > \left|M^{l}_{l+1\,l+1}\right|$. An interesting correspondence is observed between the numerical values of "nondiagonal" MEs for emission and absorption:

$$M^L_{l'\,l}(E + 2\omega, E + \omega, E) \leftrightarrows M^L_{l\,l'}(E - 2\omega, E - \omega, E).$$

In particular, the MEs in which the change in energy and in the orbital angular momentum occurs "in the same direction" have the largest magnitude in both cases in the major part of the frequency range. This corresponds to the well-known Bethe rule for single-photon transitions in a discrete spectrum [55]. However, for two-photon transitions in the continuous spectrum, this rule turns out to be not very stringent; it is violated in the low-frequency range, this region expanding with increasing angular momentum *l*.

The existence of exact results makes it possible to verify the correctness of approximations used for calculating $M^L_{l'\,l}(E', \mathscr{E}, E)$. The simplest among them is the "pole" approximation, which consists in the inclusion of only the imaginary part of $M^L_{l'\,l}$ in relation (57) (originating from the term with the δ function in Eq. (58)). In the conditions of applicability of perturbation theory in the wave field, the model of "significant states" [66, 67] in the theory of multiphoton transitions in a strong field can also be reduced to this approximation. Asymptotic estimates (66) and numerical calculations show that the imaginary part dominates in the low-frequency range for low initial electron energies (the accuracy of the pole approximation for "nondiagonal" MEs in this case is much higher than for "diagonal" MEs). In the pole approximation, a two-photon transition can be regarded as a "cascade" transition, i.e., a transition occurring only via an intermediate state of the continuum with energy $\mathscr{E}$, which corresponds to the factorization of the process amplitude:

$$M^L_{l'\,l}(E', \mathscr{E}, E) \longrightarrow i\,\mathrm{Im}\,M^L_{l'\,l}$$
$$= -i\pi \langle R_{E'l'}|D(l', L)|R_{\mathscr{E}L}\rangle \langle R_{\mathscr{E}L}|D(L, l)|R_{El}\rangle.$$

As the frequency and/or the electron energy increases, the contribution of the omitted real part of MEs increases. In the high-frequency region ($a \ll 1$, $\omega/E' \gg 1$, $\omega/E \sim 1$ for emission and $a' \ll 1$, $\omega/E' \sim 1$, $\omega/E \gg 1$ for absorption), the real part of $M^L_{l'\,l}$ becomes dominating, while the imaginary part has a relative smallness of the order of $1/\sqrt{\omega}$. In the intermediate frequency range $\omega \sim E$, the quantities $\mathrm{Re}\,M^L_{l'\,l}$ and $\mathrm{Im}\,M^L_{l'\,l}$ are of the same order of magnitude so that transitions through various intermediate states corresponding to the real part of $M^L_{l'\,l}$ become as significant as "cascade" transitions. By way of an example, we give below a number of MEs $M^L_{l_f l_i}(E + 2\omega, E + \omega, E)$ for the energy $E = 0.0536 = 1.458$ eV and $\omega = 0.0735 = 2.0$ eV, which appear when we estimate the contribution of corrections to the photoionization cross section of the state of a hydrogen atom with $n = 5$, $l = 4$, which are quadratic in intensity and associated with virtual transitions in the continuum [68] (the results are given for the dipole interaction operator in the "form of length," which was used in [68]):

$$M^4_{35} = -(14.71 + i \times 24.76),$$

$$M^4_{55} = -(3.882 + i \times 0.910) \times 10^2,$$

$$M^6_{55} = (3.323 - i \times 0.594) \times 10^2,$$

$$M^6_{75} = -(2.386 - i \times 3.100) \times 10^2,$$

$$M^2_{13} = -(1.353 + i \times 2.793) \times 10^2,$$

$$M^2_{33} = -(1.369 + i \times 0.606) \times 10^3,$$

$$M^4_{33} = (1.141 - i \times 0.346) \times 10^3,$$

$$M^4_{53} = -(0.819 + i \times 1.270) \times 10^3.$$

It can be seen that, in the case under investigation, the pole approximation (as well as the Bethe rule) is inapplicable; this situation is typical of "superthreshold" multiphoton processes, when the photon frequencies are comparable to the electron energy in the continuum. It should also be borne in mind that individual radial MEs in the total amplitude of the process "interfere" considerably (cancelled out) as a rule; this renders the requirements to their accuracy much more stringent.

Approximation (59) (1-delta approximation [14]) takes into account exactly the real part of the integrated terms in relations (38)–(40) along with the imaginary part of $M^L_{l'\,l}$. It was established in Section 5 that this leads to correct results in the low-frequency range (for any values of the initial electron energy) in the Born region and gives a quite accurate result for two out of four MEs $M^L_{l'\,l}$ (those whose final state has the smallest possible orbital angular momentum, see Subsection 5.2) as well as the correct form of the frequency dependence and the order of magnitude of the remaining two MEs in the high-frequency region. Consequently, this approximation is in good agreement with exact results practically for all values of the laser field frequency and electron energy (see Figs. 3 and 4). A noticeable discrepancy is observed only for small energies and for small values of momentum *l* (the largest discrepancy is observed for the MEs in which the integrated terms do not provide a correct high-frequency asymptotic form).

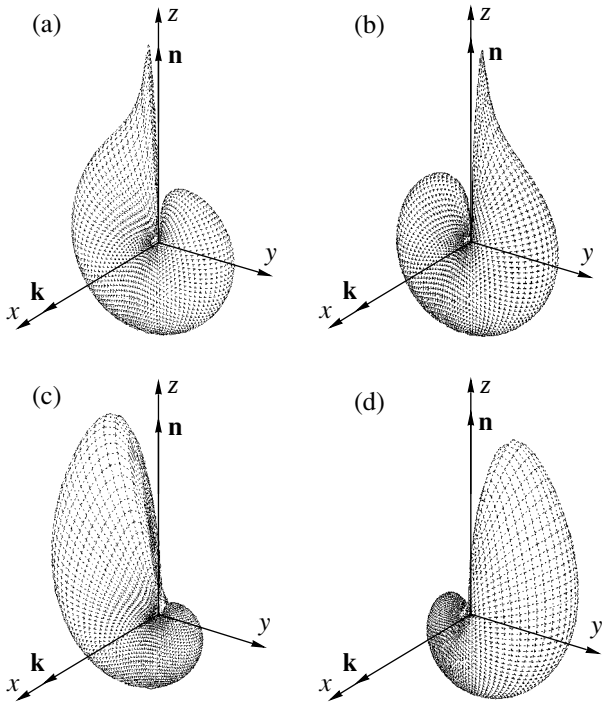

Fig. 5. Spatial distribution of electrons in 2BrS, which are scattered (with initial energy $E = 1.0$) by a Coulomb center in the presence of a circularly polarized wave with frequency $\omega = 0.01$ (a, b) and $\omega = 0.1$ (c, d) for $\xi = 1$ (a, c) and $\xi = -1$ (b, d). The initial electron momentum lies in the polarization plane (*yz* plane).

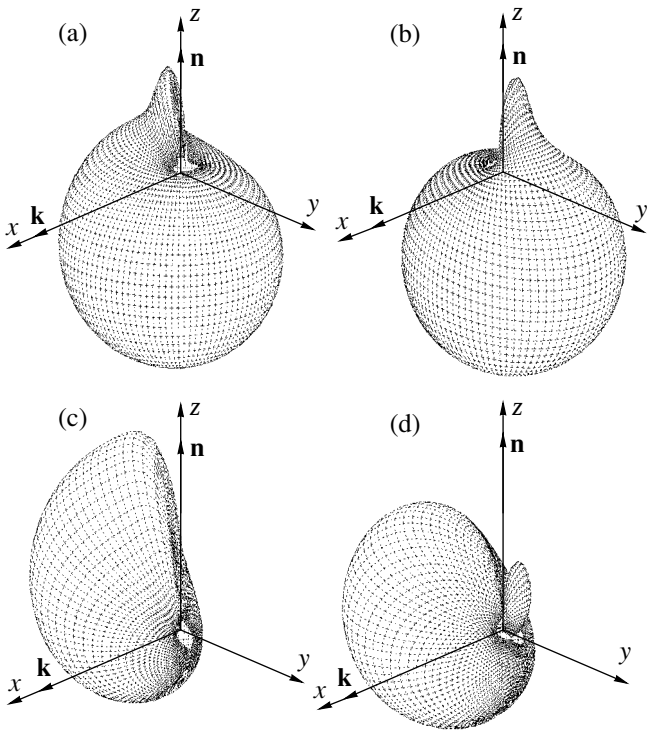

Fig. 6. The same as in Fig. 5, but in the field with elliptical polarization and frequency $\omega = 0.1$: (a) $\alpha = \pi/2$. $\xi = 1/\sqrt{2}$; (b) $\alpha = \pi/2$, $\xi = -1/\sqrt{2}$; (c) $\alpha = \pi/4$, $\xi = 1/\sqrt{2}$; (d) $\alpha = \pi/4$, $\xi = -1/\sqrt{2}$.

6.2. Angular Distributions and Dichroism in Induced Bremssrahlung Processes

It was established in Subsection 2.3 that angular distributions depend considerably not only on the initial electron energy E and frequency ω, but also on the polarization of photons. Figure 5 shows qualitative features of the spatial distribution of electrons scattered by a Coulomb center in the presence of a circularly polarized wave with $\xi = \pm 1$ in the case of induced 2BrS for two frequency values of $\omega = 0.01$ and 0.1, In accordance with the geometry presented in Fig. 2, the direction $\mathbf{k}$ of the light beam is chosen to be orthogonal to the initial momentum $\mathbf{p} = p\mathbf{n}$ of electrons with energy $E = p^2/2 = 1.0$ au. Figure 5 clearly demonstrates the presence of CD: cross sections $d\sigma/d\Omega$ for $\xi = +1$ and $\xi = -1$ differ considerably (at the same time, they are transformed into each other upon reflection relative to the *xz* plane; see Subsection 2.3). The CD effect decreases with frequency since the low-frequency asymptotic form (68) contains only the "regular" term. However, in the range of small scattering angles, the values of $d\sigma/d\Omega$ for $\xi = \pm 1$ differ significantly even for $\omega/E = 0.01$ (see Figs. 5a and 5b and discussion in Subsection 5.1). As the value of θ decreases further, the value of Δ_{CD} again becomes smaller than f_{reg}, which is also confirmed by numerical calculations: it can be seen from Fig. 5 that the values of $d\sigma/d\Omega$ for $\xi = +1$ and -1 coincide for $\theta = 0$.

In a field with elliptic polarization, the asymmetry in the angular distribution is caused, apart from CD, by the effect of ED (the term with Δ_{ED} in relation (24)). In this case, the cross section depends to a considerable extent on the orientation of the polarization ellipse, which is defined in Fig. 2 by the angle α between vector $\boldsymbol{\epsilon}$ and the *y* axis. Figure 6 shows the angular distribution of electrons for the same values of E and ω as in Figs. 5c and 5d, but for $\xi = \pm 1/\sqrt{2}$ and for two values of angle α: $\alpha = \pi/2$ ($\boldsymbol{\epsilon} \parallel \mathbf{p}$) and $\alpha = \pi/4$ (vector $\mathbf{p}$ forms the angle $\pi/4$ with the principal axis of the polarization ellipse). Figures 6c and 6d visually illustrate the reduction of symmetry upon a transition from the circular to elliptical polarization, which was considered in Subsection 2.3: for $\alpha = \pi/4$, the results obtained for $\xi = 1/\sqrt{2}$ and $\xi = -1/\sqrt{2}$ differ qualitatively, although the *yz* plane remains the symmetry plane as before. It should be noted that although the term Δ_{ED} in general formula (24) has no smallness parameter, numerical calculations show, however, that the effect of elliptical dichroism on the asymmetry of angular distributions is considerably weaker than the effect of circular dichroism.

By way of illustration of the absolute value of two-photon cross sections and their dependences on elliptic-

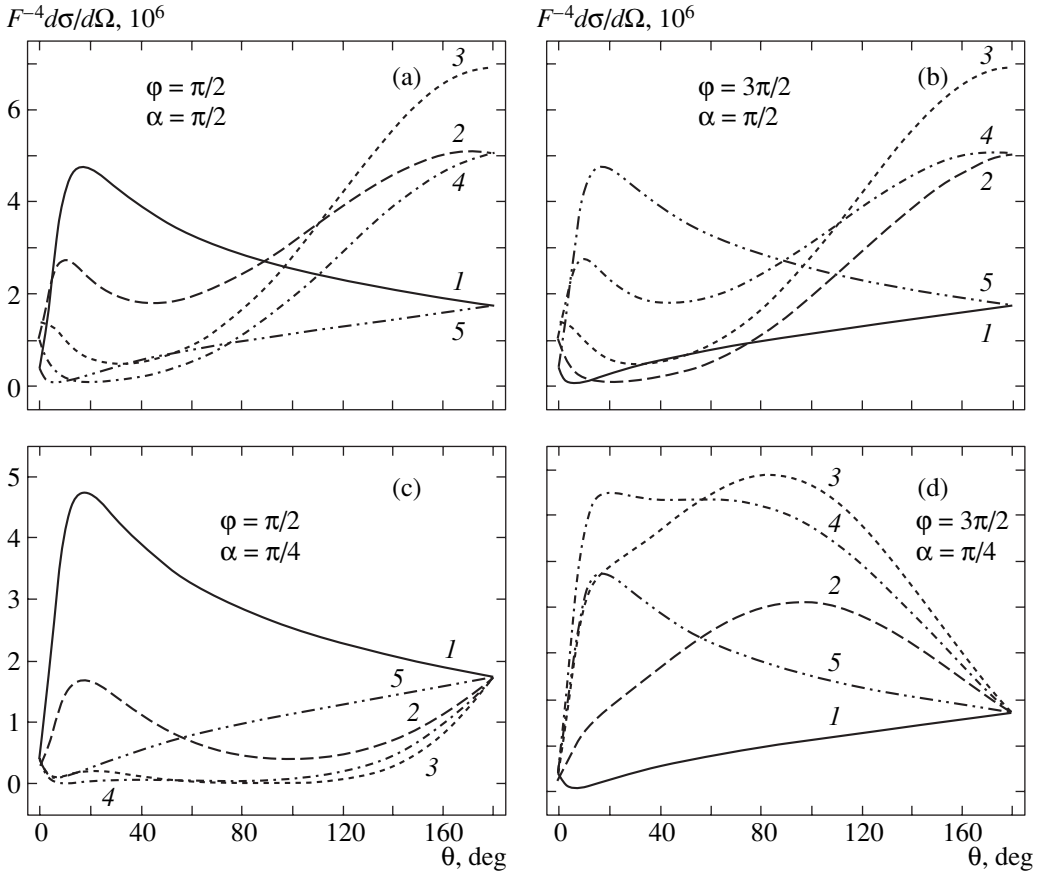

Fig. 7. Dependence of the 2BrS cross section for electrons with $E = 1.0$ and $\omega = 0.1$ on the scattering angle θ in the polarization ellipse plane: $\xi = -1$ (*1*), $-1/\sqrt{2}$ (*2*), 0 (*3*), $1/\sqrt{2}$ (*4*), and 1 (*5*). The values of angles α and φ in the geometry of Fig. 2 are given in the figures.

ity, Fig. 7 shows the angular distributions in angle θ between $\mathbf{p}$ and $\mathbf{p}'$ (in the plane of polarization ellipse) for induced 2BrS for $E = 1.0$, $\omega/E = 0.1$, and for various values of ξ (the curves for double bremsstrahlung absorption have an analogous form with the substitution $\xi \longrightarrow -\xi$). The results are given for $\alpha = \pi/2$ and $\alpha = \pi/4$. In the former case ($\alpha = \pi/2$), for $\theta = \pi$, the cross sections are exactly identical for $\xi = \pm 1$ due to the absence of CD for backward scattering. At the same time, the cross sections virtually coincide in the case of elliptic polarization with $\xi = \pm 1/\sqrt{2}$ also in view of the smallness of Δ_{ED} as compared to the regular term f_{reg} in Eq. (24) for $\theta = \pi$. In the latter case ($\alpha = \pi/4$), four curves (with $\xi = \pm 1$ and $\xi = \pm 1/\sqrt{2}$) converge at one point for $\theta = \pi$ since the regular term f_{reg} for these values of angles α, θ, and φ is independent of polarization to a high degree of accuracy (>95%) and makes a dominating contribution to the cross section. It can be seen that the polarization sign reversal in the range of small angles changes the cross section by almost an order of magnitude. A considerable dependence of the results on the orientation of vector $\mathbf{p}$ relative to the principal axis of the polarization ellipse and the absence of symmetry $d\sigma(\xi; \varphi) = d\sigma(-\xi; -\varphi)$ for $\alpha = \pi/4$ are also worth noting.

The dependence of the two-photon absorption cross section on energy E for the same values of ξ and ω as in Fig. 7 is shown in Fig. 8 for two values of angle θ and orientation of $\mathbf{p}$ at right angles to the principal polarization axis ($\alpha = 0$). Dichroism effects are most significant for $\omega \sim E$, the energy dependence in this region changing qualitatively upon a variation of θ.

Double bremsstrahlung absorption differs from 2BrS in the existence of the "critical" scattering geometry, in which the transferred momentum $\Delta\mathbf{p} = \mathbf{p} - \mathbf{p}'$ turns out to be orthogonal to the polarization plane so that $\mathbf{e} \cdot \Delta\mathbf{p} = 0$. In this case, the Born approximation (81) and the low-frequency asymptotic form (64) give zero value for the cross section, for which the value of $d\sigma/d\Omega$ is finite when the scattering potential is accurately taken into account. Figure 9 shows the dependence of the double bremsstrahlung absorption cross section on angle φ (see Fig. 2) in the "critical" region. For energy $E = 1.0$ and $\omega = 1/6$ (Fig. 9a), the Bunkin–Fedorov formula (81) describes the cross section quite satisfactorily (although the Born parameters are not very small in this region: $\alpha \approx 0.7$ and $\alpha' \approx 0.6$) except in the small angular region near the "critical" point $\theta = \pi/6$, $\varphi = 0$ at which the Born results vanishes, and the exact cross section has a clearly manifested minimum.

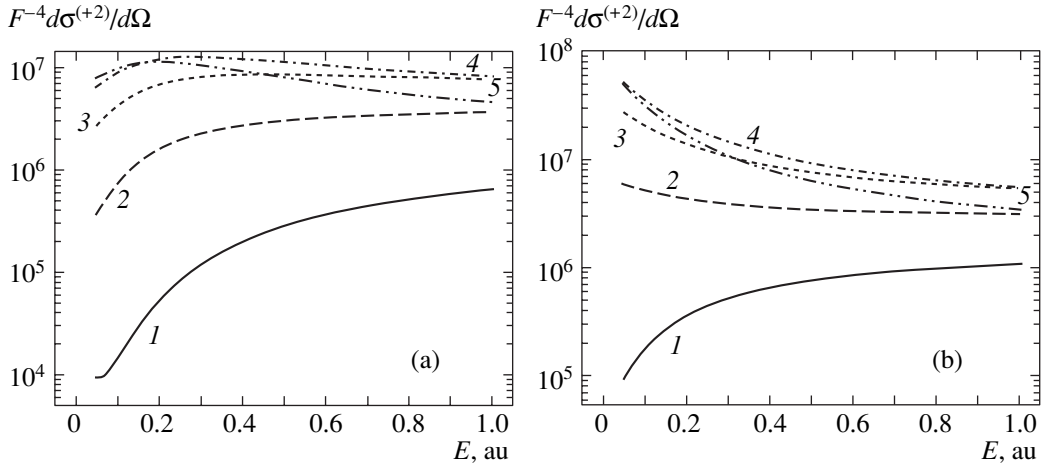

Fig. 8. Dependence of the two-photon absorption cross section on energy E for $\omega = 0.1$, $\alpha = 0$, $\varphi = \pi/2$ and for various ξ (notation of the curves is the same as in Fig. 7) (a) $\theta = \pi/6$; (b) $\theta = \pi/3$.

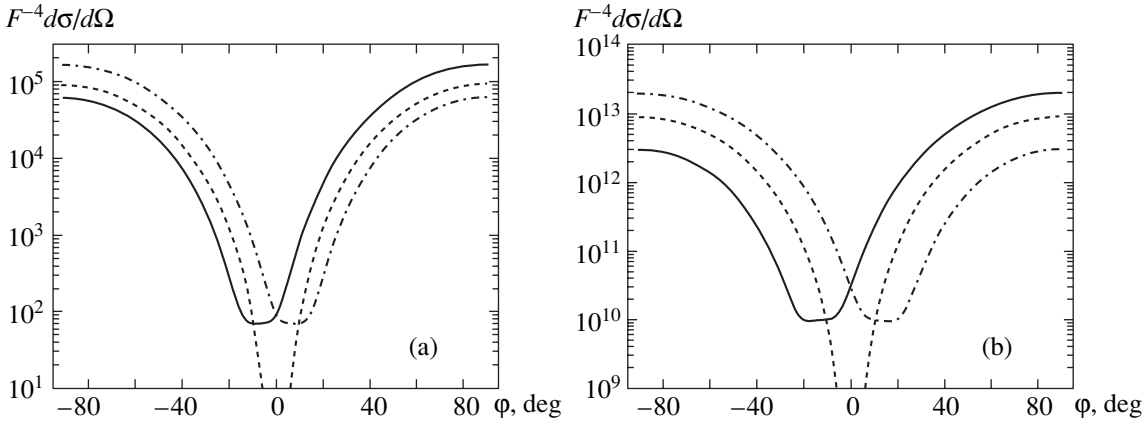

Fig. 9. Dependence of the double bremsstrahlung absorption cross section on angle φ for $\theta = \pi/6$ (solid curves correspond to $\xi = 1/\sqrt{2}$ and dot-and-dash curves to $\xi = -1/\sqrt{2}$), $E = 1.0$, $\omega = 1/6$ ((a), the dashed curve corresponds to the Born approximation (81)) and $E = 0.1$, $\omega = 1/60$ ((b), the dashed curve corresponds to the low-frequency asymptotic form (64)).

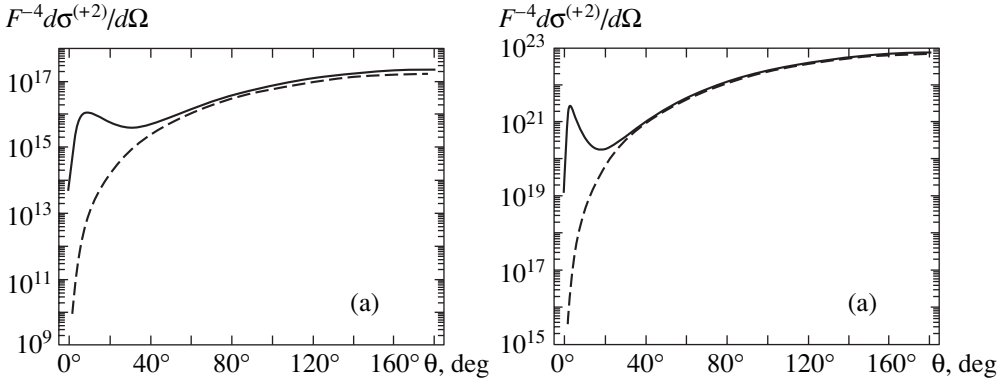

Fig. 10. Double bremsstrahlung absorption cross section for electrons with energy $E = 0.1$ by a Coulomb center in the field of a linearly polarized wave with frequency $\omega = 0.005$ (a) and 0.001 (b). The initial electron momentum is directed along the polarization vector of the wave; θ is the scattering angle. Solid curves correspond to the exact result and the dashed curves to the low-frequency approximation (64).

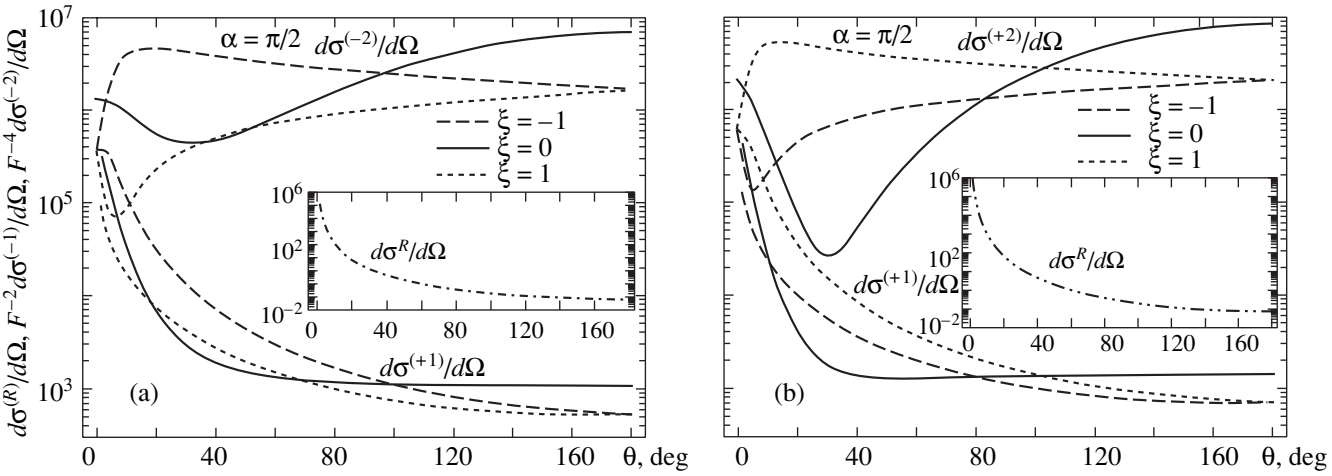

Fig. 11. Scattering cross sections for electrons with energy $E = 1.0$ in the fields of linearly ($\xi = 0$) and circularly ($\xi = \pm 1$) polarized waves with frequency $\omega = 0.1$, The momentum of a scattered electron lies in the polarization plane; $\varphi = \pi/2$. The quantities $d\sigma^{(n)}/d\Omega$ with $n = -1, -2$ and $n = +1, +2$ correspond to (a) emission and (b) absorption of one or two photons. The insets show the cross section $d\sigma^{(R)}/d\Omega$ of Rutherford scattering in zero field.

At the same time, the low-frequency asymptotic form (64) for $E = 0.1$ and $\omega = 1/60$ (Fig. 9b) leads to a much worse quantitative agreement with exact results. Another region of "critical" parameters, in which the low-frequency Kroll–Watson asymptotic form leads to a strong discrepancy with experimental values and which has been discussed actively during recent years (see references in [32]) is the low-energy scattering (with energy E on the order of several electronvolts) via small angles in a linearly polarized field with the initial momentum **p** along the direction of polarization. Figure 10 shows the double bremsstrahlung absorption cross sections for $E = 0.1$ and $\omega/E = 0.01$ and 0.05 in this geometry. It can be seen that the difference between exact and approximate results for small angles can be as large as five to six orders of magnitude, although an increase in θ leads to nearly complete agreement (the results for 2BrS are qualitatively the same as in Fig. 10, but the difference for small angles θ in this case does not exceed one or two orders of magnitude). Thus, the problem of simple approximations of bremsstrahlung cross sections for describing small-angle scattering at low energies (when the Born approximation is inapplicable) requires special analysis.

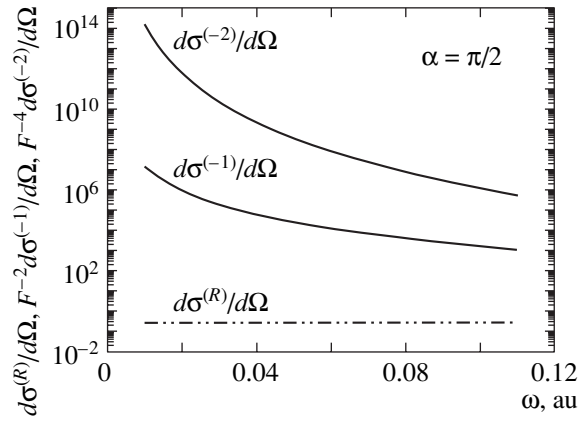

Fig. 12. Frequency dependence of the single-photon ($d\sigma^{(-1)}/d\Omega$) and double bremsstrahlung ($d\sigma^{(-2)}/d\Omega$) emission of electrons with energy $E = 1.0$ by a Coulomb center in the field of a circularly polarized wave with $\xi = 1$ in the geometry of Fig. 2 with $\theta = \varphi = \pi/2$; $d\sigma^{(R)}/d\Omega$ is the Rutherford scattering cross section.

Figure 11 illustrates the relation between the cross sections of one- and two-photon scattering as functions of the laser radiation parameters and scattering angle. The cross sections of conventional Rutherford scattering ($d\sigma^{(R)}/d\Omega$) and one- and two-photon absorptions ($d\sigma^{(n)}/d\Omega$ with $n = \pm 1, \pm 2$) are given as functions of angle θ in the polarization plane (analytic expressions for factors Q in the amplitude of single-photon processes (3) and (4) are given in [4] for the Coulomb potential). It can be seen that the cross sections ($d\sigma^{(n)}/d\Omega$ are more sensitive to a change in the ellipticity for angles $\theta < \pi/2$; in both cases, for small angles, the cross sections have maximal values for circular polarization, while scattering via angles $\theta > \pi/2$ is more effective in a field with linear polarization. In contrast to the sharp angular dependence of the Rutherford cross section $d\sigma^{(R)}/d\Omega$ for small angles θ, the cross sections of bremsstrahlung processes depend on θ more smoothly, although single-photon cross sections also increase by more than two orders of magnitude for small angles, while two-photon processes exhibit a nonmonotonic dependence. Dichroism effects are the most significant for small angles, although the difference in the cross sections for scattering at right angles attains 100% upon the sign reversal of ξ. For a fixed initial electron energy, the absolute value of bremsstrahlung cross sections increases sharply with decreasing frequency (Fig. 12); in this case, the frequency dependences are successfully approximated by the expression

$$d\sigma^{(\pm n)}(\omega)/d\Omega \sim 1/\omega^{4n}.$$

It should be noted in conclusion that the above results make it possible to qualitatively estimate the limits of applicability of perturbation theory in the laser field for describing bremsstrahlung processes. For example, in the range of small angles, for $E \approx 1$ and $\omega \approx 0.1$, a typical ratio of two-photon to one-photon cross sections amounts to $(10^3–10^4)F^2$ and attains unity (when perturbation theory becomes obviously inapplicable) for an intensity $I_{cr} \sim (10^{12}–10^{13})$ W/cm^2, which is much smaller than the intraatomic intensity $I_0 = 3.51 \times 10^{16}$ W/cm^2. The value of I_{cr} decreases rapidly with frequency (in proportion to ω^4) so that the effective parameter of perturbation theory in the optical frequency range is F/ω^2 (or the ratio of the amplitude of classical oscillations of an electron in a laser field to the Born radius). For small θ, the ratio $d\sigma^{(\pm 2)}(\omega)/d\sigma^{(\pm 1)}$ attains unity only in ultrastrong fields with $I_{cr} \sim I_0$ (see Fig. 11), while the dominating contribution to the cross section of scattering via small angles in weaker fields comes from single-photon processes.

ACKNOWLEDGMENTS

This study was partly financed by the CRDF and the Ministry of Education of the Russian Federation (grant no. VZ-010-0) as well as by the Russian Foundation for Basic Research (project no. 00-02-17843), the Competition Center of the Education Ministry of the Russian Federation (grant no. E00-3.2-515), and the National Science Foundation of the USA (AFS, grant no. PHY-0070980).

APPENDIX A

Using the recurrence relations for the degenerate hypergeometric function $\Phi(\alpha, \beta; x)$, we can present the action of the dipole operators (22) on the Coulomb wave function $R_{El}(r)$ of the continuous spectrum in the form

$$\begin{aligned} D(l+1, l)R_{El}(r) &= -p\frac{l+1-ia}{|l+1-ia|}R_{El+1}(r) \\ &- \frac{2ZC_{El}}{(2l+3)!}(2pr)^l \exp(-ipr) \\ &\times [(l+2+ia)\Phi(l+3+ia, 2l+4; 2ipr) \\ &+ (l+1-ia)\Phi(l+2+ia, 2l+4; 2ipr)], \end{aligned} \tag{A.1}$$

$$\begin{aligned} D(l+1, l+2)R_{El+2}(r) &= p\frac{|l+2-ia|}{l+2-ia}R_{El+1}(r) \\ &- \frac{2ZC_{El+2}}{(2l+3)!(l+2-ia)}(2pr)^l \exp(-ipr) \\ &\times [\Phi(l+3+ia, 2l+4; 2ipr) \\ &- \Phi(l+2+ia, 2l+4; 2ipr)]. \end{aligned} \tag{A.2}$$

Since the first terms on the right-hand sides of relations (A.1) and (A.2) are proportional to $R_{El+1}(r)$, the corresponding terms in the MEs $M^L_{l'l}$ in relations (36) can be expressed in terms of MEs (37) in accordance with relations (38)–(40). The values of $d_{l'l}$ can easily be calculated using relations (A.1) and (A.2), which gives formulas (41) for $d_{l+1\,l}$ and $d_{l+1\,l+2}$, in which the integral

$$\begin{aligned} I^{m'm}(E', E) &= \int_0^\infty dr r^{2l+3} \exp[-i(p'+p)r - \varepsilon r] \\ &\times \Phi(l+3-m'+ia', 2l+4; 2ip'r) \\ &\times \Phi(l+3-m+ia, 2l+4; 2ip'r) \end{aligned} \tag{A.3}$$

is a tabular integral [56], which can be reduced to the functions ${}_2F_1$ (see relation (42)).

The double integral $J^{m'm}$ in relations (38)–(40) contains the radial Coulomb Green's function $g_l(r, r', \mathscr{E})$:

$$\begin{aligned} J^{m'm} &= \int_0^\infty dr' dr (r'r)^{l+2} \exp[-ip'r' - ipr - \varepsilon r] \\ &\times \Phi(l+3-m'+ia', 2l+4; 2ip'r) \\ &\times g_{l+1}(\mathscr{E}, r, r')\Phi(l+3-m+ia, 2l+4; 2ipr). \end{aligned} \tag{A.4}$$

In order to evaluate this integral, it is convenient to use the integral representation of g_L [69]:

$$\begin{aligned} g_L(r, r', \mathscr{E}) &= \frac{2}{\sqrt{rr'}}\int_0^1 \frac{dt}{1-t} t^{-(1/2)-Z\nu} \\ &\times \exp\left[-\frac{r+r'}{\nu}\frac{1+t}{1-t}\right] I_{2L+1}\left(\frac{4\sqrt{rr't}}{\nu(1-t)}\right), \end{aligned} \tag{A.5}$$

where $I_k(t)$ is a modified Bessel's functions $\nu = 1/\sqrt{-2\mathscr{E}}$. It should be noted that integrals (A.3) and (A.4) with oscillating functions contain regularizing factors $\exp(-\varepsilon r)$ with $\varepsilon \longrightarrow +0$. Substituting expression (A.5) into integral (A.4) and using the integral representation of the function $\Phi(\alpha, \beta, x)$ [56], we obtain

$$\begin{aligned} &J^{m'm}(E', E, \mathscr{E}) \\ &= \frac{2(2l+3)!}{\Gamma(l+1+m+ia)\Gamma(l+3-m-ia)} \\ &\times \int_0^1 dt \frac{t^{-Z\nu-1/2}}{1-t}\int_0^1 du u^{l+m+ia}(1-u)^{l+2-m'-ia} \\ &\times \int_0^\infty dr' r'^{l+3/2} \exp\left[-\left(\frac{1}{\nu}\frac{1+t}{1-t} + ip'\right)r'\right] \\ &\times \Phi(l+1+m'+ia', 2l+4; 2ip'r')\int_0^\infty dr r^{l+3/2} \\ &\times \exp\left[-\left(ip + \frac{1}{\nu}\frac{1+t}{1-t} - 2ipu\right)r\right] I_{2l+3}\left(\frac{4\sqrt{rr't}}{\nu(1-t)}\right). \end{aligned} \tag{A.6}$$

The special relation between the index of Bessel's function I_k, the parameter β in $\Phi(\alpha, \beta; x)$, and the exponents r and r' in integral (A.6), which was obtained using transformations (A.1) and (A.2), makes it possible to express the integrals with respect to r and r' in terms of elementary functions [63]. As a result, the integral with respect to u in relation (A.6) gives a definition of the hypergeometric function of two variables (Appel's function),

$$F_1(l+1+m+ia;\ l+3-m'-ia',\ l+1+m'+ia';\ 2l+4;\ x, y),$$

which can be reduced, for the above values of parameters, to ${}_2F_1$ in accordance with the well-known reduction formulas [56], and $J^{m'm}$ assumes the final form (43).

APPENDIX B

Analytic continuation of formulas (38)–(40) in variables p and p' to the range of negative energies, $p \longrightarrow iZ/n$ and $p' \longrightarrow iZ/n'$, makes it possible to obtain the MEs of two-photon transitions between the states $|nl\rangle$ and $|n'l'\rangle$ of the discrete spectrum:

$$M^L_{l'l}(n', n, \mathscr{E}) = \left\langle n'l' \middle| D(l', L) g_L(\mathscr{E}) D(L, l) \middle| nl \right\rangle. \quad \text{(B.1)}$$

As a result of such a substitution for p and p', the parameters of the functions ${}_2F_1$ and the exponents in the denominator in integral (43) become integral:

$$J^{m'm}(n', n, \mathscr{E}) \propto \int_0^1 dt \frac{t^{l+1-Z\nu}\, {}_2F_1(l+1+m'-n',\ l+1+m-n,\ 2l+4;\ \lambda)}{(1-t/y)^{l+1+m-n}(1-yt)^{l+1+m'-n'}(1-y't)^{2-m'-m+n'+n}}, \quad \text{(B.2)}$$

where

$$y = \frac{(\alpha-\nu)(\alpha'+\nu)}{(\alpha+\nu)(\alpha'-\nu)}, \quad y' = \frac{(\alpha-\nu)(\alpha'-\nu)}{(\alpha+\nu)(\alpha'+\nu)},$$

$$\lambda = \frac{16\alpha\alpha'\nu^2}{(\alpha^2-\nu^2)(\alpha'^2-\nu^2)} \frac{t}{(1-yt)(1-t/y)},$$

$$\alpha = n/Z, \quad \alpha' = n'/Z.$$

The integral in formula (B.2) can be expressed in terms of the known functions by transforming the integrand with the help of the relation (see formula (2.5.2.12) in [56])

$$\frac{(1-yt)^{n'-l-m'-1}(1-t/y)^{n-l-m-1}}{(1-y't)^{n+n'+2-m-m'}}$$

$$\times {}_2F_1(l+1+m'-n',\ l+1+m-n,\ 2l+4;\ \lambda)$$

$$= \sum_{k=0}^{\infty} \frac{(2l+4)_k}{k!} (y't)^k\, {}_2F_1(l+1+m-n, -k;\ 2l+4;\ z)$$

$$\times {}_2F_1(l+1+m'-n', -k;\ 2l+4;\ z'),$$

where $z = -4\alpha\nu/(\alpha-\nu)^2$, $z' = -4\alpha'\nu/(\alpha'-\nu)^2$. After this, the integral in formula (B.2) can be evaluated easily and has the form identical for formula (13) from [49]. Using the results obtained in [49], we can write $J^{m'm}$ in terms of the hypergeometric polynomials ${}_2F_1(-k, b; c; x)$ and Appel's function $F_1(a; -k, k+2l+2; d; x, y)$ of special form, which can be expressions through the sum of $k+1$ complete functions ${}_2F_1$ or (in the case of negative integral a) through the hypergeometric polynomial of two variables:

$$J^{m'm} = 2^{-2l-4}\Gamma^2(2l+4)(\alpha\alpha')^{l+2} \times g^{l+1}_{n-l-1-m,\, n'-l-1-m'}(\nu;\ \alpha, \alpha'), \quad \text{(B.3)}$$

where

$$g^l_{kk'}(\nu;\ \alpha, \alpha') = \nu \frac{(4\nu\sqrt{\alpha\alpha'})^{2l+2}}{\Gamma(2l+2)} \frac{(\alpha-\nu)^k}{(\alpha+\nu)^{k+2l+2}} \frac{(\alpha'-\nu)^{k'}}{(\alpha'+\nu)^{k'+2l+2}} \left[\frac{{}_2F_1(-k, l+1-\eta;\ 2l+2;\ z)}{l+1-\eta} \right.$$

$$\times F_1(l+1-\eta;\ -k';\ k'+2l+2;\ l+2-\eta;\ y, y')$$

$$\left. + \sum_{p=1}^{k} C_k^p (-z)^p \frac{{}_2F_1(-k+p, l+1-\eta+p;\ 2l+2+p;\ z)}{(2l+2)_p} \Phi_p(k', l, \eta;\ y, y') \right], \quad \text{(B.4)}$$

$$\Phi_p(k', l, \eta; y, y') = -\frac{(l+2+\eta-p)_{p-1}(1-y)^{k'}}{(1-y')^{k'+2l+2}}$$
$$\times F_1(-p+1; -k', k'+2l+2; l+2+\eta-p; 1/(1-y), 1/(1-y')),$$

C_k^p is the binomial coefficient, and $\eta = Z\nu$.

In order to transform $J^{m'm}$ to (B.3), (B.4), it is sufficient that only one of the two numbers (n or n') in formula (B.2) be an integer (this number will determine the upper limit k of the sum over p in formulas (B.4)). Consequently, the amplitudes of free–bound (but not free–free) transitions can also be presented in closed form. Explicit expressions for all $M^L_{l'l}(n', n, \mathscr{E})$ in formula (B.1), which are allowed by the dipole selection rules, in the form of linear combinations of $g^l_{kk'}$, as well as analogous expressions for the MEs of bound–free transitions (two-photon Gordon's formula), are given in [49].

REFERENCES

1. A. Sommerfeld, Ann. Phys. (Leipzig) **11**, 257 (1931); A. Sommerfeld, *Atomic Structure and Spectral Lines* (Methuen, London, 1934; Gostekhizdat, Moscow, 1956), Vol. 2.
2. L. Bess, Phys. Rev. **77**, 550 (1950); A. Nordsieck, Phys. Rev. **93**, 785 (1954).
3. V. B. Berestetskii, E. M. Lifshitz, and L. P Pitaevskii, *Course of Theoretical Physics*, Vol. 4: *Quantum Electrodynamics* (Nauka, Moscow, 1980; Pergamon, New York, 1982).
4. N. L. Manakov, S. I. Marmo, and V. V. Volovich, Phys. Lett. A **27A**, 42 (1995); J. Electron Spectrosc. Relat. Phenom. **79**, 327 (1996).
5. L. C. Biedenharn, Phys. Rev. **102**, 262 (1956).
6. W. Heitler and L. Nordheim, Physica (Amsterdam) **1**, 1059 (1934).
7. J. C. Altman and C. A. Quarles, Phys. Rev. A **31**, 2744 (1985).
8. D. L. Kahler, J. Liu, and C. A. Quarles, Phys. Rev. Lett. **68**, 1690 (1992); Phys. Rev. A **47**, 2819 (1993); J. Liu and C. A. Quarles, Phys. Rev. A **47**, R3479 (1993).
9. R. Hippler, Phys. Rev. Lett. **66**, 2197 (1991); R. Hippler and H. Schneider, Nucl. Instrum. Methods Phys. Res. B **87**, 268 (1994).
10. A. I. Smirnov, Yad. Fiz. **25**, 1030 (1977) [Sov. J. Nucl. Phys. **25**, 548 (1977)].
11. M. Gavrila, A. Maquet, and V. Veniard, Phys. Rev. A **32**, 2537 (1985); V. Veniard, M. Gavrila, and A. Maquet, Phys. Rev. A **35**, 448 (1987); M. Gavrila, A. Maquet, and V. Veniard, Phys. Rev. A **42**, 236 (1990).
12. V. Florescu and V. Djamo, Phys. Lett. A **119**, 73 (1986); M. Dondera and V. Florescu, Phys. Rev. A **48**, 4267 (1993).
13. N. L. Manakov, S. I. Marmo, and A. G. Faĭnshteĭn, Zh. Éksp. Teor. Fiz. **108**, 1569 (1995) [JETP **81**, 860 (1995)].
14. A. V. Korol, J. Phys. B **28**, 3873 (1995).
15. A. V. Korol, J. Phys. B **29**, 3257 (1996).
16. T. A. Fedorova, A. V. Korol, and I. A. Solovjev, J. Phys. B **33**, 5007 (2000).
17. A. V. Korol, J. Phys. B **30**, 413 (1997).
18. M. Dondera and V. Florescu, Phys. Rev. A **58**, 2016 (1998).
19. A. V. Korol, J. Phys. B **27**, 155 (1994).
20. G. Kracke, J. S. Briggs, A. Dubois, *et al.*, J. Phys. B **27**, 3241 (1994).
21. D. Andrick and L. Langhaus, J. Phys. B **9**, L459 (1976).
22. A. Weingartshofer, J. K. Holmes, G. Caudle, *et al.*, Phys. Rev. Lett. **39**, 269 (1977).
23. B. Wallbank and J. K. Holmes, Phys. Rev. A **48**, R2515 (1993); J. Phys. B **27**, 1221 (1994); **27**, 5405 (1994); **29**, 5881 (1996).
24. N. J. Mason, Rep. Prog. Phys. **56**, 1275 (1993).
25. F. V. Bunkin and M. V. Fedorov, Zh. Éksp. Teor. Fiz. **49**, 1569 (1965) [Sov. Phys. JETP **22**, 1071 (1966)].
26. F. V. Bunkin, A. E. Kazakov, and M. V. Fedorov, Usp. Fiz. Nauk **107**, 559 (1972) [Sov. Phys. Usp. **15**, 416 (1972)].
27. N. M. Kroll and K. M. Watson, Phys. Rev. A **8**, 804 (1973).
28. M. H. Mittleman, Phys. Rev. A **19**, 134 (1979); **20**, 1965 (1979); **21**, 79 (1980).
29. L. Rosenberg, Phys. Rev. A **23**, 2283 (1981).
30. S. Geltman, Phys. Rev. A **53**, 3473 (1996); **55**, 3755 (1997).
31. L. B. Madsen and K. Taulbjerg, J. Phys. B **31**, 4701 (1998).
32. N. J. Kylstra and C. J. Joachain, Phys. Rev. A **58**, R26 (1998); **60**, 2255 (1999).
33. L. W. Garland, A. Jaroń, J. Z. Kamiński, and R. M. Potvliege, J. Phys. B **35**, 2861 (2002).
34. I. Ya. Berson, Zh. Éksp. Teor. Fiz. **80**, 1727 (1981) [Sov. Phys. JETP **53**, 891 (1981)].
35. F. Ehlotzky, A. Jaroń, and J. Z. Kamiński, Phys. Rep. **297**, 63 (1998).
36. A. G. Fainshtein, N. L. Manakov, and S. I. Marmo, Phys. Lett. A **195**, 358 (1994).
37. R. V. Karapetyan and M. V. Fedorov, Zh. Éksp. Teor. Fiz. **75**, 816 (1978) [Sov. Phys. JETP **48**, 412 (1978)].
38. R. Daniele and E. Fiordilino, Nuovo Cimento D **18**, 547 (1996).
39. A. Florescu and V. Florescu, Phys. Rev. A **61**, 033406 (2000).
40. V. P. Kraĭnov and S. P. Roshchupkin, Zh. Éksp. Teor. Fiz. **84**, 1302 (1983) [Sov. Phys. JETP **57**, 754 (1983)].
41. A. Florescu and V. Florescu, Phys. Lett. A **226**, 280 (1997).
42. M. H. Mittleman, J. Phys. B **26**, 2709 (1993).

43. P. D. Fainstein and A. Maquet, J. Phys. B **27**, 5563 (1994).
44. D. Khalil, O. E. Akramine, A. Makhoute, *et al.*, J. Phys. B **31**, 1115 (1998); O. E. Akramine, A. Makhoute, D. Khalil, *et al.*, J. Phys. B **32**, 2783 (1999).
45. N. L. Manakov, S. I. Marmo, and A. V. Meremianin, J. Phys. B **29**, 2711 (1996).
46. A. A. Balakin and G. M. Fraĭman, Zh. Éksp. Teor. Fiz. **120**, 797 (2001) [JETP **93**, 695 (2001)].
47. L. P. Rapoport and A. S. Kornev, Zh. Éksp. Teor. Fiz. **116**, 1241 (1999) [JETP **89**, 664 (1999)]; L. P. Rappoport and A. S. Kornev, J. Phys. B **33**, 87 (2000).
48. A. Cionga, F. Ehlotzky, and G. Zloh, Phys. Rev. A **62**, 063406 (2000); J. Phys. B **33**, 4939 (2000).
49. A. A. Krylovetskiĭ, N. L. Manakov, and S. I. Marmo, Zh. Éksp. Teor. Fiz. **119**, 45 (2001) [JETP **92**, 37 (2001)].
50. D. A. Varshalovich, A. N. Moskalev, and V. K. Khersonskii, *Quantum Theory of Angular Momentum* (Nauka, Leningrad, 1975; World Sci., Singapore, 1988).
51. N. L. Manakov, A. V. Meremianin, and A. F. Starace, Phys. Rev. A **57**, 3233 (1998).
52. J. S. Briggs and V. Schmidt, J. Phys. B **33**, R1 (2000).
53. N. L. Manakov, A. Maquet, S. I. Marmo, *et al.*, J. Phys. B **32**, 3747 (1999).
54. N. L. Manakov and A. V. Merem'yanin, Zh. Éksp. Teor. Fiz. **112**, 1984 (1997) [JETP **84**, 1080 (1997)].
55. H. A. Bethe and E. E. Salpeter, *Quantum Mechanics of One- and Two-Electron Atoms* (Academic, New York, 1957; Fizmatgiz, Moscow, 1960).
56. *Heigher Transcendental Functions (Bateman Manuscript Project)*, Ed. by A. Erdelyi (McGraw-Hill, New York, 1953; Nauka, Moscow, 1974), Vol. 1.
57. L. D. Landau and E. M. Lifshitz, *Course of Theoretical Physics*, Vol. 3: *Quantum Mechanics: Non-Relativistic Theory* (Nauka, Moscow, 1974; Pergamon, New York, 1977).
58. L. C. Biedenharn, J. L. McHale, and R. M. Thaler, Phys. Rev. **100**, 376 (1955).
59. N. L. Manakov, M. A. Preobrazhenskiĭ, L. P. Rapoport, and A. G. Faĭnshteĭn, Zh. Éksp. Teor. Fiz. **75**, 1243 (1978) [Sov. Phys. JETP **48**, 626 (1978)]; N. C. Sil, M. A. Crees, and M. J. Seaton, J. Phys. B **17**, 1 (1984); B. Gao and A. F. Starace, Comput. Phys. **6**, 70 (1987).
60. J. L. Madajczyk and M. Trippenbach, J. Phys. A **22**, 2369 (1989).
61. L. Pan, J. Mod. Opt. **36**, 877 (1989); V. Veniard and B. Piraux, Phys. Rev. A **41**, 4019 (1990); A. V. Korol, J. Phys. B **27**, L103 (1994); T. Mercouris, Y. Komninos, S. Dionissopoulou, and C. A. Nicolaides, J. Phys. B **29**, L13 (1996).
62. N. L. Manakov, S. I. Marmo, and A. V. Shaposhnikov, in *Atoms and Molecules in Strong Field of Laser Radiation*, Ed. by F. V. Bunkin and I. I. Tugov (Wiley-Nauka, Moscow, 1992), p. 87.
63. I. S. Gradshteyn and I. M. Ryzhik, *Table of Integrals, Series, and Products* (Nauka, Moscow, 1971; Academic, New York, 1980).
64. S. D. Oh and R. H. Pratt, Phys. Rev. A **45**, 1583 (1992).
65. C. D. Shaffer, R. H. Pratt, and S. D. Oh, Phys. Rev. A **57**, 227 (1998).
66. Z. Deng and J. H. Eberly, Phys. Rev. Lett. **53**, 1810 (1984); J. Opt. Soc. Am. B **2**, 486 (1985).
67. M. Trippenbach, K. Rzazewski, M. V. Fedorov, and A. E. Kazakov, J. Phys. B **22**, 1193 (1989).
68. O. V. Tikhonova, A. M. Popov, and M. V. Fedorov, Phys. Rev. A **65**, 053404 (2002).
69. L. Hostler, J. Math. Phys. **5**, 591 (1964).

Translated by N. Wadhwa

Journal of Experimental and Theoretical Physics, Vol. 95, No. 6, 2002, pp. 1033–1039.
Translated from Zhurnal Éksperimental'noĭ i Teoreticheskoĭ Fiziki, Vol. 122, No. 6, 2002, pp. 1198–1206.

PLASMA, GASES

Pulsed Volume Discharge with Preionization in Two-Dimensional Gasdynamic Flow

I. A. Znamenskaya*, I. É. Ivanov, I. A. Kryukov, and T. A. Kuli-Zade

Moscow Institute of Aviation (State Technical University), Volokolamskoe sh. 4, Moscow, 125871 Russia
**e-mail: znamen@rdm.ru*

Received June 6, 2002

Abstract—The interaction between a pulsed volume discharge with preionization by ultraviolet radiation from plasma sheets and a gasdynamic flow with a known density distribution is studied experimentally. The complex quasi-two-dimensional flow that emerges after the diffraction of a plane shock wave by rectangular obstacles in the channel is experimentally studied and numerically simulated. The glow intensity fields for an unsteady gasdynamic flow are imaged for the first time when recording the plasma radiation from a pulsed discharge in the flow. Since the ionization duration is short (150–200 ns), the gas-flow structure does not change and the flow does not heat up in the glow time of the discharge plasma in the flow. Our images are compared with the reciprocal-density fields of the corresponding two-dimensional gas flow. The effects of gasdynamic structures on the discharge plasma redistribution in the flow are analyzed. The energy contribution is localized into low-density zones (vortices, rarefaction waves) and into regions of density jumps and significant density gradients. The discharge current from adjacent regions with low E/N is redistributed into these zones. Breakdown channels are formed along rarefaction waves, vortices, and discontinuity surfaces between high-electron-density regions. © *2002 MAIK "Nauka/Interperiodica".*

1. INTRODUCTION

In recent years, the interactions between gas discharges of various types and gasdynamic flows have been studied extensively. The possibility of influencing the flow around bodies using gas discharges is mainly discussed. Theoretical [1] and experimental [2–4] data on the effects of discharges on gasdynamic flows were obtained. It was shown that a discharge could significantly affect the flow parameters, the discontinuity structure, and the aerodynamic drag of the model. At the same time, the physical mechanism of the discharge influence on flows is still of current interest. Since the ionization of the medium by a discharge is accompanied by a change in the translational flow temperature, the effects of ionization on discontinuities and on the flow as a whole are difficult to study experimentally. Separating out the ionization and thermal components in the nonequilibrium discharge plasma, analyzing the space–time parameters of the discharge region, and predicting their influence on gasdynamic structures are complex problems that require special studies. It is of considerable interest to investigate the interaction of a discharge with a gas flow when the flow is not heated by the discharge. Such conditions are provided by the pulsed volume ionization of a flow segment during a time in which the translational gas temperature does not change. It was suggested that a pulsed volume discharge with preionization by ultraviolet radiation from plasma sheets be used to study the pulsed ionization of gasdynamic flows and to visualize the spatial structure of unsteady flows [5]. This type of discharge is widely used to pump excimer and CO_2 lasers [6, 7]. Ultraviolet radiation from plasma sheets preionizes the main discharge gap, whereupon (several nanoseconds later) the pulsed ionization of the volume takes place. Preexposure to ultraviolet radiation causes the volume-discharge current to rise in several nanoseconds and facilitates the formation of diffuse glow at the initial discharge stages. Density perturbations in the discharge region result in significant fluctuations of the local energy contribution [7].

The initiation of a pulsed volume discharge with preionization in a shock tube allows the steady-flow segment in the interelectrode region to be uniformly ionized for a time shorter than 200 ns. Thus, the ionization time is much shorter than the interaction time scales for gasdynamic flow elements (microseconds). In such a short flow ionization time, the gasdynamic flow structure does not change and the gas is not heated by the discharge.

In the case of flow ionization by a discharge, gasdynamic nonuniformities cause a plasma redistribution because of the density dependence of the electron number density. The spatial unsteady gasdynamic structures are imaged when the glow of a pulsed volume discharge is recorded in a gasdynamic flow. The structure of the gasdynamic flows simulated in a shock tube was visualized and studied by the method proposed in [5, 8].

Here, our goal is to analyze the redistribution of the pulsed volume discharge plasma in a nonuniform gas flow with a known density field. Localizing the energy

1063-7761/02/9506-1033$22.00

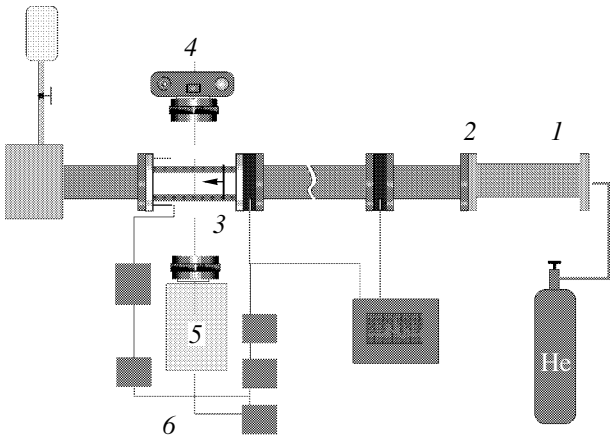

Fig. 1. A scheme of the experimental setup.

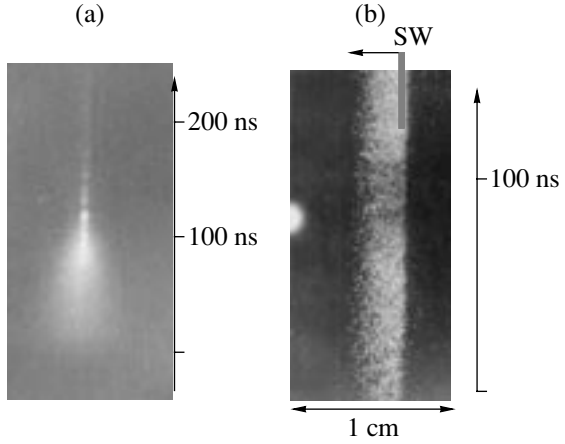

Fig. 2. (a) A photoscan of the pulsed volume-discharge glow in the shock-tube channel; the scanning rate is 250 ns cm^{-1}. (b) A slit photoscan of the glow of the flow segment with a plane shock wave. The preshock air pressure is 15 Torr, the shock Mach number is 3.9, and the scanning rate is 50 ns cm^{-1}.

contribution into specified flow segments and controlling the discharge structure are of current interest.

We recorded the glow of unsteady two-dimensional flow fields for pulsed volume ionization by the discharge initiated at various stages of the gasdynamic process. We compare the gasdynamic fields experimentally visualized by plasma glow with the numerically simulated density fields of the corresponding complex unsteady flows (with obstacles in the flow). Given the model of the volume-discharge current distribution in a known field of parameters, the gasdynamic flows can be adjusted via the influence of the localized energy contribution on flow elements. On the other hand, a controllable volume-discharge current redistribution is possible in a specified density field.

2. EXPERIMENTAL SIMULATION OF THE PULSED IONIZATION OF A TWO-DIMENSIONAL GASDYNAMIC FLOW

The experiments were carried out in air with a 48 × 24-mm shock tube (Fig. 1) composed of a high-pressure chamber (*1*), a diaphragm section (*2*), and a discharge section (*3*). Helium was used as the "pushing" gas. A pulsed volume discharge with preionization by ultraviolet radiation from plasma electrodes was produced in a 10-cm-long flow segment in the discharge chamber. The electrode spacing was 2.4 cm. The two chamber sidewalls were quartz windows; the top and bottom walls were flat plasma electrodes. A discharge was initiated at a given time of the unsteady gasdynamic process that proceeded in the channel in the interelectrode gap. Plasma electrodes flush-mounted with the tube walls in the shock tube were as close to the flow under study as possible, and they introduced minimum perturbations into the flow. The volume-discharge current in the gasdynamic flow was measured by using a noninductive shunt. Analysis of the discharge-glow scans in the flow obtained with image converters (Fig. 1, *5*) shows that all segments of the gasdynamic flow were ionized in a time of less than 10 ns; subsequently, the discharge glowed for about 150–180 ns and was quenched in 15–20 ns (Fig. 2a). The gasdynamic perturbations and discontinuities traveled a distance of no larger than 10^{-4} m in the discharge-glow time. Therefore, the recording of the discharge glow in the flow gives a snapshot (from a gasdynamic standpoint) of the discharge plasma glow distribution. Figure 2b shows a slit glow photoscan for the flow segment with the incident plane shock wave moving in the discharge gap at the time of discharge initiation. The pressure behind the plane shock wave calculated from the Rankine–Hugoniot relations at the shock was 260 Torr; it increased approximately by a factor of 18 at the shock front. As we see from Fig. 2b, in this case, the discharge glowed only in the preshock region, in the low-pressure region. Analysis of the space–time parameters for the discharge glow in a flow with nonuniformities and discontinuities using glow scans indicates that the spatial localization of the discharge glow in the gas flow field changed only slightly in the discharge-glow time and only at the initial and final stages for 10–15 ns.

To study the spatial redistribution of the pulsed volume discharge glow in an ionized gasdynamic flow with discontinuities and nonuniformities, we experimentally simulated the pulsed volume ionization of the two-dimensional flow in a rectangular channel with obstacles that emerged after the passage of a plane shock wave and made a comparison with our calculations of the corresponding flow. We numerically solved the corresponding gasdynamic two-dimensional problem, compared the images obtained when recording the volume-discharge glow in the flow and the density fields of the corresponding two-dimensional flows, and

analyzed effects of the gasdynamic nonuniformities on the redistribution of the pulsed volume discharge glow.

We investigated the flow that emerged in the channel with obstacles behind the incident shock with Mach numbers M = 2.5–4.5. Rectangular 2 × 6 × 48-mm obstacles were located on the top and bottom channel walls (Fig. 3). A pulsed volume discharge was initiated by a clock system (Fig. 1, *6*) at a specified instant of time in the flow that emerged in the channel after the passage of a plane shock. The integrated glow of the flow field in the ionization time was recorded with a photocamera (Fig. 1, *4*) through the window of the working chamber in a direction perpendicular to the flow axis.

When the plasma sheets were fired, gas photoionization began and the electron number density reached 10^9 cm^{-3}. Subsequently, a volume discharge was fired and ionization took place; the electron number density increased to 10^{12}–10^{13} cm^{-3}. After completion of the volume-discharge current pulse, energy was pumped into the vibrational and excited electronic states of the molecules. The input energy was 0.01–0.05 J cm^{-3}. The volume-discharge current reached 1000 A.

Figure 4 shows an integrated photograph of the discharge glow in the flow after the passage of a plane shock through the obstacles: the Mach number of the unperturbed flow behind the plane shock was 1.5.

Density nonuniformities in a gas flow ionized by a pulsed volume discharge cause a redistribution of the volume-discharge current, because the electron number density and conductivity depend on the ionization coefficient. The latter is a nonlinear function of E/ρ, where E is the electric field strength. The specific energy contribution to the gas per particle is

$$\frac{W}{N} = n_e(\rho)\tau e^2 m_e \langle \sigma_0(\rho) V_0(\rho)\rangle \frac{E^2(\rho)}{N^2(\rho)}.$$

Here, τ is the current-pulse duration; n_e is the electron number density; V_{dr} is the electron drift velocity,

$$V_{dr} = \frac{eE}{m_e\langle \sigma_0 V_0\rangle N};$$

σ_0 is the collision cross section; and V_0 is the thermal velocity of the molecules. The regions of low gas density ρ (or particle number density N) correspond to an enhanced intensity of the discharge plasma glow. It is of considerable interest to directly compare the computed unsteady two-dimensional flow density fields with the glow field imaged in the time of the volume-discharge current pulse.

3. NUMERICAL SIMULATIONS OF THE FLOW

When we carried out our computational experiment, we chose the model of an ideal single-component gas with an adiabatic index of $\gamma = 1.4$ as the physical model of the medium. Analysis of the local thermodynamic parameters for the flow indicates that the temperature range in the flow field under study is 600–2000 K. In this case, because the vibrational degrees of freedom of the air molecules are excited, the minimum local adiabatic index γ in the flow field is 1.31 [9]. This value was observed in a small region behind the shock. The adiabatic index averaged over the computational region is no lower than 1.38–1.41. Therefore, it seems legitimate to use the model of an ideal diatomic gas.

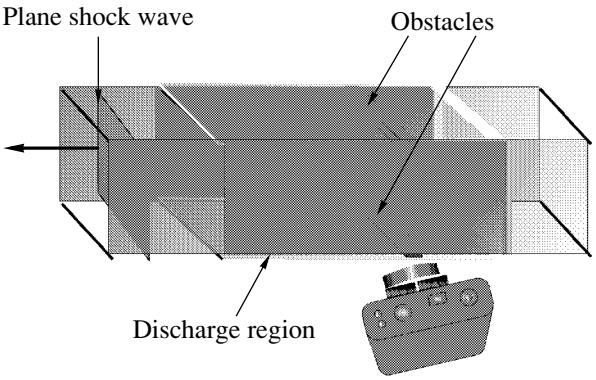

Fig. 3. A scheme of the experiment.

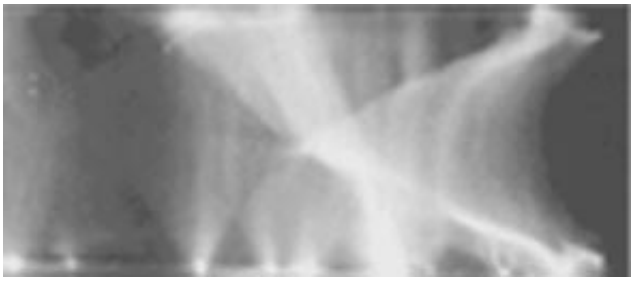

Fig. 4. Discharge glow in the unsteady flow behind the obstacles 70 μs after the passage of a plane shock with the Mach number M = 3.8. The density of the steady gas flow behind the plane shock is 2×10^{-5} g/cm^3.

We took the system of two-dimensional unsteady-state Euler equations with appropriate boundary conditions as the mathematical model. This system for the compressible flow of an ideal, calorifically perfect gas can be written as

$$\mathbf{q}_t + \mathbf{f}_x(\mathbf{q}) + \mathbf{g}_y(\mathbf{q}) = \mathbf{H}, \tag{1}$$

$$\mathbf{q} = \begin{bmatrix} \rho \\ \rho u \\ \rho v \\ E \end{bmatrix}, \quad \mathbf{f}(q) = \begin{bmatrix} \rho u \\ \rho u^2 + p \\ \rho uv \\ (E+p)u \end{bmatrix}, \quad \mathbf{g}(q) = \begin{bmatrix} \rho v \\ \rho uv \\ \rho v^2 + p \\ (E+p)v \end{bmatrix}. \tag{2}$$

Here, ρ, p, and E are the density, pressure, and total energy, respectively; u and v are the Cartesian velocity vector components; and $\mathbf{H}$ is the vector of the source

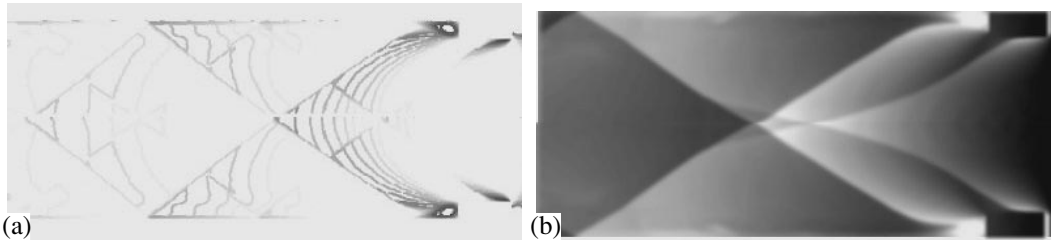

Fig. 5. Numerical calculation of the flow.

terms. The system of four equations (1) and (2) is closed by the equation of state for a polytropic gas,

$$p = (\gamma - 1)\left(E - \frac{\rho}{2(u^2 + v^2)}\right), \tag{3}$$

where γ is the ratio of the specific heat capacities.

The system of equations was numerically solved by using an explicit, quasi-monotonic numerical scheme with an increased order of accuracy, which is a modification of the Godunov scheme. We used a piecewise-linear distribution of the parameters at the computational layer and two-dimensional procedures for data recovery in the computational cells [10, 11]. The nonleakage conditions were specified as the boundary conditions on the channel walls; the conditions for a supersonic flow and for the absence of reflection were specified in the input and output cross sections, respectively. Our numerical scheme has peculiarities that can reveal subtle features of the flow inaccessible with standard schemes.

In differential-difference representation, the basic system of equations written for a quadrilateral computational cell *ABCD* is

$$\frac{\partial \bar{\mathbf{q}}_{ij}(t)}{\partial t} = -\frac{1}{a_{ij}} \times [\hat{\mathbf{f}}_{AB}(t) + \hat{\mathbf{f}}_{BC}(t) + \hat{\mathbf{f}}_{CD}(t) + \hat{\mathbf{f}}_{DA}(t)], \tag{4}$$

where a_{ij} is the cell area and

$$\bar{\mathbf{q}}_{ij}(t) = \frac{1}{a_{ij}} \int_{ABCD} \int \mathbf{q}(x, y, t)\,dx\,dy \tag{5}$$

is the cell-averaged value of q at time t. The flux $\hat{f}$ through the face of cell *ABCD* is defined as the line integral of the second kind,

$$\hat{\mathbf{f}}_{AB}(t) = \oint_{AB} (\mathbf{f}\,dy - \mathbf{g}\,dx), \tag{6}$$

numericaly approximated by the Gaussian quadrature formulas. The solution of the problem on the decay of an arbitrary discontinuity (Riemann problem) is used to determine the numerical fluxes through the lateral cell faces (at Gaussian points). The algorithm for an exact solution of the Riemann problem is used in our problem.

Equation (4) can be discretized in time by a modified Runge–Kutta method:

$$\bar{\mathbf{q}}_{ij}^{(l)} = \sum_{m=0}^{l-1} [\alpha_{lm}\bar{\mathbf{q}}_{ij}^{(m)} + \beta_{lm}\Delta t L_{ij}^{(m)}], \quad l = 1, 2, \ldots, p,$$

$$L_{ij}^{(m)} = (L\bar{\mathbf{q}})_{ij}^{m}, \quad \bar{\mathbf{q}}_{ij}^{(0)} = \bar{\mathbf{q}}_{ij}^{(n)}, \quad \bar{\mathbf{q}}_{ij}^{(n+1)} = \bar{\mathbf{q}}_{ij}^{(p)}.$$

The order of accuracy, as well as the conservation of TVD properties (the scheme with a reducible total variation of the grid), is achieved by choosing an appropriate set of α_{lm}, β_{lm}, and p.

The numerical scheme uses a piecewise-linear distribution of the parameters at the computational layer and two-dimensional procedures for data recovery in the computational cells to determine the values of vector $\mathbf{q}$ on the cell faces (at Gaussian points) from the averaged values at the cell centers [10]. The procedure for recovering the flow parameters at the computational layer allows us to more accurately and properly approximate the fluxes through the lateral faces of the computational cells and enhances the possibilities of the method to take into account two-dimensional effects.

4. ANALYSIS OF THE RESULTS

Figure 5a shows the computed density isolines in the flow behind the obstacles in the range $1.1 \times 10^{-5} < \rho < 2 \times 10^{-5}$ g/cm^3 (zones of minimum density). To analyze the spatial ionization of the gasdynamic flow, we suggest comparing the glow images of the flow during pulsed ionization with the computed reciprocal flow density field. In Fig. 5b, the numerical calculations of the reciprocal-density ($1/\rho$) field are visualized on a continuous gray scale. The conditions in the flow are the same as those in Figs. 4 and 5a. Figure 6 visualizes the numerical calculations of the flow density field (the lower part of the image) with the glow field of a pulsed discharge in the flow (the upper part of the image).

When comparing the digitized images of the discharge-glow fields in the flow with the computed recip-

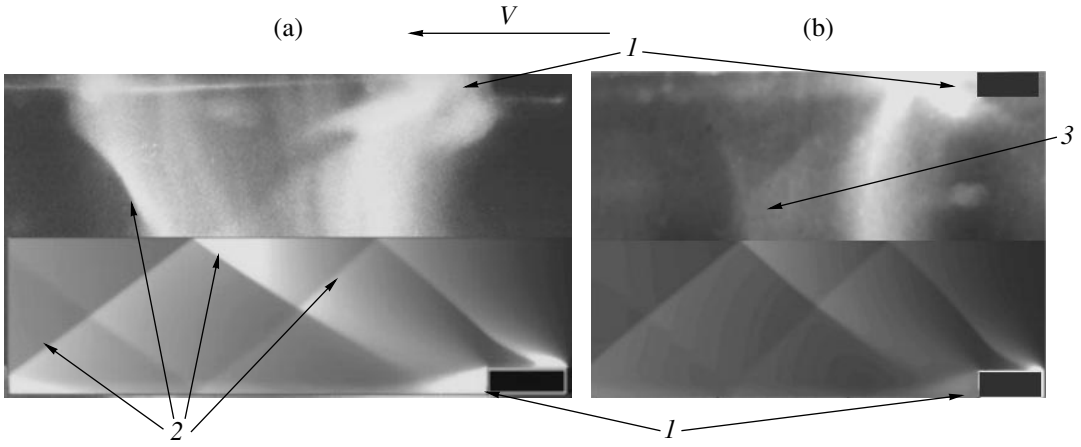

Fig. 6. Visualization of the numerically computed flow density field and the corresponding images of the pulsed-discharge glow in the flow. (a) 165 μs after the passage of a (M = 3.1) shock through an obstacle, the density of the steady gas glow behind the plane shock is 17×10^{-5} g/cm^3; (b) 150 μs after the passage of a (M = 2.9) shock through an obstacle, the density of the steady gas glow behind the plane shock is 24×10^{-5} g/cm^3.

rocal flow density field under the same conditions as those in the experiment, we found the major structural elements of the quasi-two-dimensional flow to be well reproduced by the discharge plasma glow field in the flow. The flow separation regions and the vortices behind the obstacles (*1* in Fig. 6) correspond to the regions of maximum glow intensity. The low-density regions in front of the oblique shocks (*2* in Fig. 6) and the rarefaction fan are marked by an intense glow.

Figure 7a shows the intensity profile of the discharge plasma glow (the reciprocal of the film blackening) along the channel wall of the discharge chamber behind an obstacle (x = 540). The experimental conditions are the same as those for Figs. 4 and 5. The chosen region is located near the boundary layer of the complex flow and near the plasma electrode region; i.e., the glow intensity is determined both by the properties of the discharge that slides over the dielectric surface and forms the plasma electrode and by the density nonuniformities attributable to the interaction of gasdynamic structures with the chamber wall and the boundary layer. Nevertheless, the intensity profile of the discharge plasma glow in the flow qualitatively coincides with the corresponding reciprocal density profile when the computed reciprocal density is visualized on a gray scale (Fig. 7b).

We imaged the unsteady Mach configuration (during the shock's crossing in the flow symmetry plane) for an ionized flow. The discharge-visualized Mach configuration 150 μs after the shock's passage through an obstacle is seen in Fig. 6b (*3*). In our calculations, we recorded the two-dimensional Mach configuration for this regime at an earlier stage of the process and the shock interaction becomes regular 90 μs later. This discrepancy may result from hysteresis when passing from Mach reflection to regular reflection and back [12].

The density in the steady airflow behind the incident shock wave calculated from the Rankine–Hugoniot relations,

$$\frac{\rho_1}{\rho_0} = \frac{(\gamma + 1)M_0^2}{(\gamma - 1)M_0^2 + 2},$$

in our experiments was within the range 10^{-5}–5×10^{-4} g/cm^3. The parameter E/N in the steady flow varied over the range 100–700 Td. As the gas density in the flow behind the plane shock (or the Mach number M_0 and the preshock density ρ_0) increased, the mean E/N decreased. In this case, local breakdown conditions are created in different segments of the gasdynamic flow.

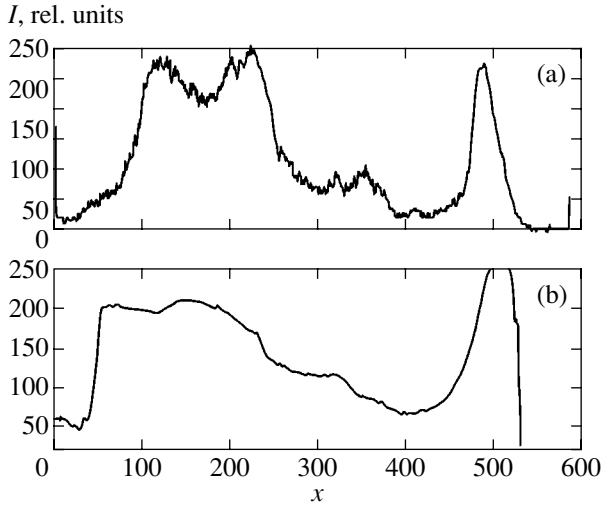

Fig. 7. (a) The profile of discharge plasma glow intensity I along the channel wall of the discharge chamber behind an obstacle and (b) the computed profile of relative reciprocal gas density.

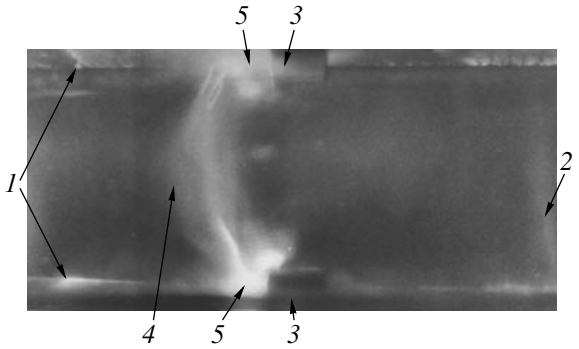

Fig. 8. The formation of a breakdown channel. The density of the steady gas flow behind the plane shock is 44×10^{-5} g/cm^3.

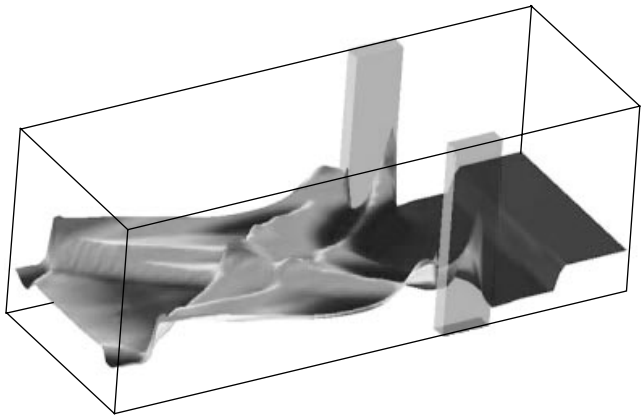

Fig. 9. A numerical reciprocal-density surface in the flow.

High-current filaments are formed in the regions of enhanced local E/N; the energy from nearby discharge zones is redistributed into these filaments.

The local energy-contribution density is defined as

$$\varepsilon = \iint_s j(x, y)E(x, y)dxdy,$$

where x and y are the coordinates of the discharge region along the flow and along the electric vector, respectively. The parameters are uniformly distributed along the z axis. At a given time-independent discharge current I, the electric field is

$$E(x, y) = \frac{I}{e\iint_s n_e(x, y)\mu(x, y)dxdy},$$

where $n_e(x, y)$ and $\mu(x, y)$ are the spatial distributions of the electron density and mobility, respectively.

The local density in the transonic flow behind the obstacles varied significantly. The density difference in the vortex regions in the separation zone behind the obstacles in a 1-cm-long segment was 700–900%. The jump in density reached 200–300% in the shock-crossing region on the flow axis. The energy contribution went into low-density zones (vortices, rarefaction waves) and into regions of density jumps and sharp density gradients; the discharge current from adjacent regions with low E/N was redistributed into these regions.

Since there is a region of low gas density and, accordingly, high electron number density during ionization, the two opposite vortex zones of flow separation behind the obstacles are effective plasma electrodes. As the density in the unperturbed onflow increases, local breakdown conditions arise between these regions and a breakdown channel is formed in the rarefaction-fan region at densities in the flow behind the incident shock that are higher than 3×10^{-4} g/cm^3 (Fig. 6b and 8). Figure 8 shows an image of the discharge glow in the flow at a density in the unperturbed flow behind the incident shock of 4.4×10^{-4} g/cm^3. We see the following gasdynamic structures: the trails of the shocks (*1*) as they cross the plasma sheets, the deceleration wave (*2*) formed upstream of the obstacles (*3*), and the rarefaction fan (*4*) between the separation zones (*5*) behind the obstacles in which a breakdown channel is formed between the zones of enhanced electron number density.

At densities in the flow behind the incident shock within the range 10^{-5}–2×10^{-4} g/cm^3, the overall flow structure determined from a snapshot of the flow glow is in satisfactory agreement with the structure of the computational region—the shocks, vortices, and local rarefaction regions are clearly visualized. Our technique for numerically visualizing the results on a gray scale for a layer-by-layer reproduction of the regions with constant reciprocal density can be considered as a numerical visualization of the glow of a pulsed volume discharge in the flow in terms of the model in question (the dependence of local discharge plasma glow intensity on the reciprocal gas density in the flow in the absence of local breakdown conditions).

Three-dimensional color animation of the process allows us to visualize and trace the dynamics of the development of regions with minimum gas density and, accordingly, the redistribution of the volume-discharge current under prebreakdown conditions when a discharge is initiated at various stages of the gasdynamic process. Figure 9 shows an image of the density isosurface as an element of numerical animation.

Thus, comparison of the quasi-two-dimensional flow visualized by the method of pulsed volume discharge and the numerically computed reciprocal-density field visualized on a continuous gray scale indicates that the model in which the glow intensity is proportional to the reciprocal gas density satisfactorily describes the plasma redistribution for a pulsed volume discharge in a given flow density field. Enhanced discharge plasma glow intensities visualize the regions of low density ρ (or gas particle number density N) or the

regions of density gradients. By analyzing the images, we can determine the validity range of this proportionality for specific flow configurations and channel geometries. As the pressure in the flow between the local zones of enhanced electron number density increases, breakdown channels are formed along rarefaction waves and discontinuities in the low-density regions.

5. CONCLUSION

We have studied a two-dimensional unsteady gasdynamic flow in a channel with obstacles ionized by a pulsed volume discharge with preionization. In comparison with other types of discharge, a pulsed volume discharge with preionization by ultraviolet radiation from plasma electrodes ensures that the unperturbed gas has a high spatial uniformity, that the flow is not heated in the discharge-glow time, and that the exposure used to record the discharge glow in the flow is short. By recording the discharge glow in the flow, we can image the major elements of the flow structure—the unsteady configurations of discontinuities, vortices, and rarefaction and compression waves.

By comparing the recorded glow of a pulsed volume discharge and the numerically computed reciprocal-density fields visualized on a continuous gray scale, we can determine the validity range for the physical model in which the glow intensity is proportional to the reciprocal gas density and analyze the validity range of this proportionality for specific flow configurations. The formation of regions with local breakdown conditions (associated with high E/ρ) in the flow leads to deviations of the dependence of the discharge plasma glow intensity on the reciprocal gas density from the model. Since the electron impact ionization and excitation rates depend sharply on E/ρ, the discharge is rapidly pulled into these regions, where the current density significantly increases. Breakdown channels are formed along rarefaction waves, vortices, and discontinuity surfaces between the high-electron-number-density regions that emerge in low-density zones. The spatial distribution of the volume-discharge current can be predicted and corrected by initiating a pulsed volume discharge in a gas flow with a given density distribution.

ACKNOWLEDGMENTS

This study was supported by the Ministry of Education of Russia (TOO-6-7-778) and the Research Program of the Ministry of Education of Russia (project no. 09.01.023).

REFERENCES

1. R. F. Avramenko, A. A. Rukhadze, and S. F. Teselkin, Pis'ma Zh. Éksp. Teor. Fiz. **34**, 485 (1981) [JETP Lett. **34**, 463 (1981)].
2. P. K. Tret'yakov, A. F. Garanin, G. N. Grachev, *et al.*, Dokl. Akad. Nauk **351**, 339 (1996) [Phys. Dokl. **41**, 566 (1996)].
3. S. A. Bystrov, I. S. Zaslonko, Yu. K. Mukoseev, and F. V. Shugaev, Dokl. Akad. Nauk SSSR **310**, 70 (1990) [Sov. Phys. Dokl. **35**, 39 (1990)].
4. Y. Ionikh, N. Chernysheva, A. Meshchanov, *et al.*, Phys. Lett. A **259**, 387 (1999).
5. I. A. Znamenskaya, T. A. Kuli-zade, and I. V. Stepanets, Prikl. Mekh. Tekh. Fiz., No. 3, 84 (1995).
6. N. V. Karlov, G. P. Kuz'min, and A. M. Prokhorov, Izv. Akad. Nauk SSSR, Ser. Fiz. **48**, 1430 (1984).
7. E. P. Velikhov, V. Yu. Baranov, V. S. Letokhov, *et al.*, *Pulse CO_2 Lasers and Their Application for Channel Separation* (Nauka, Moscow, 1983).
8. I. A. Znamenskaya, in *Proceedings of 21st International Symposium on Shock Waves, Keppel, 1997*, p. 489.
9. A. L. Suris, *Thermodynamics of High-Temperature Processes* (Nauka, Moscow, 1985).
10. I. É. Ivanov and I. A. Kryukov, Mat. Model. **8**, 47 (1996).
11. U. G. Pirumov, I. E. Ivanov, and I. A. Kryukov, in *Progress and Challenges in CFD Methods and Algorithms* (Seville, Spain, 1995), p. 13.
12. N. Sudani, M. Sato, T. Karasawa, *et al.*, in *Proceedings of 22nd International Symposium on Shock Waves, London, 1999*, p. 1223.

Translated by V. Astakhov

Journal of Experimental and Theoretical Physics, Vol. 95, No. 6, 2002, pp. 1040–1043.
Translated from Zhurnal Éksperimental'noĭ i Teoreticheskoĭ Fiziki, Vol. 122, No. 6, 2002, pp. 1207–1211.

FLUIDS

A Free Convective Boundary Layer in a Conducting Fluid in the Presence of a Transverse Magnetic Field

L. A. Bolshov, A. M. Dykhne, P. S. Kondratenko*, and L. V. Matveev
Nuclear Safety Institute, Russian Academy of Sciences, Moscow, 113191 Russia
**e-mail: kondrat@ibrae.ac.ru*
Received July 18, 2002

Abstract—The properties of free convection in a conducting fluid in laminar regime near a hot solid vertical wall in the presence of a transverse magnetic field are theoretically analyzed. The existence of two regimes of heat transfer from the wall to the fluid are established. In the first regime, at small heights $x \ll x_*$ where the magnetic field effect can be disregarded, heat transfer is described by the well-known results for a free convective boundary layer in a nonconducting fluid with the Nusselt number $\mathrm{Nu}_x \propto x^{3/4}$. In the second regime, at $x \gg x_*$ where the magnetic field plays a crucial role, the dependence of heat transfer on the height and field strength is $\mathrm{Nu}_x \propto \sqrt{x}/B$. The location of the boundary between these regimes strongly depends on the magnetic field, $x_* \propto B^{-4}$. © *2002 MAIK "Nauka/Interperiodica".*

1. INTRODUCTION

Whereas free convective boundary layers in nonconducting fluids have been studied extensively (see, e.g., [1]), these layers for conducting fluids in the presence of a magnetic field have been studied inadequately. For instance, in their monograph [2], which gives an overview of this problem, Blum *et al.* consider a problem that admits a self-similar solution if the magnetic field strength has a specific dependence on the coordinate along a hot surface ($\propto x^{1/4}$). Without this dependence (in particular, in a uniform field), the problem becomes much more complicated. In any case, the solutions from [2] have the form of infinite power series that are difficult to use. At the same time, knowing the laws of heat transfer for a conducting fluid in the presence of a magnetic field is important for many practical problems, for example, the problems of conducting-fluid flows in tubes [3] or processes pertaining to electrolytic metallurgy.

Here, our goal is to analyze the properties of the steady laminar free conductive boundary layer of a conducting fluid near a vertical wall at a wall temperature that differs from the fluid temperature in a uniform magnetic field normal to the wall. Below, for definiteness, we consider a situation where the wall temperature is higher than the fluid temperature, but all our results, with appropriate changes, also apply to the reverse situation.

2. STATEMENT OF THE PROBLEM

Consider the distributions of the flow velocity and the conducting-fluid temperature in the presence of a magnetic field near a hot wall. The fluid far from the wall is assumed to be isothermal and motionless. The magnetic field normal to the wall is assumed to be uniform near it. Denote the temperature difference between the wall and the fluid far from it by ΔT. The temperature is counted off from its value far from the wall. We direct the x axis upward and the y axis perpendicular to the wall, so $y = 0$ on the wall itself. Since the system is assumed to be homogeneous along the z axis, there is no z velocity component.

Suppose that the validity condition for the boundary layer approximation is satisfied. This condition implies that the Rayleigh number is large compared to unity:

$$\mathrm{Ra} = \frac{g\beta\Delta T H^3}{\nu\chi} \gg 1.$$

Here, g is the acceleration of Earth's gravity, β is the thermal expansion coefficient, H is the vertical scale size, ν is the kinematic viscosity, and χ is the thermal diffusivity. In addition, we assume the magnetic Reynolds number to be small,

$$\mathrm{Re}_m = \frac{4\pi\sigma}{c^2} VH \ll 1,$$

where σ is the fluid conductivity, c is the speed of light, and V is the characteristic flow velocity. This condition allows us to ignore the inverse effect of the fluid flow on the magnetic field.

The current in a fluid in the presence of a magnetic field is defined by the relation

$$\mathbf{j} = \sigma\left(\mathbf{E} + \frac{1}{c}\mathbf{V} \times \mathbf{B}\right).$$

Since the magnetic field is directed along the y axis and since the velocity vector lies in the xy plane, the vector $\mathbf{V} \times \mathbf{B}$ is directed along the z axis. It follows from the equation

$$\mathrm{div}\,\mathbf{j} = 0$$

at constant conductivity that

$$\mathrm{div}\mathbf{E} = 0.$$

In addition, the following equation is valid:

$$\mathrm{curl}\mathbf{E} = 0.$$

Thus, we conclude that under the short-circuit condition, which is assumed to be satisfied, the electric-field strength becomes identically equal to zero:

$$\mathbf{E} \equiv 0.$$

Let us derive the equations of motion for the boundary layer. In comparison with a nonconducting fluid, the hydrodynamic equations for a conducting fluid in a magnetic field contain an additional Lorentz force. In the geometry under consideration, this force enters only into the longitudinal component of the Navier–Stokes equation (along the x axis). As usual, having used the transverse component in this equation to eliminate the pressure, we obtain the following system of equations of motion for the free convective boundary layer of a conducting fluid in a transverse magnetic field:

$$\frac{\partial u}{\partial x} + \frac{\partial v}{\partial y} = 0, \tag{1}$$

$$u\frac{\partial u}{\partial x} + v\frac{\partial u}{\partial y} = g\beta T + \nu\frac{\partial^2 u}{\partial y^2} - \frac{\nu}{\delta_M^2}u, \tag{2}$$

$$u\frac{\partial T}{\partial x} + v\frac{\partial T}{\partial y} = \chi\frac{\partial^2 T}{\partial y^2}. \tag{3}$$

Here, u and v are the longitudinal and transverse velocities (along the x and y axes, respectively). The temperature T is counted off from its value for the fluid far from the wall. The magnetic thickness appearing in Eq. (2) is defined as

$$\delta_M = \sqrt{\frac{\eta}{\sigma}}\frac{c}{B}, \tag{4}$$

where η is the dynamic viscosity of the fluid. As usual, the boundary conditions for system (1)–(3) are zero u and T in the limit $y \longrightarrow \infty$, zero u and v at $y = 0$, and $T = \Delta T$ at $y = 0$.

3. STRUCTURE OF THE BOUNDARY LAYER

We see from Eq. (2) that the magnetic field produces additional braking. Let us show that in the initial segment of fluid acceleration (at small x), the contribution from the term containing the magnetic field strength can be neglected. Estimate the total contribution from the viscous and inertial terms in Eq. (2) by assuming that

$$\delta_M^{-2} \propto B^2 = 0.$$

According to the well-known results for an ordinary boundary layer (see [1]), which are valid in the absence of a magnetic field, for the quantity

$$A \equiv u\frac{\partial u}{\partial x} + v\frac{\partial u}{\partial y} - \nu\frac{\partial^2 u}{\partial y^2}$$

we then have

$$A \sim \frac{\nu u}{x^2}(\mathrm{Ra}_x S)^{1/2}, \tag{5}$$

where

$$\mathrm{Ra}_x = \frac{g\beta\Delta T x^3}{\nu\chi}$$

and $S = 1$ if the Prandtl number $\mathrm{Pr} \equiv \nu/\chi \gtrsim 1$ and $S = \mathrm{Pr}^{-1}$ if $\mathrm{Pr} \lesssim 1$. Comparing estimate (5) with the magnetic term in Eq. (2), we conclude that in the initial segment of the boundary layer at $x \ll x_*$, where

$$x_* = \delta_M\left(\frac{\delta_M}{H}\right)^3 \mathrm{Ra}S, \tag{6}$$

the magnetic field effect on the boundary layer can be ignored. In this case, the thickness of the thermal boundary layer is $\delta_T \propto x^{1/4}$ and the Nusselt number

$$\mathrm{Nu}_x \equiv -\frac{x}{\Delta T}\left(\frac{\partial T}{\partial y}\right)_{y=0}, \tag{7}$$

which is the dimensionless heat transfer coefficient, is given by

$$\mathrm{Nu}_x \sim \left(\frac{\mathrm{Ra}_x}{S}\right)^{1/4}.$$

Let us now consider the properties of the boundary layer at $x \gg x_*$. In this range of x, we can now discard the inertial term and, at $y > \delta_M$, the viscous term in favor of the magnetic term in momentum balance equation (2). Under these conditions, according to Eq. (2), $u \approx \bar{u}$, where

$$\bar{u} = \frac{g\beta\delta_M^2}{\nu}T. \tag{8}$$

As we show below, the thickness of the thermal boundary layer δ_T at $x \gg x_*$ is much larger than δ_M:

$$\delta_T \gg \delta_M. \tag{9}$$

Thus, the difference between $\bar{u}$ defined in (8) and the longitudinal flow velocity u in the energy balance equation (3) can be neglected. Therefore, taking into account the linearity of Eq. (3) in temperature, we

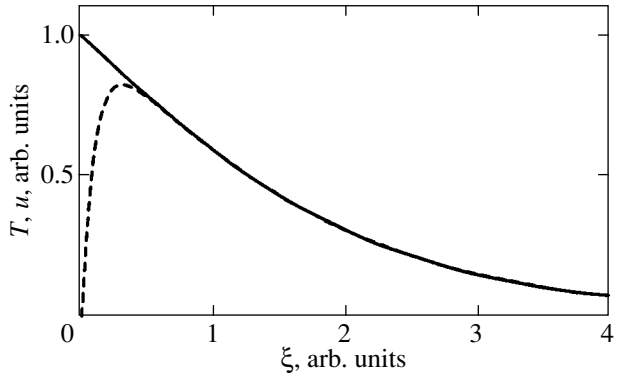

Temperature (solid line) and longitudinal velocity (dashed line) versus variable ξ normalized to ΔT and $\frac{g\beta\delta_M^2}{\nu}\Delta T$, respectively, for $\delta_T/\delta_M = 10$.

obtain a closed system of equations for $\bar{u}$ from Eqs. (1) and (3):

$$\frac{\partial \bar{u}}{\partial x} + \frac{\partial \bar{v}}{\partial y} = 0, \tag{10}$$

$$\bar{u}\frac{\partial \bar{u}}{\partial x} + \bar{v}\frac{\partial \bar{u}}{\partial y} = \chi\frac{\partial^2 \bar{u}}{\partial y^2} \tag{11}$$

with the boundary conditions

$$\bar{u}|_{y=0} = U \equiv \frac{g\beta\Delta T\delta_M^2}{\nu}, \quad \bar{v}|_{y=0} = \bar{u}|_{y\to\infty} = 0. \tag{12}$$

Formally, the system of Eqs. (10)–(11) matches the corresponding system for a shear boundary layer [4] if we substitute $\nu \longrightarrow \chi$ in the latter. However, the boundary conditions for these two cases differ fundamentally.

Just as in the case of a shear boundary layer, system (10) and (11) can be reduced to an ordinary differential equation for the dimensionless stream function $f(\xi)$:

$$ff'' + 2f''' = 0, \tag{13}$$

$$f(0) = f'(\infty) = 0, \quad f'(0) = 1. \tag{14}$$

The self-similar variable ξ is defined as

$$\xi = y\sqrt{\frac{U}{\chi x}}. \tag{15}$$

The quantities $\bar{u}$ and $\bar{v}$ are related to the function f by the relations

$$\bar{u} = Uf'(\xi), \quad \bar{v} = \frac{1}{2}\sqrt{\frac{\chi U}{x}}(\xi f' - f). \tag{16}$$

In turn, the temperature, according to equality (8), is given by

$$T = \Delta T f'(\xi). \tag{17}$$

Naturally, the characteristic scale of the dependence of f on ξ is on the order of unity. Therefore, according to equality (15), the thickness of the thermal boundary layer can be estimated as

$$\delta_T \sim \sqrt{\frac{x}{x_*}}S\delta_M, \tag{18}$$

which confirms inequality (9) if $x \gg x_*$.

Let us return to determining the longitudinal flow velocity in the boundary layer at $x \gg x_*$. For $y \gg \delta_M$, it is defined by expression (8). For $y \lesssim \delta_M$, the convective terms in Eq. (2) are still small but viscosity becomes important. Instead of relation (8) for the velocity u, we then have the equation

$$g\beta T + \nu\frac{\partial^2 u}{\partial y^2} - \frac{\nu}{\delta_M^2}u = 0. \tag{19}$$

Since temperature T at distances on the order of δ_M changes only slightly if $\delta_T \gg \delta_M$, the solution of Eq. (19) takes the form

$$u = \frac{g\beta\delta_M^2}{\nu}T(1 - e^{-y/\delta_M}). \tag{20}$$

We emphasize that this expression is valid over the entire range of transverse y coordinates.

As follows from (18), the total thickness of the boundary layer δ_T increases with the longitudinal coordinate proportionally to $\sqrt{x}$, while the thickness of the viscous sublayer δ_M remains constant. Therefore, as x increases, the temperature perturbation caused by the deviation of the velocity profile from the temperature profile near the wall [formula (19)] will decrease in importance.

According to Eq. (18) and with account of Eq. (4), the thickness of the thermal boundary layer at $x \gg x_*$ is proportional to the magnetic field strength:

$$\delta_T \propto B\sqrt{x}.$$

4. HEAT TRANSFER FROM THE WALL IN THE REGIME OF MAGNETIC BRAKING

The heat flux from the wall is determined by the Nusselt number (7). In the regime of magnetic braking (at $x \gg x_*$), with account of relations (7), (15), and (17), this number is determined as

$$\mathrm{Nu}_x = -f''(0)\frac{\delta_M}{x}\mathrm{Ra}_x^{1/2} \propto \frac{\sqrt{x}}{B}.$$

In this regime, the heat flux density is inversely proportional to the magnetic field strength and proportional to the square root of the longitudinal coordinate.

To determine $f''(0)$, the set of Eqs. (13)–(14) was solved numerically. We emphasize that, although Eq. (13) coincides with the corresponding equation for a shear boundary layer, the boundary conditions for the function $f(\xi)$ for the latter have the following form instead of (14):

$$f(0) = f'(0) = 0, \quad f'(\infty) = 1.$$

We numerically solved Eqs. (13) and (14) using the fourth-order Runge–Kutta method. The second derivative at zero was found to be $f''(0) = -0.44$. As a result, the ultimate expression for the Nusselt number is

$$\mathrm{Nu}_x = 0.44\frac{\delta_M}{x}\mathrm{Ra}_x^{1/2}.$$

In the figure, the temperature and longitudinal velocity are plotted against the coordinate ξ. Their profiles were obtained by numerically solving system of Eqs. (13)–(14) using relations (17) and (20) for $\delta_T/\delta_M = 10$.

The condition for heat transfer in the regime of magnetic braking requires that the wall height H be simultaneously large compared to the boundary-layer thickness and to the lower boundary of the regime in longitudinal coordinate x_*. With account of expressions (5) and (17), this requirement reduces to the inequalities

$$(\mathrm{Ra}S)^{1/4} < \frac{H}{\delta_M} \ll \mathrm{Ra}^{1/2}. \tag{21}$$

For typical parameters $\beta \approx 10^{-4}$ K^{-1}, $\sigma \approx 3 \times 10^{16}$ s^{-1}, $\chi \approx 0.1$ cm^2 s^{-1}, $\Delta T \approx 10$ K, and $H = 40$ cm, inequality (21) takes the form of the following condition for the magnetic field strength:

$$100 \text{ G} < B \ll 6 \times 10^3 \text{ G}.$$

Another condition for this regime is the stability of the laminar fluid flow in the range of parameters under consideration. Since the complete problem of flow stability in the boundary layer concerned requires an independent analysis, here we only note the following. According to [4], the motion in a laminar boundary layer is stable if the Reynolds number determined with respect to the displacement thickness δ (see [4] for the definition of δ) does not exceed a critical value $\mathrm{Re}_{\delta\mathrm{cr}} \sim 10^2$. Substituting boundary-layer thickness (18) for the displacement thickness and expression (8) with $T = \Delta T$ for the maximum velocity yields the following estimate for the Reynolds number at $\mathrm{Pr} \approx 1$ and $B \approx 500$ G: $\mathrm{Re}_{\delta T} \approx 10$. As the magnetic field increases in strength, the Reynolds number decreases in inverse proportion to the field strength. Therefore, one might expect the laminar flow in the boundary layer concerned to be stable for the parameters under consideration.

5. CONCLUSION

The main results of our analysis are as follows. In the presence of a transverse magnetic field, a free convective boundary layer is subdivided in the longitudinal coordinate into two regions; the spatial location of the boundary between these regions is determined by the magnetic field strength. In the first region of the boundary layer adjacent to its front edge, the magnetic field effect is negligible. In the second region that follows the first one, the magnetic field brakes the boundary layer. Here, as the longitudinal coordinate x increases, the longitudinal velocity becomes saturated and the boundary-layer thickness acquires a steeper dependence ($\propto \sqrt{x}$) instead of $x^{1/4}$, as in the first region. In turn, this behavior results in a significant suppression of the heat flux from the fluid to the wall, which is inversely proportional to the magnetic field strength.

ACKNOWLEDGMENTS

We are grateful to D.V. Nikolskii, who performed the numerical calculations.

REFERENCES

1. B. Gebhart, Y. Jaluria, R. Mahajan, and B. Sammakia, *Buoyancy-Induced Flows and Transport* (Hemisphere, New York, 1988; Mir, Moscow, 1991), Vol. 1.
2. É. Ya. Blum, Yu. A. Mikhaĭlov, and R. Ya. Ozols, *Heat and Mass Exchange in Magnetic Field* (Zinante, Riga, 1980).
3. L. G. Genin and V. G. Sviridov, *Hydrodynamics and Heat Exchange of Magnetohydrodynamic Flows in Channels* (Mosk. Énerg. Inst., Moscow, 2001).
4. L. D. Landau and E. M. Lifshitz, *Course of Theoretical Physics*, Vol. 6: *Fluid Mechanics* (Nauka, Moscow, 1986; Pergamon, New York, 1987).

Translated by V. Astakhov

Journal of Experimental and Theoretical Physics, Vol. 95, No. 6, 2002, pp. 1044–1055.
Translated from Zhurnal Éksperimental'noĭ i Teoreticheskoĭ Fiziki, Vol. 122, No. 6, 2002, pp. 1212–1225.

SOLIDS
Structure

Noncollinear Cluster Ferromagnetism in Lanthanum Manganite Perovskites with an Excess of Manganese

É. E. Zubov[a], V. P. Dyakonov[a, b, *], and H. Szymczak[b]

[a]*Galkin Physicotechnical Institute, National Academy of Sciences of Ukraine, Donetsk, 83114 Ukraine*
[b]*Institute of Physics, Polish Academy of Sciences, 02-668 Warsaw, Poland*
**e-mail: dyakon@dyakon.fti.ac.donetsk.ua*

Received February 28, 2002

Abstract—A theoretical substantiation is provided for realization of the spin structure in a weakly doped subsystem based on $LaMnO_3$, which is observed in compounds with an excess of manganese, $(La_{1-y}Ca_y)_{1-x}Mn_{1+x}O_3$, where $y = 0$ and 0.3, $x = 0$–0.4. It is proved experimentally that samples with $x > 0.1$ exhibit an anomalous behavior of magnetization at $T < 45$ K. The magnetization decreases in fields $H < 100$ Oe and increases for $H > 200$ Oe. It is assumed that this is associated with the emergence of a canted phase in clusters of manganese ions with difference valences. A theoretical analysis indicates that a competition between double and superexchange interaction is in principle possible in such clusters, since the charge carrier concentration in them is considerably lower than in the host matrix. It is shown that the inclusion of quantum properties of spin leads to a considerable modification of the thermodynamic behavior of a magnet with collectivized electrons. The results of analysis are compared with analogous results in the de Gennes classical theory. The possibility of formation of a state with a canted magnetic sublattice in the weakly doped subsystem in the low-temperature region is substantiated on the basis of calculations. An analysis of the thermodynamic behavior of the weakly doped subsystem based of $LaMnO_3$ taking into account quantum-mechanical properties of spin shows that relaxation phenomena determined, to a considerable extent, by the relation of parameters of intra- and interplanar indirect exchange, as well as the electron transport energy, can take place in the region of phase transition to the canted state. The microscopic parameters of interactions are estimated quantitatively. The results of calculations are in qualitative agreement with experimental data. *© 2002 MAIK "Nauka/Interperiodica".*

1. INTRODUCTION

The magnetism of doped manganites is due to indirect exchange and the double exchange mechanism [1–3]. Superexchange dominates in compounds containing exclusively Mn^{3+} and Mn^{4+} and forms the antiferromagnetic (AFM) structure. Partial replacement of lanthanum by cations with the lowest valence in *A* positions (positions of the rare-earth ion R in the structure of $RMnO_3$ crystal) in lanthanum-manganese oxides leads to the formation of holes at the Mn^{3+} ion, facilitating the emergence of mixed Mn^{3+}/Mn^{4+} ionic states. Considering that magnetism in manganites is determined by the number of Mn^{3+} and Mn^{4+} ions, oxides with an excess of manganese and with a deficit of lanthanum, which are self-doped systems, are of special interest. In such systems, manganese ions with different valences, as well as vacancies, are formed and charge carriers generated in this process facilitate ferromagnetic ordering of localized spins of manganese via the double exchange mechanism. It should be noted that the magnetism in compounds with excess manganese was not investigated intensely. It is known that EPR and NMR studies have been carried out in manganites with superstoichiometric content of manganese [4, 5] as well as spin-wave resonance studies in $La_{0.7}Mn_{1.3}O_3$ [6].

Clusters in which the mixture of manganese ions with charges of 3+ and 4+ also exists can be formed in the vicinity of cation vacancies or implanted manganese ions. A canted AFM structure (CS) can emerge both in clusters and in weakly doped manganites at a certain concentration of charge carriers.

In spite of the suggestion by some authors [7–9] that the CS is unstable to phase separation into ferro- and antiferromagnetic states, some experimental results [10–12] cannot be described within the existing theories [7–9].

In this paper, we theoretically substantiate the realization of noncollinear antiferromagnetism in a weakly doped $LaMnO_3$-based subsystem, which is confirmed by the results of investigation of the effect of superstoichiometric manganese content on the features of the magnetic state in $(La_{1-y}Ca_y)_{1-x}Mn_{1+x}O_3$ compounds, where $y = 0$ and 0.3 and $x = 0$–0.4.

2. EFFECT OF SUPERSTOICHIMETRIC MANGANESE ON THE MAGNETIC PROPERTIES OF $(La_{1-y}Ca_y)_{1-x}Mn_{1+x}O_3$

In this work, the system $LaMnO_3$ was chosen as the basic structure. Since the properties of manganites are very sensitive to the conditions of synthesis, all the

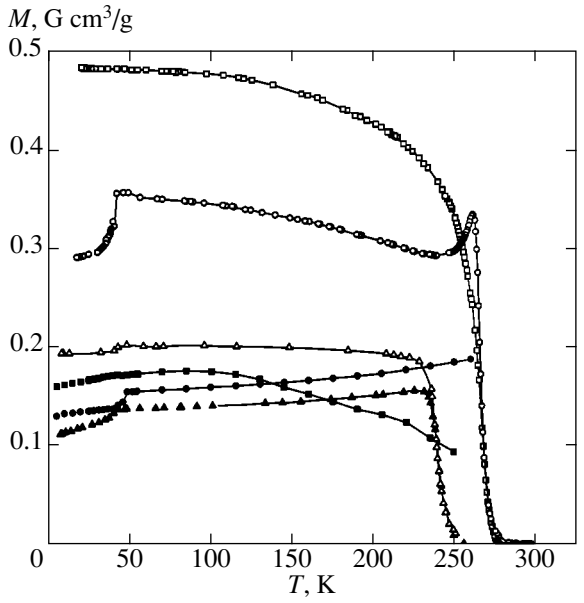

Fig. 1. Temperature dependences of FC and ZFC magnetizations for samples of $La_{0.8}Mn_{1.2}O_3$ (△ and ▲, respectively), $(La_{0.7}Ca_{0.3})_{0.8}Mn_{1.2}O_3$ (○ and ●), and $La_{0.7}Ca_{0.3}MnO_3$ (□ and ■) in the field 2 Oe.

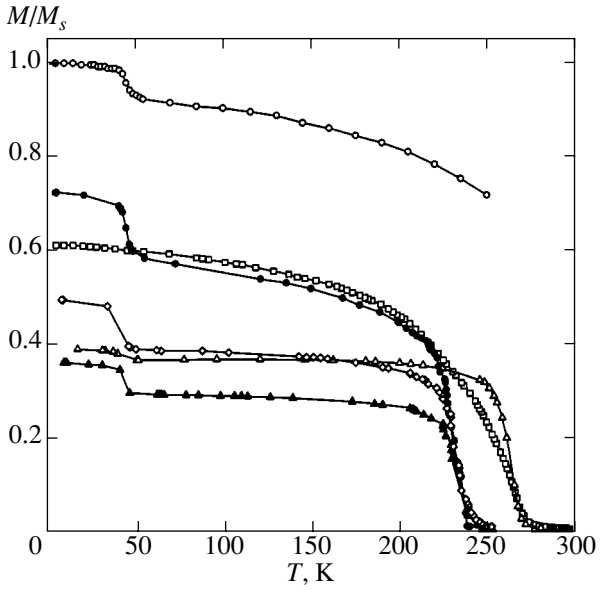

Fig. 2. Temperature dependences of FC magnetizations M/M_s for samples of $La_{0.8}Mn_{1.2}O_3$ in magnetic fields H = 0.5, 1, and 10 kOe (▲, ◇, and ●, respectively), $(La_{0.7}Ca_{0.3})_{0.8}Mn_{1.2}O_3$ for H = 0.5 and 10 kOe (△ and ○), and $La_{0.7}Ca_{0.3}MnO_3$ for H = 1 kOe (□).

samples were obtained according to the same technology, which allowed us to compare their properties. Ceramic targets were obtained using two-stage (at 900 and 950°C) 20-h synthesizing annealing followed by fritting of pressed (P = 0.5 MPa) samples in air at 1150°C. The detailed procedure of synthesis and characteristics of the crystal structure of manganites with excess manganese are described in [13]. We analyzed the structure of the ceramic samples under investigation at room temperature with a DRON-3 X-ray diffractometer using CuK_α radiation. We determined the phase composition, the type of the crystal lattice, and its parameters. According to X-ray diffraction data, the samples contain only one phase with the orthorhombic (*Pnma*) distorted perovskite structure. An increase in the manganese concentration did not cause a change in the structural symmetry. An increase in the manganese content from x = 0.1 to 0.4 leads to a decrease in the lattice parameters and an increase in the Curie temperature T_C, indicating complete solubility of excess manganese in the matrix structure of these perovskites in the absence of secondary phases in them. The X-ray structural analysis, taking into account the diffuse halo, proved that manganese ions in combination with vacancies form clusters in the ceramic samples under investigation. It will be shown below that some features of the low-temperature magnetic behavior of the samples are associated with magnetism of these clusters.

The magnetization $M(T, H)$ was measured in fields varying from 2 Oe to 12 kOe on samples cooled both in zero magnetic field (ZFC) and in an applied field (FC) in the temperature range 4.2–300 K.

Figure 1 shows the temperature dependence of FC and ZFC magnetizations of three samples, $La_{0.8}Mn_{1.2}O_3$, $La_{0.7}Ca_{0.3}MnO_3$, and $(La_{0.7}Ca_{0.3})_{0.8}Mn_{1.2}O_3$ in the field 2 Oe. Figure 2 shows the temperature dependences of the reduced magnetization M/M_s of the same samples in magnetic fields H = 0.5–10 kOe, where M_s is the saturation magnetization of $(La_{0.7}Ca_{0.3})_{0.8}Mn_{1.2}O_3$ in the field 10 kOe at T = 4.2 K. All samples exhibit the ferromagnetic behavior below the paramagnetic–ferromagnetic transition temperature. The magnetic phase transition is narrow, which is characteristic of the first-order phase transition. It can be seen from Figs. 1 and 2 that the magnetization remains almost constant below 220 K. The FC magnetization in weak fields (Fig. 1) exceeds the ZFC magnetization below the characteristic "freezing" temperature, which is slightly lower than T_C. As the magnetic field increases (H > 1 kOe), the difference between the magnetizations M_{FC} and M_{ZFC} nearly vanishes.

In fields H < 100 Oe, the magnetization decreases at low temperatures (see Fig. 1). In fields 100 < H < 200 Oe, the magnetization does not change upon cooling. In magnetic fields H > 200 Oe, the $M_{FC}(T)$ dependence displays an upward jump at T < 45 K (Fig. 2). The difference between the magnetizations at T = 4.2 K and T > 50 K increases with the manganese content. The $M_{ZFC}(T)$ dependence also exhibits a similar dependence below 45 K. It is assumed that the decrease and increase in the magnetizations observed at low temperatures are associated with a change in the spin configu-

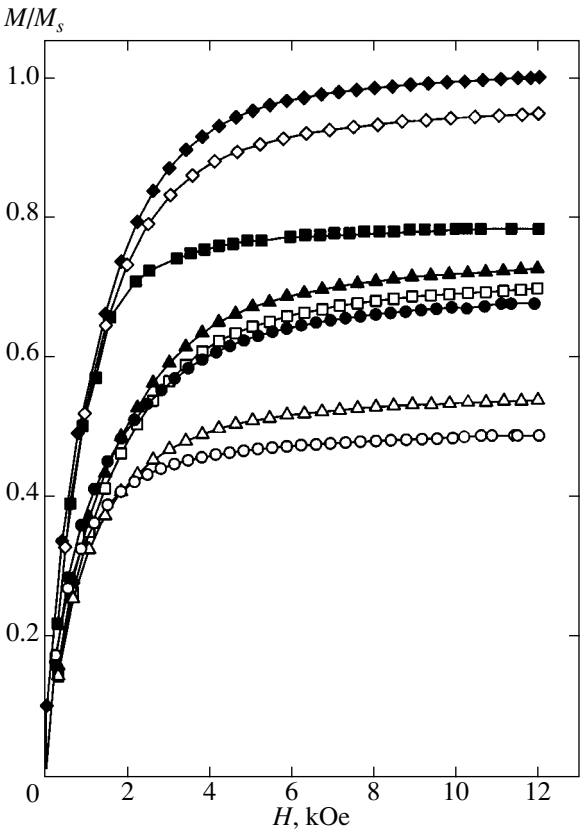

Fig. 3. Field dependences of the reduced magnetization M/M_s for samples of $La_{0.8}Mn_{1.2}O_3$ (△ and ▲), $La_{0.9}Mn_{1.1}O_3$ (● and ○), $La_{0.6}Mn_{1.4}O_3$ (■ and □), and $(La_{0.7}Ca_{0.3})_{0.8}Mn_{1.2}O_3$ (◆ and ◇) at 4.2 and 100 K, respectively.

ration in clusters formed by manganese ions of different valences.

Figure 3 shows the field dependences of the reduced magnetization M/M_s measured at 4.2 and 100 K in the field interval H = 0–12 kOe. The saturation magnetization is attained even in fields of the order of 4 kOe at temperatures $T < 150$ K. It can be seen from Fig. 3 that the $M(H)$ dependences exhibit a typical ferromagnetic behavior. The mean values of magnetic moments for completely ordered spins, which were calculated by the formula $m(\mu_B) = 3\mu_B x_A + 4\mu_B x_B$ (the magnetic moments of Mn^{4+} and Mn^{3+} are equal to $3\mu_B$ and $4\mu_B$, respectively, and the concentrations are x_A and x_B) exceed the experimental values. This is due to the fact that part of the spins do not participate in the establishment of the long-range magnetic order.

3. QUANTUM-MECHANICAL ANALYSIS OF THE MAGNETIC STRUCTURE OF A WEAKLY DOPED $LaMnO_3$-BASED SUBSYSTEM

In order to analyze the experimental data on magnetization, we must study the magnetic structure of weakly doped $LaMnO_3$ at temperatures $T \ll T_C$. We assume, on the basis of experimental data, that the clusters of manganese ions with difference valences, which are formed in the $La_{1-x}Mn_{1+x}O_3$ compound, have a composition very close to that of weakly doped $LaMnO_3$. It is well known that de Gennes [3] provided a detailed description of the magnetic state of this compound and proved that a noncollinear structure is realized in the low-temperature range for a low hole concentration. This is the result of the *A*-type distortion (planes are ferromagnetic) of the AFM ordering typical of $LaMnO_3$. However, the analysis was confined to the use of classical ion spins only. It will be shown below that the inclusion of quantum properties of spin can considerably affect the final results of thermodynamic analysis, giving rise to some specific features such as the change in the type of phase transition and magnetic relaxation. The role of the ratio of parameters of intra- and interplanar indirect exchange interactions becomes very significant.

Let us carry out a theoretical analysis, assuming that there are charge states of the Mn^{4+} and Mn^{3+} ions in the existing clusters. In order to determine the conditions under which the ferromagnetic (FM), AFM or canted phases exist, we must find the interaction energies for double and indirect exchanges. We write the system Hamiltonian in the form

$$H = H_0 + H_{\text{int}}, \tag{1}$$

$$H_0 = -\sum_i J_H S_i \sigma_i - \sum_{i,j} J_{ij} S_i S_j - \mu \sum_i n_i, \tag{2}$$

$$H_{\text{int}} = \sum_{\langle ij\rangle, \sigma} t_{ij} c_{i\sigma}^{\dagger} c_{j\sigma}. \tag{3}$$

Here, the Hund exchange $J_H > 0$—i.e., the interaction of the spin σ of a collectivized electron with the spin S of the Mn^{4+} core is ferromagnetic; J_{ij} is the indirect exchange, which is positive in the planes and negative between the planes; μ is the chemical potential; n_i is the operator of the number of electrons at the ith site; t_{ij} is the jump integral, which is assumed to be isotropic; and $c_{i\sigma}^{\dagger}$ and $c_{i\sigma}$ are the creation and annihilation operators for an electron with spin σ at the ith ion. We assume that the relation $J_H \gg t \gg J_{ij}$, which permits the application of perturbation theory in H_{int}, is satisfied. Unfortunately, it is difficult to use relation (2) directly as the initial Hamiltonian even after separating the mean-field Heisenberg part in it, since the electron degrees of freedom appearing in it considerably extend the basis used. It is clear, however, that, for an infinitely strong Hund bond, it is meaningless to take into account the mutual orientations of the electron and ion spins. Consequently, we can use the same procedure of separating the mean field to the Hund part of Hamiltonian H_0 also. In this case, operator terms of the type of $J_H S\langle\sigma\rangle$ can be formally cancelled out with $J_H\langle S\rangle\langle\sigma\rangle$ since the ion and electron spins are parallel. Thus, the initial Hamiltonian

now contains two commuting mean-field Hamiltonians for electrons and ions, respectively:

$$H_0^{\rm el} = -\sum_i J_H\{\langle S_i^x\rangle\sigma_i^x + \langle S_i^z\rangle\sigma_i^z\} - \mu\sum_i n_i, \quad (4)$$

$$H_0^{\rm ion} = -\sum_i \{C_i S_i^x + DS_i^z\} + H_0^{\rm const}, \quad (5)$$

where

$$D = 2J(0)\langle S\rangle\cos a,$$

$$C_i = -2J(\mathbf{k}_0)\langle S\rangle\sin\alpha\cos(\mathbf{k}_0\cdot\mathbf{r}_i),$$

$$J(0) = 4J_1 + 2J_2, \quad J(\mathbf{k}_0) = 4J_1 - 2J_2$$

are the Fourier components of indirect exchange $J(k)$ for the ferromagnetic, $k = 0$, and antiferromagnetic, $k = k_0 = (0, 0, \pi/a)$ (A-type magnetic structure) types of ordering, respectively, and a is the lattice constant. The quantities $J_1 > 0$ and $J_2 < 0$ are the parameters in intraplanar FM interaction and interplanar paired superexchange AFM interaction, respectively. In expression (5), we assume the existence of different types of magnetic order, which can be presented in the general case in the form

$$\langle S_i^z\rangle = \langle S\rangle\cos\alpha, \quad \langle S_i^x\rangle = -\langle S\rangle\sin\alpha\cos(\mathbf{k}_0\cdot\mathbf{r}_i), \quad (6)$$

where $\alpha = 0$ and $\alpha = \pi/2$ for the FM and AFM structures, respectively, while for the CS phase we have $0 < \alpha < \pi/2$, where α is the angle between the mean spin $\langle S\rangle$ and the z axis and k_0 is the wave vector of the AFM structure. Here, we assume that there are no preferred directions along the y axis, and the anisotropy field determining the direction of the z axis is equal to zero.

In expression (5), $H_0^{\rm const}$ is the operator constant of Hamiltonian H_0:

$$H_0^{\rm const} = N\langle S\rangle^2\{J(\mathbf{k}_0)\sin^2\alpha + J(0)\cos^2\alpha\}, \quad (7)$$

where N is the number of magnetic sites.

Thus, taking into account initial Hamiltonians, we can analyze the electron and ion subsystems separately; in this case, the coupling between these subsystems is carried out through the self-consistent field parameters. We must now diagonalize Hamiltonians (4) and (5), which can be carried out with the help of unitary transformation of spin operators for the ion subsystem,

$$S_i^x = \tilde{S}_i^x\cos\gamma_i - \tilde{S}_i^z\sin\gamma_i,$$
$$S_i^z = \tilde{S}_i^x\sin\gamma_i + \tilde{S}_i^z\cos\gamma_i, \quad (8)$$

and via a similar transformation for electron spins. It can easily be verified that the transformed initial Hamiltonian for electrons assumes the form

$$H_0^{\rm el} = -\tilde{h}\sum_i\tilde{\sigma}_i^z - \mu\sum_i n_i, \quad (9)$$

where $\tilde{h} = J_H\langle S\rangle$ and $\tilde{\sigma}_i^z$ is the electron spin operator in the system associated with the mean spin $\langle S\rangle$ of the magnetic ion. The spin Hamiltonian for Mn^{4+} ions in the mean field approximation becomes diagonal:

$$H_0^{\rm ion} = -\tilde{H}\sum_i\tilde{S}_i^z, \quad (10)$$

where the effective field is given by

$$\tilde{H} = 2\sqrt{J^2(0)\cos^2\alpha + J^2(\mathbf{k}_0)\sin^2\alpha}\langle S\rangle, \quad (11)$$

and the angle γ_i from formula (8) satisfies the equation

$$\tan\gamma_i = \frac{4J_1 - 2J_2}{4J_1 + 2J_2}\tan\alpha\cos(k_0 r_i). \quad (12)$$

The expression for the free energy of superexchange interactions can now be written in the following form:

$$F_{\rm exch} = -T\ln\left\{\sum_{m=-S}^{S}\exp\left(\frac{\tilde{H}m}{T}\right)\right\} + H_0^{\rm const}. \quad (13)$$

It should be noted that this expression takes into account the quantum nature of the spin, which was disregarded in the de Gennes theory [3]. It should also be observed that an analog of Eq. (12) for ordinary magnets defines the trivial angles corresponding to the easy magnetization axes. In our case, the electron subsystem is coupled with the ion subsystem through the perturbation Hamiltonian $H_{\rm int}$ (3). On account of electron jumps at a magnetic site, a certain mean spin $\langle S\rangle$ is formed, whose magnitude does not exceed 2, and the angle α of the canted structure is determined by the ratio of contributions from $H_{\rm int}$ and $H_0^{\rm ion}$. At low temperatures, the role of the contribution from $H_0^{\rm el}$ is mainly reduced to a shift in the chemical potential.

Let us now consider the contribution to the system thermodynamics associated with the electron subsystem. In order to simplify subsequent calculations, we use the Hubbard operators technique, disregarding states with double filling of a site. In this case, for the three electron states at a site ($|+\rangle$, $|0\rangle$, and $|-\rangle$) for the cases spin up, hole, and spin down, we realize a basis of nine Hubbard operators $X^{\alpha\beta} = |\alpha\rangle\langle\beta|$, in which $H_{\rm int}$ assumes the form

$$H_{\rm int} = \sum_{ij} t_{ij}\{X_i^{+0}X_j^{0+} + X_i^{-0}X_j^{0-}\}. \quad (14)$$

Since the initial Hamiltonian has already been transformed, we must transform $H_{\rm int}$ also. As in the case of spinors, the Hubbard operators $\tilde{X}_i^{\sigma 0}$ in the ith local system have the form

$$\tilde{X}_i^{\sigma 0} = -\sigma X_i^{\bar{\sigma}0}\sin\frac{\gamma_i}{2} + X_i^{\sigma 0}\cos\frac{\gamma_i}{2}, \quad (15)$$

where $\sigma = -\bar{\sigma} = \pm 1$, and angle γ_i is determined from Eq. (12). Substituting Eq. (15) into relation (14), we obtain

$$H_{\text{int}} = \sum_{\langle ij\rangle\sigma} t_{ij}\left\{\cos\frac{\gamma_i-\gamma_j}{2}\tilde{X}_i^{\sigma 0}\tilde{X}_j^{0\sigma} - \sigma\sin\frac{\gamma_i-\gamma_j}{2}\tilde{X}_i^{\sigma 0}\tilde{X}_j^{0\bar{\sigma}}\right\}. \quad (16)$$

This expression shows that the first term describing the intraplanar dynamics of electrons coincides with the kinematic contribution derived by Anderson and Hasegawa [14]. In the case of an AFM structure, this contribution vanishes, $\cos(\pi/2) = 0$. However, electrons jump between the planes since the last term in relation (16) is not equal to zero for $\gamma_i - \gamma_j = \pi$. It is this part of H_{int} that describes the interplanar kinematics of collectivized electrons. It would be interesting to find the Fourier components of intra- and interplanar jump integrals taking into account the transformation coefficients. For jump integrals in and between the planes, these components are given by

$$t_1(\mathbf{q}) = 2t[\cos(q_x a) + \cos(q_y a) + \cos\gamma\cos(q_z a)],$$
$$t_2(\mathbf{q}) = \frac{2t}{i}\sin(q_z a)\sin\gamma, \quad (17)$$

where we have used the nearest neighbors approximation for jumps with integral t and γ is the absolute value of the angle γ_i determined from Eq. (12).

In order to calculate the corrections to free energy or to the electron magnetization, we will use the diagrammatic approach on the basis of the scattering matrix formalism. The corresponding results for the FM, AFM, and paramagnetic states were published in [15, 16]. Using relation (16), we can immediately write, in the zeroth approximation of the self-consistent field, the expression for the effective interaction line,

$$B^{\sigma 0,\,0\sigma}(\mathbf{q}, i\omega_p) = \frac{t_1(\mathbf{q})(i\omega_p - \varepsilon_\sigma) - [t_1^2(\mathbf{q}) + t_2^2(\mathbf{q})]\langle F^{\sigma 0}\rangle}{(i\omega_p - \omega_{\mathbf{q}^+})(i\omega_p - \omega_{\mathbf{q}^+})}(i\omega_p - \varepsilon_{\bar{\sigma}}), \quad (18)$$

where $\omega_p = (2p+1)\pi T$, p are integers, T is the temperature, $\varepsilon_\sigma = -\tilde{h}\sigma/2 - \mu$ are the levels of the one-electron Hamiltonian (9), and $\langle F^{\sigma 0}\rangle = \langle X^{\sigma\sigma} + X^{00}\rangle = 1 - n/2 + \sigma\langle\sigma\rangle$ is the mean combined population of a site by an electron or a hole. The frequencies $\omega_{\mathbf{q}\sigma}$ of elementary excitations caused by jumps between sites are defined as

$$\omega_{\mathbf{q}\sigma} = \frac{1}{2}\{\varepsilon_+ + \varepsilon_- + t_1(\mathbf{q})(\langle F^{+0}\rangle + \langle F^{-0}\rangle)\} - \sigma\left\{\left(\frac{\varepsilon_+ - \varepsilon_-}{2}\right)^2 + \frac{1}{4}t_1^2(\mathbf{q})[\langle F^{+0}\rangle - \langle F^{-0}\rangle]^2 - t_2^2(\mathbf{q})\langle F^{+0}\rangle\langle F^{-0}\rangle + \frac{1}{2}t_1(\mathbf{q})(\varepsilon_+ - \varepsilon_-)(\langle F^{+0}\rangle - \langle F^{-0}\rangle)\right\}^{1/2}. \quad (19)$$

This expression shows that the kinematic part of the interaction, which is associated with interplanar jumps, is an effect of a higher order of smallness since it is proportional to $t_2^2(\mathbf{q})/J_H$. On the other hand, if $t_1(\mathbf{q}) \sim 0$, which is typical of G structures (staggered order in the AFM structure), the main contribution comes from $t_2(\mathbf{q})$. It describes the electron dynamics against the AFM background. This problem is being developed intensely in connection with the ground state of HTSC, and many results were obtained in the framework of the t–J model. However, we are not interested in this case at the moment and will mainly pay attention to the term with $t_1(\mathbf{q})$. Disregarding $t_2(\mathbf{q})$, we obtain from Eq. (18) the following expression for the effective line:

$$\beta B^{\sigma 0,\,0\sigma}(\mathbf{q}, i\omega_n) = \beta\frac{t_1(\mathbf{q})(i\omega_n - \varepsilon_\sigma)}{i\omega_n - E_{\mathbf{q}\sigma}}, \quad (20)$$

where $E_{\mathbf{q}\sigma} = \varepsilon_\sigma + t_1(\mathbf{q})\langle F^{\sigma 0}\rangle$. The effective interaction (20) describes the electron dynamics against the FM background of ion cores of Mn^{4+}. The effects of the type of ordering of FM planes on electron jumps are controlled by the factor $\cos\gamma$ in formula (17) for $t_1(\mathbf{q})$. It can be seen that for $\alpha = \pi/2$, i.e., in the case of antiferromagnetically ordered planes, the band is narrower than for $\alpha = 0$ for the FM structure. Since the band in the A-type structure is narrower, this renders the B-type (fully ferromagnetic) structure more advantageous and underlies the double-exchange mechanism discovered by Zener.

A more detailed analysis of the magnetic structure requires the study of the ground state of the electron subsystem. Since $t \ll J_H$, we have a sufficiently favorable relation for the application of perturbation theory in parameter t. In the first order in the reciprocal effective radius of interaction, the corresponding diagrammatic expansion for mean combined populations in the paramagnetic or FM phase was presented in [16]. This relation can be written analytically in the form

$$\langle F^{\sigma 0}\rangle = \langle F^{\sigma 0}\rangle_1 - \frac{1}{N}\sum_{\mathbf{q}} f(E_{\mathbf{q}\sigma}) + f(\varepsilon_\sigma), \quad (21)$$

where

$$\langle F^{\sigma 0}\rangle_1 = \frac{e^{\beta E_\sigma} + 1}{e^{\beta E_\sigma} + e^{\beta E_{\bar{\sigma}}} + 1},$$

$f(\varepsilon) = 1/[\exp(\beta\varepsilon) + 1]$ is the Fermi distribution function,

$$\beta = \frac{1}{T}, \quad E_\sigma = -\varepsilon_\sigma + \delta\mu_{\bar{\sigma}},$$

$$\delta\mu_\sigma = \frac{1}{N}\sum_{\mathbf{q}} t_1(\mathbf{q})\, f(E_{\mathbf{q}\sigma}).$$

Let us analyze various limiting cases of system (21). For $T \ll T_C$, where T_C is the Curie temperature, for the rectangular density of states $\rho = 1/W$, where $W = 4t(2 + \cos\gamma)$ is the bandwidth, we have the solution to system (21) in the form

$$\langle\sigma\rangle = \frac{n}{2}, \quad \frac{\mu}{W} = n - \frac{1}{2} - \frac{\tilde{h}}{2W} \tag{22}$$

for $n > 1/2$ ($\varepsilon_+ < 0$, $\varepsilon_- > 0$). Thus, the electron subsystem is magnetized to saturation, and the chemical potential is greater than zero. In the case of a low electron concentration, $n < 1/2$. We have the same solution (22), the only difference being $\mu < 0$ and $\varepsilon_+ > 0$.

At a temperature $T \sim T_C$ and $\alpha = 0$, we can expand system of equations (21) into a series in the small parameter $\langle\sigma\rangle$ and derive equations for the chemical potential and the temperature T_C of the phase transition to the FM state:

$$1 - n = \frac{1}{1 + 2e^{\beta(\mu + \delta\mu_0)}} - \frac{2}{N}\sum_q f(E_q) + 2f(-\mu),$$

$$T^2 = \frac{1}{2 + e^{-\beta(\mu + \delta\mu_0)}} \frac{1}{N}\sum_q t_1^2(q)\, f(E_q) \tag{23}$$

$$\times [1 - f(E_q)] - \frac{T}{N}\sum_q t_1(q)\, f(E_q)[1 - f(E_q)],$$

where

$$E_a = -\mu + \left(1 - \frac{n}{2}\right) t_1(q), \quad \delta\mu_0 = \frac{1}{N}\sum_q t_1(q)\, f(E_q).$$

For solving system of equations (23), we use the density of states

$$\rho(\varepsilon) = \frac{1}{N}\sum_{\mathbf{q}} \delta\left(\varepsilon - \frac{t_1(\mathbf{q})}{2t}\right),$$

which is presented in Fig. 4 for a simple cubic lattice, where $\delta(x)$ is the Dirac delta function. In particular, if we introduce the relative chemical potential $\tilde{\mu} = \mu/W$,

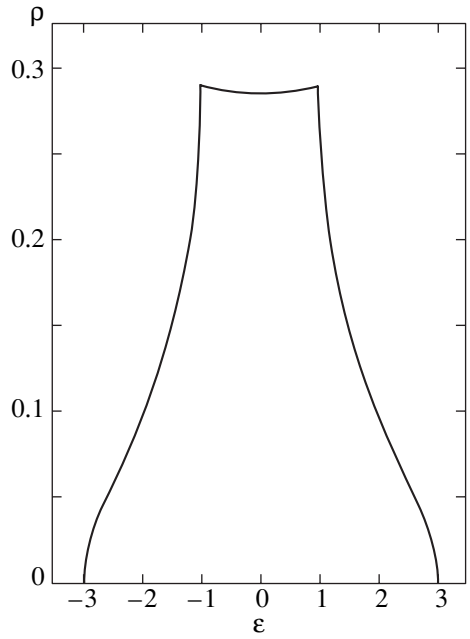

Fig. 4. Density of states of collectivized electrons in the cubic lattice.

we can derive the approximate formula for T_C for electron concentrations $n \sim 1$:

$$\frac{T_C}{W} = \frac{3\tilde{\mu}^2 \rho\left(\frac{6\tilde{\mu}}{1 - 0.5n}\right)}{(1 - 0.5n)^3 + 6\tilde{\mu}(1 - 0.5n)\rho\left(\frac{6\tilde{\mu}}{1 - 0.5n}\right)}. \tag{24}$$

Since $\tilde{\mu} \approx 1/4$ in the paramagnetic phase for $T \sim 0$ [16], it follows from relation (24) that $T_C/W \longrightarrow 0$ for $n \longrightarrow 1$. For $n \approx 0.9$, the ratio T_C/W is maximal and does not exceed a value of 0.045.

Figure 5 shows the result of numerical solution of system (23) in the form of the concentration dependence of T_C in units of W. It can be seen that the peak value of the ratio T_C/W corresponds to an electron concentration of $n \approx 0.85$ and amounts to $(T_C/W)_{\max} \approx 0.035$, which is 30% lower than the analogous value obtained in the dynamic molecular field (MF) method [17, 18]. The difference between the presented dependence and that obtained by the MF method is that the T_C peak is shifted in concentration n from half the band filling towards larger values of $n \approx 0.85$. If we assume that the bandwidth $W \sim 1$ eV in perovskite-type manganites, we can use the value of $(T_C/W)_{\max} \approx 0.035$ to obtain a rough estimate of $T_C \approx 400$ K for the present case. It is closer to the experimentally observed values of T_C than in an analogous case in the MF approximation. The values of T_C/W were calculated in the electron concentration range from $n = 0.2$ to $n = 0.98$, although the accuracy of the theory deteriorates upon a decrease

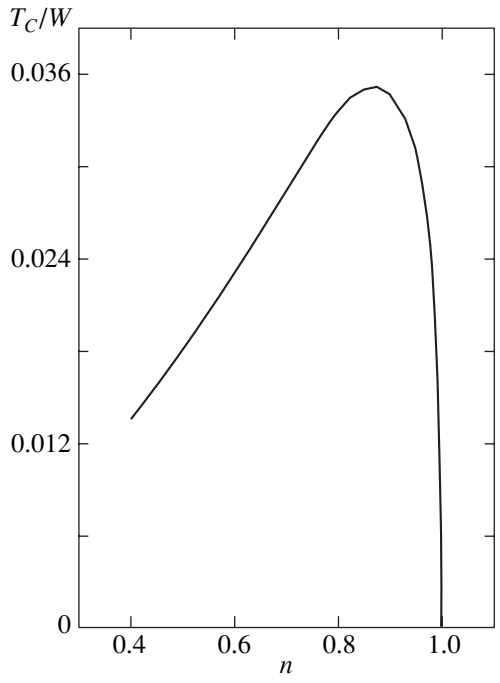

Fig. 5. Concentration dependence of temperature T_C (in units of W) of the ferromagnetic ordering of the electron subsystem.

in the electron concentration and the value of chemical potential since the initial Hamiltonian in the first approximation is proportional to μn and may be of the same order of magnitude as H_{int} for small μ and n.

Let us now consider the region of low temperatures, $T \ll W$. In order to determine the internal energy of the electron subsystem, we must take into account all one-loop contributions to Green's function $G^{0\sigma,\,\sigma 0}(i\omega_n, \mathbf{q})$. Carrying out the analytic continuation $G^{0\sigma,\,\sigma 0}(i\omega_n, \mathbf{q}) \longrightarrow G^{0\sigma,\,\sigma 0}(\omega + i\delta, \mathbf{q})$, we can easily find the spectral density $\Lambda^{\sigma}(\mathbf{q}, \omega)$:

$$\Lambda^{\sigma}(\mathbf{q}, \omega) = \frac{\beta\pi}{i}\{G^{0\sigma,\,\sigma 0}(\omega - i\delta, \mathbf{q}) - G^{0\sigma,\,\sigma 0}(\omega + i\delta, \mathbf{q})\}.$$

Then the internal energy of the electron subsystem is given by

$$E^{\text{el}} = \frac{1}{N}\sum_{\mathbf{q}\sigma}\int_{-\infty}^{\infty}\frac{d\omega}{2\pi}\frac{(\omega - \varepsilon_{\sigma})\Lambda^{\sigma}(\mathbf{q}, \omega)}{e^{\beta\omega} + 1}.$$

The exact Green function of the electron subsystem was investigated in [16]. It was proved that its contributions to the electron energy are different in different regions of concentration n and have a quite complicated structure. However, the case $n \sim 1$ is the simplest since it allows the application of $G^{0\sigma,\,\sigma 0}(i\omega_n, \mathbf{q})$ in the form

$$G^{0\sigma,\,\sigma 0}(i\omega_n, \mathbf{q}) = \frac{\langle F^{\sigma 0}\rangle}{\beta(i\omega_n - E_{\mathbf{q}\sigma})},$$

which implies that

$$E^{\text{el}} = \frac{1}{N}\sum_{\mathbf{q}\sigma} t_1(\mathbf{q})\, f(E_{\mathbf{q}\sigma})\langle F^{\sigma 0}\rangle^2. \tag{25}$$

The meaning of this formula is quite clear: $t_1(\mathbf{q})\langle F^{\sigma 0}\rangle$ is the excitation energy for an electron–hole pair, $f(E_{\mathbf{q}\sigma})$ is the Fermi distribution function, and $\langle F^{\sigma 0}\rangle$ is the probability of the electron–hole state with spin σ. We can write analytic expression (25) at low temperatures $T \ll W$ in the form

$$E^{\text{el}} = W\left\{\frac{1}{2}n(n-1) + \frac{\pi^2 T^2}{6W^2}\right\}, \tag{26}$$

where we assume that $\langle F^{+0}\rangle = 1$, $\langle F^{-0}\rangle = 0$.

Let us consider the case of zero temperature and determine the boundaries for the existence of the CS and FM phases. The total internal energy of the entire system is the sum of the free energy of the ion (13) and electron (26) subsystems at $T = 0$. We can easily find that

$$\begin{aligned} E_{\text{exch}} &= -S\tilde{H} \\ &+ \{J(\mathbf{k}_0)\sin^2\alpha + J(0)\cos^2\alpha\}\langle S\rangle^2, \end{aligned} \tag{27}$$

where $\tilde{H}$ is defined by formula (11). Differentiating Eq. (27) with respect to parameter $\langle S\rangle$, we obtain the following expression for the self-consistent mean spin:

$$\langle S\rangle = \frac{\sqrt{J^2(0)\cos^2\alpha + J^2(\mathbf{k}_0)\sin^2\alpha}}{J(0)\cos^2\alpha + J(\mathbf{k}_0)\sin^2\alpha}S. \tag{28}$$

It follows from this expression that $\langle S\rangle \geq S$. This is quite possible if we take into account electron dynamics. In any case, however, the value of $\langle S\rangle$ should not exceed $S + n/2$. The free energy attains its minimum for

$$\tan^2\alpha \geq \tan^2\alpha_{\text{cr}} = -\frac{1+d}{1-d}.$$

For $d > -1$, this inequality automatically holds. For $d < -1$, the slope of the sublattices $\alpha > \alpha_{\text{cr}}$. We will consider the range of parameter $d > -1$. Substituting relation (28) into (27) and taking into account expression (26) for the electron energy, we obtain the formula for the total energy E_{tot} of the indirect and double exchanges:

$$\frac{E_{\text{tot}}}{4J_1S^2} = E = 4b_0 d(2 + \cos\gamma) + \frac{1-d^2}{1-d+2d\cos^2\alpha}, \tag{29}$$

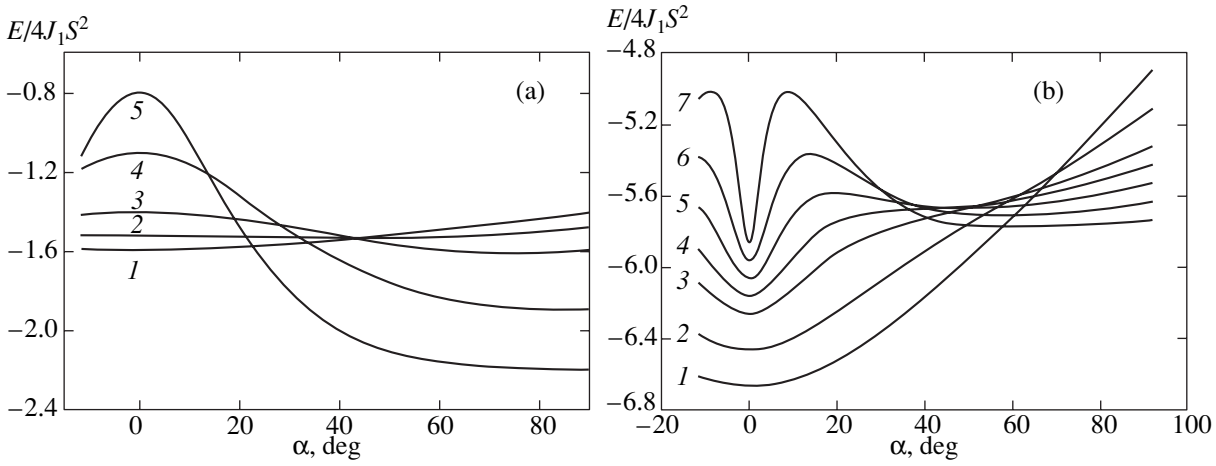

Fig. 6. Angular dependence of the free energy $E/4J_1S^2$ of the electron and ion subsystems for $n = 0.9$, $T = 0$, and the following values of parameters: (a) $b = 0.2$, $d = -0.01$, -0.08, -0.2, -0.5, and -0.8 (curves *1–5*, respectively); (b) $b = 1.92$, $d = -0.1$, -0.3, -0.5, -0.6, -0.7, -0.8, and -0.9 (curves *1–7*, respectively).

where

$$b_0 = \frac{tn(1-n)}{4|J_2|S^2}, \quad \cos\gamma = \frac{(1+d)\cos\alpha}{\sqrt{(1-d)^2 + 4d\cos^2\alpha}}.$$

Expression (29) for angles α close to $\pi/2$ gives an equilibrium angle for the canted structure, $\cos\alpha = b_0$, obtained by de Gennes [3] for $b_0 \ll 1$. Figure 6 shows the $E(\alpha)$curves for various values of d for fixed values of parameters $n = 0.9$ and $b = 4b_0|d| = 0.2$ and 1.92. It can be seen that for small values of b, an increase in d gradually transforms the system from the FM to the CS phase. For large values of b, there exists a region of coexistence of the CS and FM phases, in which the thermodynamic potential has two minima. In this case, various relaxation phenomena may take place due to thermally excited energy levels on the opposite banks of potential wells. Figure 7 shows the phase diagram in the b vs. d coordinates for $n = 0.9$. The solid phase-transition line was determined from the equality of energies at two minima of the thermodynamic potential. The metastability region of the FM phase can easily be determined knowing the second derivative $d^2E/d\alpha^2$ provided that it is positive at point $\alpha = 0$. It can easily be found that the solution $\cos\alpha = 1$ exists for $d > -1/7$. The coordinates of the bicritical point on the phase diagram are as follows: $d_{cr} = -1/7$, $b_{cr} = 3/7$. Above and below the solid phase-transition line, one minimum exists for the FM and CS structures, respectively. This region is typical of a second-order phase transition. Metastable phases emerge for $d < -1/7$. The metastability boundary for the FM phase is determined by the curve $b_0 = (1 + d)/(1 - d)$. The metastability boundary of the CS phase was determined numerically from the condition that the real roots of the equation $d^2E/d(\cos\gamma)^2 = 0$, which determine the positions of the maximum and minimum for the CS structure, vanish.

It should be noted that the presence of irreversibility effects in the present case is directly connected to the quantum origin of spin. The factor $(1 + d)/(1 - d)$ appearing in calculations is a direct consequence of the

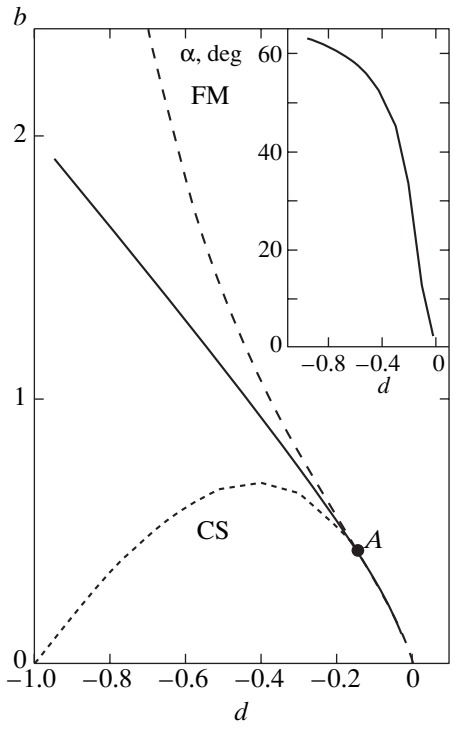

Fig. 7. Phase diagram of magnetic states of a weakly doped $LaMnO_3$-based system at $T = 0$. The solid curve is the phase-transition line; dashed curves correspond to the stability boundaries of the FM and CS structures. The coordinates of bicritical point A are $d_{cr} = -1/7$, $b_{cr} = 3/7$. The inset shows the dependence of the noncollinearity angle of ion magnetic moments on the parameter d in the CS phase on the phase-transition line at $T = 0$.

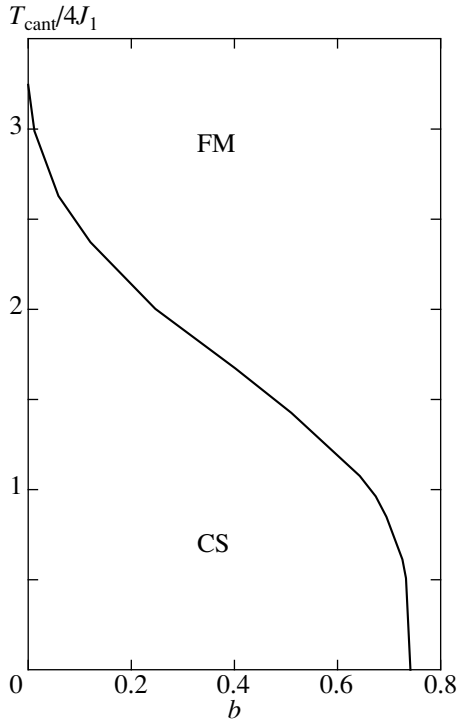

Fig. 8. Dependence of the temperature T_{cant} of phase transition to the CS state (in units of $4J_1$) on the parameter b for $d = -0.3$.

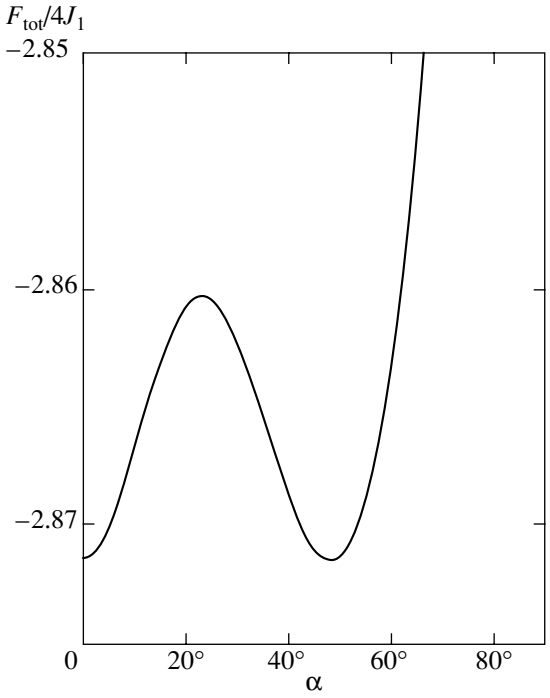

Fig. 9. Angular dependence of the total free energy for the values of parameters $T/4J_1 = 0.64$, $b = 0.72$, and $d = -0.3$.

unitary transformation of spin operators. This constitutes the main difference from the de Gennes theory, in which the spin is assumed to be classical. In our opinion, the inclusion of quantum properties of spin improves the agreement between the theory and experiments. In particular, the experimental temperature dependences of magnetization clearly exhibit irreversibility phenomena typical of potentials with numerous minima. The inset to Fig. 7 shows the dependence of the slope α of the sublattices on the parameter d on the line of phase transition from the FM to the CS structure at $T = 0$.

Let us consider the case of low temperatures $T \ll W$, such that the ratio T/J_1 is not small. The mean nodal spin is defined by the expression

$$\langle S \rangle = \frac{\sqrt{J^2(0)\cos^2\alpha + J^2(\mathbf{k}_0)\sin^2\alpha}}{J(0)\cos^2\alpha + J(\mathbf{k}_0)\sin^2\alpha} \times \frac{\sum_{m=-S}^{S} m\exp\left(-\frac{m\tilde{H}}{T}\right)}{\sum_{m=-S}^{S}\exp\left(-\frac{m\tilde{H}}{T}\right)}, \quad (30)$$

where $\tilde{H}$ has form (11). Figure 8 shows the dependence of temperature T_{cant} (in units of $4J_1$) of the phase transition from FM to CS structure on the parameter b for $d = -0.3$ and $n = 0.9$. The curve was determined from the equality of the total free energy at the minima corresponding to the FM and CS states. It can be seen from the figure that a decrease in the parameter b increases the temperature of formation of the canted structure, which approaches the Curie temperature for indirect exchange,

$$\frac{T_{MF}}{4J_1} = \frac{2}{3}S(S+1)(1-d),$$

in the molecular field approximation. Figure 9 shows the angular dependence of free energy F_{tot} of the electron and ion subsystem for $T/4J_1 = 0.64$, $b = 0.72$, and $d = -0.3$, which indicates that the FM ($\alpha = 0$) and CS ($\alpha = 48°$) phases are thermodynamically stable at this temperature. Obviously, the external magnetic field may change the ratio of the volumes occupied by the FM and CS phases by transferring part of the magnetic ions through the potential barrier. Relaxation phenomena associated with the existence of the potential barrier between two thermodynamically stable states can also be observed depending on the conditions of sample cooling.

4. DISCUSSION

In accordance with Fig. 1, the ZFC magnetization remains almost unchanged between 50 and 230 K, which is apparently due to magnetic-moment blocking

below T_C, when the sample is cooled in zero or very weak magnetic field. This complicates the motion of domain walls during magnetization and facilitates the manifestation of relaxation effects. The magnetic field helps domains to overcome "freezing" and rotates them so that they become aligned with the magnetic field, thus increasing magnetization. As a result, the ZFC and FC magnetizations in strong magnetic fields are in fact identical (see Fig. 2).

The changes in the ZFC and FC magnetizations observed at $T < 45$ K, viz., a decrease in the magnetization in weak magnetic fields ($H < 150$ Oe) and its increase for $H > 200$ Oe, indicate a change in the spin configuration.

The sign reversal in the change of magnetizations M_{ZFC} and M_{FC} (see Figs. 1 and 2) at $T < 45$ K cannot be explained within the model of phase separation into AFM and FM regions in manganites [7–9], which is very popular at present and according to which the CS structure is unstable to the formation of a ferro–antiferromagnetic (F–AF) state. However, certain other experimental evidence [10–12] does not fit the simple pattern of phase separation. It is important to note in this connection that Nagaev's theory is valid for an infinitely low hole concentration, which rules out a rigorous transition to the thermodynamic limit. The wave functions in [7] describe the dynamics of a single hole in the ion core matrix with the *A*-type magnetic structure.

We used here the statistical method based on the separation of the effective field, which does not specify the form of the wave function of a moving electron. It was found in the first approximation in the reciprocal effective radius of interaction that the energy associated with the electron dynamics in the noncollinear phase at $T = 0$ has form (26). It can easily be seen that, in the linear approximation in the hole concentration $1 - n$, the compressibility $k^{-1} = d^2E_{\rm el}/d(1-n)^2$ of the electron gas is positive. Consequently, the homogeneous CS structure may be stable, although the polaron state also cannot be excluded from the analysis. This is due to the fact that, in the linear approximation of perturbation theory, we cannot state with confidence that the compressibility of the electron gas is positive since all quadratic corrections in carrier concentration must be taken correctly into account. For this reason, we cannot confine our analysis to the linear order of perturbation theory alone. Unfortunately, an analysis of second-order diagrams in the reciprocal effective radius of interaction complicates the problem considerably and is beyond the scope of this paper.

In connection with this, it should be noted that a detailed analysis of inhomogeneous charge states and phase separation in manganites is given in [8]. It was proved, in particular, that $k^{-1} < 0$ for classical de Gennes canted structures. This circumstance was treated as a warning symptom questioning the stability of the CS state. It cannot be ruled out that localized electron states may exist against the background of the homogeneous noncollinear phase. These states lead to local spin distortions in the homogeneous magnetic structure with the formation of magnetic polarons. De Gennes [3] was the first to indicate the possibility of realization of such a complex structure for a layered antiferromagnet. In order to demonstrate that the polaron state in the AFM matrix and the homogeneous AFM state are close in energy in a certain temperature range, we consider the relation between the free energies for these phases at a temperature $T \ll T_C$.

In analogy to the results obtained in [8] for $T = 0$, we can write the expression for energy $E^{\rm el}$ taking into account the electron localization in a spherical polaron of radius R:

$$\frac{E_p^{\rm el}}{4J_1S^2} = 4b_0 d\left(3 - \frac{a^2\pi^2}{2R^2}\right). \tag{31}$$

In accordance with relation (29), we write $b_0 = pn(1-n)$, where $p = t/(4|J_2|S^2)$. In this way, we can take into account the energy loss in indirect exchange due to the formation of the polaron by introducing the effective field H_p:

$$\frac{H_p}{4J_1} = 2\langle S_p\rangle\left(1 - d + d(1-n)\frac{4\pi}{3}\left(\frac{R}{a}\right)^3\right), \tag{32}$$

where $\langle S_p\rangle$ is the mean spin taking into account polaron states, determined from Eq. (30), in which $\alpha = \pi/2$ and $\tilde{H} = H_p$. The expression for the free energy F_p (see formula (13)) of the inhomogeneous F–AF state can be written in the form

$$\frac{F_p}{4J_1S^2} = \frac{1}{4J_1S^2} \times\left\{E_p^{\rm el} - T\ln\left[\sum_{m=-S}^{S}\exp\left(-\frac{mH_p}{T}\right)\right]\right\} + \frac{1}{S^2}(1-d)\langle S\rangle^2. \tag{33}$$

Minimizing this expression in radius R, we obtain the self-consistent equation for determining the polaron radius R_p,

$$R_p = a\left(\frac{\pi pnS^2}{2\langle S_p\rangle^2}\right)^{1/5}, \tag{34}$$

which coincides with the analogous results obtained in [8] for $T = 0$. Comparing the energy (29) of the noncollinear phase in the limit $b_0 \ll 1$ and the energy (33) of the inhomogeneous F–AF phase at $T = 0$, we can easily find that phase separation occurs for

$$p \geq p_0 = \left(\frac{5}{6}\right)^{5/2}\frac{2\pi^4}{n} > 123.5,$$

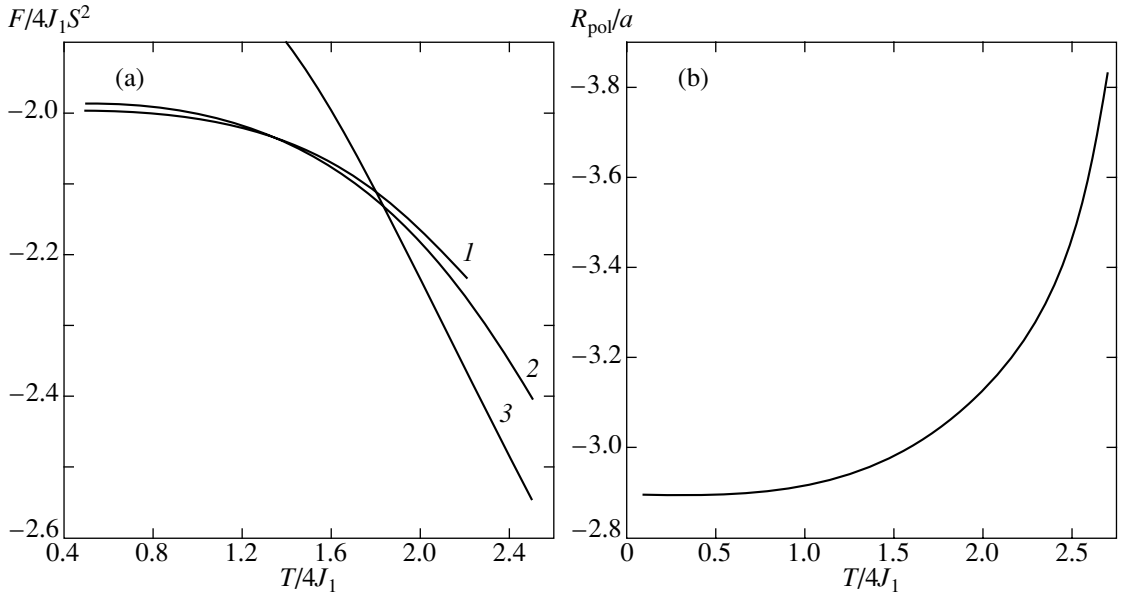

Fig. 10. Temperature dependences of (a) the free energies of the CS, F–AF, and FM phases (curves *1–3*, respectively) and (b) the spherical polaron radius in units of lattice constant a for the values of parameters $n = 0.998$, $p = 140$, and $d = -0.3$.

while the noncollinear phase is stable for $p < p_0$. The estimates of parameters for lanthanum manganite perovskites lead to a value of $p \sim 10$, which is an order of magnitude smaller than p_0.

For $T \neq 0$ and $p \sim p_0$, a transition from the stable CS structure to the AFM state with polaritons may occur upon an increase in temperature. Figure 10a shows the temperature dependences of the free energy F of the noncollinear inhomogeneous F–AF phase and the homogeneous FM phase (curves *1–3*, respectively) for $d = -0.3$, $n = 0.998$, $b_0 = 0.279$, and $p = 140$. The point of intersection of curves *1* and *3* corresponds to the temperature $T_{cant}/4J_1 = 1.8$ of the transition from the CS to the FM phase. It can be seen from Fig. 10a that the CS structure is stable for $T/4J_1 < 1.36$, while the AFM state with polaron subsequently transformed into the homogeneous FM state is realized for $1.36 < T/4J_1 < 1.8$. It should be noted that the energy difference between the CS and the F–AF phases is very small and does not exceed 0.8 K on account of the value of J_1 (see below). Figure 10b shows the temperature dependence of the spherical polaron radius in the unit of lattice constant a, which was obtained as a result of numerical solution of Eq. (34). It can be seen that the polaron radius increases with temperature. The critical value of R for which polarons overlap is equal to $4.92a$.

The observed singularities on the temperature dependences of magnetization can be explained on the basis of the following considerations. ZFC below $T_{cant} = 45$ K leads to the formation in the clusters of a canted structure which gives on the average zero contribution to the increment of magnetization in fields $H <$ 200 Oe in view of the random distribution of crystallographic axes. The clusters make a positive paramagnetic contribution to the total magnetization at $T > T_{cant}$, while at $T < T_{cant}$ this contribution vanishes since the emerging magnetic moments of the clusters are distributed chaotically and the total contribution is equal to zero. It can be stated that the application of a magnetic field $H \approx 200$ Oe disturbs the relation between the magnetic moment of the canted structure and the crystallographic direction of a crystallite. Thus, the thermodynamic behavior of the magnetic moment of a cluster is the same as that for a paramagnet. In magnetic field $H > 200$ Oe, at $T < 45$ K, a phase transition to the ordered state with the preferred direction along the external magnetic field is realized. The above differences in the jumps of M_{ZFC} and M_{FC} are associated with irreversibility effects as well as with the strong interaction between the spins of a cluster and the spin system of the host matrix. Indeed, at $T \sim T_C$, strong fluctuations in the host matrix are responsible for the long-range nature of spin correlations between the two subsystems. The cooling from temperatures $T \sim T_C$ at the phase-transition point $T = T_{cant}$ apparently leads to ferromagnetic ordering of spins in a cluster with the magnetization directed along the magnetic moment m of the host matrix, which results in a positive increment in the magnetization.

The observed experimental dependences $M(T, H)$ suggest the existence of regions with different magnetic orders at low temperatures: the major part of the sample is ordered ferromagnetically, while a small part is a canted spin structure with the FM interaction between the magnetic moments in clusters of manganese ions with difference valences.

In order to confirm this assumption, we give some estimates of microscopic parameters of interaction, which are obtained on the basis of the above theory. It

should be noted from the very outset that, in spite of the approximate nature of these estimates due to the absence of additional experimental data, they demonstrate qualitative agreement between the theory and experiments. Indeed, Fig. 5, depicting the concentration dependence of T_C/W, shows that the optimal concentration n corresponds to $T_C/W \approx 0.035$. For $T_C = 240$ K, we have $W \approx 6900$ K and $t = W/12 = 570$ K. The volume fraction of clusters is equal to 0.2, and the magnetization jump at $T = 45$ K is of the order of 15%. In this case, $0.15/0.2 \approx 0.7 = \cos\alpha$, whence $\alpha \approx 45°$. On the phase diagram in Fig. 7, the angle 45° (see also the inset to Fig. 7) corresponds to the coordinates $b = 0.72$ and $d = -0.3$. Using the experimental values of the indirect exchange parameters $J_1 = 9.6$ K and $J_2 = -6.7$ K for $LaMnO_3$ [20], we obtain $d = -0.35$, which matches the value 0.3 obtained above on the basis on the data on the magnetization jump and the volume fraction of clusters. For $b = 0.72$, we have $n(1 - n) \approx 0.05$; i.e., the hole concentration in the clusters is small. Let us take the experimental value of $d = -0.35$. On the phase diagram in Fig. 7, this value of d corresponds to $b = 0.8$. This leads to the ratio $T_{cant}/4J_1 = 0.7$, whence $T_{cant} \approx 27$ K, which corresponds to the experimental value of 45 K for our rough estimates. Taking into account the obtained values of parameters, we find that the potential barrier height is approximately equal to 0.9 K. Thus, irreversibility effects must disappear in fields above 7 kOe, which is confirmed by experiments. Using the values of parameters obtained, we can determine the temperature width of the phase transition over which the FM and CS structures coexist. According to estimates, this width is of the order of 10 K, which is in accordance with experiment (see Figs. 1 and 2).

5. CONCLUSIONS

We investigated theoretically and experimentally the features of magnetic behavior of a number of lanthanum manganite perovskites with an excess of manganese. An increase in the manganese content increases the magnetic transition temperature insignificantly. Samples with $x > 0.1$ exhibit an anomalous behavior of magnetization at low temperatures in addition to a transition from the paramagnetic to the ferromagnetic phase. At $T < 45$ K, the magnetization decreases in weak fields ($H < 150$ Oe) and increases in fields $H >$ 200 Oe. These anomalies in the magnetic behavior are most probably associated with a transition from the ferromagnetic phase to a canted phase in clusters containing manganese ions with different valences. This is due to the fact that the concentration of charge carriers in these clusters formed in the vicinity of vacancies in the cation sublattice is considerably lower than in the host matrix. A theoretical analysis indicates the possibility of competition between the double and superexchange interactions in clusters, which may facilitate the formation of a state with a canted magnetic sublattice in the low-temperature region. An analysis of the thermodynamic behavior of the weakly doped $LaMnO_3$-based subsystem, taking into account the quantum-mechanical properties of spin, revealed that relaxation effects may appear in the region of phase transition to the slanted state. These effects are determined, to a considerable extent, by the relation of the parameters of intra- and interplanar indirect exchange as well as by the energy of electron transport.

ACKNOWLEDGMENTS

The authors are grateful to V.N. Krivoruchko for a number of valuable remarks made during the discussion of this paper.

This study was partly supported by the KBN Poland (project no. 2PO3B13918).

REFERENCES

1. A. P. Ramírez, J. Phys.: Condens. Matter **9**, 8171 (1997).
2. J. M. D. Coey, M. Viret, and S. von Molnar, Adv. Phys. **48**, 167 (1999).
3. P.-G. de Gennes, Phys. Rev. **118**, 141 (1960).
4. V. P. Pashchenko, A. A. Shemyakov, V. K. Prokopenko, *et al.*, J. Magn. Magn. Mater. **220**, 52 (2000).
5. V. N. Krivoruchko, S. I. Khartsev, A. D. Prokhorov, *et al.*, J. Magn. Magn. Mater. **207**, 168 (1999).
6. V. Dyakonov, A. Prokhorov, V. Shapovalov, *et al.*, J. Phys.: Condens. Matter **13**, 4049 (2001).
7. E. L. Nagaev, Phys. Rev. B **60**, 455 (1999).
8. M. Yu. Kagan and K. I. Kugel', Usp. Fiz. Nauk **171**, 577 (2001) [Phys. Usp. **44**, 553 (2001)].
9. E. Dagotto, T. Hotta, and A. Moreo, Phys. Rep. **344**, 1 (2001).
10. K. N. Mikhalev, S. A. Lekomtsev, A. P. Gerashchenko, *et al.*, Pis'ma Zh. Éksp. Teor. Fiz. **72**, 867 (2000) [JETP Lett. **72**, 599 (2000)].
11. M. Muroi and R. Street, Aust. J. Phys. **52**, 205 (1999).
12. J. Geck, B. Büchner, M. Hücker, *et al.*, Phys. Rev. B **64**, 144 430 (2001).
13. V. P. Pashchenko, A. A. Andreev, A. A. Shemyakov, *et al.*, Neorg. Mater. **34**, 62 (1998).
14. P. W. Anderson and H. Hasegawa, Phys. Rev. **100**, 675 (1955).
15. É. E. Zubov, Fiz. Nizk. Temp. **19**, 274 (1993) [Low Temp. Phys. **19**, 193 (1993)].
16. É. E. Zubov, Teor. Mat. Fiz. **105**, 311 (1995).
17. A. Georges, G. Kotliar, W. Krauth, and M. J. Rozenberg, Rev. Mod. Phys. **68**, 13 (1996).
18. N. Furukawa, in *Proceedings of Conference on Physics of Manganites, Michigan State University, 1998;* cond-mat/9812066.
19. F. Moussa, M. Hennion, J. Rodríguez-Carvajal, *et al.*, Phys. Rev. B **54**, 15 149 (1996).

Translated by N. Wadhwa

Journal of Experimental and Theoretical Physics, Vol. 95, No. 6, 2002, pp. 1056–1061.
Translated from Zhurnal Éksperimental'noĭ i Teoreticheskoĭ Fiziki, Vol. 122, No. 6, 2002, pp. 1226–1232.

SOLIDS
Structure

Antiferromagnetic Spin Correlations in Palladium-Based Pd–Fe, Pd–Fe–Ag, and Pd–Fe–Rh Magnetic Alloys

N. N. Delyagin*, A. L. Erzinkyan, V. P. Parfenova, and S. I. Reyman

Skobel'tsyn Research Institute of Nuclear Physics, Moscow State University, Vorob'evy gory, Moscow, 119992 Russia
**e-mail: delyagin@srd.sinp.msu.ru*

Received May 30, 2002

Abstract—The magnetic structure of $Pd_{1-x}Fe_x$ (x = 0.03, 0.06, 0.10, 0.15, and 0.20) alloys is investigated using the method of ^{57}Fe-Mössbauer spectroscopy. The distribution functions $P(B_{hf})$ of hyperfine magnetic fields have a discrete structure defined by variations of the contribution to B_{hf} from the magnetic moment of the neighboring Fe atoms. The anomalies of intensities of components of the functions $P(B_{hf})$, which increase with the concentration of iron, are indicative of the instability of configurations with a large total spin and of the formation of local spin configurations with the antiferromagnetic orientation of magnetic moments. The probability of formation of such configurations is defined by the competition of the ferromagnetic Fe–Pd exchange interaction with the direct antiferromagnetic exchange between the nearest neighboring atoms of Fe. An Ag or Rh impurity effectively induces the process of spin flipping, which explains the anomalously strong effect of impurities on the magnetic ordering temperature. The results confirm the presence in Pd–Fe alloys of perturbations of long-range ferromagnetic order revealed by neutron diffraction. © *2002 MAIK "Nauka/Interperiodica".*

1. INTRODUCTION

Palladium-based Pd–Fe alloys represent a well-known system with "giant" magnetic moments. The ferromagnetic ordering of spins of Fe atoms in these alloys arises even in the case of an iron concentration of less than 1 at.%, with the mean magnetic moment per Fe atom exceeding $10\mu_B$. The universally accepted explanation for this phenomenon is based on a model according to which the emergence of ferromagnetism in dilute Pd–Fe alloys is due to the overlapping of extended "clouds" of polarized atoms of the palladium matrix. These alloys have been the subject of numerous investigations for several decades. The basic results of these investigations are summed up in the review by Nieuwenhuys [1]. In spite of significant progress made toward understanding the general pattern of this phenomenon, some important properties of Pd–Fe alloys (and of other systems with giant moments) remained unexplained. The greatest difficulties were associated with the problem of correct treatment of local effects, whose importance was emphasized by Nieuwenhuys [1]. As a rule, the magnetic susceptibility, which is a macroscopic parameter, was treated as the main factor defining the magnetic behavior of systems with giant moments. Within such an approach, it proved impossible to explain the diffusion of magnetic phase transitions, the anomalous effect of impurities on the Curie temperature, and other phenomena [1]. In early microscopic investigations performed using Mössbauer spectroscopy (see, for example, [2, 3]), only averaged characteristics were determined (for example, mean hyperfine magnetic fields); therefore, no information on local effects could be obtained.

The most intensive studies were performed on the nature of ferromagnetism arising in alloys with a low concentration of iron. Because the magnetic ordering temperature of Pd–Fe alloys increases monotonically with the concentration of iron, it was assumed that the mechanisms of exchange interaction remained qualitatively unchanged in a wide range of concentration (at least up to 20–30 at.% Fe) and that all of these alloys were systems with a simple (collinear) ferromagnetic alignment of magnetic moments. However, experimental data have become available recently that compel one to reconsider the traditional point of view on the mechanisms of exchange interaction in Pd–Fe alloys. Diffuse satellite reflections were revealed in the spectra of magnetic scattering of neutrons by single crystals of $Pd_{1-x}Fe_x$ (x = 0.10 and 0.15), whose presence is clearly indicative of significant violations of the long-range ferromagnetic order in these alloys [4, 5]. According to the authors of the latter papers, the investigated Pd–Fe alloys are characterized by the presence of antiferromagnetic interaction causing space-modulated variations in the mutual orientation of spins of Fe atoms. It is important that, according to Tsunoda and Abe [4], the antiferromagnetic exchange coupling between Fe atoms is realized at small interatomic distances. We have recently found an explanation for the strong effect of rhodium impurity on the Curie temperature of the ferromagnetic alloy $Pd_{0.9}Fe_{0.1}$ [6, 7]. As a result of investigation of the "fine structure" of distribution functions of hyperfine magnetic fields using Mössbauer

spectroscopy, it was found that rhodium impurity causes a reorientation of a part of magnetic moments of Fe atoms. This leads to the formation of local antiferromagnetic spin configurations, a decrease in effective exchange interaction, and an abrupt decrease in the magnetic ordering temperature. We assumed [6] that the antiferromagnetic exchange coupling between the nearest neighboring atoms of Fe was always present in Pd–Fe alloys; however, in the case of a low concentration of iron, this coupling does not show up because of predomination of strong ferromagnetic exchange interaction with the palladium matrix. The verification of this assumption is of fundamental importance from the standpoint of understanding the singular features of the behavior of systems with giant magnetic moments.

This paper contains the results of detailed investigation of the spin structure of Pd–Fe alloys, as well as of Pd–Fe–Ag and Pd–Fe–Rh alloys, using ^{57}Fe-Mössbauer spectroscopy. The main objective of the study was to verify the hypothesis of the presence of antiferromagnetic Fe–Fe exchange interaction in a wide range of the concentration of iron in Pd–Fe alloys, as well as to investigate the evolution of the spin structure of these alloys under the effect of two different types of impurities (Ag and Rh).

2. EXPERIMENT

$Pd_{1-x}Fe_x$ ($x = 0.03$, 0.06, 0.10, 0.15, and 0.20) alloys and $(Pd_{1-x}Fe_x)_{1-y}Ag_y$ and $(Pd_{1-x}Fe_x)_{1-y}Rh_y$ ($0.03 \le x \le 0.10$, $0.05 \le y \le 0.20$) alloys were prepared by fusing together 99.99% (or better) pure metals by arc melting in an argon atmosphere. The ingots were annealed at 1200 K and quenched. The powders prepared from the ingots for performing Mössbauer measurements were likewise annealed and quenched. We believe that such a thermal treatment ensures statistical distributions of atoms in these alloys. The Mössbauer absorption spectra were measured in the temperature range from 5 to 300 K. In order to increase the effect of resonant absorption and the resolution, resonant detectors were used for recording the Mössbauer radiation of ^{57}Fe with an energy of 14.4 keV. The magnetic ordering temperature was determined from the temperature dependences of hyperfine magnetic field and by thermal scanning.

The Mössbauer spectra were processed in two stages. First, the distribution functions $P(B_{hf})$ of hyperfine magnetic fields were calculated. These calculations were performed using the histogram method employed by us previously in the investigation of the fine structure of the functions $P(B_{hf})$ for Rh–Fe and Pd–Fe alloys [6–8]. For all alloys, the $P(B_{hf})$ distribution had a structure corresponding to a set of discrete spin configurations with well-defined values of hyperfine magnetic field (B_{hf}). Then, the spectra were approximated by the superposition of discrete magnetic subspectra. The number of subspectra required for correct approximation was not fixed but was determined during processing (as well as the intensity of the subspectra and the values of B_{hf}).

3. EXPERIMENTAL RESULTS AND DISCUSSION

Previously, the example of the $Pd_{0.9}Fe_{0.1}$ alloy was used to demonstrate [6, 7] that the structure of the distribution functions $P(B_{hf})$ is defined by the dependence of hyperfine magnetic field on the magnitude of the total magnetic moment that developed in the nearest environment of a given Fe atom by the neighboring magnetic Fe atoms. In this case, the hyperfine magnetic field on the site of the central Fe atom in a concrete spin configuration may be given by [6, 7]

$$B_{hf} = a\mu_{Fe} + bM\mu_{Fe}, \quad (1)$$

where a and b are constant coefficients; $M = n\uparrow - n\downarrow$ is the total magnetic moment of the nearest environment (in units of the magnetic moment of an Fe atom, μ_{Fe}); and $n\uparrow$ and $n\downarrow$ denote the number of neighboring Fe atoms with a spin parallel and antiparallel to the spin of the central atom. For the $Pd_{0.9}Fe_{0.1}$ alloy, the coefficients a and b were found to be $a = 8.4$ T/μ_B and $b = 0.3$ T/μ_B [6, 7]. Because the coefficients a and b are of the same sign, the hyperfine field is maximal for a purely ferromagnetic configuration, when $M = n\uparrow = n$ (where n is the total number of the nearest neighboring Fe atoms). If all spin configurations are fully ferromagnetic, the relative intensities of configurations with different values of M in the case of statistical distribution of Fe atoms in fcc-lattice sites must correspond to the binomial distribution $W(n) = C_{12}^n x^n (1 - x)^{12-n}$. The $P(B_{hf})$ distribution must include magnetic subspectra with an equidistant set of B_{hf} values; the difference between the values of B_{hf} for the neighboring subspectra ($\Delta M = \pm 1$) is $b\mu_{Fe}$. The change in the orientation of one of the spins to the opposite must cause a reduction of B_{hf} by $2b\mu_{Fe}$. As we will see below, these regularities following from the representation of a hyperfine magnetic field in the form of Eq. (1) agree well with the experimental results. Sections 3.1 and 3.2 below deal with the experimental data obtained at a temperature of 5 K, which corresponds to the ground state of the investigated systems. The magnetic ordering temperature is discussed in Section 3.3.

3.1. $Pd_{1-x}Fe_x$ *Alloys*

The $P(B_{hf})$ distribution functions for five $Pd_{1-x}Fe_x$ alloys are given in Fig. 1. One can see that the $P(B_{hf})$ distribution for all alloys has a well-defined discrete structure corresponding to spin configurations with different values of M. The experimentally found values of relative intensity of magnetic subspectra are given in Table 1. In Fig. 2, the measured relative intensities of

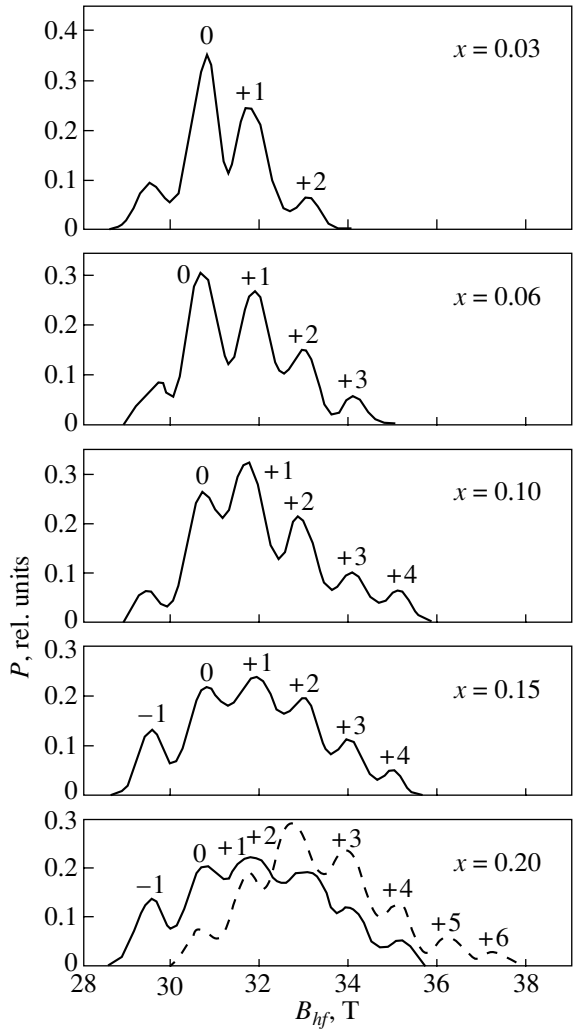

Fig. 1. The hyperfine magnetic field distribution functions $P(B_{hf})$ for $Pd_{1-x}Fe_x$ alloys at $T = 5$ K. For the $Pd_{0.80}Fe_{0.20}$ alloy (bottom graph), the dashed curve indicates the predicted distribution calculated for the case of ferromagnetic orientation of magnetic moments.

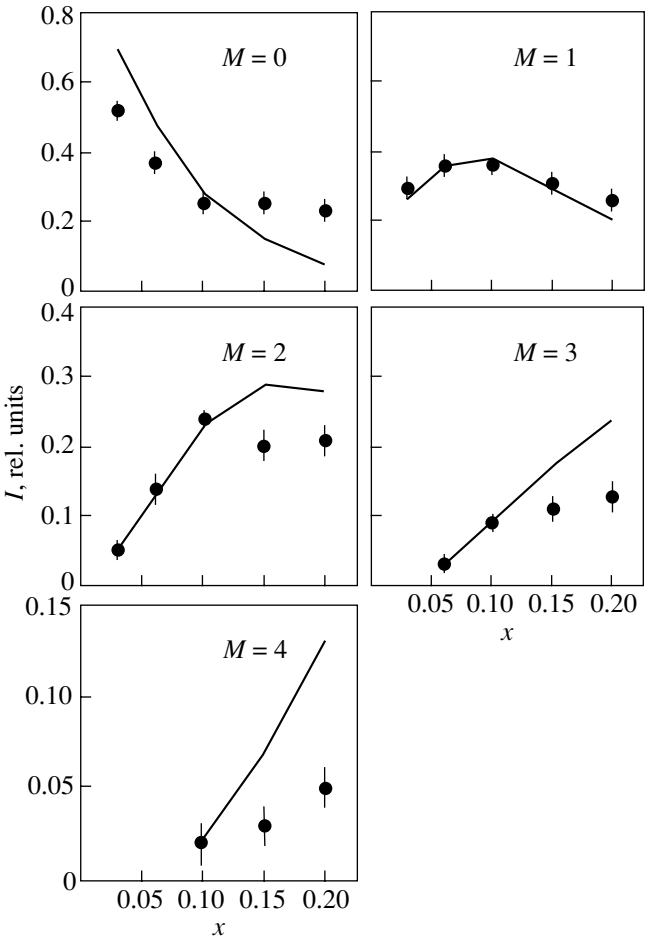

Fig. 2. The relative intensity of magnetic subspectra with $M = 0$, +1, +2, +3, and +4 as a function of the concentration of iron in $Pd_{1-x}Fe_x$ alloys at $T = 5$ K (symbols). The solid line indicates the relative intensity calculated for the case of ferromagnetic orientation of magnetic moments in configurations with n atoms of Fe in the nearest environment of the central atom (binomial distribution $W(n)$, $n = M$).

magnetic subspectra are compared with the results of calculation of these intensities for purely ferromagnetic spin configurations with a random (statistical) distribution of Fe atoms in fcc-lattice sites (binomial distribution).

Analysis of these results leads to the following conclusions.

(i) For alloys with $x = 0.03$ and 0.06, the measured values of the intensity of magnetic subspectra with $M = +1$, +2, and +3 agree well with the predicted values. This means that the configurations with other-than-zero total spin of the nearest environment are fully ferromagnetic, as is expected for alloys with a relatively low concentration of Fe atoms. Almost as good an agreement between the measured and predicted values of intensity is observed for an alloy with $x = 0.10$.

(ii) When the concentration of iron increases to $x = 0.15$ and 0.20, a strong difference arises between the measured and predicted values of the intensity of magnetic subspectra. One can see in Table 1 and Fig. 2 that, for these alloys, the measured values of the intensity of subspectra with $M = +2$, +3, and +4 turn out to be grossly underestimated, and no high-spin components with $M = +5$ and +6 are observed at all. In Fig. 1, the experimentally obtained $P(B_{hf})$ distribution for an alloy with $x = 0.20$ is compared with the distribution calculated for ferromagnetic alignment of spins in all configurations. One can see that high-spin components are completely absent from the experimentally obtained distribution, with the entire distribution shifted (relative to the predicted one) to the region of low hyperfine fields.

Table 1. Comparison of the relative intensity of magnetic subspectra with the predicted probability of formation of atomic configurations with n atoms of Fe in the nearest coordination sphere in $Pd_{1-x}Fe_x$ alloys

x	n		0	1	2	3	4	5	6
	$B_{hf}(T)$	<30.0	30.9	32.0	33.1	34.1	35.2	36.3	37.4
0.03	$W(n)$		0.69	0.26	0.05				
	I	0.14(3)	0.52(2)	0.29(3)	0.05(1)				
0.06	$W(n)$		0.48	0.36	0.13	0.03			
	I	0.10(3)	0.37(3)	0.36(3)	0.14(2)	0.03(1)			
0.10	$W(n)$		0.28	0.38	0.23	0.09	0.02		
	I	0.04(2)	0.25(3)	0.36(2)	0.24(1)	0.09(1)	0.02(1)		
0.15	$W(n)$		0.15	0.30	0.29	0.17	0.07	0.02	
	I	0.10(3)	0.25(3)	0.31(3)	0.20(2)	0.11(2)	0.03(1)	<0.01	
0.20	$W(n)$		0.07	0.21	0.28	0.24	0.13	0.05	0.02
	I	0.12(3)	0.23(3)	0.26(3)	0.21(2)	0.13(2)	0.05(1)	<0.01	<0.01

Note: The following notation is used in the table: I, measured relative intensity of a subspectrum; $W(n)$, predicted probability of configuration (binomial distribution); and B_{hf}, hyperfine magnetic field.

(iii) The behavior of a subspectrum with $M = 0$ differs significantly from the behavior of subspectra with nonzero spin of the nearest environment. In the case of a low concentration of iron ($x = 0.03$ and 0.06), the intensity of this subspectrum is much lower than the predicted value; on the contrary, in alloys with $x = 0.15$ and 0.20, this intensity is much higher than the predicted value.

These results confirm the existence of perturbations of long-range ferromagnetic order in a real magnetic structure of Pd–Fe alloys. Most characteristic is an abrupt decrease in the probability of the formation of high-spin configurations in alloys with $x = 0.15$ and 0.20 (compared to their predicted values for a fully ferromagnetic orientation of spins of Fe). This fact may be attributed to antiferromagnetic spin correlations whose importance rises rapidly with increasing concentration of iron. The direct antiferromagnetic exchange interaction between the nearest neighboring atoms of Fe in the lattice of Pd–Fe alloys must be regarded as the most natural reason for the emergence of such correlations. This interaction does not show up (or shows up to a small extent) in the case of a low concentration of iron when contribution by direct interaction between Fe atoms is small compared to the strong ferromagnetic exchange interaction of Fe atoms with the palladium matrix. As the concentration of pairs of interacting Fe–Fe atoms increases, the importance of antiferromagnetic correlations rises and the competition between two exchange interactions of opposite sign brings about a local violation of ferromagnetic ordering. In regions with a high local concentration of iron, the ferromagnetic alignment of spins becomes unstable. This explains the absence of high-spin components with $M = +5$ and +6 in the $P(B_{hf})$ distribution and the abrupt decrease in the intensity of components with $M = +2$, +3, and +4 (compared to the predicted values for purely ferromagnetic spin configurations). The transformation of ferromagnetic configurations to fully or partially antiferromagnetic ones proceeds with the parity of M unchanged. Therefore, an abrupt increase in the intensity of a subspectrum with $M = 0$ in alloys with $x = 0.15$ and 0.20 corresponds to anomalously low values of the intensity of subspectra with $M = +2$ and +4 (and to the complete destruction of a subspectrum with $M = +6$). The flipping of spins in configurations with odd values of M in these alloys leads, in particular, to the formation of a subspectrum with $M = -1$ ($B_{hf} \approx 29.8$ T).

Ferromagnetic spin configurations predominate in alloys with $x \le 0.10$; however, these alloys are not ideally ordered ferromagnets either. It follows from Table 1 that the intensity of a subspectrum with $M = 0$ for alloys with $x = 0.03$ and 0.06 is much less than the predicted value. For a low concentration of iron, this subspectrum corresponds to isolated Fe atoms which have no magnetic Fe atoms in their nearest environment. A decrease in the intensity of the subspectrum with $M = 0$ implies that some part of such isolated atoms turns out to be affected by a weakened exchange field. This results in a decrease in the average value of the atomic magnetic moment and in a corresponding decrease in the hyperfine field. This explains the emergence of a "satellite" component ($B_{hf} < 30$ T, see Table 1 and Fig. 1) in the $P(B_{hf})$ distribution. The intensity of this component decreases as the concentration of iron increases from $x = 0.03$ to $x = 0.10$.

3.2. $(Pd_{1-x}Fe_x)_{1-y}Ag_y$ *and* $(Pd_{1-x}Fe_x)_{1-y}Rh_y$ *Alloys*

The effect of Ag and Rh impurities on the spin structure was investigated for alloys with an iron concentration of $x = 0.03$ and 0.06. This effect was qualitatively similar

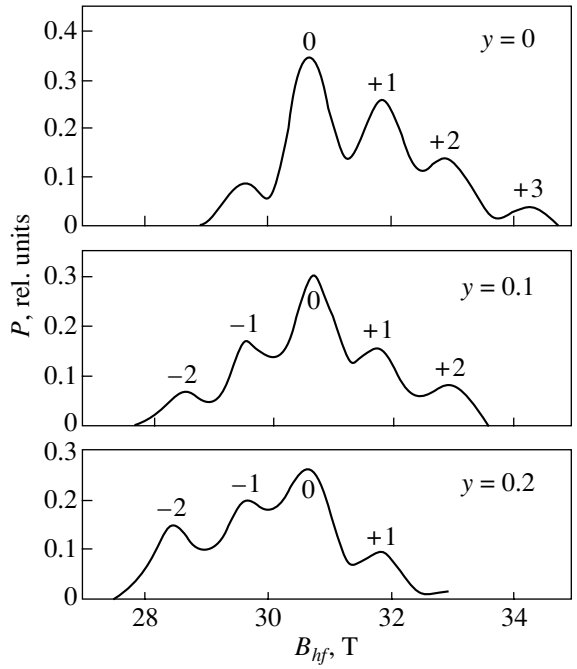

Fig. 3. The hyperfine magnetic field distribution functions $P(B_{hf})$ for $(Pd_{0.94}Fe_{0.06})_{1-y}Rh_y$ alloys.

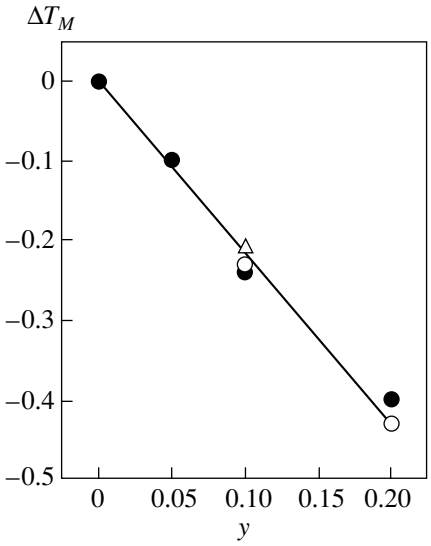

Fig. 4. The relative variation of the magnetic ordering temperature $\Delta T_M(y) = (T_M(y) - T_M(0))/T_M(0)$ as a function of rhodium concentration for $(Pd_{1-x}Fe_x)_{1-y}Rh_y$ alloys at x = 0.03 (hollow triangle), 0.06 (solid dots), 0.10 (hollow dots).

to that found previously for the $(Pd_{0.90}Fe_{0.10})_{1-y}Rh_y$ (y = 0.10, 0.20, and 0.30) alloys [6, 7]. Given in Fig. 3 by way of example are the $P(B_{hf})$ distribution functions for $(Pd_{0.94}Fe_{0.06})_{1-y}Rh_y$ (y = 0, 0.1, and 0.2). (For alloys with an Ag impurity, an analogous dependence of the structure of functions $P(B_{hf})$ on the concentration of the impurity was observed.) One can see that the impurity effectively destroys the ferromagnetic structure of the alloys and causes the formation of antiferromagnetic configurations (subspectra with M = –1 and –2) and an overall shift of distribution to the region of low hyperfine fields. This process develops very rapidly and, with an impurity concentration of y = 0.20, the intensity of subspectra with positive values of M becomes very low. The substitution of Pd atoms by atoms of Rh or Ag causes a weakening of the matrix polarization and shifts the balance of competing exchange interactions in favor of direct antiferromagnetic Fe–Fe exchange, which develops conditions for the formation of local spin configurations of the antiferromagnetic type. Even with an impurity concentration of y = 0.10, alloys cannot be regarded as ferromagnetic, because the intensities of ferro- and antiferromagnetic spin configurations become comparable. The magnetic structure of such alloys may be qualitatively interpreted using the model of collinear spin glass, which was previously treated for a Rh–Fe–Pd system [7].

3.3. Magnetic Ordering Temperature

The measured values of magnetic ordering temperature (T_M) for all investigated alloys are given in Table 2. Ag and Rh impurities cause a very strong reduction of T_M of alloys, which is naturally attributed to the destruction of the ferromagnetic spin structure accompanied by a decrease in the mean electron polarization and effective exchange fields. The spin flipping and random distribution of Fe atoms in lattice sites result in the emergence of a strong spatial nonuniformity of exchange interaction, which, in turn, entails the observed blurring of magnetic transition (increasing with the impurity concentration) [1, 7]. We cannot offer a quantitative explanation of the observed dependences of T_M on composition; however, we will give our atten-

Table 2. The magnetic ordering temperature T_M (in K) of $(Pd_{1-x}Fe_x)_{1-y}Ag_y$ and $(Pd_{1-x}Fe_x)_{1-y}Rh_y$ alloys

		Ag			Rh		
y	0.00	0.05	0.10	0.20	0.05	0.10	0.20
$Pd_{0.97}Fe_{0.03}$	105(2)		72(2)			83(2)	
$Pd_{0.94}Fe_{0.06}$	176(2)	144(2)	129(2)	115(3)	159(2)	133(2)	105(4)
$Pd_{0.90}Fe_{0.10}$	246(1)					190(2)	140(4)

tion to a remarkable feature of the behavior of T_M for $(Pd_{1-x}Fe_x)_{1-y}Rh_y$ alloys. Figure 4 gives the dependence of relative variation of T_M, $(T_M(y) - T_M(0))/T_M(0)$, on the rhodium concentration. One can see that this dependence is linear and is the same for all alloys (regardless of the iron concentration). It is obvious that such a behavior of T_M reflects some important features of the mechanisms of magnetic ordering in a system with competing exchange interactions. In view of this, a further study into the effect of various impurities on T_M may be of great interest. It appears to be most desirable to develop a theory of systems with giant moments that would take into account the direct antiferromagnetic exchange coupling between magnetic centers.

4. CONCLUSIONS

The results of detailed investigation of the distribution functions of hyperfine magnetic fields and local spin configurations have demonstrated that the magnetic behavior of $Pd_{1-x}Fe_x$ ($0.03 \le x \le 0.20$) alloys is largely determined by the competition of ferromagnetic Fe–Pd exchange interaction with the direct antiferromagnetic exchange between the nearest neighboring atoms of Fe. The antiferromagnetic exchange has little effect on the spin structure of dilute alloys, but it becomes very significant as the concentration of iron increases. For alloys with $x = 0.15$ and 0.20, the spin configurations with antiferromagnetic orientation of spins of Fe represent a significant fraction of all spin configurations of the system. The experimental data obtained by us (as well as the results of studying the neutron diffraction spectra [4, 5]) lead us to conclude that nominally ferromagnetic Pd–Fe alloys should not be treated as simple ferromagnets with exchange interaction of a single type. For detailed analysis of the magnetic properties of these alloys, one must take into consideration the presence of antiferromagnetic spin correlations due to direct antiferromagnetic Fe–Fe exchange. The presence of antiferromagnetic Fe–Fe exchange shows up clearly in the observed evolution of the spin structure of Pd–Fe alloys under the effect of impurities.

It is interesting to compare the revealed special features of the magnetic behavior of Pd–Fe alloys with the well-known properties of Pd–Mn magnetic alloys [9]. In the case of a low concentration of manganese, Pd–Mn alloys are ferromagnetic; however, at a concentration of above 4 at. % Mn, a transition to the state of spin glass is observed. It is well known that this transition is caused by direct antiferromagnetic Mn–Mn exchange [9]. One can assume that the behavior of two systems of alloys, Pd–Fe and Mn–Fe, is qualitatively similar; however, the balance between competing exchange interactions in Pd–Mn alloys is strongly biased in favor of direct antiferromagnetic exchange between magnetic centers. This may be caused both by a stronger antiferromagnetic Mn–Mn interaction (compared to the similar Fe–Fe interaction) and by a weaker polarization of the palladium matrix in Pd–Mn alloys.

ACKNOWLEDGMENTS

This study was supported financially by INTAS (grant no. 00-00195).

REFERENCES

1. G. J. Nieuwenhuys, Adv. Phys. **24**, 515 (1975).
2. R. A. Levy, J. J. Burton, D. I. Paul, and J. I. Budnick, Phys. Rev. B **9**, 1085 (1974).
3. E. R. Domb, D. J. Sellmyer, T. M. Quick, and R. J. Borg, Phys. Rev. B **17**, 2233 (1978).
4. Y. Tsunoda and R. Abe, Phys. Rev. B **55**, 11 507 (1997).
5. R. Abe, Y. Tsunoda, M. Nishi, and K. Kakurai, J. Phys.: Condens. Matter **10**, L79 (1998).
6. A. L. Erzinkyan, N. N. Delyagin, V. P. Parfenova, and S. I. Reyman, J. Magn. Magn. Mater. **231**, L20 (2001).
7. V. P. Parfenova, A. L. Erzinkyan, N. N. Delyagin, and S. I. Reyman, Phys. Status Solidi B **228**, 731 (2001).
8. V. P. Parfenova, N. N. Delyagin, A. L. Erzinkyan, and S. I. Reĭman, Fiz. Tverd. Tela (St. Petersburg) **42**, 1425 (2000) [Phys. Solid State **42**, 1465 (2000)].
9. T. Tsunoda, A. Harigae, J. L. Robertson, and M. L. Crow, Phys. Rev. B **62**, 9511 (2000).

Translated by H. Bronstein

Journal of Experimental and Theoretical Physics, Vol. 95, No. 6, 2002, pp. 1062–1073.
Translated from Zhurnal Éksperimental'noĭ i Teoreticheskoĭ Fiziki, Vol. 122, No. 6, 2002, pp. 1233–1246.

SOLIDS
Structure

Interlayer Interaction in a Fe/Cr/Fe System: Dependence on the Thickness of the Chrome Interlayer and on Temperature

S. O. Demokritov[a], A. B. Drovosekov[b], N. M. Kreines[b], H. Nembach[a], M. Rickart[a], and D. I. Kholin[a, *]

[a]*Universität Kaiserslautern, Kaiserslautern, 67653 Germany*
[b]*Kapitza Institute for Physical Problems, Russian Academy of Sciences, ul. Kosygina 2, Moscow, 117334 Russia*
**e-mail: kholin@kapitza.ras.ru*

Received June 22, 2002

Abstract—A three-layer sample of Fe(100 Å)/Cr(0–20 Å)/Fe(100 Å) is used to study the dependence of interlayer exchange on the thickness of the chrome interlayer and on temperature. The method of Kerr magnetometry in the temperature range from 77 to 473 K and the method of Brillouin scattering of light by spin waves at room temperature are used. The data for magnetization curves and spin wave spectra are treated in the model of biquadratic exchange. The range of validity of this model is established, which is apparently determined by interlayer exchange. The resultant dependence of the constant of bilinear interaction on the interlayer thickness demonstrates an oscillating behavior with two oscillation periods of about 3 and 18 Å. Within the experimental error, the magnitude of this constant, the amplitude, and the period and phase of its oscillation are independent of temperature. It is found that the constant of biquadratic exchange decreases in inverse proportion to the chrome thickness, the proportionality factor decreasing linearly as the temperature rises. In order to interpret the observed singularities in the behavior of the biquadratic exchange constant, a theoretical model is suggested which includes the nonideality of the interface and the presence of magnetic hardness in the chrome interlayer. This rigidity exceeds in magnitude the interaction on the interface between iron and chrome. The suggested model gives an adequate qualitative description of the experimental results. © *2002 MAIK "Nauka/Interperiodica".*

1. INTRODUCTION

The investigation of interlayer interaction between ferromagnetic layers via a nonferromagnetic interlayer in multilayer metal structures (superlattices) remains urgent as before. This interaction is treated in a large number of experimental and theoretical studies. The results of those studies were described in a number of review papers (see, for example, [1–6]). At present, it has been found that, in the case of rather thin (from several to tens of angstroms) interlayers, this interaction brings about magnetic ordering of a multilayer structure. Depending on the interlayer thickness, ferromagnetic or antiferromagnetic ordering of magnetic moments of neighboring ferromagnetic layers may be realized. Noncollinear magnetic ordering is observed in many structures; i.e., an angle other than zero or π is observed between the moments of neighboring ferromagnetic layers. In the majority of cases, all of the magnetic structures identified above are described relatively well within the theory of biquadratic exchange, with the interaction energy represented in the form of the sum of two contributions, namely, a contribution which is bilinear with respect to the magnetizations of neighboring layers and describes the regular (Heisenberg) exchange with the interaction constant J_1 and a contribution which is biquadratic with respect to these magnetizations with the constant J_2,

$$\begin{aligned} E_{BQ} &= J_1(\mathbf{m}_1 \cdot \mathbf{m}_2) + J_2(\mathbf{m}_1 \cdot \mathbf{m}_2)^2 \\ &= J_1\cos\theta + J_2\cos^2\theta. \end{aligned} \quad (1)$$

Here, $\mathbf{m}_1$ and $\mathbf{m}_2$ are unit vectors directed along the magnetizations of ferromagnetic layers and θ is the angle between them. Depending on the sign of J_1, the first term in formula (1) describes the ferromagnetic or antiferromagnetic ordering of the superlattice. When the constant J_2 is positive, the second term has a minimum at $\theta = 90°$ and, therefore, the combination of two contributions may, generally speaking, produce an arbitrary angle θ; i.e., it brings about noncollinear magnetic ordering in a multilayer structure.

As was experimentally demonstrated in a number of studies, the dependence of bilinear exchange on the thickness of the chrome interlayer is oscillating and includes two harmonics with periods of 3 and 18 Å [5]. This behavior of interlayer interaction finds a theoretical explanation within the framework of models based on the RKKY theory [6–8] and that treat the interaction of localized magnetic moments of iron as proceeding via the conduction electrons of chrome.

For interpreting the effect of noncollinear magnetic ordering in the structures being treated, a number of authors suggested that the models of indirect exchange via conduction electrons should include higher order

corrections leading to the emergence of additional terms in the effective energy of interlayer interaction [9]. However, the estimation of the magnitude of these corrections produces values of the constant J_2 that are two orders lower than the actually observed values.

In view of this, the so-called extrinsic models of emergence of noncollinear ordering are treated, i.e., models which either include the roughness of the interlayer boundaries (the fluctuation model of [10] and magneto-dipole mechanism of [11]) or presume the presence of magnetic impurities within the nonmagnetic interlayer (the loose spin model [12]). The above-identified models bring about a biquadratic (over the magnetic moments of iron layers) addition in expression (1); the value of the constant J_2 may, in principle, turn out to be fairly high.

Of special interest are systems in which the nonferromagnetic interlayer exhibits an antiferromagnetic structure of its own. First of all, this applies to Fe/Cr/Fe and Fe/Mn/Fe systems. In order to explain the emergence of noncollinear magnetic ordering in such superlattices, Slonczewski [13] proposed the mechanism of "magnetic proximity" (or "torsion" model) allowing for the presence of intrinsic magnetic hardness in the interlayer. He obtained a form of the energy of interaction between the neighboring layers of ferromagnetic material in a superstructure, which was different from the model of biquadratic exchange,

$$E_{\text{Sloncz}} = C_1\theta^2 + C_2(\theta - \pi)^2. \quad (2)$$

Here, θ is the angle between the magnetizations of neighboring ferromagnetic layers, and C_1 and C_2 are phenomenological constants. Schreyer *et al*. [14] used this model to describe the experimental data obtained by the method of neutron scattering in a Fe/Cr superlattice, and Pierce *et al*. [15] used it to describe the properties of a three-layer Fe/Mn/Fe system.

For the same class of objects, as an alternative to the model of biquadratic exchange, Levchenko *et al*. [16] point to the possibility of emergence in a sample of a peculiar domain structure in the presence of fairly large, atomically smooth regions on the interface. Unfortunately, the results of Levchenko *et al*. [16] are presented in a form which makes difficult their comparison with the available experimental data.

In what follows, we will restrict ourselves to treating the data pertaining to a Fe/Cr system.

This system has already been under investigation for two decades, and it is in this system that such effects as antiferromagnetic and noncollinear magnetic ordering and giant magnetoresistance were observed for the first time. Nevertheless, by virtue of the complexity of the electronic and magnetic structure of chrome, the question of the mechanism of interlayer exchange through the chrome interlayer remains open. Intensive experimental and theoretical investigations of this system are being continued.

The pattern of the magnetic structure of the chrome interlayer as a function of the interlayer thickness and of the temperature in Fe/Cr superlattices was studied experimentally, in particular, using neutron scattering (for more detail, see [5, 17]), and theoretically [18, 19]. The experimentally obtained phase diagram of chrome in a superlattice differs essentially from the respective phase diagram of bulk chrome. It contains two lines of characteristic temperatures and an additional region which, according to Schreyer *et al.* [17], corresponds to the presence of a long-range magnetic order with a commensurable wave of spin density. Men'shov and Tugushev [19] proposed a mechanism predicting the formation of a short-range antiferromagnetic order with a spin density wave in chrome in the vicinity of the Fe/Cr interface. Men'shov and Tugushev [19] demonstrated that the redistribution of the discharge (and, as a consequence, spin) density in the neighborhood of the interface between the layers in the case of low values of the interlayer thickness causes instability of the paramagnetic phase at temperatures significantly exceeding the Neel temperature for bulk chrome. Men'shov and Tugushev [19] further used this approach to interpret noncollinear magnetic ordering observed in superstructures of the type of Fe/Cr/Fe [20]. They made a microscopic substantiation of the model of "biquadratic exchange" and specified the restrictions of its range of validity with respect to the interlayer thickness, the temperature, and the degree of roughness of the interface between layers.

The results of investigations of Fe/Cr superlattices by different methods demonstrate that, in quite a number of cases, the model of biquadratic exchange given by Eq. (1) adequately describes the available experimental data [2, 4]. Nevertheless, a number of authors interpret the results obtained using the model of "magnetic proximity" given by Eq. (2) [5, 17].

We have previously investigated ferromagnetic-resonance spectra and magnetization curves of a series of $[Fe/Cr]_n$ superlattices at room temperature [21, 22]. The experimentally obtained data for samples with the chrome interlayer thickness within 7.7–14 Å could be adequately described within the model of biquadratic exchange. However, the absolute values of the constant J_2 (for one and the same value of the chrome interlayer thickness), obtained in different studies (including our work) as a result of treatment of experimental data using Eq. (1), differ considerably from one another. The reasons for such divergence are discussed in numerous papers (in maximum detail in [5, 23]) and are associated with the microscopic difference in the structural characteristics of the samples being investigated. For the choice of the model of interlayer interaction to be better justified, it appeared useful to experimentally investigate its temperature dependence. This problem was raised in a number of studies performed on three-layer samples of Fe/Cr/Fe using different experimental techniques. In [24, 25], the method of ferromagnetic

resonance was used; in [26, 27], the method of Brillouin scattering of light and the magnetooptical Kerr effect; and in [28], a vibrating-coil magnetometer. The experimental data obtained were used to determine the temperature dependences either of the saturation fields H_S [25, 28] or of the exchange constants J_1 and J_2 [24, 26, 27] obtained using the model of biquadratic exchange.

The results of studies into the temperature dependence of interlayer interaction obtained by us, which involved the use of the method of ferromagnetic resonance in two $[Fe/Cr]_n$ superlattices with chrome interlayers 10 and 11 Å thick in a wide temperature range from 400 to 2 K, were given in [29, 30]. It has been demonstrated that the model of biquadratic exchange describes well the resonance spectra of the investigated lattices in the investigated temperature range.

In all of the studies referred to above, the obtained temperature dependences of saturation fields or of exchange constants for both three-layer and multilayer samples pertain only to several concrete values of the chrome interlayer thickness. Such limited data prevent one from making sufficiently reliable inferences about the validity of various theoretical models. Moreover, an added complication consists in the difficulty of ensuring the same quality of the interfaces for different samples.

Much more complete information may be obtained by studying the dependences of interlayer interaction on the intermediate layer thickness and on the temperature in a three-layer sample with a wedge-shaped chrome interlayer. In this case, by using the magnetooptical investigation methods, one can perform measurements in one and the same sample while continuously varying the interlayer thickness t_{Cr}. In doing so, in addition to obtaining information about the temperature dependence of biquadratic exchange, it is possible to study the temperature dependence of the phase and amplitude of the oscillation of biquadratic exchange. To the best of our knowledge, no such systematic investigations of the temperature dependence of interlayer interaction $J_1(t_{Cr})$ and $J_2(t_{Cr})$ were performed heretofore.

The object of our investigation was a three-layer sample of Fe/Cr/Fe with a wedge-shaped chrome interlayer. For this sample, the Kerr magnetometry was used to investigate the magnetization curves for different values of interlayer thickness at different temperatures. On the same sample, spectra of Brillouin scattering of light by magnetic excitations were taken at room temperature for different values of chrome thickness. The obtained dependences were discussed in detail within different theoretical concepts. The treatment of the experimental data within the model of biquadratic exchange resulted in revealing the range of validity of this model. In order to interpret the obtained dependences of the constant of biquadratic interaction on the chrome interlayer thickness and on temperature, a model is suggested which takes into account the presence of magnetic ordering in chrome and the roughness of the interlayer boundary.

2. SAMPLE AND MEASUREMENT PROCEDURE

We studied a three-layer sample of Fe(100 Å)/Cr(0–22 Å)/Fe(100 Å) with a wedge-shaped chrome interlayer whose thickness varied from zero to 22 Å over a length of 10 mm. The sample was grown by molecular-beam epitaxy. The substrate was provided by an MgO plate 10×10 mm in size and oriented in the (100) plane, onto which was deposited a thin (10 Å) seeding film of iron followed by a buffer layer of silver 1500 Å thick. The sample was grown at a substrate temperature of 200°C. The [001] crystallographic axis of the iron and chrome films coincided with a normal to the sample plane. The single-crystal type and orientation of the resultant structure were monitored by the method of low-energy electron diffraction (LEED).

In the thus grown sample, measurements were performed of magnetization curves in the temperature range from 77 to 473 K and of spectra of Brillouin scattering of light by heat spin waves at room temperature.

The magnetization curves were measured using the magnetooptical Kerr effect. Magnetic field was applied in the sample plane. At room temperature, the meridional Kerr effect was used; i.e., the magnetic field lay in the plane of incidence of light (for more detail about the classification of magnetooptical effects, see [31, 32]). At temperatures above and below room temperature, the configuration of the experimental apparatus enabled one to use only a much weaker equatorial Kerr effect. As a result, the precision of measurement of magnetization curves at room temperature was appreciably higher than at other temperatures. A light beam was focused on the sample surface in a spot of approximately 0.3 mm. The magnetic field varied in the range from –4 to 4 kOe. The magnetization curves were taken in succession at points spaced 0.1 mm from one another over the wedge length, this corresponding to a step of variation of the chrome interlayer thickness of about 0.2 Å. After scanning along the entire sample was completed, the temperature was varied and measurements at the new temperature were performed. This procedure was used to measure series of hysteresis curves for seven values of temperature, namely, 77, 127, 175, 226, 276, 373, and 473 K.

Given in Fig. 1 in the form of a three-dimensional diagram is the set of all magnetization curves measured in the chrome thickness–magnetic field–relative magnetization coordinates, the latter coordinate being M/M_S, where M_S is the saturation magnetization. The figure shows the presence of regions with both ferromagnetic and nonferromagnetic ordering and the oscillation of the saturation field with the variation of the interlayer thickness.

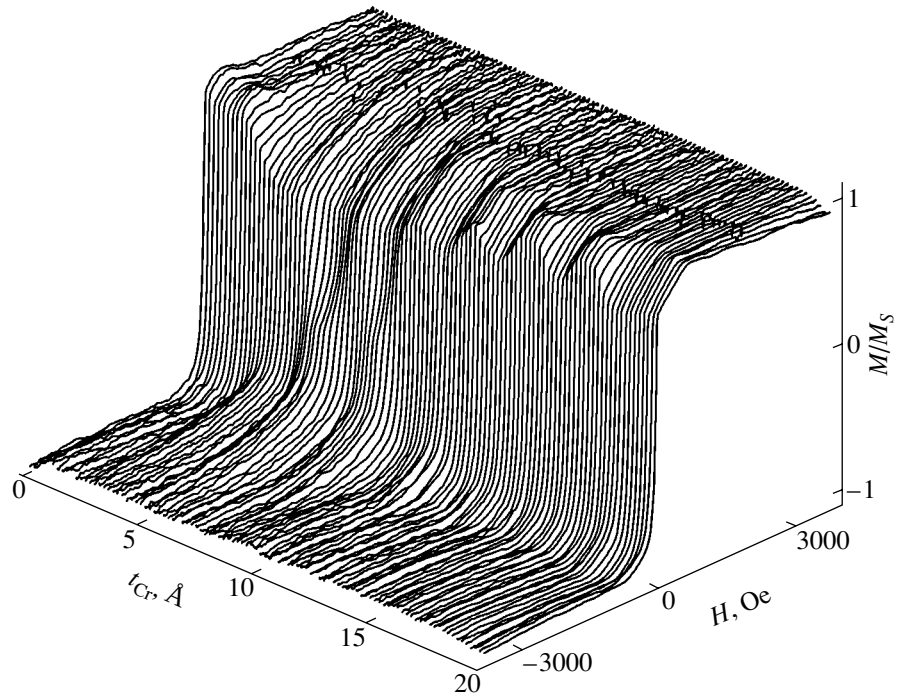

Fig. 1. A series of hysteresis loops recorded at room temperature for different values of the chrome interlayer thickness.

The Brillouin scattering of light by heat spin waves was investigated at room temperature using a spectrometer incorporating a high-contrast multipass tandem Fabry–Perot interferometer [33]. The light source was provided by an argon laser (wavelength, 514.5 nm; operating power, 300 mW). The measurements were performed in a backscattering configuration. A light beam was focused on the sample in a spot of approximately 0.1 mm in diameter. The angle of incidence was 50°, which corresponded to a wave vector of magnons being investigated of 1.57×10^5 cm^{-1}. The incident beam polarization lay in the plane of incidence, while the observation of scattered light was performed in cross polarization. Magnetic field was applied in the sample plane normally to the plane of light incidence. The Brillouin spectra were taken in succession at points spaced 0.2 mm from one another, this corresponding to a step of 0.4 Å over the chrome interlayer thickness.

Examples of experimental records of spectra for an interlayer thickness of t_{Cr} = 8.3 Å are given in Fig. 2. Plotted on the horizontal axis on the graph is the frequency shift of scattered light, and on the vertical axis, the scattering intensity (number of photons per channel for the time of signal accumulation, which amounted to approximately 20 min). The exhibited curves were obtained at one and the same point of the sample for three values of magnetic field specified in the graph. In each record, the arrows indicate the positions of two lines of Brillouin scattering corresponding to the optical and acoustic modes of spin waves of the system being investigated. The dependence of the spin-wave

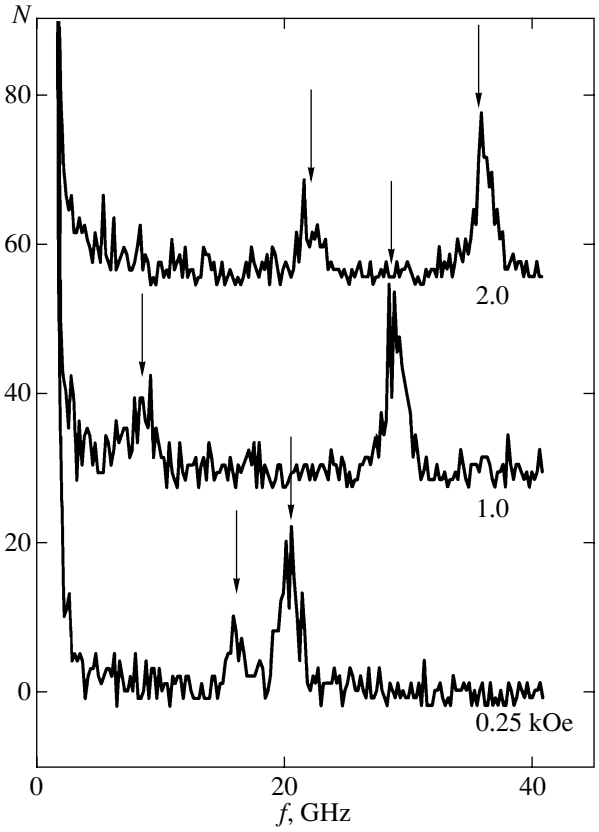

Fig. 2. Examples of experimental records of Brillouin spectra for a chrome interlayer thickness of 8.3 Å. The arrows indicate the positions of two lines of Brillouin scattering.

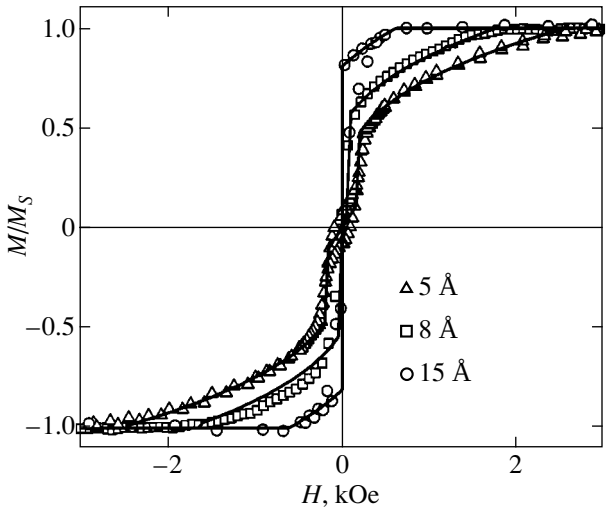

Fig. 3. Examples of records of hysteresis loops for three values of the chrome interlayer thickness, taken at room temperature. The points indicate the experimental data. The continuous lines indicate the results of calculation using the model of biquadratic exchange.

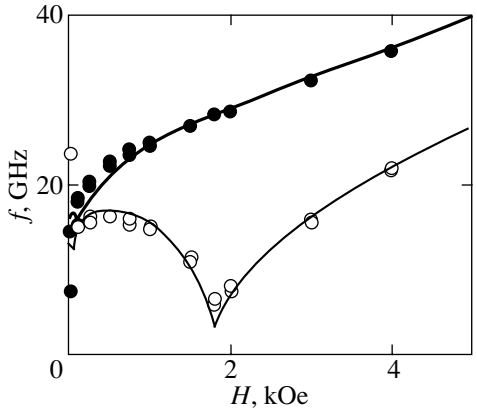

Fig. 4. The frequency shift of scattered light as a function of magnetic field for t_{Cr} = 8 Å at room temperature. The dots indicate the experimental data: solid dots, acoustic mode of spin waves; hollow dots, optical mode of spin waves. The continuous lines indicate the results of calculation using the model of biquadratic exchange.

frequency on magnetic field is given in Fig. 4 and will be discussed below.

3. EXPERIMENTAL RESULTS AND THEIR DISCUSSION

3.1. Choice of Model

The authors of a large number of papers devoted to the investigation of Fe/Cr/Fe multilayers managed to interpret the obtained experimental data within the framework of the model of biquadratic exchange given by Eq. (1) [4, 5, 23, 34, 35]. In particular, in [21, 22] this model made possible a successful description of the magnetization curves and spectra of ferromagnetic resonance of $[Fe/Cr]_n$ superlattices. In view of this, we will analyze our experimental data using, first of all, the model of biquadratic exchange.

Shown in Fig. 3 are three hysteresis loops obtained for different values of the chrome interlayer thickness. The measurements were performed at room temperature in a magnetic field applied along the four-fold hard magnetization axis in iron. One can see in the figure that the experimentally obtained curves demonstrate significantly different values of the saturation fields and residual magnetization. Solid curves plotted in the same graph are the results of calculation of magnetization curves in the model of biquadratic exchange.

In the calculation, the energy of a three-layer Fe/Cr/Fe sample per unit area was written in the following form:

$$\begin{aligned} E &= -d\mathbf{H}\cdot(\mathbf{M}_1+\mathbf{M}_2) + \frac{J_1}{M_S^2}\mathbf{M}_1\cdot\mathbf{M}_2 \\ &+ \frac{J_2}{M_S^4}(\mathbf{M}_1\cdot\mathbf{M}_2)^2 + d\frac{K_{\text{eff}}}{2}[(\mathbf{M}_1\cdot\mathbf{z})^2+(\mathbf{M}_2\cdot\mathbf{z})^2] \\ &- d\frac{H_a}{4M_S^3}[(\mathbf{M}_1\cdot\mathbf{x})^4+(\mathbf{M}_1\cdot\mathbf{y})^4+(\mathbf{M}_1\cdot\mathbf{z})^4 \\ &+ (\mathbf{M}_2\cdot\mathbf{x})^4+(\mathbf{M}_2\cdot\mathbf{z})^4+(\mathbf{M}_2\cdot\mathbf{y})^4], \end{aligned} \tag{3}$$

where J_1 and J_2 are the constants of bilinear and biquadratic exchange; $\mathbf{M}_1$ and $\mathbf{M}_2$ denote the magnetization of iron layers; d is the thickness of iron films; K_{eff} is the effective coefficient of uniaxial anisotropy, which includes a demagnetizing field and surface anisotropy of iron films; and H_a is the four-fold anisotropy field with easy magnetization axes **x**, **y**, and **z** (the **z** axis is perpendicular to the sample plane). In order to construct a magnetization curve, the energy given by Eq. (3) was numerically minimized in the directions of magnetizations $\mathbf{M}_1$ and $\mathbf{M}_2$ in the presence of external magnetic field **H**. The constants J_1 and J_2 were selected such as to reach the best fit with the experimentally obtained magnetization curves. For determining H_a, we also used magnetization curves measured along the easy axis of anisotropy of iron. The obtained value of H_a = 500 Oe corresponds to the known value of cubic anisotropy of bulk iron. Figure 3 demonstrates that the magnetization curves obtained in our sample may be quite successfully described within the model of biquadratic exchange in a fairly large range of chrome thickness.

Figure 4 gives a spin wave spectrum measured for the interlayer thickness t_{Cr} = 8 Å. The spectrum consists of two vibration branches, namely, optical (solid dots) and acoustic (hollow dots). The solid curves in the graph indicate the results of calculation of the spectrum of spin waves of a three-layer Fe/Cr/Fe system in the model of biquadratic exchange. In calculating the spec-

trum, the equilibrium orientation of the magnetic moments of iron was determined, as in the case of calculation of the magnetization curves, by way of numerical minimization of the energy given by Eq. (3). After this, the magnetic excitation frequency was calculated using the formulas derived by Rezende *et al.* [35]. The data in Fig. 4 correspond to the same interlayer thickness as the middle magnetization curve in Fig. 3 (shown by hollow squares). In calculating the magnetization curve and the spectrum, the same values of J_1 and J_2 were used, which were determined from the experimentally obtained magnetization curve. The calculated curves are in excellent agreement with experiment, and this further supports the view that the model of biquadratic exchange is suitable for describing both the static and dynamic properties of the system being investigated.

Schreyer *et al.* [14, 17] used Slonczewski's model of "magnetic proximity" given by Eq. (2) to describe their experimental results. In view of this, note the following. The magnetization curves calculated using the model of "magnetic proximity" reach saturation asymptotically, whereas our experimental curves have, as a rule, a well-defined saturation point. Nevertheless, because of the shape of these curves, it is not always that one can give preference to some or other model. The decisive argument in favor of the model of biquadratic exchange is the form of spin wave spectra. The calculation of these spectra using the model of "magnetic proximity" for a three-layer sample was performed by Chirita *et al.* [36]. A qualitative difference exists in the behavior of the optical mode for these two mechanisms. In the model given by Eq. (1), the frequency of the optical mode exhibits a clearly defined minimum in the saturation field, which corresponds well to our experimental data (see Fig. 4). In the model given by Eq. (2), the frequency of this mode increases monotonically with the magnetic field, which is obviously inconsistent with our data.

Therefore, the model of biquadratic exchange in the majority of cases enables one to adequately describe both the magnetization curves and the magnon spectra for our sample. However, a more detailed analysis reveals that, for certain values of the chrome interlayer thickness, this model gives significant deviations from experiment. This may be demonstrated very clearly if we construct magnetization curves in the H/M, M^2 coordinates. In the case where the behavior of the system corresponds to the model of biquadratic exchange, the magnetization curve before saturation must be described by the equation

$$H = AM + BM^3, \tag{4}$$

where

$$A = \frac{4J_1 - 8J_2}{dM_S^2} - \frac{H_a}{M_S}, \quad B = \frac{16J_2}{dM_S^4} - 2\frac{H_a}{M_S^3}$$

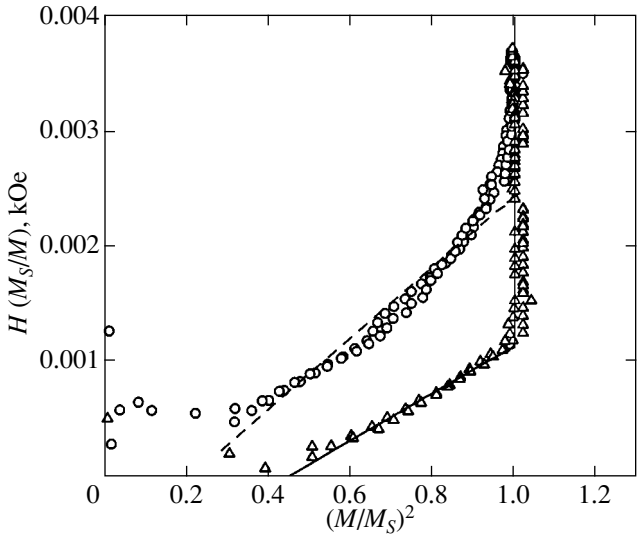

Fig. 5. Magnetization curves in Arrott coordinates for two values of the chrome interlayer thickness (hollow dots, 5.7 Å; hollow triangles, 11.6 Å). The continuous and dashed curves indicate the results of calculation using the model of biquadratic exchange.

(it is assumed that the field is applied along the hard magnetization axis of anisotropy of iron) [22]. In the H/M, M^2 coordinates (this construction is also referred to as the Arrott plot), this region must appear as a straight line segment reaching saturation values behind the kink. Given in Fig. 5 are two magnetization curves measured for chrome interlayers of different thicknesses. The first curve (triangles) has a clearly defined linear segment, with the prediction graph being in good agreement with experiment (broken solid line). The second curve (circles) has no linear segment; therefore, it is poorly described by the model of biquadratic exchange. The fitting of this curve using the model of biquadratic exchange (broken dashed line), suggested in Fig. 5, is rather subjective.

Figure 6 gives the dependence of the quantity $J_2 + 2J_2$ on the interlayer thickness t_{Cr}, obtained from the magnetization curves and from the spin wave spectra at room temperature. It is this combination of exchange constants that defines the saturation field H_S of the multilayer structure and is related to this field, in the case of a field applied along the hard magnetization axis, as [22]

$$H_S = 4(J_1 + 2J_2)/dM_S + H_a. \tag{5}$$

The hollow dots in the graph indicate the data obtained from the Brillouin spectra. Unfortunately, for most of the values of the interlayer thickness, these spectra were measured much less thoroughly than is demonstrated in Fig. 4; therefore, in treating the spectra, the region of magnetic fields above the saturation field of the multilayer structure was primarily involved. This fact will be of importance in what follows.

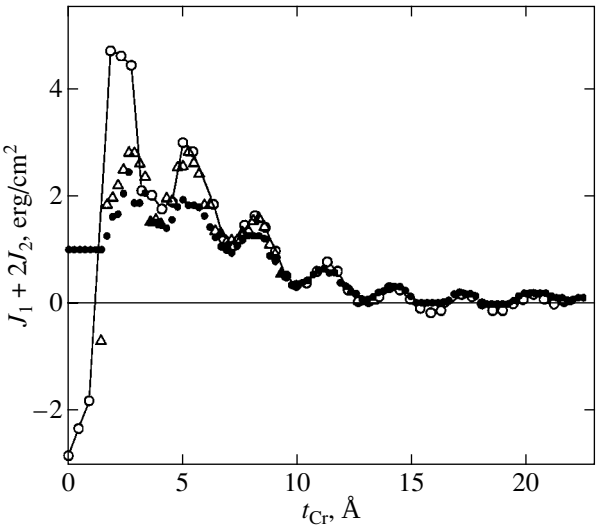

Fig. 6. The total exchange $J_1 + 2J_2$ as a function of the thickness of the chrome interlayer: hollow dots, data obtained by the method of Brillouin scattering of light; solid dots and hollow triangles, data obtained from the magnetization curves.

The solid dots and hollow triangles indicate the data obtained from the magnetization curves, and the difference between them consists in the following. As was already mentioned, for some values of the chrome layer thickness, the magnetization curves were poorly described by the model of biquadratic exchange. In these cases, the procedure of extracting exchange constants from these curves is ambiguous, if at all legitimate. Such curves (Fig. 5, hollow dots) were treated by two methods. The first method consisted in trying to best describe the magnetization curve using the model of biquadratic exchange, i.e., identify in the Arrott plot a segment which may be regarded as linear and use this particular region in fitting (dashed curve in Fig. 5). The use of this procedure produced the data shown in Fig. 6 by solid dots. The second, much more objective, method of treatment consisted in extracting the combination of exchange constants $J_1 + 2J_2$ with the aid of formula (5), using only the real value of the saturation field for the given curve, i.e., the point at which the difference of the sample magnetization from saturation magnetization becomes indistinguishable from noise. This method was used to obtain the data shown in Fig. 6 by hollow triangles. If the model of biquadratic exchange was valid for all values of the interlayer thickness, the solid dots and hollow triangles in Fig. 6 would have coincided. The difference between them, though qualitative, is a fairly clear indicator of the deviation of the system behavior from that predicted by the model of biquadratic exchange.

Of great importance is the comparison of the value of exchange obtained by the method of Brillouin scattering of light (hollow dots) with the values obtained from the magnetization curves. Given a chrome thickness in excess of approximately 8 Å, the treatment of magnetization curves and spin wave spectra produces one and the same result (the exception is provided by regions with a negative value of total exchange, where the magnetization curves are purely ferromagnetic and give no way of determining the true value of interlayer interaction). The model of biquadratic exchange offers excellent agreement with experiment for these values of chrome thickness. In the case of a smaller thickness of interlayers (the values of $t_{Cr} < 2.5$ Å are omitted from treatment, because it is most probable that so thin a layer of chrome is not continuous), the Brillouin data faithfully reproduce the curve obtained from Kerr measurements by the second method, i.e., using only the value of the saturation field (hollow triangles). This coincidence is observed even in the case where the magnetization curves have an "irregular" shape and the solid dots in Fig. 6 deviate significantly from the hollow dots and triangles.

One can fairly easily explain the agreement between the values of $J_1 + 2J_2$ obtained by the method of Brillouin scattering of light and from the saturation field of magnetization curves. As was already mentioned, the points above the saturation field of the structure were of first importance in treating the spectra. In this case, the spin wave frequencies depend on the form of the first terms in the expansion of the energy of interaction between two layers of iron in the vicinity of the value $\theta = 0$ of the angle between magnetizations. The same local form of the interaction energy defines the instant of complete collapse of magnetizations of iron layers. For any recording of the interlayer interaction energy, its behavior in the vicinity of $\theta = 0$ will be defined by a single parameter which is the same for the magnetization curves and for the spin wave spectra. Agreement between the data obtained from the Brillouin spectra and from the value of the static saturation field (Fig. 6) is indicative only of the fact that the deviation of the magnetization curves from the shape predicted by the model of biquadratic exchange is not a result of the nonuniform behavior of the sample on scales smaller than the light spot diameter, or of any other imperfection of the measurement procedure.

It is of importance that the range of validity of the model of biquadratic exchange in our case is restricted by the value of interlayer exchange rather than by the chrome interlayer thickness. One can see in Fig. 6 that the model is hardly valid in the vicinity of the maxima of the saturation field, at a value of total exchange $J_1 + 2J_2 \gtrsim 1.5$ erg/cm^2. In the vicinity of the minima of the saturation field, even for values of thickness of less than 5 Å, the model becomes valid again.

3.2. Dependence of the Interlayer Interaction Constants on the Interlayer Thickness

Figure 7 shows the constants J_1 and J_2 as functions of the chrome interlayer thickness t_{Cr} at room tempera-

ture. Our data on Brillouin scattering of light proved to be insufficient for reliable division of interlayer exchange into bilinear and biquadratic; therefore, the values of exchange given in Fig. 7 were derived from the magnetization curves. The points for which the model of biquadratic exchange produced poor agreement with experiment are indicated in the graph by rhombs instead of dots, and the division of exchange into J_1 and J_2 for these points is rather conventional. Nevertheless, the remaining data prove to be quite sufficient for describing the basic regularities of the behavior of exchange constants depending on the interlayer thickness.

It is known that the RKKY theory in the case of chrome predicts at least two oscillation periods in the dependence of bilinear exchange J_1 on the interlayer thickness, namely, short-wave oscillations with a period of about two monolayers and long-wave oscillations with a period of the order of ten monolayers. In this case, the long-wave oscillation amplitude decays in inverse proportion to the square of interlayer thickness, as in the case of free electrons, and the short-wave oscillation amplitude decays simply in proportion to the inverse thickness because of the nesting effect [5, 8, 9]. So, the formula for J_1 in the RKKY theory is given by an expression such as

$$J_1 = J_1^{(1)}\frac{\sin(q_1 t_{\mathrm{Cr}} + \varphi_1)}{t_{\mathrm{Cr}}} + J_1^{(2)}\frac{\sin(q_2 t_{\mathrm{Cr}} + \varphi_2)}{t_{\mathrm{Cr}}^2}, \quad (6)$$

where q_1 and q_2 define the short and long periods of exchange oscillations, φ_1 and φ_2 are the phases, and $J_1^{(1)}$ and $J_1^{(2)}$ are the amplitudes of these oscillations.

The solid curve in Fig. 7 is a result of fitting the experimentally obtained dependence $J_1(t_{\mathrm{Cr}})$ by a two-period function of the form of (6) and is described by the equation

$$J_1(t_{\mathrm{Cr}}) = 1.36\sin\left(2\pi\frac{t_{\mathrm{Cr}}}{2.9} + 1.5\right)/t_{\mathrm{Cr}}^{0.94} + 6\sin\left(2\pi\frac{t_{\mathrm{Cr}}}{19} - 0.9\right)/t_{\mathrm{Cr}}^{1.25}, \quad (7)$$

where the energy constants are taken to be measured in erg/cm^2, and the thickness, in ångströms. So, the bilinear exchange has two oscillation periods, namely, 2.9 and 19 Å, which corresponds well to the existing concepts [5].

It is more interesting to discuss the damping rate of the exchange oscillations. As was already mentioned, the RKKY model predicts the $1/t_{\mathrm{Cr}}$ dependence for the short-wave oscillation amplitude; this corresponds, with the accuracy available to us, to our result of $1/t_{\mathrm{Cr}}^{0.94}$. As to the long-wave oscillation amplitude, the $1/t_{\mathrm{Cr}}^{1.25}$ dependence obtained by us does not correspond to the predicted dependence $1/t_{\mathrm{Cr}}^2$. This result, however, can hardly be regarded as reliable, because our thickness range covers only one long-wave period.

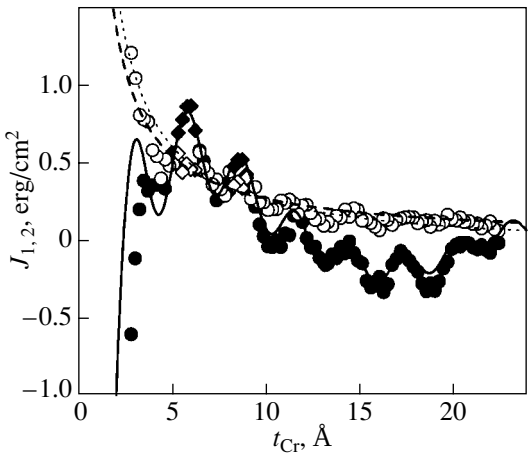

Fig. 7. The constants J_1 (solid dots) and J_2 (hollow dots) as functions of the thickness of chrome interlayer. The curves indicate the calculation results.

One must say a few words about the exchange oscillation phase. The technology of sample growing prevented us from exactly determining the position of the initial point of the wedge-shaped chrome interlayer. This causes an error of 1–2 Å in determining the absolute value of interlayer thickness at each point. Therefore, it does not appear possible to compare the short-wave oscillation phase with, for example, the results of [23]. The wedge gradient was monitored with an accuracy of at least 95%, this leading to an error of 1 Å or less for a thickness of 20 Å.

We will now describe the dependence of the constant of biquadratic exchange on the interlayer thickness. The fluctuation model of [10] takes into account the nonideality of the Fe–Cr interface. In view of the presence of fast oscillation of the sign of exchange integral, the interface roughness causes competition between the ferromagnetic and antiferromagnetic states; as a result, noncollinear ordering arises in a multilayer structure, which is described by the biquadratic term in the interaction energy equation (1), with the constant of biquadratic interaction defined by the expression

$$J_2 = \frac{4L(\Delta J_1)^2}{\pi^3 A}\coth\frac{\pi D}{L}, \quad (8)$$

where A is the exchange hardness of a ferromagnetic layer of thickness D and L is the width of steps on the interface. In accordance with formula (6), the amplitude of short-wave oscillation J_1 decreases in inverse proportion to the interlayer thickness; so, the biquadratic interaction in this model decreases with thickness as $1/t_{\mathrm{Cr}}^2$.

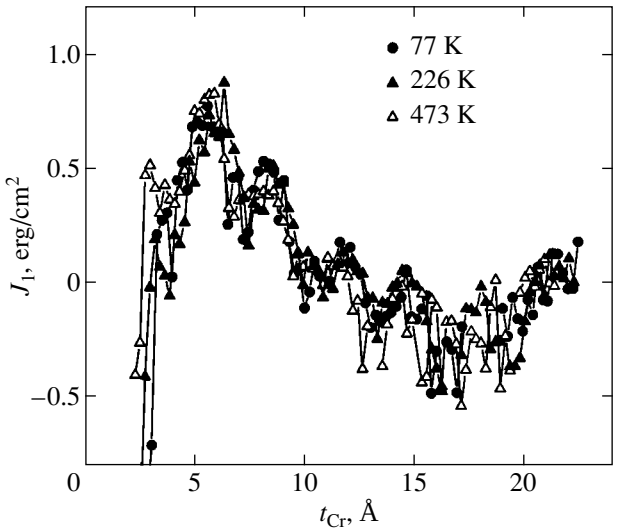

Fig. 8. Bilinear exchange as a function of interlayer thickness for three values of temperature. The data were obtained from the magnetization curves.

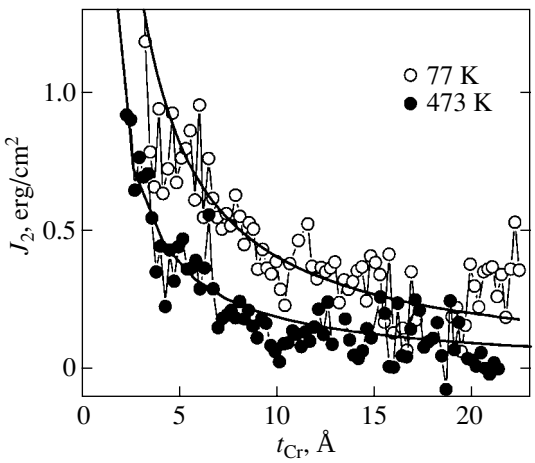

Fig. 9. Biquadratic exchange as a function of interlayer thickness for two values of temperature. The data were obtained from the magnetization curves.

The approximation of experimentally obtained curve $J_2(t_{Cr})$ at room temperature by a power function of the form A/t_{Cr}^{α} gives the exponent $\alpha = 1.2 \pm 0.2$. This is significantly closer to the inverse proportionality than to the dependence $1/t_{Cr}^2$ predicted by the fluctuation model. The dashed curve in Fig. 7 is a result of fitting the experimentally obtained curve of $J_2(t_{Cr})$ to a function of the form A/t_{Cr} and is described by the equation

$$J_2(t_{Cr}) = 2.7/t_{Cr} \qquad (9)$$

with the same units of measurements as in formula (7).

The dotted curve in Fig. 7 indicates the result of fitting of the dependence $J_2(t_{Cr})$ within the model of [12]. We do not give the appropriate formulas for the reason of their awkwardness. One can see in the figure that this model enables one to quite successfully describe the dependence of the constant of biquadratic exchange on the interlayer thickness. However, the required value of the energy of interaction between impurity spins and ferromagnetic layers must amount to approximately 1000 K, and the related oscillation amplitude of bilinear exchange must be three orders of magnitude higher than the experimentally observed value. This difference causes doubts in the validity of the loose spin model of [12] in our case.

3.3. Temperature Dependence of Interaction Constants

Figure 8 gives the dependences $J_1(t_{Cr})$ for three different temperatures. One can see that, within our error, the value of the constant of bilinear exchange does not vary with temperature. In spite of the wide scatter of experimental data, one can maintain that the phase and period of oscillation of $J_1(t_{Cr})$ are independent of temperature.

The weak temperature dependence of bilinear exchange may be readily understood within the RKKY model. According to this theory [8], the temperature dependence of the constant J_1 has the form

$$J_1(T) = J_1(0)\frac{T/T_0}{\sinh(T/T_0)}. \qquad (10)$$

In this formula, the characteristic temperature T_0 is of the order $\hbar v_F/2\pi k_B t_{Cr}$, where v_F is the Fermi velocity for electrons involved in interlayer exchange. This velocity is, generally speaking, different for the Fermi surface regions responsible for the long-wave and short-wave exchange oscillations; however, the substitution of the typical values of $v_F \sim 10^8$ cm/s and $t_{Cr} \sim$ 20 Å gives a value of $T_0 \sim 1000$ K. This high value of T_0 explains well the fact that the value of J_1 is almost constant in the temperature range from 0 to 500 K.

Figure 9 gives the dependence of the constant J_2 on the chrome interlayer thickness at 77 and 473 K. The biquadratic exchange is observed to increase with decreasing temperature. The $J_2(t_{Cr})$ dependence was best described by a function of the form $J_2^0(T)/t_{Cr}$ (solid curves in Fig. 9) for all temperatures values.

Figure 10 gives the temperature dependence of the parameter J_2^0 defining the dependence of the constant of biquadratic exchange on thickness at each temperature value. In the investigated temperature range, this dependence may be described as linear (solid curve in Fig. 10), although the observed experimental error permits more complex interpretations of this dependence. If this linear dependence is extrapolated into the region

of higher temperatures, the biquadratic exchange in our structure must go to zero at a temperature of about 650 K. This value is much lower than the Curie temperature in iron and is much higher than the Néel temperature in bulk chrome. However, it is close to the temperature of transition to the paramagnetic phase, which is observed in thin chrome layers adjoining iron [37]. This agreement is an indirect argument in favor of the fact that it is to the unusual structure of chrome that the observed biquadratic exchange owes its origin.

Before proceeding to the next section, we will formulate once again some of our results which cannot be explained within the existing theoretical models. First, the dependence of biquadratic exchange on the chrome interlayer thickness has the form $1/t_{Cr}$, which contradicts the fluctuation model of [12] which is often used in interpreting experimental data. Second, the temperature dependence of biquadratic exchange indicates that its origin is closely related to the antiferromagnetic order in the chrome interlayer. As a rule, the models taking into account the presence of intrinsic magnetic order in the interlayer lead to forms of notation of the interlayer interaction energy other than biquadratic exchange [13, 20] or predict too small a magnitude of this exchange [20]. Furthermore, the results of Men'shov and Tugushev [20] cannot be directly applied to our experimental data because the interlayer thickness in our sample is too small.

4. UPDATED FLUCTUATION MODEL OF BIQUADRATIC EXCHANGE

In order to interpret the foregoing data, a model is suggested which takes into account the presence of magnetic structure in chrome and the interface roughness. Under these conditions, if the layers of iron are assumed to be uniformly magnetized, the total energy of a multilayer system is made up by the bulk energy of the chrome interlayer and by the surface energy of interaction on the interface between Fe and Cr. In distinction to Slonczewski's model of magnetic proximity, in which the interaction on the interface prevails over the interaction within chrome and brings about a strong distortion (twisting) of the chrome structure, we will treat the inverse situation of weak exchange on the interface between Fe and Cr. This situation brings about only a weak distortion of the chrome structure. In order to calculate the energy, we will deal with a simplified case, in which one interface is ideally smooth and the other represents a periodic series of monatomic steps, as demonstrated in Fig. 11. In addition, we will proceed from the simplified concept of chrome as a layered antiferromagnet with localized spins. In this case, the distortion of the chrome structure is characterized by a deflection of the antiferromagnetic vector. One can see in the figure the averaging of exchange interaction because of the roughness of the upper interface; therefore, the fluctuations of the antiferromagnetic vector occur in the vicinity of the direction of magnetization of

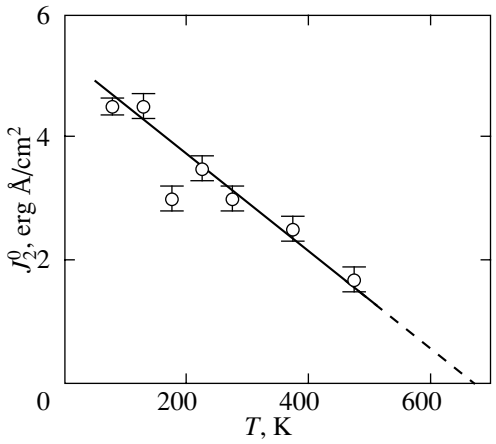

Fig. 10. The parameter J_2^0, which describes the dependence of biquadratic exchange on the interlayer thickness, as a function of temperature. The points indicate the experimental data; the straight line indicates the results of linear approximation of these data.

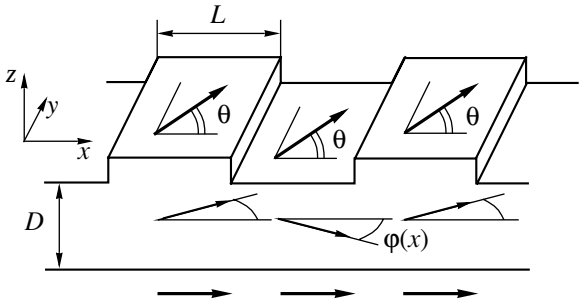

Fig. 11. The updated fluctuation model of the emergence of biquadratic exchange.

the bottom layer of iron. In the case of a fairly thin interlayer and large terraces, the deflection of the antiferromagnetic vector in chrome may be assumed to be uniform over the thickness and, therefore, the value of this deflection φ may be treated as a function of the coordinate x alone (Fig. 11). In the suggested model, the surface part of energy may be written in the form

$$E_S = \int_S J_0 \cos\varphi dxdy + \int_{S_1} J_0 \cos(\varphi - \theta) dxdy - \int_{S_2} J_0 \cos(\varphi - \theta) dxdy, \quad (11)$$

where J_0 is the exchange interaction between iron and chrome on the surface. The bulk part of energy is

$$E_V = t_{Cr} \int_S A \left(\frac{d\varphi}{dx}\right)^2 dxdy, \quad (12)$$

where A is a parameter characterizing the magnetic hardness of chrome. The dependence $E(\theta)$ is found by minimization of the total energy $E(\theta, \varphi) = E_S + E_V$ with respect to φ. The pattern of this dependence may be estimated as follows. The surface and bulk contributions to energy per unit area are given by

$$\begin{aligned}\varepsilon_S &\approx J_0 + \frac{J_0}{2}\cos(\varphi_1 - \theta) - \frac{J_0}{2}\cos(\varphi_2 - \theta)\\ &\approx J_0 - \frac{J_0}{2}\sin\theta(\varphi_2 - \varphi_1),\end{aligned} \tag{13}$$

$$\varepsilon_V \approx t_{\mathrm{Cr}} A \frac{(\varphi_2 - \varphi_1)^2}{L^2}. \tag{14}$$

From the condition of minimum of $\varepsilon = \varepsilon_S + \varepsilon_V$, we find

$$\varphi_2 - \varphi_1 = \frac{J_0 L^2}{4 t_{\mathrm{Cr}} A}\sin\theta. \tag{15}$$

We derive

$$\varepsilon \approx 2J_0 - \frac{J_0^2 L^2}{4 t_{\mathrm{Cr}} A}\sin^2\theta = \varepsilon_0 + J_2\cos^2\theta, \tag{16}$$

i.e., the biquadratic form of energy. The expression for the constant of biquadratic interaction has the form

$$J_2 = \frac{J_0^2 L^2}{16 t_{\mathrm{Cr}} A}, \tag{17}$$

with J_2 being inversely proportional to the interlayer thickness t_{Cr}. The condition of smallness of the angle of deviation of magnetic order in chrome from the middle position will be written as

$$\frac{J_0 L^2}{16 t_{\mathrm{Cr}} A} \ll 1. \tag{18}$$

In this case, the condition of disregarding the dependence of the deviation angle φ on the coordinate z reduces to the simple expression

$$t_{\mathrm{Cr}} \ll L. \tag{19}$$

The suggested model is similar to the fluctuation model of Slonczewski [13] with the difference that we treat the distortion of the magnetic structure of chrome, while Slonczewski deals with the distortion of magnetization of ferromagnetic layers. Therefore, it is not surprising that the result coincides with that obtained using the fluctuation model, with the parameters characterizing chrome being replaced by the respective parameters for iron.

In the foregoing reasoning, chrome was treated as a regular antiferromagnet with localized spins; in reality, however, the magnetic structure of chrome is a spin density wave in which, generally speaking, a correlation exists between the amplitude and angle of twisting. Therefore, for the calculation results to remain valid, one must impose an additional condition that the contribution to energy due to the nonuniform distribution of the amplitude of spin density wave should be insignificant.

5. CONCLUSIONS

We will briefly formulate the main inferences made as a result of applying an integrated experimental approach to studying the interlayer interaction in a Fe/Cr system.

A three-layer Fe/Cr/Fe sample with a wedge-shaped chrome interlayer was used to measure the magnetization curves (by the method of magnetooptical Kerr effect) in the temperature range from 77 to 473 K and the spin wave spectra (by the method of Brillouin scattering of light) at room temperature for different values of thickness of the chrome interlayer (0–20 Å) in a magnetic field parallel to the sample plane and directed along the hard magnetization axis. The acoustic and optical modes of spin wave oscillation were observed in Brillouin spectra.

It has been demonstrated that the experimentally obtained magnetization curves and spin wave spectra measured at room temperature are well described within the model of biquadratic exchange for almost all values of chrome interlayer thickness. The range of validity of this model has been determined, which is apparently defined by the interlayer exchange.

The data for magnetization curves were used to calculate the dependence of the exchange constants (bilinear, J_1, and biquadratic, J_2) on the chrome layer thickness for different values of temperature.

In accordance with the literature data, the obtained dependence $J_1(t_{\mathrm{Cr}})$ exhibits an oscillating pattern with two periods of oscillation of 3 and 19 Å and, by and large, is well described within the RKKY theory. It has been demonstrated that, within the experimental error, the magnitude, amplitude, period, and phase of oscillation of $J_1(t_{\mathrm{Cr}})$ are independent of temperature in the temperature range employed.

Unlike bilinear exchange, the magnitude of biquadratic exchange $J_2(t_{\mathrm{Cr}})$ was found to significantly depend on the temperature T.

For all temperature values involved, the magnitude of biquadratic exchange has been shown to decrease in inverse proportion to the chrome interlayer thickness and to be described by the formula $J_2(t_{\mathrm{Cr}}) = J_2^0(T)/t_{\mathrm{Cr}}$, where $J_2^0(T)$ is a temperature-dependent coefficient. The models of biquadratic exchange available in the literature lead to other $J_2(t_{\mathrm{Cr}})$ dependences.

The magnitude of $J_2^0(T)$ in the range of 77–473 K has been found to decrease linearly with rising temperature. The extrapolation of the obtained straight line of

$J_2^0(T)$ to the region of high temperatures leads one to assume that the constant of biquadratic exchange goes to zero in the neighborhood of 600–700 K. According to the results of diffraction of neutrons by Fe/Cr superlattices [17], in this temperature region, with the interlayer thickness ranging from 10 to 20 Å, chrome changes into a paramagnetic state.

In order to interpret the new experimental results pertaining to the behavior of the biquadratic exchange constant , a theoretical model has been suggested which takes into account the nonideality of the interface between the Fe and Cr layers and the presence of magnetic hardness in the structure in the chrome interlayer. In doing so, the magnetic hardness of chrome was assumed to exceed the interaction between iron and chrome on the interface. It must be emphasized that, though being simplified, the employed model enables one to fairly well describe the experimentally obtained data.

ACKNOWLEDGMENTS

In conclusion, we would like to thank Prof. B. Hillebrands for the possibility of performing the experimental part of our work in his laboratory.

We are grateful to V.V. Tugushev for numerous valuable discussions of the problem and for letting us to familiarize ourselves, with the results of his theoretical studies, including unpublished ones.

This study was supported in part by the Russian Foundation for Basic Research (project nos. 01-02-16716 and 00-15-96574).

REFERENCES

1. P. E. Wigen and Z. Zang, Braz. J. Phys. **22**, 267 (1992).
2. B. Heinrich and J. Cochran, Adv. Phys. **42**, 523 (1993).
3. A. Fert, P. Grünberg, A. Barthelemy, *et al.*, J. Magn. Magn. Mater. **140–144**, 1 (1995).
4. S. O. Demokritov, J. Phys. D **31**, 925 (1998).
5. D. T. Pierce, J. Unguris, R. J. Celotta, and M. D. Stiles, J. Magn. Magn. Mater. **200**, 290 (1999).
6. M. D. Stiles, J. Magn. Magn. Mater. **200**, 332 (1999).
7. D. M. Edwards, J. Mathon, R. B. Muniz, and M. S. Phan, Phys. Rev. Lett. **67**, 493 (1991).
8. P. Bruno and C. Chappert, Phys. Rev. B **46**, 261 (1992).
9. P. Bruno, Phys. Rev. B **52**, 411 (1995).
10. J. C. Slonczewski, Phys. Rev. Lett. **67**, 3172 (1991).
11. S. O. Demokritov, E. Tsymbal, P. Grünberg, *et al.*, Phys. Rev. B **49**, 720 (1994).
12. J. C. Slonczewski, J. Appl. Phys. **73**, 5957 (1993).
13. J. C. Slonczewski, J. Magn. Magn. Mater. **150**, 13 (1995).
14. A. Schreyer *et al.*, Phys. Rev. B **52**, 16 066 (1995).
15. D. T. Pierce, A. D. Davis, J. A. Strocio, *et al.*, J. Magn. Magn. Mater. **222**, 13 (2000).
16. V. D. Levchenko, A. I. Morozov, A. S. Sigov, and Yu. S. Sigov, Zh. Éksp. Teor. Fiz. **114**, 1817 (1998) [JETP **87**, 985 (1998)].
17. A. Schreyer, C. F. Majkrzak, T. Zeidler, *et al.*, Phys. Rev. Lett. **79**, 4914 (1997).
18. Zhu-Pei Shi and R. S. Fishman, Phys. Rev. Lett. **78**, 1351 (1997).
19. V. N. Men'shov and V. V. Tugushev, Zh. Éksp. Teor. Fiz. **120**, 899 (2001) [JETP **93**, 786 (2001)].
20. V. N. Men'shov and V. V. Tugushev, Zh. Éksp. Teor. Fiz. **122**, 1044 (2002) [JETP **95**, 901 (2002)].
21. A. B. Drovosekov, N. M. Kreĭnes, D. I. Kholin, *et al.*, Pis'ma Zh. Éksp. Teor. Fiz. **67**, 690 (1998) [JETP Lett. **67**, 727 (1998)].
22. A. B. Drovosekov, O. V. Zhotikova, N. M. Kreĭnes, *et al.*, Zh. Éksp. Teor. Fiz. **116**, 1817 (1999) [JETP **89**, 986 (1999)].
23. B. Heinrich, J. F. Cochran, T. Monchesky, and R. Urban, Phys. Rev. B **59**, 14 520 (1999).
24. A. Azevedo, C. Chesman, M. Lucena, *et al.*, J. Magn. Magn. Mater. **177–181**, 1177 (1998).
25. C. Chesman, N. S. Almeida, A. Azevedo, *et al.*, J. Magn. Magn. Mater. **226–230**, 1770 (2001).
26. M. From, L. X. Liao, J. F. Cochran, and B. Heinrich, J. Appl. Phys. **75**, 6181 (1994).
27. P. Vavassori, M. Grimsditch, and E. E. Fullerton, J. Magn. Magn. Mater. **223**, 284 (2001).
28. J. Dekoster, J. Meersschaut, S. Hogge, *et al.*, J. Magn. Magn. Mater. **198–199**, 303 (1999).
29. A. B. Drovosekov, D. I. Kholin, N. M. Kreines, *et al.*, J. Magn. Magn. Mater. **226–230**, 1779 (2001).
30. A. B. Drovosekov, D. I. Kholin, N. M. Kreines, *et al.*, Fiz. Met. Metalloved. **91**, Suppl. 1, 74 (2001).
31. G. S. Krinchik, *Physics of Magnetic Phenomena* (Mosk. Gos. Univ., Moscow, 1976).
32. L. Blanco-Gutiérrez, M. Vélez, J. Diaz, *et al.*, Phys. Rev. B **64**, 024417 (2001).
33. J. R. Sandercock, in *Light Scattering in Solids III*, Ed. by M. Cardona and G. Güntherodt (Springer-Verlag, Berlin, 1982), p. 173.
34. M. Grimsditch, S. Kumar, and E. E. Fullerton, Phys. Rev. B **54**, 3385 (1996).
35. S. M. Rezende, C. Chesman, M. A. Lucena, *et al.*, J. Appl. Phys. **84**, 958 (1998).
36. M. Chirita, G. Robins, R. L. Stamps, *et al.*, Phys. Rev. B **58**, 869 (1998).
37. H. Zabel, J. Phys.: Condens. Matter **11**, 9303 (1999).

Translated by H. Bronstein

Journal of Experimental and Theoretical Physics, Vol. 95, No. 6, 2002, pp. 1074–1084.
Translated from Zhurnal Éksperimental'noĭ i Teoreticheskoĭ Fiziki, Vol. 122, No. 6, 2002, pp. 1247–1259.

SOLIDS
Electronic Properties

Andreev States and the Josephson Effect in Superconducting Heterojunctions on Thin $YBa_2Cu_3O_x$ Films

P. V. Komissinski[a, b, *], G. A. Ovsyannikov[a, **], Yu. V. Kislinskiĭ[a], I. M. Kotelyanskiĭ[a], and Z. G. Ivanov[b]

[a] *Institute of Radio Engineering and Electronics, Russian Academy of Sciences, ul. Mokhovaya 18, Moscow, 101999 Russia*
[b] *Chalmers University of Technology, SE-41296, Göteborg, Sweden*
**e-mail: filipp@hitech.cplire.ru*
***e-mail: gena@hitech.cplire.ru*
Received April 8, 2002

Abstract—Conductance anomalies at low bias voltages and superconducting currents in $Au/YBa_2Cu_3O_x$ and $Nb/Au/YBa_2Cu_3O_x$ heterojunctions in which the *c* axis of the $YBa_2Cu_3O_x$ (YBCO) epitaxial film is rotated in the (110) YBCO plane through 11° with respect to the normal to the substrate plane were studied experimentally. The films were prepared by laser deposition onto (7 2 10)-oriented $NdGaO_3$ substrates. The current–voltage characteristics of the heterojunctions exhibit conductance anomalies at low voltages. The behavior of these anomalies is studied at various temperatures and in various magnetic fields. The critical current and Shapiro steps observed in the current–voltage characteristics of $Nb/Au/YBa_2Cu_3O_x$ were evidence of the Josephson effect in these heterojunctions. The experimental results are analyzed in terms of the model of the arising of bound states caused by Andreev reflection in superconductors with *d*-type symmetry of the superconducting order parameter. *© 2002 MAIK "Nauka/Interperiodica".*

1. INTRODUCTION

It has been established that most metal oxide superconductors with high critical temperatures of the superconducting transition (high-T_c superconductors) are characterized by a complex symmetry type of the superconducting order parameter, in which the $d_{x^2-y^2}$ component dominates (*d*-wave superconductors) (e.g., see review [1]). As distinguished from superconductors with a completely isotropic (*s*) symmetry type of the superconducting order parameter (*s*-wave superconductors), the superconducting order parameter in *d*-wave superconductors changes sign under quasiparticle momentum rotations over 90° in the *ab* plane.

In tunnel junctions between a *d*-wave superconductor (D) and a normal metal (N/D, where the slash denotes the tunnel barrier), an *s*-wave superconductor (S/D), or another *d*-wave superconductor (D/D'), quasiparticles experience Andreev reflection in addition to the usual mirror reflection. An additional phase shift π arises for incident and Andreev-reflected quasiparticles when the superconducting order parameter of a *d*-wave superconductor changes sign.

Such phenomena are, for instance, observed in an N/D contact with the (110)-oriented *d*-wave superconductor. A sequence of mirror and Andreev reflections of quasiparticles then causes the formation of Andreev bound states with low energies (zero-energy states, ZES) on the (110) surface of *d*-wave superconductor. These states are localized close to the interface at a distance of about the coherence length [2].[1] As a result, a peak of the density of states is formed on the Fermi surface, which manifests itself by the appearance of a conductance anomaly in the current–voltage characteristic, that is, a zero bias conductance peak (ZBCP) [2–4].

Studies of the tunnel spectra of high-T_c materials, in particular, $YBa_2Cu_3O_x$ (YBCO), are impeded by the small coherence length of the material (≈3 nm) and the high sensitivity to crystal lattice defects and to the presence of impurities. At the same time, ZBCP was experimentally observed in N/D and S/D heterojunctions [5–9], bicrystal and ramp-type junctions [10, 11], and in point contacts of a scanning tunneling microscope [12]. Currently, of two possible reasons for the appearance of conductance anomalies in N/D heterojunctions (the presence of magnetic impurities in the barrier [5] and ZES on the *d*-wave superconductor surface [2]), preference is given to the second mechanism. Theoretical studies predict the existence of ZES on *d*-wave superconductor crystallographic planes somewhat different from the (110) plane [4], for instance, on faceted (100) surfaces [13]. These theoretical predictions have been confirmed experimentally [7–9]. Splitting of ZES in a strong magnetic field observed in [6–8] has been explained by a Doppler shift of ZES levels caused by a screening current flow, that is, by excitation of the *is*

[1] If the *d*-wave order parameter is suppressed near the interface, bound states with finite energies can also be formed in N/D contacts [2].

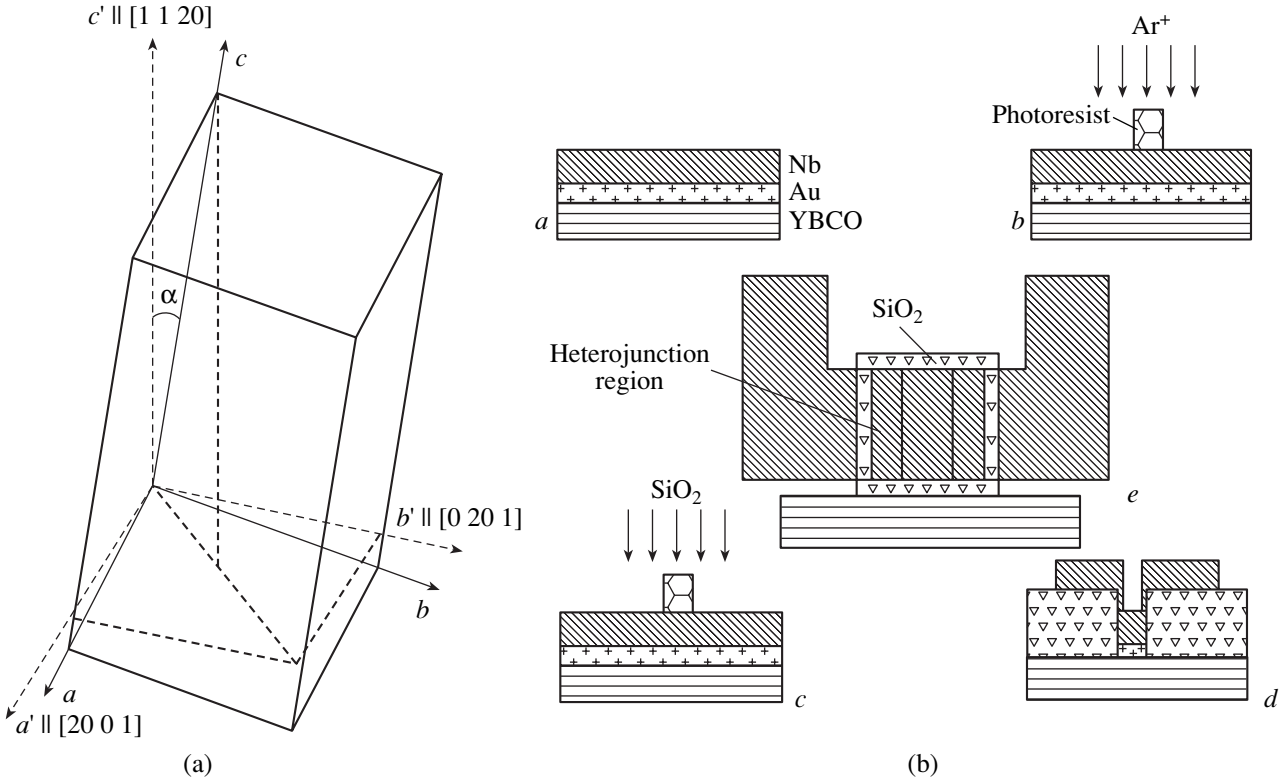

Fig. 1. (a) Schematic representation of growth of (1 1 20) YBCO films on (7 10 2) $NdGaO_3$ substrates. The rotation angles of the *a*, *b*, and *c* crystallographic axes of the YBCO film with respect to the *a*', *b*', and *c*' axes of the standard (001)-oriented YBCO film on the (110) $NdGaO_3$ substrate are $aa' = 7.6°$, $bb' = 7.9°$, and $\alpha \equiv cc' = 11°$. (b) Technological sequence for preparing Nb/Au/YBCO heterojunctions.

component in the surface layer of *d*-wave superconductors [13].

In this work, we report the results obtained in an experimental study of Au/YBCO and Nb/Au/YBCO heterojunctions on single-domain YBCO films prepared on (7 10 2)-oriented $NdGaO_3$ (NGO) substrates [14]. The temperature and magnetic field dependences of ZBCP were determined for heterojunctions of both types. Superconducting current was observed in Nb/Au/YBCO heterojunctions, and changes in the shape of the current–voltage characteristics under the action of electromagnetic monochromatic millimeter-range radiation were studied.

2. GROWTH OF FILMS AND THE PROCEDURE FOR PREPARING HETEROJUNCTIONS

The tunnel heterojunctions were prepared on (7 10 2)-oriented NGO substrates tilted by angle $\alpha \approx 11°$ from the (110) plane of NGO, which is used for growing (001)-oriented YBCO films. As a result, the *c* axis of the YBCO film grown on such a tilted substrate was rotated in the (110) YBCO plane over 11° with respect to the normal to the substrate plane; that is, the orientation of the YBCO film was close to (1 1 20) (Fig. 1a). Epitaxial YBCO films 150 nm thick were laser deposited at 770–790°C in oxygen at a pressure of 0.6 mbar. The films had a critical temperature of T_c = 85–90 K, which was measured by the magneto-induction method.

Microbridges 20 μm long and 4 μm wide, parallel to substrate sides (the [20 0 1] and [0 20 1] directions in Fig. 1a), were used to measure the critical current density in YBCO films. At T = 77K, the critical current density in the microbridges of one of the samples was 7.5×10^4 and 2.0×10^4 A/cm^2 with an anisotropy of 3.75. X-ray diffraction patterns of YBCO films grown on NGO substrates with the (7 10 2) orientation showed these films to be single-domain and that they demonstrate the presence of a single twin complex [14], in contrast, for instance, to YBCO films on $SrTiO_3$ substrates with the (110) orientation and NGO substrates with the (120) orientation [14–16].

The morphology of the YBCO films was studied by atomic force microscopy. The surface of the films on tilted NGO substrates with the (7 10 2) orientation consisted of large-sized growth steps, which formed terraces much wider and higher than those present on the substrate surface (Fig. 2a). The long and short sides of growth steps were oriented in the (001) and (110) planes of YBCO, respectively (segments *AA* and *BB* in Fig. 2b). For this reason, the total transport current in

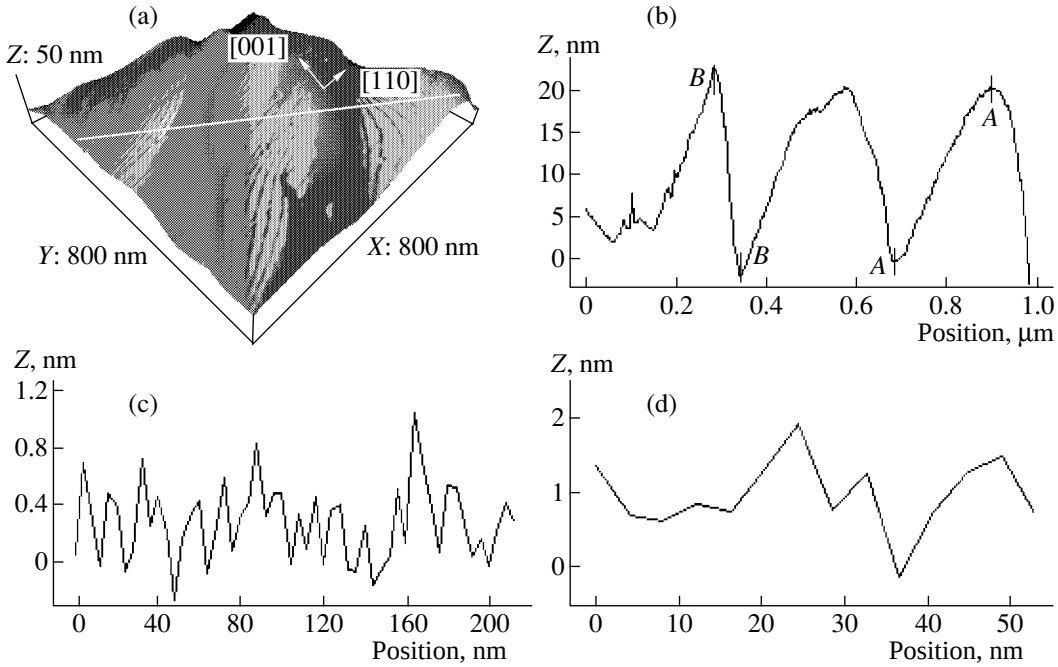

Fig. 2. Profile of the surface of YBCO films with a (1 1 20) orientation measured with an atomic-force microscope: (a) three-dimensional image of a 0.8×0.8 μm^2 surface region; (b) surface profile along the white line in Fig. 2a; *AA* and *BB* are the (001) and (110) YBCO film growth steps, respectively; and (c, d) flattened YBCO film surface profiles in the *AA* and *BB* regions, respectively.

planar Au/YBCO and Nb/Au/YBCO heterojunctions prepared on such YBCO films was the sum of currents flowing through contacts to the (001) and (110) crystallographic planes of YBCO films. Because of conductance anisotropy, the major current fraction flowed through facets with the (110) orientation of the YBCO film [17].

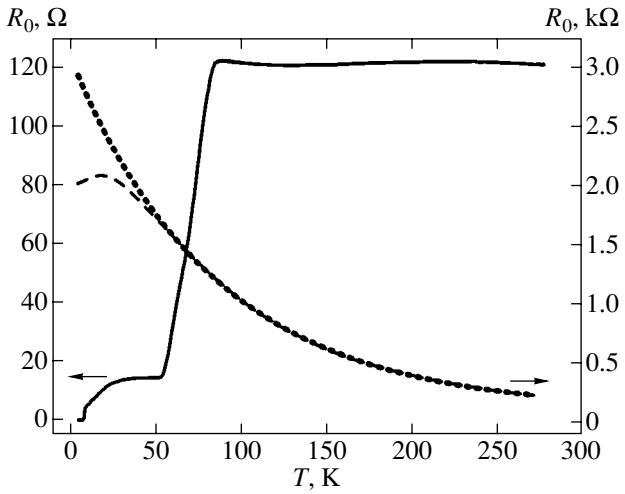

Fig. 3. Temperature dependences of resistance of heterojunctions of two types, Nb/Au/YBCO (solid line) and Au/YBCO (dashed line), measured at a 1 μA bias current. The dotted line is the dependence $R[\text{k}\Omega] = 0.11 + 3\exp(-T[\text{K}]/85)$, which closely approximates the $R_d(T)$ dependence for the Au/YBCO heterojunction at $T > T_c = 53$ K.

Detailed studies of the morphology of the surface of YBCO films on the facets with the (001) and (110) orientations (*AA* and *BB*, respectively) showed that the maximum surface roughness was of 1–2 lattice constants of the YBCO film (see Figs. 2c, 2d). The root-mean-square surface roughness values on the *AA* and *BB* facets equaled $h_{(001)} \approx 0.6$ nm and $h_{(110)} \approx 1.3$ nm, respectively. Taking into account the quasiparticle wavelength in the *ab* plane, $\lambda_{ab} \approx \hbar / p_{F_{ab}} \sim 10$ nm ($\hbar$ is the Planck constant, and $p_{F_{ab}}$ is the quasiparticle momentum on the Fermi surface of YBCO), we could consider reflection of quasiparticles from the Au/YBCO interface as mirror reflection and the interface itself as consisting of a sequence of disoriented facets [13, 18]. Note that, for YBCO films deposited onto a (110)-oriented NGO substrate ($\alpha = 0$), the surface is (001)-oriented and its maximum roughness equals 3–4 nm (see Fig. 4a in [19]). Growth steps appear as α increases, and their height amounts to $\eta \approx 20$ nm (see Fig. 2b) on (7 10 2)-oriented NGO substrates ($\alpha \approx 11°$).

In preparing Nb/Au/YBCO heterojunctions, the deposited YBCO films were coated with gold (film 10 nm thick) immediately after cooling to room temperature without loss of vacuum (in situ). Additional Au and Nb layers for Au/YBCO and Nb/Au/YBCO heterojunctions were deposited in other vacuum chambers by electron-beam evaporation and radiofrequency magne-

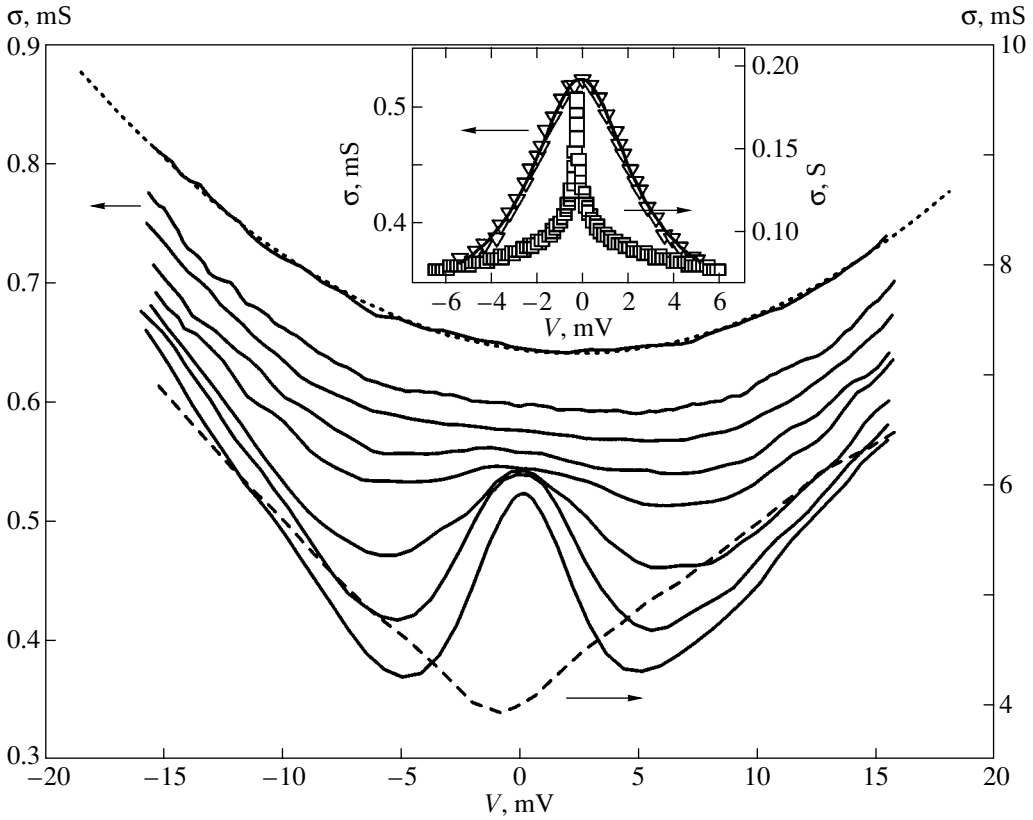

Fig. 4. The σ(*V*) dependences for Au/YBCO heterojunctions at various temperatures (solid lines), from bottom to top: 4.2, 10, 20, 30, 35, 40, 45, and 55 K. The dotted line is the parabola that approximates the σ(*V*) dependence at $T = 55$ K. The dashed line corresponds to the σ(*V*) dependence at 4.2 K for Au/YBCO heterojunctions on (001)-oriented YBCO films [19]. The σ(*V*) dependences for Au/YBCO at $T = 4.2$ K (turned over triangles) and Nb/Au/YBCO at $T = 10$ K (squares) at low voltages $V < 6$ mV are shown in the inset. The solid line is the Lorentzian approximation of the σ(*V*) dependence.

tron sputtering.[2] The deposition of Au films for Au/YBCO heterojunctions was performed with loss of vacuum (ex situ). Heterojunctions with sizes of 5×5 to 30×30 μm^2 were produced by photolithography and ion-beam etching in argon. The insulating SiO_2 layer deposited by the electron-beam method allowed the region of current flow to be localized and undesirable contacts at the ends of YBCO films to be excluded. Up to 20 heterojunctions were usually prepared on a 5×5 mm^2 substrate. The technological sequence for preparing Nb/Au/YBCO heterojunctions is shown in Fig. 1b.

The electrophysical parameters were measured using the four-point scheme in the current-bias mode in the temperature range $T = 4.2$–300 K and magnetic fields up to 5 T and under electromagnetic radiation of frequencies of 40–100 GHz. The results of electrophysical parameter measurements at $T = 4.2$ K are listed in the table.

3. RESULTS AND DISCUSSION

3.1. Temperature Dependences of Heterojunction Resistances

The temperature dependences of resistances R of Au/YBCO and Nb/Au/YBCO heterojunctions measured at a current of 1 μA are shown in Fig. 3. The resistance of the Au/YBCO heterojunction increases exponentially as temperature decreases at $T \gtrsim 53$ K; at $T \lesssim 53$ K, the $R(T)$ dependence deviates from exponential. No substantial change in R at $T \approx T_c$ is observed for the Au/YBCO heterojunction because the R_N resistance of the heterojunction itself[3] is much larger than the R_e resistance of YBCO leads. This behavior is typical of heterojunctions prepared by depositing Au films ex situ. The accompanying escape of oxygen atoms from the surface layer of YBCO decreases interface transparency. The characteristic interface resistance $r \equiv R_N A$, where A is the area of the heterojunction, varies in the wide range 10^{-2}–10^{-6} Ω cm^2 depending on the technique for heterojunction preparation. In particular, the

[2] As distinguished from Pb used in [5, 7], Nb does not mix with Au when deposited on it. Note that the direct Nb/YBCO contact has a very large characteristic resistance [19].

[3] For Nb/Au/YBCO heterojunctions, $R_N \equiv R(T_c)$, and for Au/YBCO heterojunctions, the R_N value was determined from current–voltage characteristics as a maximum resistance at 4.2 K.

Heterojunction parameters

	No.	A, μm^2	I_c, μA	R_N, Ω	R_NA, mΩ cm^2	I_cR_N, μV	ΔV, mV T = 4.2 K	σ_0/σ_{min} T = 4.2 K
Nb/Au/YBCO	J9	10 × 10	45	6	0.006	270	–	–
	J10	20 × 20	10	15	0.06	150	–	–
	J11	30 × 30	13	12	0.108	156	–	–
	J12	30 × 30	2	40	0.36	80	–	–
Au/YBCO	J9	10 × 10	–	2900*	2.9*	–	5.65	1.37
	J10	20 × 20	–	7200*	28.8*	–	9.14	1.25
	J11	20 × 20	–	6700*	26.8*	–	6.6	1.81
	J13	30 × 30	–	1400*	12.6*	–	6.4	1.57
	J16	20 × 20	–	2700*	10.8*	–	4.8	1.65

Note: The R_N values for Au/YBCO heterojunctions determined from current–voltage characteristics as maximum resistance values at 4.2 K are labeled by asterisks.

resistance of heterojunctions with the Au/YBCO interface formed by depositing the Au film ex situ increased 3–4 orders of magnitude compared with the resistance of the Au/YBCO interface produced in situ. As the r value unambiguously determines the interface transparency averaged over momentum directions $\langle D(\theta)\rangle \equiv \bar{D}$ [19], $\bar{D}$ decreases as much as r increases.

The $R(T)$ dependence was quite different at $R_N \ll R_e$. This inequality held if the Au film was deposited in situ, as in the preparation of Nb/Au/YBCO heterojunctions. The $R(T)$ dependence for such a heterojunction is shown in Fig. 3. A sharp decrease in R caused by the transition of the leads into the superconducting state was observed at $T \approx T_c$ = 53 K.[4] Resistance R slowly decreased as temperature decreased below T_c to the temperature of the transition of the Nb electrode into the superconducting state, $T_{cNb} \approx 9.2$ K. The T_c = 53 K temperature coincided with the temperature at which the $R(T)$ dependence of the Au/YBCO heterojunction deviated from the exponential curve. The $R(T)$ dependence for Au/YBCO and Nb/Au/YBCO heterojunctions at $T \lesssim T_c$ was determined by the "switching on" of the current transport channel involving Andreev reflections as temperature decreased [20]. In our heterojunctions, the influence of Andreev reflection strengthened because of the presence of ZES at the boundary of the *d*-wave superconductor [1, 2]. Note that a ZBCP appeared in heterojunction current–voltage characteristics only at $T < T_c$, which cannot be explained by the presence of magnetic impurities in the barrier [5].

[4] The critical temperature of the leads was low, T_c = 53 K, because open *ab* planes of YBCO films were depleted of oxygen during sample preparation.

3.2. Broadening of Andreev States

Changes in the bias voltage dependence of conductivity $\sigma(V)$ for the Au/YBCO heterojunction caused by a decrease in temperature are shown in Fig. 4. At $T > T_c$, the $\sigma(V)$ dependence (the upper solid line in Fig. 4) can be closely approximated by a parabola (the dashed line in Fig. 4) in conformity to the tunnel theory of N/N' junctions, taking into account a finite potential barrier height [21]. At $T < T_c$, the $\sigma(V)$ dependence deviates from parabolic at low V voltages, and there appears a conductivity peak at zero bias (that is, a ZBCP), which increases as temperature decreases (the solid curves from top to bottom in Fig. 4). The temperature at which the $R(T)$ dependence of the Au/YBCO heterojunction deviates from exponential coincides with that of arising ZBCP in the current–voltage characteristics. Note that, for Au/YBCO heterojunctions prepared on *c*-oriented films, no ZBCP is observed (see dashed lines in Fig. 4) [19].

The $\sigma(V)$ dependences for the Nb/Au/YBCO heterojunction in the temperature range 9–40 K are shown in Fig. 5. These dependences are characterized by the most pronounced ZBCP. At $T > T_c$, $\sigma(V) \approx$ const, which corresponds to the tunneling of quasiparticles through a delta-shaped barrier uniform across the junction area. At $T < T_c$, the current–voltage characteristics of Nb/Au/YBCO heterojunctions, like those of Au/YBCO, contain ZBCP. Decreasing temperature increases the amplitude and decreases the halfwidth (ΔV) of conductivity anomalies for both types of heterojunctions (see Fig. 6). Apart from thermal smearing of conductivity anomalies, Andreev state levels broaden because of the influence of finite ZES lifetimes. For a quasiparticle of energy $\varepsilon < \Delta_0$ [Δ_0 is the amplitude energy gap value for

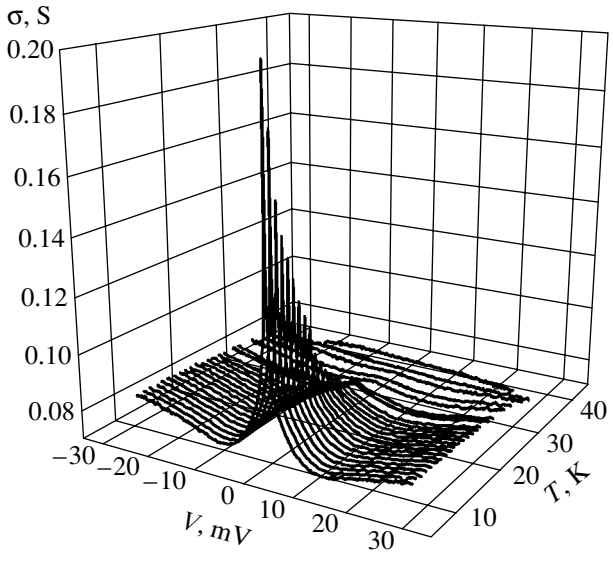

Fig. 5. The $\sigma(V, T)$ dependences for Nb/Au/YBCO heterojunctions.

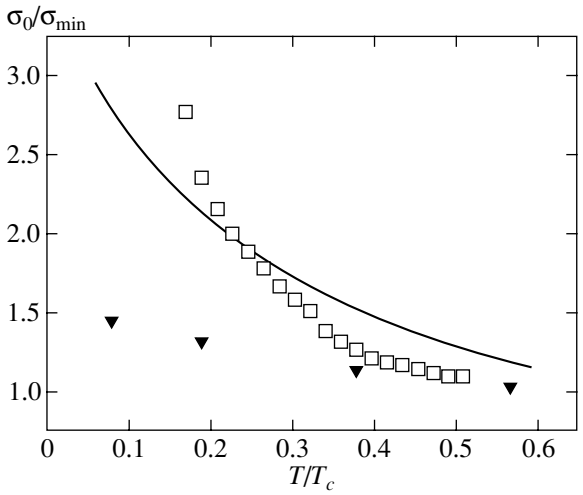

Fig. 6. Experimental $\sigma(V = 0, T) \equiv \sigma_0(T)$ dependences for Au/YBCO (turned over solid triangles) and Nb/Au/YBCO (squares) heterojunctions calculated from current–voltage characteristics and normalized by minimum conductivity values $\sigma_{min}(T)$ at a given temperature. The solid line was obtained in theoretical calculations [4] for $\rho = 0.1$.

a *d*-wave superconductor, $\Delta(\theta) = \Delta_0\cos(2\theta)]$, the $N(\varepsilon, \theta)$ density of states is written in the form [22]

$$N(\varepsilon, \theta) = \frac{\pi^{-1}\Gamma^2(\theta)}{(\varepsilon - \varepsilon_b)^2 + \Gamma^2(\theta)}, \quad (1)$$

where θ is the angle of incidence of the quasiparticle with respect to the normal to the boundary and ε_b describes the shift of ZES caused, for instance, by current flow over the *N*/*D* interface. In (1), the $\Gamma(\theta) \sim \hbar/\tau(\theta)$ parameter, where $\tau(\theta)$ is the quasiparticle lifetime in ZES, characterizes level broadening. Generally, $\Gamma(\theta)$ is determined by the tunneling of quasiparticles $\Gamma^{tunn}(\theta)$, diffusive scattering caused by YBCO film roughness $\Gamma^{diff}(\theta)$, *U*-scattering of quasiparticles with changes in the normal momentum component $\Gamma^U(\theta)$, and scattering by crystal lattice defects and impurities Γ^{imp} [22]; that is,

$$\Gamma(\theta) = \Gamma^{tunn}(\theta) + \Gamma^{diff}(\theta) + \Gamma^U(\theta) + \Gamma^{imp}. \quad (2)$$

If scattering by defects and impurities Γ^{imp}, which does not depend on the direction of the quasiparticle momentum, makes the predominant contribution to the broadening of ZES in their formation, then, as follows from (1) and (2), the ZBCP has the form of a Lorentzian of width Γ. The experimental $\sigma(V)$ dependences at low voltages ($V < 6$ mV) are shown in the inset in Fig. 4 for the Au/YBCO heterojunction at $T = 4.2$ K (turned over open triangles) and for the Nb/Au/YBCO heterojunction at $T = 10$ K (open squares). The $\sigma(V)$ dependence of Au/YBCO heterojunctions is well approximated by a Lorentzian (the solid line in the inset in Fig. 4).[5] It follows that scattering by defects and impurities determines the halfwidth of ZBCP. The inset in Fig. 4 also shows that the shape of the $\sigma(V)$ dependence of the Nb/Au/YBCO heterojunction is not Lorentzian.

In our experiments, the Au/YBCO interface was formed with loss of vacuum (ex situ), and the surface of the YBCO film before Au deposition was held under atmospheric conditions for approximately an hour. Interaction with the atmosphere causes the deposition of various impurities such as CO_2 and OH ions on the surface of YBCO films. In addition, regions depleted of oxygen, which are crystal lattice defects, are formed. As a result, a large number of scattering centers are formed in the surface layer of YBCO films. These centers can play the determining role in broadening ZBCP. The degree of surface layer diffusivity at the Au/YBCO interface can be characterized by the $\rho = d/l$ parameter, where *d* is the thickness of the disordered layer and *l* is the quasiparticle mean-free path [4]. The $\rho = 0$ value corresponds to the ideal Au/YBCO interface, and $\rho = \infty$, to a fully diffuse interface.

The $\sigma_0(T)$ temperature dependences of conductivity at a zero bias voltage are shown in Fig. 6 for the Au/YBCO (turned over solid triangles) and Nb/Au/YBCO (open squares) heterojunctions. These dependences are normalized to the minimum conductivity $\sigma_{min}(T)$ at the given temperature. For both types of heterojunctions, the $\sigma_0/\sigma_{min}(T)$ ratio monotonically increases as temperature decreases. The $\sigma_0(T)$ dependence for $\rho = 0.1$ constructed based on the calculations performed in [4] is shown in Fig. 6 by a solid line. For the Nb/Au/YBCO heterojunction, $\sigma_0(T)$ decreases as temperature decreases more rapidly than this is predicted in [4]. At the same time, the $\sigma_0(T)/\sigma_{min}(T)$ normalized

[5] The shape of the ZBCP of Au/YBCO heterojunctions remains Lorentzian at $T < T_c$.

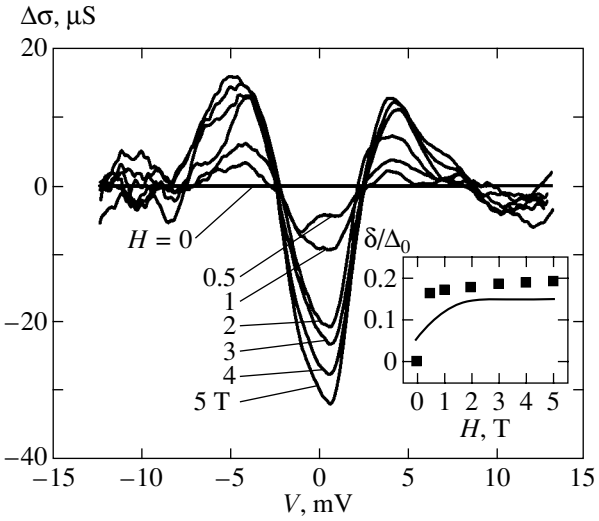

Fig. 7. Dependences $\Delta\sigma(V, H) = \sigma(V, H) - \sigma(V, 0)$ at $T = 4.2$ K for Au/YBCO heterojunctions at magnetic fields of 0 to 5 T applied normally to the substrate surface. The curve at $H = 0$ is a straight line passing through zero. Magnetic field dependence of splitting calculated as half the distance between $\Delta\sigma(V, H)$ dependence maxima and normalized by $\Delta_0 = 20$ meV is shown in the inset (squares). The solid line in the inset corresponds to calculations by the model of the generation of an additional *s* component of the order parameter in YBCO at a temperature below $T_s \lesssim 7$ K; $\Delta_{s\text{-YBCO}} = 1.2$ meV, $\Delta_0 = 20$ meV, $H_0 = 16$ T, and $H_c = 1$ T [13].

values for the Au/YBCO heterojunction differ several times from the theoretical values at $\rho = 0.1$ [4]. Unfortunately, data on $\rho > 0.1$, which correspond to our experimental situation for Au/YBCO heterojunctions, are absent in [4].

Tunneling, scattering by the rough surface of YBCO, and scattering with a change in the quasiparticle momentum direction are the mechanisms of broadening of ZES that depend on the direction of incident quasiparticle momenta. The probability of escape of quasiparticles from ZES by tunneling through the barrier increases as the barrier becomes more transparent, which should increase $\Gamma^{\text{tunn}}(\theta)$ [23, 24]. In our experiments with Nb/Au/YBCO heterojunctions, the $\overline{D}$ value was, however, at least one order of magnitude larger than for Au/YBCO heterojunctions, but the ΔV value for Nb/Au/YBCO heterojunctions at low temperatures was several times lower than for Au/YBCO heterojunctions. For instance, at $T = 10$ K, ΔV equaled 1 and 6.8 mV for the Nb/Au/YBCO and Au/YBCO heterojunctions, whose conductivity anomalies are shown in Fig. 6, respectively. It follows that in the heterojunctions studied in this work, ΔV decreases as $\overline{D}$ increases, and, therefore, the tunneling of quasiparticles is not the factor that determines broadening of ZBCP.

The broadening of ZES, which results in a non-Lorentzian shape of ZBCP, is likely to be determined by two processes, namely, diffusion scattering caused by YBCO film surface roughness and *U*-scattering of quasiparticles with a change in the normal momentum component. Experimental studies of the influence of each of these processes on ZBCP broadening is hindered by the necessity of determining the exact transparency distribution over the junction area and angles θ and the $\Gamma(\theta)$ dependences for each process.

3.3. Magnetic Field Dependences

When an N/D heterojunction is placed into a perpendicular magnetic field, screening currents are generated in superconductor D. These currents shift ZES levels (the Doppler shift of levels) [13]. Similarly, spontaneous currents can also arise in the absence of an external magnetic field if the transition to a mixed $d_{x^2-y^2} + is$ symmetry type of the superconducting order parameter occurs on the surface of D, for instance, when temperature decreases below some critical value T_s. In both cases, ZES levels experience splitting. As a result, the ZBCP peak in the N/D heterojunction splits into two peaks.

The splitting of ZES levels in perpendicular magnetic field H is described by the formula [13]

$$\varepsilon_b = \frac{e}{c} v_F H \lambda_L \sin\theta, \qquad (3)$$

where c is the velocity of light in vacuum, e is the charge of the electron, v_F is the Fermi velocity in the *ab* plane of YBCO, and λ_L is the London penetration depth in the *c* direction of YBCO. We studied Au/YBCO heterojunctions in magnetic fields up to 5 T perpendicular to the substrate plane (the angle between the magnetic field and the *ab* planes of YBCO was about 79°). No splitting of ZBCP was directly observed in the $\sigma(V)$ dependences. However, if the $\sigma(V)$ dependence at $H = 0$ is subtracted from the dependence measured in a magnetic field, the presence of ZBCP splitting becomes obvious (see Fig. 7).[6] The dependence of ZBCP splittings on the magnetic field value, $\delta(H)$, for the Au/YBCO heterojunction at $T = 4.2$ K is shown in the inset in Fig. 7 (squares). In strong magnetic fields ($H > 2$ T), $\delta(H)$ is virtually constant and, qualitatively, can be well approximated by the $\delta(H)$ dependence obtained for the model of the Doppler shift of ZES levels caused by the generation of an additional *s* component of the superconducting order parameter at $T < T_s$ (YBCO) ≈ 7 K (the solid line in the inset in Fig. 7) [6, 13]. In this case, the ZBCP should also split in a zero magnetic field. This splitting was not observed in our experiments although the condition $T < T_s$ was satisfied (also see Fig. 4). It was shown in [25] that zero-field splitting of ZBCP disappeared in the transition of

[6] This procedure for analyzing the experimental $\sigma(V, H)$ dependences was used because of small $\sigma(V)$ changes under the action of magnetic fields; a similar procedure was applied in [10, 11].

superconductor D from excessive to deficient doping with carriers. It is likely that the deficient level of doping with carriers caused by the depletion of oxygen characterizes YBCO films in our experiments, which is indirectly substantiated by the low temperature of the transition to the superconducting state, T_c = 53 K. In weak magnetic fields (H < 1 T), we do not have enough experimental data to compare them with theory [13].

Recently, alternative explanations of ZES level splittings in a magnetic field have been suggested. Laughlin [26] relates these splittings to the formation of a magnetic moment in samples in a magnetic field. Deutscher *et al.* [25] suggest the existence of the id_{xy} component of the superconducting order parameter in high-T_c superconductors, spontaneous or induced by an external magnetic field. In the latter case, the $\delta(H)$ dependence is nonlinear.

3.4. The Influence of Andreev States on Superconducting Current in Nb/Au/YBCO Heterojunctions

The current–voltage characteristics of the Nb/Au/YBCO heterojunction (sample J9) and the dependence of the differential resistance $R_d(V)$ on voltage at T = 4.2 K are shown in Fig. 8. The narrow maximum at V = 0 and the dip of the $R_d(V)$ dependence at V = 1.2 mV characterize the Josephson current and the superconducting energy gap of Nb (Δ_{Nb}), respectively. The wide $R_d(V)$ minimum at V < 5 mV corresponds to the ZBCP. The dependence of the energy of Andreev bound states on phase difference φ of the superconducting order parameters of the electrodes that form the Josephson junction determines the superconducting current (e.g., see [27–29]),

$$I_s(\varphi) \propto \sum_n \int_{-\pi/2}^{\pi/2} \cos\theta_n \frac{dE_n(\theta, \varphi)}{d\varphi} f(E_n(\theta)) d\theta, \qquad (4)$$

where the summation over n is over all states with energies E_n. For contacts between two identical s-wave superconductors, we have

$$E_n(\theta, \varphi) = \pm\Delta_1\sqrt{1 - D(\theta)\sin^2(\varphi/2)}, \qquad (5)$$

where Δ_1 is the amplitude of the order parameter in the s-wave superconductor. Substituting (5) into (4) yields the well-known sine phase dependence of the superconducting current $I_s(\varphi) = I_c\sin\varphi$ obtained by Ambegaokar and Baratoff for tunnel transitions [30]. Note that the energies of Andreev bound states are close to the superconducting energy gap for tunnel junctions from s-wave superconductors ($\bar{D} \ll 1$).

For the Andreev bound states of the contact between an s-wave superconductor (Δ_1) and the (110) plane of a d-wave superconductor ($S/D_{(110)}$), we have not only levels (5) but also ZES levels at $\varepsilon \ll \Delta_0$ [27–29, 31], namely,

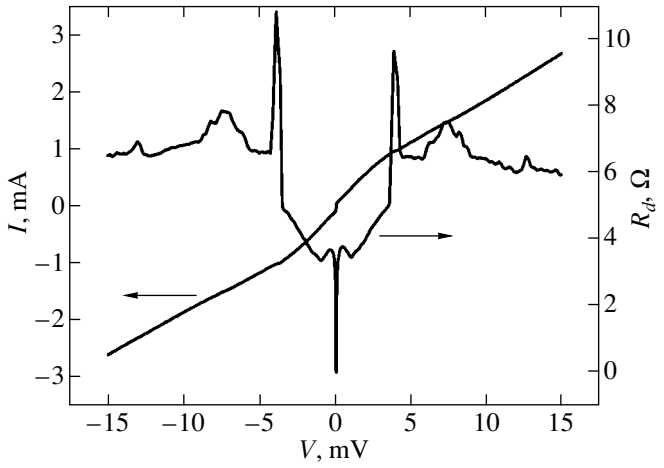

Fig. 8. Current–voltage characteristic and $R_d(V)$ for the Nb/Au/YBCO heterojunction (sample J9) at T = 4.2 K.

$$E_n(\varphi) = \pm\frac{\Delta_1\Delta_0 D(\theta)\sin\varphi}{2\Delta_1 + D(\theta)(\Delta_0 - \Delta_1)}. \qquad (6)$$

It follows from (4) and (6) [29] that, as in S/S junctions, $I_c \propto \bar{D}$ and $I_cR_N \sim \Delta_0/e$ in $S/D_{(110)}$ junctions at low temperatures $kT \ll \bar{D}\Delta_0$ (k is the Boltzmann constant), but $I_s(\varphi)$ is substantially different from the sine dependence, $I_s(\varphi) \sim \cos\varphi$ ($0 < \varphi < \pi$) [case (a)]. At higher temperatures, $\bar{D}\Delta_0 \leq kT$, we have $I_c \propto \bar{D}^2$, $I_cR_N \sim \Delta_1^2\bar{D}/ekT$, and $I_s(\varphi) \sim \sin 2\varphi$ [case (b)]. The Nb/Au/YBCO heterojunctions studied in this work are characterized by $\bar{D} \sim 10^{-5}$. It follows that, at Δ_0 = 20 meV, $\bar{D}\Delta_1 < 0.01$ K, and we have case (b) at T = 4.2 K. For instance, $I_cR_N \sim 2$ μV at $\bar{D} \sim 10^{-5}$, which is much smaller than the experimental value.

In addition, a low-temperature peak should be noticeable in the $I_c(T)$ temperature dependence of the critical current if the superconducting current in $S/D_{(110)}$ heterojunctions largely flows through Andreev states [28, 29, 31]. The experimental $I_c(T)$ critical currents in the Nb/Au/YBCO heterojunction (sample J9) monotonically decrease as temperature increases. It follows that the contribution of ZES to superconducting current transfer in our experiments can be ignored and the superconducting current in the Nb/Au/YBCO heterojunction flows through Andreev states close to the superconducting energy gap, see (5). An alternative explanation of the absence of a low-temperature $I_c(T)$ peak is a d-wave superconductor surface irregularity (faceting). In our view, the determining factor for the Nb/Au/YBCO heterojunction, as distinguished from bicrystal junctions, is the low transparency of the

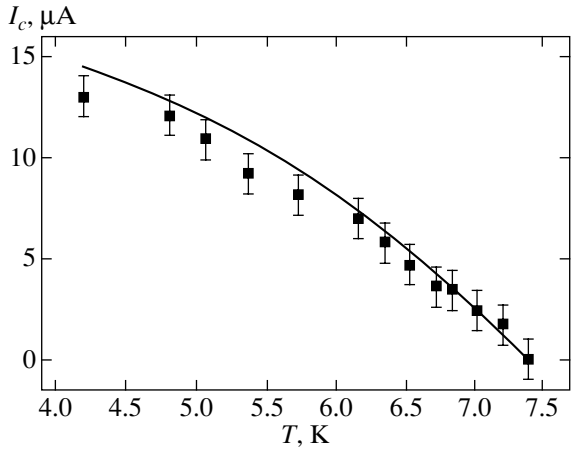

Fig. 9. Temperature dependence of the critical current for Nb/Au/YBCO (sample J9).The solid line is the $I_c(T)$ dependence calculated by (7) with T_s = 7.4 K, T_c' = 7.4 K, Δ_1 = 1.2 meV, and Δ_0 = 20 meV and with $\Delta_{s\text{-YBCO}}(T)$ and $\Delta_{Nb}(T)$ corresponding to the Bardeen–Cooper–Schrieffer theory.

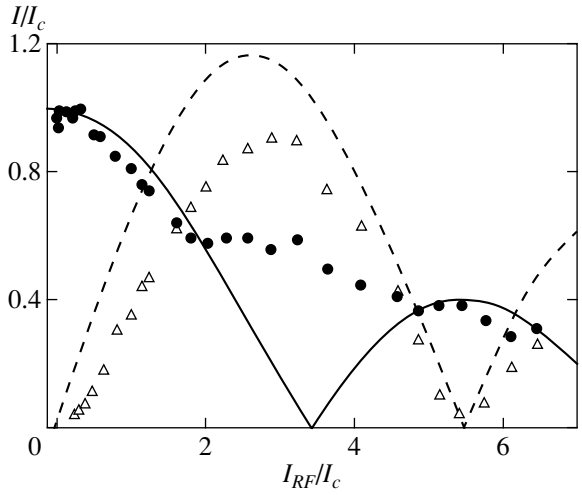

Fig. 10. Dependences of critical current (circles) and the first Shapiro step (triangles) observed in current–voltage characteristics of the Nb/Au/YBCO heterojunction (sample J9) on the amplitude of electromagnetic radiation of frequency f_e = 46.4 GHz normalized by I_c; T = 4.2 K. The solid and dashed lines are the corresponding dependences according to the resistively shunted model of Josephson junctions.

Au/YBCO interface, which decreases the influence of the *d*-symmetrical component of the superconducting order parameter of YBCO.

Close agreement between our experimental data and the theoretical $I_c(T)$ dependence for tunnel junctions between different *s*-wave superconductors (S_1IS_2) (see Fig. 9) is evidence of the predominance of the *s*-symmetrical component of the order parameter of YBCO close to the Au/YBCO interface. Several experiments showed the presence of an additional *s* component of the superconducting order parameter of YBCO with energy gap $\Delta_{s\text{-YBCO}}$. This *s* component is either excited at the interface (see Section 3.3) or present in YBCO because of its orthorhombic structure. The superconducting current is then determined similarly to a current through a Josephson junction between two different *s*-wave superconductors [32],

$$I_c R_N \approx \frac{2\ln(3.56\Delta_0/kT_c')}{\pi e\Delta_0}\Delta_{s\text{-YBCO}}(T)\Delta_1(T). \qquad (7)$$

Equation (7) takes into account the proximity effect existing between Au and Nb and responsible for the induces order parameter with a critical temperature of $T_c' \le T_{cNb}$ in the Au interlayer because of the high transparency of the Nb/Au interface. The dependence calculated by (7) with T_s = 7.4 K, T_c' = 7.4 K, Δ_1 = 1.2 meV, and Δ_0 = 20 meV shown in Fig. 9 by a solid line was obtained on the assumption that the $\Delta_{s\text{-YBCO}}(T)$ dependence was determined by the classical Bardeen–Cooper–Schrieffer theory. Figure 9 shows that the $I_c(T)$ dependence calculated by (7) is in qualitative agreement with the experimental dependence for Nb/Au/YBCO heterojunctions.

3.5. Phase Dependence of Superconducting Current in Nb/Au/YBCO Heterojunctions

Josephson current transfer through Andreev states close to the superconducting energy gap does not exclude the appearance of the second harmonic in the $I_s(\varphi)$ dependence because of the *d*-symmetrical component of the order parameter of YBCO. The $I_s(\varphi)$ dependences of Josephson junctions in high-T_c superconductors are often determined by calculating them from measured amplitude-frequency characteristics of a radiofrequency resonator connected with an superconducting quantum interferometer, in which the Josephson junction under study is shunted by superconducting inductance coil L [33]. The main restriction in using this method is the critical current value, which determines Josephson inductance, $L_J = \Phi_0/2\pi I_c$ (Φ_0 is the magnetic flux quantum). Reliable $I_s(\varphi)$ measurements require the fulfillment of the condition $L < L_J$. At a real inteferometer size of several dozen microns, the I_c current for a Josephson junction should not exceed 10 μA, which severely limits the selection of samples.

The $I_s(\varphi)$ value can also be determined by applying a different technique based on measuring the dependences of the critical current and the Shapiro steps in the current–voltage characteristics of Josephson junctions on the amplitude of external monochromatic electromagnetic radiaction $I_m(I_{RF})$ [34]. The appearance of subharmonic Shapiro steps is evidence of deviations of the $I_s(\varphi)$ dependence from a sinusoidal function. Sha-

piro steps appeared in the current–voltage characteristic under the action of external electromagnetic monochromatic radiation of frequency $f_e \approx 46.4$ GHz at voltages corresponding to f_e and its harmonics. At small external radiaction amplitudes, the first Shapiro step was symmetrical with respect to the autonomous current–voltage characteristic, which was evidence of coherence of Josephson generation in autonomous junctions. We were, however, unable to detect subharmonic Shapiro steps in the current–voltage characteristics. The accuracy of step amplitude measurements was determined by the noise current of the measuring system, which equaled the maximum deviation (in current) of the current–voltage characteristic from the autonomous characteristic at $R_d \approx R_N/2$ in the vicinity of the Shapiro step, that is, at half the normal resistance [34, 35]. The measured noise current in our experiments at $T = 4.2$ K was $I_f = 0.4$ μA; therefore, arbitrary steps of height $I_m \gtrsim 2.5I_f$ could be detected. The maximum amplitude of the first step was 11 μA, whereas subharmonic steps were not observed. It follows that the $I_s(\varphi)$ dependence at $T > 4.2$ K in the junction subjected to measurements corresponds to a sine dependence with an accuracy of not lower than 9% of the autonomous critical current value. The *d*-symmetrical order parameter of YBCO requires the presence of the second harmonic in the $I_s(\varphi)$ dependence; its absence is likely to be caused by the low transparency of the interface, $\overline{D} \sim 10^{-4}$. At the same time, asymmetric (with a 45° angle) bicrystal junctions are characterized by interface transparency $\overline{D} \sim 10^{-2}$, and the second harmonic is present in the corresponding $I_s(\varphi)$ dependences [36].

The dependences of the critical current and the amplitude of the first Shapiro step on the radiofrequency current amplitude are shown in Fig. 10. The theoretical $I_1(a)$ and $I_c(a)$ dependences, where $a = I_{RF}/I_c$ is the experimental normalized radiofrequency current value, which was determined by fitting the experimental $I_1(I_{RF})$ dependences (shown by solid lines) at the first $I_1(a)$ minimum [34]. The $I_1(a)$ dependence is nonmonotonic, which corresponds to the dependence reported in [34]. At the same time, $I_c(a)$ oscillations are not observed. The I_c current monotonically decreases as the amplitude of external radiation increases. The $I_c(H)$ dependence shows a similar behavior. Note that both the $I_c(a)$ and $I_1(a)$ dependences of symmetrical bicrystal junctions oscillate [37, 38].

The normalized external radiation frequency $\omega \equiv 2\pi\hbar f_e/2eI_cR_N = 1.15 \pm 0.15$ for the $f_e = 46.4$ GHz frequency and the $I_c = 13$ μA and $R_N = 6.5$ Ω values obtained from the autonomous current–voltage characteristics is somewhat different from $\omega = 0.75 \pm 0.15$ obtained from the frequency dependence of the maximum $I_1(a)/I_c(0)$ value [34]. The resistance is calculated at voltages $V > 20$ mV, at which the tunnel anomaly does not influence the current–voltage characteristic. In both cases, the major contribution to the error in frequency ω calculations is made by the error in current I_c measurements, which is caused by the deviation of the current–voltage characteristic from the resistively shunted model at bias currents close to I_c, whereas the shape of the current–voltage characteristic corresponds to this model in the vicinity of Shapiro steps. Note that close agreement between the experimental and calculated dependences of Shapiro step heights on the external signal amplitude is typical of symmetrical bicrystal junctions [37, 38].

4. CONCLUSION

The experimental study of the electrophysical, magnetic, and microwave properties of Au/YBCO and Nb/Au/YBCO heterojunctions prepared on single-domain (1 1 20)-oriented YBCO films showed the presence of a conductance peak in the current–voltage characteristics at low voltages. This is caused by the $d_{x^2-y^2}$ symmetry type of the order parameter of YBCO films. The Lorentzian shape and the $1/T$ temperature dependence of the ZBSP in Au/YBCO heterojunctions suggest that its broadening is caused by scattering on impurities and YBCO crystal lattice defects close to the interface; this scattering is independent of the quasiparticle momentum direction. The behavior of the ZBSP splitting experimentally observed in magnetic fields up to 5 T and the temperature dependence of the critical current in Nb/Au/YBCO heterojunctions qualitatively correspond to the theoretical model of an additional *s* component of the superconducting order parameter excited close to the surface of the superconductor when temperature decreases below some critical value. The study of Nb/Au/YBCO heterojunctions under the action of millimeter-range electromagnetic radiation revealed the absence of subharmonic Shapiro steps in the current–voltage characteristics of the heterojunctions with an accuracy of not lower than 9% of the autonomous critical current value. This is evidence that the phase dependence of the superconducting current in the heterojunctions under study is sinusoidal, as is typical of tunnel junctions of low-temperature superconductors with *s* symmetry of superconducting order parameter.

ACKNOWLEDGMENTS

The authors thank P.N. Dmitriev, D.V. Balashov, and K.I. Konstantinyan for help with measurements and T. Lofwander, P.B. Mozhaev, V.S. Shumeĭko, I.V. Borisenko, I.K. Bdikin, and T. Klaeson for useful discussions. This work was financially supported by the Russian Foundation for Basic Research (project nos. 02-02-06724-mac and 00-02-17046), INTAS of the European Community (grant no. 01-0809), the OXIDE program of the Swedish Foundation for Strategic Studies, and the NATO "Science for Peace" program (project no. 973559).

REFERENCES

1. C. C. Tsuei and J. R. Kirtley, Rev. Mod. Phys. **72**, 969 (2000).
2. C. Hu, Phys. Rev. Lett. **72**, 1526 (1994); T. Lofwander, V. S. Shumeiko, and G. Wendin, Supercond. Sci. Technol. **14**, R53 (2001).
3. S. Kashiwaya, Y. Tanaka, M. Koyanagi, *et al.*, Phys. Rev. B **51**, 1350 (1995).
4. Yu. S. Barash, A. A. Svidzinsky, and H. Burkhardt, Phys. Rev. B **55**, 15 282 (1997).
5. J. Lesueur, L. H. Greene, W. L. Feldmann, and A. Inam, Physica C (Amsterdam) **191**, 325 (1992).
6. M. Covington, M. Aprili, E. Paraoanu, *et al.*, Phys. Rev. Lett. **79**, 277 (1997).
7. M. Aprili, E. Badica, and L. H. Greene, Phys. Rev. Lett. **83**, 4630 (1999).
8. R. Krupke and G. Deutscher, Phys. Rev. Lett. **83**, 4634 (1999).
9. J. Lesueur, X. Grison, M. Aprili, and T. Kontos, J. Low Temp. Phys. **117**, 539 (1999).
10. L. Alff, A. Beck, R. Gross, *et al.*, Phys. Rev. B **58**, 11 197 (1998).
11. W. Wang, M. Yamazaki, K. Lee, and I. Iguchi, Phys. Rev. B **60**, 4272 (1999).
12. J. Y. T. Wei, N.-C. Yeh, D. F. Garrigus, and M. Strasik, Phys. Rev. Lett. **81**, 2542 (1998).
13. M. Fogelstrom, D. Rainer, and J. A. Sauls, Phys. Rev. Lett. **79**, 281 (1997).
14. I. K. Bdikin, P. B. Mozhaev, G. A. Ovsyannikov, *et al.*, Fiz. Tverd. Tela (St. Petersburg) **43**, 1548 (2001) [Phys. Solid State **43**, 1611 (2001)].
15. C. B. Eom, A. F. Marshall, Y. Suzuki, *et al.*, Phys. Rev. B **46**, 11 902 (1992).
16. S. Poelders, R. Auer, G. Linker, *et al.*, Physica C (Amsterdam) **247**, 309 (1995).
17. M. Yu. Kupriyanov and K. K. Likharev, IEEE Trans. Magn. **27**, 2460 (1991).
18. M. B. Walker, cond-mat/9903012.
19. F. V. Komissinskiĭ, G. A. Ovsyannikov, and Z. G. Ivanov, Fiz. Tverd. Tela (St. Petersburg) **43**, 769 (2001) [Phys. Solid State **43**, 801 (2001)].
20. A. L. Shelankov, Fiz. Tverd. Tela (Leningrad) **26**, 1615 (1984) [Sov. Phys. Solid State **26**, 981 (1984)].
21. J. G. Simmons, J. Appl. Phys. **34**, 1793 (1963).
22. M. B. Walker and P. Pairor, Phys. Rev. B **60**, 10 395 (1999); Physica C (Amsterdam) **341–348**, 1523 (2000).
23. M. B. Walker and P. Pairor, Phys. Rev. B **59**, 1421 (1999).
24. J. W. T. Wei, N.-C. Yeh, D. F. Garrigus, and M. Strasik, Phys. Rev. Lett. **81**, 2542 (1998).
25. G. Deutscher, Y. Dagan, A. Kohen, and R. Krupke, Physica C (Amsterdam) **341–348**, 1629 (2000); Y. Dagan and G. Deutscher, Phys. Rev. Lett. **87**, 177 004 (2001).
26. R. B. Laughlin, Phys. Rev. Lett. **80**, 5188 (1998).
27. S. Yip, J. Low Temp. Phys. **91**, 203 (1993).
28. Yu. S. Barash, A. V. Galaktionov, and A. D. Zaikin, Phys. Rev. B **52**, 665 (1995).
29. R. A. Riedel and P. F. Bagwell, Phys. Rev. B **57**, 6084 (1998).
30. V. Ambegaokar and A. Baratoff, Phys. Rev. Lett. **10**, 486 (1963); Phys. Rev. Lett. **11**, 104 (1963).
31. T. Löfwander, V. S. Shumeiko, and G. Wendin, Phys. Rev. B **62**, R14653 (2000).
32. P. V. Komissinski, E. Il'ichev, G. A. Ovsyannikov, *et al.*, Europhys. Lett. **57**, 585 (2002).
33. E. Il'ichev, V. Zakosarenko, L. Fritzsch, *et al.*, Rev. Sci. Instrum. **72**, 1882 (2001).
34. K. K. Likharev and B. T. Ul'rikh, *Systems with Josephson Contacts: Foundations of Theory* (Mosk. Gos. Univ., Moscow, 1978).
35. V. N. Gubankov, V. P. Koshelets, and G. A. Ovsyannikov, Zh. Éksp. Teor. Fiz. **71**, 348 (1976) [Sov. Phys. JETP **44**, 181 (1976)].
36. E. Il'ichev, V. Zakosarenko, R. P. J. Ijsselsteijn, *et al.*, Phys. Rev. B **60**, 3096 (1999).
37. A. D. Mashtakov, K. I. Konstantinyan, G. A. Ovsyannikov, and E. A. Stepantsov, Pis'ma Zh. Tekh. Fiz. **25** (7), 1 (1999) [Tech. Phys. Lett. **25**, 249 (1999)].
38. G. A. Ovsyannikov, I. V. Borisenko, K. I. Konstantinyan, *et al.*, Pis'ma Zh. Tekh. Fiz. **25** (22), 65 (1999) [Tech. Phys. Lett. **25**, 913 (1999)].

Translated by V. Sipachev

Journal of Experimental and Theoretical Physics, Vol. 95, No. 6, 2002, pp. 1085–1091.
Translated from Zhurnal Éksperimental'noĭ i Teoreticheskoĭ Fiziki, Vol. 122, No. 6, 2002, pp. 1260–1267.

SOLIDS
Electronic Properties

Calculation of the Shape of the *R* Line of the Mn^{4+} Ion in Gadolinium–Gallium Garnet

S. V. Bulyarskiĭ, A. V. Zhukov*, A. M. Zyuzin, and V. V. Prikhod'ko
Ul'yanovsk State University, Ul'yanovsk, 432700 Russia
**e-mail: avg@ulsu.ru*
Received May 7, 2002

Abstract—A model is proposed for describing the luminescence and excitation spectra of paramagnetic ions with the $3d^3$ electron configuration in gadolinium-containing crystals that is based on the approximation of strong magnetic interaction between paramagnetic ions of transition metals and Gd^{3+} ions. This model provides a satisfactory description for the abnormally large width of the *R* line of the Mn^{4+} ion in gadolinium–gallium garnet. It is shown that the large Stokes shift in the luminescence spectrum of the Mn^{4+} ion in gadolinium–gallium garnet relative to the excitation spectra is associated with the splitting of energy levels as a result of magnetic interaction. An algorithm is developed for calculating the spectral shape of the *R* line of Mn^{4+} in gadolinium–gallium garnet. The possibility of determining the degree of sublevel broadening associated with the presence of inhomogeneities in the crystal and with thermal vibrations from an analysis of the width of the *R* line is demonstrated as well as the exchange interaction constant.

1. INTRODUCTION

In most materials, the *R* lines in the luminescence spectra of paramagnetic ions with $3d^3$ electron configuration are narrow lines with a halfwidth on the order of 1 cm^{-1} at liquid nitrogen temperature [1–6]. For example, the following results are described in the literature for the width of the *R* line for tetravalent manganese ions in various materials with octahedral ligand surroundings: $\Delta \approx 10$ cm^{-1} for $MgO : Mn^{4+}$ ($T = 77$ K) [7], $\Delta \approx 10$ cm^{-1} for $Y_3Al_5O_{12} : Mn^{4+}$ ($T = 80$ K) [8], and $\Delta \approx 3$ cm^{-1} for $Li_4Ge_5O_{12} : Mn^{4+}$ ($T = 50$ K) [9]. Such a broadening can be explained by inhomogeneities in the energy position of the ion due to the presence of defects in the lattice. Crystals containing gadolinium in the lattice are characterized by a special (anomalous) mechanism of broadening. For example, the width of the *R* line of the Mn^{4+} ion in gadolinium–gallium garnet (GGG) at 10 K attains 60 cm^{-1} [10]. Anomalous broadening of the *R* line was studied in $GdAlO_3 : Cr^{3+}$ [11], $Gd_3Sc_2Al_3O_{12} : Gr^{3+}$ [12], $Gd_3Ga_5O_{12} : Cr^{3+}$ [13], and $Gd_3Ga_5O_{12} : Mn^{4+}$ [10, 14]. Brenier *et al.* [14] attributed the *R*-line broadening to a strong electron–phonon interaction ($\hbar\omega = 8$ cm^{-1}, Huang–Riesz factor $S = 4.2$); however, they abandoned this idea later [10], assuming that the magnetic interaction of the paramagnetic ions of transition metals with gadolinium ions Gd^{3+} is responsible for the anomalous broadening of the *R* lines in these crystals.

In addition to a considerable broadening of *R* lines, an abnormally large Stokes shift in the emission spectrum relative to the excitation spectrum of the Mn^{4+} ion in GGG was also detected [14].

In this study, we propose a model for describing the luminescence and excitation spectra of paramagnetic ions with $3d^3$ electron configuration in gadolinium-containing crystals, which is based on the approximation of strong magnetic interaction of the paramagnetic ions of transition metals with Gd^{3+} ions. This model satisfactorily describes the abnormally large width of the *R* line of the Mn^{4+} ion in GGG. It is shown that the large Stokes shift in the luminescence spectrum of the Mn^{4+} ion in GGG relative to the excitation spectra is also associated with energy level splitting as a result of magnetic interaction. An algorithm for calculating the spectral shape of the *R* line of $GGG : Mn^{4+}$ was worked out from an analysis of the spin–spin interaction of the manganese ion and six gadolinium ions surrounding it. The developed model makes it possible to estimate the degree of broadening of the sublevels due to the presence of inhomogeneities in the crystal and thermal vibrations and to determine the exchange interaction constant from an analysis of the width of the *R* line.

2. CONSTRUCTION OF THE MODEL OF INTERACTION OF A Mn^{4+} ION WITH Gd^{3+} IONS IN $GGG : Mn^{4+}$

Analysis of the magnetic interaction of a manganese ion and six gadolinium ions surrounding it is facilitated by zero value of the orbital angular momentum of the Gd^{3+} ion. Indeed, an analysis of the structure of unfilled shells of Mn^{4+} and Gd^{3+} ions indicates the applicability of the Russel–Saunders scheme, in which the orbital l_i and spin s_i angular momenta can be regarded as additive independently and as forming the resultant orbital

L and spin S angular momenta of the shell as a whole. The total angular momentum of the shell can be defined as the sum of the latter quantities. In accordance with Hund's rule, the term ^8S ($L = 0$, $S = 7/2$) is the ground energy level of the Gd^{3+} ion, while the ground energy level of the Mn^{4+} ion is ^4F ($L = 3$, $S = 3/2$) and the first excited level of this ion is ^2G ($L = 4$, $S = 1/2$). As a result, the magnetic properties of these ions are mainly determined by spin angular momenta.

We used the model of isotropic spin–spin interaction [11] as the basis for calculating the shape of the R line in the luminescence spectra of GGG : Mn^{4+}. This model is applicable due to the symmetry of the surroundings: gadolinium ions are located at the sites of an octahedron with a manganese (or chromium [11]) ion at the center. Such symmetry exhibits many features in common with spherical symmetry. Moreover, in contrast to other rare-earth garnets, GGG displays absolute magnetic isotropy [15], which ensures such unique properties of this material as the absence of a long-range magnetic order up to 25 mK [16].

Isotropic spin–spin interaction can be presented by the Hamiltonian [11]

$$H = -J\mathbf{S}_{\mathrm{Mn}} \cdot \mathbf{S}_{\mathrm{Gd}}. \tag{1}$$

Here, J is the overlap integral and $\mathbf{S}_{\mathrm{Mn}}$ and $\mathbf{S}_{\mathrm{Gd}}$ are the spins of the manganese ion and the total spin of the gadolinium ions surrounding it. The overlap integral for Mn^{4+} in GGG was calculated in [10] from an analysis of the Zeeman effect, $J = 1.9$ cm^{-1}. The total spin $\mathbf{S}_{\mathrm{Gd}}$ is the vector sum $\mathbf{S}^k_{\mathrm{Gd}}$ of six spins of the gadolinium ions surrounding the manganese ion. At temperatures approximately above 3 K, the spins can be regarded as independent [15, 17] and Hamiltonian (1) splits into six independent terms of the form $H = -J\mathbf{S}_{\mathrm{Mn}} \cdot \mathbf{S}^k_{\mathrm{Gd}}$. The eigenvalues of these operators are given by

$$E_k = -\frac{J}{2}[S^k(S^k + 1) - S^k_{\mathrm{Gd}}(S^k_{\mathrm{Gd}} + 1) - S_{\mathrm{Mn}}(S_{\mathrm{Mn}} + 1)], \tag{2}$$

where $S^k(S^k + 1)/2$ is the eigenvalue of operator $(\mathbf{S}^k)^2 = (\mathbf{S}_{\mathrm{Mn}} + \mathbf{S}^k_{\mathrm{Gd}})^2$. Since $S^k_{\mathrm{Gd}} = 7/2$, while the spin of a manganese ion is $S_{\mathrm{Mn}}(^4A_2) = 3.2$ in state $^4A_2$ and $S_{\mathrm{Mn}}(^2E) = 1/2$ in state ^2E, $S^k(^4A_2)$ can assume values of 2, 3, 4, or 5, while $S^k(^2E)$ can assume the value 3 or 4.

Summation of six values of E_k gives a set of possible energy values for sublevels of terms $^4A_2$ and ^2E with different statistical weights. Indeed, $E = -59.85$ cm^{-1} can be realized, for example, for the only combination of spins of six gadolinium ions and a manganese ion, i.e., for their parallel arrangement. At the same time, the value $E = 6.65$ cm^{-1} is realized for 180 combinations of vectors.

In order to determine the statistical weights of sublevels, a random quantity distributed uniformly and assuming four discrete values (2) was juxtaposed to each Gd–Mn pair. The corresponding expression for the probability density has the form

$$p^k(E) = \frac{1}{4}\sum_{i=0}^{3}\delta_{E_i, E}, \tag{3}$$

where $\delta_{i,j}$ is the Kronecker delta.

The random quantity corresponding to all possible values of energy of the sublevels is the sum of six random quantities distributed according to law (3). The independence of these random quantities is important for the subsequent analysis. This corresponds to the physical situation without spin ordering. Such a situation is realized at temperatures above the Curie point, at which the crystal becomes paramagnetic. In this case, in accordance with probability theory, the probability densities of the sum of independent random quantities can be represented in the form [18]

$$p(E) = p^k(E) * p^k(E) * p^k(E) * p^k(E) * p^k(E) * p^k(E),$$

where the asterisk marks the convolution operation.

The values of $p(E)$ for terms $^4A_2$ and ^2E are calculated in the Appendix.

3. CALCULATION OF THE SPECTRAL SHAPE OF THE R LINE OF RADIATION FROM Mn^{4+} ION IN GGG : Mn^{4+}

Expressions (A.5) and (A.6) in the Appendix considerably facilitate the calculation of statistical weights. In accordance with these relations and Eq. (2), we calculated the level splitting of the terms $^4A_2$ and ^2E. Figure 1 shows the position of the sublevels of these terms and their statistical weights C_i. It can be seen that the figure clearly reflects the closeness of the statistical weight distribution to the normal distribution, which is in accordance with the central limiting theorem [18]. Nevertheless, the patterns of splitting of the $^4A_2$ and ^2E states differ considerably. In the former case, 57 sublevels are distributed quite chaotically in the interval from -59.85 and 76.95 cm^{-1}, while in the latter case there are seven equidistant sublevels in the interval from -19.95 to 25.65 cm^{-1}. The common feature of the two distributions is that the distribution peaks are displaced towards the short-wave region by 2.85 cm^{-1} for the $^4A_2$ term and by 12.35 cm^{-1} for the ^2E term. This fact is significant since its disregard may lead to an incorrect interpretation of spectroscopic data used for calculating the crystal field parameters.

The population of each sublevel is proportional to $f(E_i) = C_i\rho(E_i)$, where

$$\rho(E_i) = \exp(-E_i/kT) \tag{4}$$

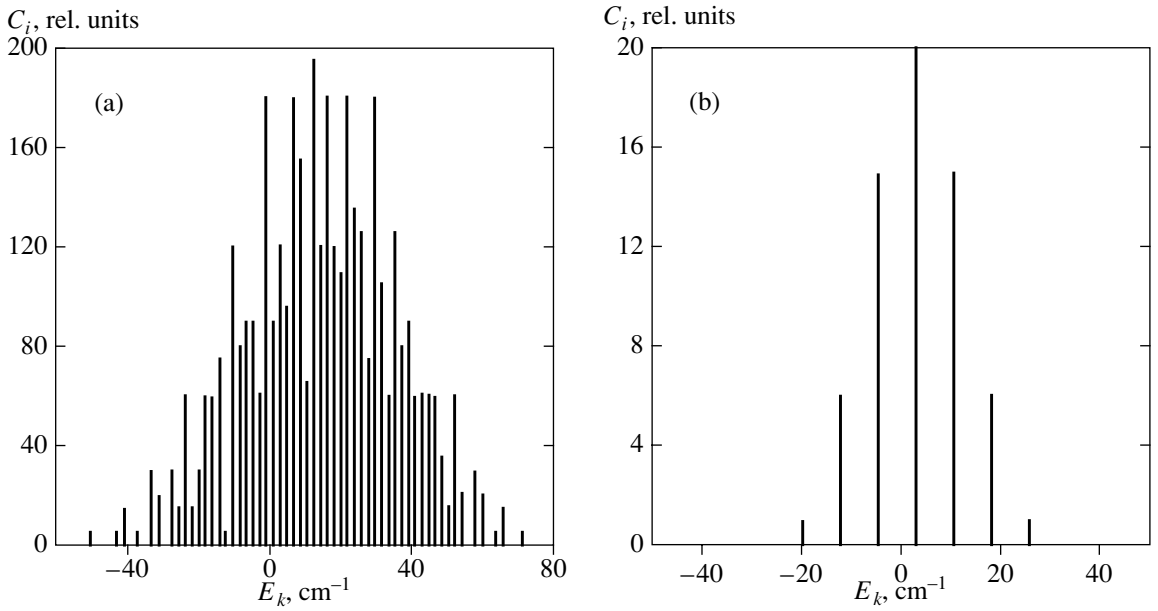

Fig. 1. Calculated splitting of $^4A_2$ (a) and ^2E (b) terms of the Mn^{4+} ion in GGG, associated with the spin–spin interaction.

is the Boltzmann function. Thus, knowing the position and occupancy of sublevels, we can find the shape of the optical transition line; the general expression for this line has the form

$$I(\hbar\omega) = \sum_{ij} \rho(E_i) C_i C_j M_{ij}^2 \delta(\hbar\omega - E_i + E_j), \qquad (5)$$

where i and j label the sublevels of the initial and final states, respectively, and M_{ij} is the matrix element of the i–j transition. To a high degree of accuracy, we can assume that M_{ij} is a constant quantity: $M_{ij} = M$. In the case when index i corresponds to the term ^2E and j to $^4A_2$, Eq. (5) describes the luminescence spectrum; in the opposite case, we obtain the excitation spectrum.

It should be noted that the sublevels in Fig. 1 and in expression (5) are presented by δ peaks. Experiments show that real crystals always contain inhomogeneities, which are manifested in a certain energy distribution (broadening) of energy levels. For this reason, a Gaussian distribution with a certain standard deviation σ associated with the presence of inhomogeneities in the crystal and thermal vibration should be used in actual practice in Eq. (5) instead of the δ function. In this case, expression (5) can be rewritten in the form

$$I(\hbar\omega) = M^2 \int \rho(E) f_2(E - \hbar\omega) f_1(E) dE, \qquad (6)$$

where

$$f_{1,2}(E) = \sum_i \frac{C_i}{\sqrt{2\pi}\sigma} \exp\left[-\frac{(E - E_i)^2}{2\sigma^2}\right].$$

The value of the standard deviation σ is determined by the crystal quality and temperature [19].

Curve *1* in Fig. 2 shows the shape of the *R* line for the $^2E \longrightarrow {}^4A_2$ optical transition, calculated by formula (5). At low temperatures, the line width is mainly determined by the splitting of the $^4A_2$ term and displays a weak temperature dependence determined by the tem-

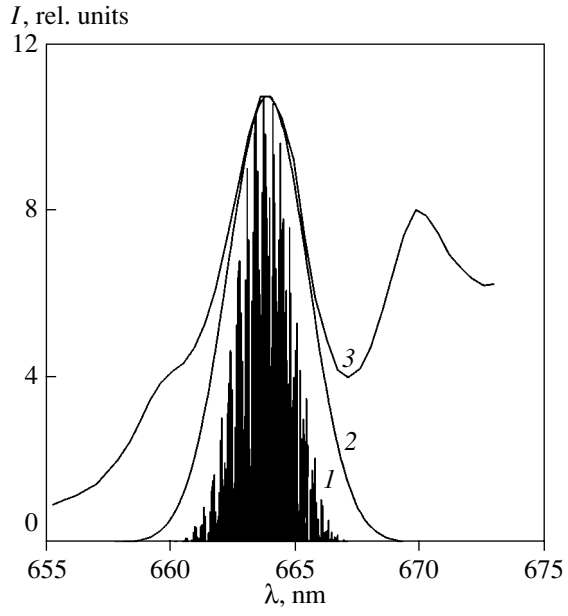

Fig. 2. *R* line of GGG : Mn^{4+} calculated by formula (6) for $\sigma = 0$ cm^{-1} (curve *1*) and $\sigma = 20$ cm^{-1} (curve *2*) and experimentally measured luminescence spectrum at 100 K (curve *3*).

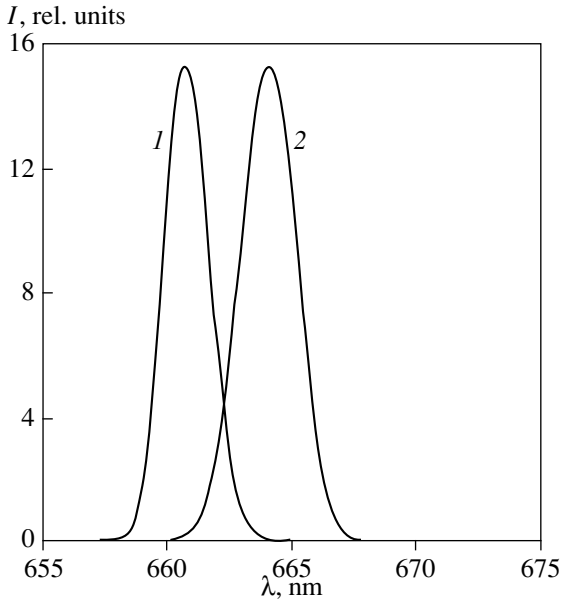

Fig. 3. Calculates shape of the *R* line in GGG : Mn^{4+} in the excitation (curve *1*) and luminescence (curve *2*) spectra at 10 K.

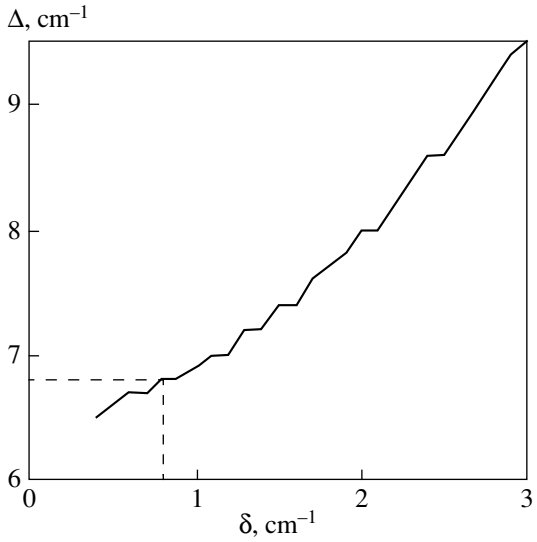

Fig. 4. Calculated dependence of the width of the *R* line for GGG : Cr^{3+} on the sublevel broadening associated with inhomogeneities in the crystal ($J = 0.24$ cm^{-1}). Dashed lines mark the experimentally observed [11] width $\Delta = 6.8$ cm^{-1} of the *R* line as well as the sublevel broadening $\delta = 0.8$ cm^{-1}.

perature dependence of the Boltzmann distribution. At extremely low temperatures, the calculated *R* line has a minimal width of about 45 cm^{-1}, which is in good agreement with experimental data [10, 14, 20].

In [21], the Gaussian shape of the *R* line of GGG : Cr^{3+} at $T = 10$ K was attributed to nonuniform broadening. Our results show that the main contribution to the line width at such temperatures comes from the splitting of the $^4A_2$ term. The Gaussian shape of the line is due to multiple convolution of random quantities E_k. It should be noted, however, that the shape of the emission and absorption lines at low temperatures is asymmetric (Fig. 3). Figure 2 shows for comparison the experimental luminescence spectrum of GGG : Mn^{4+} measured at $T = 100$ K [20] (curve *3*). The difference in the halfwidths of curves *1* and *3* indicates the presence of an additional broadening associated with inhomogeneities in the crystal and lattice vibrations. The use of Eq. (6) instead of Eq. (5) makes it possible to take this effect into consideration. For example, curve *2* in Fig. 2 shows the theoretical shape of the *R* line that best agrees with experiments. In order to obtain the width $\Delta = 84$ cm^{-1} observed, we used the value $\sigma = 20$ cm^{-1} in Eq. (6).

Temperature dependences of the width of the *R* line and sublevel broadening for Mn^{4+} ion in GGG

T, K	$\Delta(T)$, cm^{-1}	Δ_0, cm^{-1}	$\Delta_V(T)$, cm^{-1}	σ, cm^{-1}	$a_0 = \sigma/\Delta_V(T)$
100	84	52	66	20	0.303
125	101	52	87	27	0.310
150	123	52	111	34	0.306
175	149	53	139	42	0.302
200	176	53	168	50	0.298
225	210	53	204	61	0.299

4. ANALYSIS OF THE SHAPE OF THE *R* LINE OF EMISSION FROM Mn^{4+} AND Cr^{3+} IN GGG

In order to analyze how the shape of the optical transition line depends on the degree of broadening of sublevels for several values of σ in the interval from 20 to 60 cm^{-1}, the shape of the optical transition line was calculated and the halfwidth determined. The values obtained for GGG : Mn^{4+} and GGG : Cr^{3+} systems obtained in this way are presented in the table and in Fig. 4, respectively. For describing the observed nonlinear dependences, the width of the *R* line was represented in the form

$$[\Delta(T)]^2 = \Delta_0^2 + [\Delta_V(T)]^2,$$

where Δ_0 is the minimal width associated with the spin–spin interaction and $\Delta_V(T)$ is the contribution determined by lattice vibrations. These values were calculated and are presented the table. In addition to the above-mentioned quantities, the table also contains the values of σ at which the experimentally observed width

of the *R* line was attained (Fig. 5). The last column of the table contains the ratio of the quantities σ and Δ_V, which clearly demonstrates their direct proportionality with the proportionality factor $a_0 \approx 0.3$. This makes it possible to estimate the value of σ from the known width of the *R* line using the formula

$$\sigma(T) = a_0\sqrt{\Delta^2(T) - \Delta_0^2},$$

where the value of Δ_0 can be set equal to 50 cm^{-1} in a wide temperature range.

The proposed model of level splitting makes it possible to determine such fundamental characteristics as the exchange interaction constant *J* provided that the width of the *R* line is known as well as the broadening of individual sublevels. One can also obtain information on the broadening δ of individual sublevels formed as a result of the spin–spin interaction.

The value of *J* is usually determined by measuring the luminescence spectrum in a strong magnetic field at low temperatures. For example, GGG : Mn^{4+} samples in [10] were placed in a magnetic field of strength 20 T; as a result, a set of narrow lines was observed at 2.2 K in the spectrum, the positions of which were determined both by exchange interaction and by the Zeeman effect, which complicates the identification of individual lines. In the case of GGG : Mn^{4+}, identification is possible due to such an anomalously large value of *J* that exchange splitting is many times stronger than the Zeeman splitting. In the case of GGG : Cr^{3+} in the field 4.6 T attained in [13], the corresponding values of splitting are comparable, which ruled out the separation of the exchange interaction component. However, the values of the width of the *R* line and an individual sublevel given in [13] for $T = 4.2$ K are the same as in Fig. 5.

These data enabled us to calculate the exchange interaction constant using the theory of the shape of the *R* line developed in this section. Taking into account expression (6), we calculated the dependence of the width of the *R* line δ for GGG : Cr^{3+} on the broadening δ of sublevels for different values of *J*. Figure 4 shows the curve plotted for $J = 0.24$ cm^{-1}.The agreement between the experimental data is observed precisely for this value ($\delta = 0.8$ cm^{-1} corresponds to $\Delta = 6.8$ cm^{-1}). For other values of *J*, the curves lie either above or below the curve depicted in Fig. 4.

The calculated exchange interaction constant $J = 0.24$ cm^{-1} is close to the value $J = 0.25$–0.33 cm^{-1} obtained in [12] for $Gd_2Sc_2Al_3O_{12} : Cr^{3+}$.

A considerable Stokes shift of the *R* line in the luminescence spectra relative to the excitation spectra, which was mentioned in [10, 14], can also be explained in terms of the spin–spin interaction. It was mentioned above that Eq. (6) makes it possible to calculate not only the luminescence spectrum, but also the excitation spectrum. The corresponding shapes of spectral lines

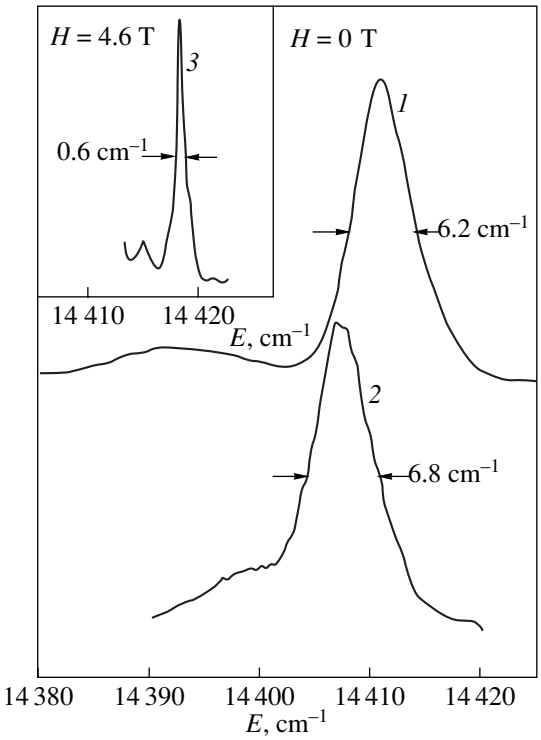

Fig. 5. Emission spectrum for the $^2E \longrightarrow {}^4A_2$ transition in GGG : Cr^{3+} at $T = 4.2$ K [11]: excitation to the $^4A_2 \longrightarrow {}^4T_2$ transition band (*1*), resonance excitation (*2*) (spectra *1* and *2* are measured in zero magnetic field), and resonance excitation in the field 4.6 T (*3*).

were calculated at various temperatures. For example, Fig. 3 shows the excitation spectra (curve *1*) and luminescence spectra (curve *2*) for GGG : Mn^{4+}, calculated for $T = 10$ K. The model spectra are in excellent agreement with the experimentally measured spectra (see Fig. 8 in [10]). The difference between the positions of the peaks at this temperature amounts to 68 cm^{-1}, which corresponds to the data described in [14].

The spectral shift is caused by nonuniform filling of sublevels of the terms $^4A_2$ and ^2E in accordance with the Boltzmann distribution (4). This is manifested in a weak temperature dependence of the Stokes shift: upon an increase in temperature, the shift decreases mainly due to the displacement of the peak in the excitation spectrum. However, to our knowledge, experimental studies of this effect have not been reported in the literature.

5. CONCLUSIONS

We have proposed a model for describing the luminescence and excitation spectra for paramagnetic ions with $3d^3$ electron configuration in gadolinium-containing crystals. The model is based on an assumption concerning the dominating role of the magnetic interaction

between paramagnetic ions of transition metals and the Gd^{3+} ions as compared to the electron-phonon or any other excitation. The shape of the *R* line in the excitation and luminescence spectra of GGG : Mn^{4+} calculated on the basis of this model was completely similar to the experimental spectra and the values of the width of the *R* line as well as the Stokes shift obtained by other authors [10, 14].

It is shown in addition that the developed model makes it possible to estimate the broadening of sublevels due to the presence of inhomogeneities and thermal vibrations in the crystal and to determine the exchange interaction constant from an analysis of the width of the *R* line. Recent calculations made for Cr^{3+} ions in GGG are in accord with the results obtained by other researchers [12].

APPENDIX

Let us prove that the values of $p(E)$ for the $^4A_2$ term are equal to the coefficients in the polynomial

$$\tilde{P}(x) = (x^{30} + x^{20} + x^{12} + x^6)^6.$$

We juxtapose each value of E^k to a random quantity ξ_k assuming the values 6, 12, 20, and 30 with the same probability. In this case, the quantities E^k can be expressed in terms of ξ_k as follows:

$$E^k = -\frac{J}{2}(\xi_k - 19.5); \tag{A.1}$$

here, the number 19.5 is the sum of the second and third terms in expression (2). The probability density of the random quantity ξ_k can be written as

$$p(\xi_k) = \frac{1}{4}\sum_{i=2}^{5}\delta_{i(i+1),\xi_k}, \tag{A.2}$$

where $\delta_{i,j}$ is the Kronecker delta.

Let us eliminate the normalization factor 1/4 and represent $i(i + 1)$ in the form $f(i)$. In this case, the convolution of two densities of the form (A.2) can be written as

$$p(\zeta) = \sum_{\xi,i,j}\delta_{f(i),\xi}\delta_{f(j),\zeta-\xi}, \tag{A.3}$$

where ζ is the random quantity which is the sum $\xi + \xi$. Carrying out the obvious substitution

$$\delta_{f(j),\zeta-\xi} = \delta_{\zeta-f(j),\xi},$$

we obtain

$$\sum_{\xi}\delta_{f(i),\xi}\delta_{\zeta-f(j),\xi} = \delta_{f(i)+f(j),\zeta}.$$

Taking into account this relation, we can write Eq. (A.3) as follows:

$$p(\zeta) = \sum_{i,j}\delta_{f(i)+f(j),\zeta}. \tag{A.4}$$

Since most values of the sum $f(i) + f(j)$ can be obtained for several combinations of i and j, each value of ζ has its own statistical weight.

Let us now consider the product of two sums of the form $\sum_i x^{f(i)} = (x^6 + x^{12} + x^{20} + x^{30})$:

$$\begin{aligned}\sum_i x^{f(i)}\sum_j x^{f(j)} &= \sum_i\sum_j x^{f(i)+f(j)} \\ &= \sum_k\sum_i\sum_j x^k\delta_{f(i)+f(j),k} = \sum_k a_k x^k,\end{aligned} \tag{A.5}$$

where $a_k = \sum_{i,j}\delta_{f(i)+f(j),k}$, which is completely identical to expression (A.4).

Thus, we have proved the equivalence of the convolution of random quantities of the type (A.2) and the product of polynomials of the form (A.5).

It can be proved similarly that the values of $p(E)$ for the ^2E term correspond to coefficients of the polynomial

$$\tilde{P}(x) = (x^{20} + x^{12})^6. \tag{A.6}$$

REFERENCES

1. S. V. Grum-Grzhimaĭlo, L. B. Pasternak, and R. K. Sviridova, *Spectroscopy of Crystals* (Nauka, Moscow, 1966), Vol. 65.
2. B. Struve and G. Huber, Appl. Phys. B **36**, 195 (1985).
3. V. M. Faĭn and Ya. I. Khanin, *Quantum Radiophysic* (Sov. Radio, Moscow, 1965).
4. M. M. Zaripov and Yu. Ya. Shamonin, Zh. Éksp. Teor. Fiz. **30**, 291 (1956) [Sov. Phys. JETP **3**, 171 (1956)].
5. S. V. Grum-Grzhimaĭlo, *Spectroscopy of Crystals* (Nauka, Moscow, 1966), Vol. 51.
6. W. Low, in *Lasers*, Ed. by M. E. Zhabotinskiĭ and T. A. Shmaonov (Inostrannaya Literatura, Moscow, 1963).
7. B. Henderson and T. P. P. Hall, Proc. Phys. Soc. London **90**, 511 (1967).
8. L. A. Riseberg and M. J. Weber, Solid State Commun. **9**, 791 (1971).
9. A. Suchocki, J. D. Allen, and R. C. Powell, Phys. Rev. B **36**, 6729 (1987).
10. A. Suchocki, M. Potemski, A. Brenier, *et al.*, J. Appl. Spectrosc. **65**, 181 (1995).
11. J. Murphy and R. C. Ohlmann, in *Optical Properties of Ions in Crystals*, Ed. by H. M. Crosswhite (Wiley, New York, 1967), p. 239.
12. M. Yamaga, Y. Gao, K. P. O'Donnell, and B. Henderson, J. Phys.: Condens. Matter **5**, 915 (1993).

13. A. Monteil, M. Ferrari, and F. Rossi, Phys. Rev. B **43**, 3646 (1991).
14. A. Brenier, A. Suchocki, C. Pedrini, *et al.*, Phys. Rev. B **46**, 3219 (1992).
15. O. A. Petrenko, D. McK Paul, C. Ritter, *et al.*, Physica B (Amsterdam) **266**, 41 (1999).
16. A. P. Ramírez and R. N. Kleiman, J. Appl. Phys. **69**, 5252 (1991).
17. O. A. Petrenko, C. Ritter, M. Yethiraj, and D. McK Paul, Physica B (Amsterdam) **241**, 241 (1997).
18. V. S. Korolyuk, N. I. Portenko, A. V. Skorokhod, and A. F. Turbin, *Handbook of Probability Theory and Mathematical Statistics* (Nauka, Moscow, 1985).
19. A. L. Schawlow, in *Advances in Quantum Electronics* (Columbia Univ. Press, New York, 1961), p. 50.
20. S. V. Bulyarskiĭ, A. V. Zhukov, and V. V. Prikhod'ko, Pis'ma Zh. Éksp. Teor. Fiz. **74**, 616 (2001) [JETP Lett. **74**, 543 (2001)].
21. M. Yamaga, B. Henderson, and K. P. O'Donnell, J. Lumin. **46**, 397 (1990).

Translated by N. Wadhwa

Journal of Experimental and Theoretical Physics, Vol. 95, No. 6, 2002, pp. 1092–1096.
Translated from Zhurnal Éksperimental'noĭ i Teoreticheskoĭ Fiziki, Vol. 122, No. 6, 2002, pp. 1268–1273.

MISCELLANEOUS

Decrease in Entropy as a Result of Measuring the Time of Escape from a Potential Well

O. A. Chichigina
Moscow State University, Vorob'evy gory, Moscow, 119899 Russia
e-mail: chichigina@squeez.phys.msu.su
Received March 28, 2002

Abstract—The decrease in entropy when passing from an equilibrium thermodynamic system to a slightly nonequilibrium system is investigated. A quasi-equilibrium Boltzmann distribution is used to prove the conservation of free energy during this passage. Results are obtained for a Brownian particle in a potential well with a low escape probability. The escape is interpreted as a measurement. It is shown that because of the measurement itself, the distribution function is narrower than that for a system undisturbed by measurement, i.e., an equilibrium system. In this case, the entropy difference between the equilibrium and measurement-disturbed systems is equal to the amount of information entered into the system. *© 2002 MAIK "Nauka/Interperiodica".*

1. INTRODUCTION

Brownian motion is a fundamental concept of statistical physics and thermodynamics. Fluctuations in thermodynamic parameters can be represented as the motion of Brownian particles in complex potentials. Of particular importance is the description of these fluctuations in the theory of phase transitions, where the change in order parameter corresponds to the displacement of a Brownian particle and the free energy acts as the potential in which it moves. The phase transition itself then corresponds to the particle's escape from a potential well.

In addition, a Brownian particle is a simple but complete model of an open system that exchanges not only energy but also information with external bodies. It is convenient to use this particle as an example to elucidate many fundamental questions, including the second law of thermodynamics in generalized formulation.

Let us consider the Brownian motion of a single particle in a potential well $U(\mathbf{r}) \le 0$ under the action of external noise with temperature T. Its velocity obeys a Maxwellian distribution. The particle can escape from this well by overcoming the potential barrier along which $U = 0$, but the probability of this event is low. This is an equilibrium process in velocities but a nonequilibrium process in coordinates, because the velocity correlation time is much shorter than the coordinate correlation time τ_c.

A formula to calculate the escape constant a (i.e., the reciprocal of the mean lifetime τ) for a quasi-equilibrium system was derived in [1–4]. The constant a has the meaning of escape probability per unit time.

It was also shown in the above papers that, because a is small, the escape is an exponential process, thereby resembling a spontaneous decay. More specifically, the probability that a particle located in a well at the initial time will be detected there at time t is given by

$$P(t) = \exp(-at). \tag{1}$$

According to [5, 6], a depends on the mean particle energy in the well as follows:

$$a = C\exp\left(\frac{\langle U\rangle}{kT}\right) = \frac{1}{\tau}, \tag{2}$$

where C is a function that depends on T alone and that does not depend on U. On the other hand, this probability is related to the probability distribution in coordinates near the well boundary S_0, which imposes certain conditions on the form of this probability distribution $w(\mathbf{r})$. For example, for two-dimensional motion, we have

$$a = \sqrt{\frac{kT}{2m\pi}}Lw(S_0) = \frac{1}{\tau},$$

where L is the length of the boundary through which the particle escapes. If the particle can escape from a potential well in the course of time, then the motion in the well is a nonequilibrium process and, strictly speaking, it cannot be described by a stationary probability distribution.

However, the authors of [5, 6] obtained a stationary probability distribution in coordinates for a particle in a potential well with the possibility of escape from this well. Clearly, this distribution can be used only if the system lifetime is large compared to the correlation time, $\tau \gg \tau_c$. This quasi-equilibrium Boltzmann distribution is given by

$$w(\mathbf{r}) = \frac{1}{\Omega}\exp\left(\frac{\langle U\rangle - U(\mathbf{r})\alpha}{kT}\right), \tag{3}$$

1063-7761/02/9506-1092$22.00

where Ω is the well volume. The constant α characterizes the degree of system nonequilibrium. For $\alpha = 1$, we simply obtain the Boltzmann distribution. To determine α and $\langle U\rangle$, we have the system of equations

$$\begin{aligned}\int \exp\left(\frac{-U\alpha}{kT}\right)d\mathbf{r} &= \Omega\exp\left(\frac{-\langle U\rangle}{kT}\right),\\ \int U\exp\left(\frac{-U\alpha}{kT}\right)d\mathbf{r} &= \langle U\rangle\Omega\exp\left(\frac{-\langle U\rangle}{kT}\right).\end{aligned} \tag{4}$$

The first equation can be derived from the normalization condition and the second equation can be derived from the fact that $\langle U\rangle$ is the mean of U. It is easy to verify that (3) satisfies all of the above conditions, which relate the escape probability to the mean energy and to the probability distribution in coordinates.

If we compare (3) with the nonstationary distribution that is the solution to the Fokker–Planck equation [7–9], then our quasi-equilibrium distribution corresponds to a conditional distribution within the potential well, provided that the escape has not yet occurred.

It was also shown in [5, 6] that $\alpha \geq 1$ for any T and $U(\mathbf{r})$. Thus, the probability distribution for a nonequilibrium process is narrower than that for an equilibrium process in a well with the same potential relief but with a wall at the top of the potential barrier, which prevents particle escape. Such an equilibrium system is described by the Boltzmann distribution and all its related quantities are marked by the subscript B. Therefore, the mean particle energy in a well with the possibility of escape is lower than that in an equilibrium system. According to (2), the mean time of escape from the well, τ, is larger than the mean time between collisions with the wall in the closed region, τ_B. This result is confirmed by computer experiments [6].

Imagine an experiment in which we catch the particle that escaped from a well, throw it back into the well with a velocity corresponding to an elastic collision with the wall, and wait for the next particle escape. In this case, our system differs from an equilibrium system with a wall only in the measurement of escape times (or times of collision with the wall). The fact that a measurement causes the distribution function to narrow resembles the problem of quantum measurements and it can serve as a classical analog of the partial collapse of the wave function.

In the classical case, the difference between the mean lifetimes can be explained by the fact that our model of a nonequilibrium process excludes fast escapes from the potential well, i.e., those that occurred in a time shorter than the correlation time.

Otherwise, the narrowing of the probability distribution can be interpreted as a decrease in the effective temperature similar to the cooling of a fluid as it evaporates. Only a fluid decreases the temperature after (as a result of) the escape of a molecule. In our case, the possibility of escape itself (a nonzero probability of this event) causes a decrease in the temperature as the coefficient that determines the probability distribution.

The decrease in entropy in the system as a result of measurement can be assumed to be equal to the amount of information on the escape time:

$$S_B - S = I, \tag{5}$$

where S_B is the entropy of the equilibrium system described by the Boltzmann distribution, S is the entropy of the quasi-equilibrium system, and I is the amount of information on the escape time. This relation between entropy and information for a thermodynamically isolated system was discussed in [10, 11] in connection with an analysis of the so-called Maxwell demon. Here, we confirm and interpret the result (5).

2. CHANGE IN ENTROPY

The entropy of an equilibrium state without the additive constant is

$$\begin{aligned}S_B &= -k\langle \ln w_B(\mathbf{r})\rangle\\ &= k\frac{\langle U\rangle}{kT} + k\ln\int_\Omega \exp\left(\frac{-U}{kT}\right)d\mathbf{r}.\end{aligned} \tag{6}$$

The integral in the second term can be transformed as follows:

$$\begin{aligned}J &= \int \exp\left(\frac{-U}{kT}\right)d\mathbf{r} = \exp\left(\frac{-U^*}{kT}\right)\\ &\times\int\exp\left(\frac{(U^*-U)\alpha-(\alpha-1)(U^*-U)}{kT}\right)d\mathbf{r}.\end{aligned}$$

We chose such U^* that $\exp(-(\alpha-1)(U^*-U)/kT)$ could be expanded in a series in which only the linear term was retained and the error would be at a minimum; we then obtain

$$\begin{aligned}J &= \exp\left(\frac{-U^*}{kT}\right)\int\exp\left(\frac{(U^*-U)\alpha}{kT}\right)\\ &\times\left(1-\frac{(\alpha-1)(U^*-U)}{kT}\right)d\mathbf{r}.\end{aligned}$$

Using system (4), we derive

$$\begin{aligned}J &= \exp\left(\frac{U^*(\alpha-1)-\langle U\rangle}{kT}\right)\\ &\times\Omega\left(1-\frac{(\alpha-1)(U^*-\langle U\rangle)}{kT}\right).\end{aligned} \tag{7}$$

Let us now find out at which U^* the error in the expansion of the exponential function in a series is at a minimum. Let us introduce the function

$$f(U^*) = \int\exp\left(\frac{-U\alpha}{kT}\right)$$

$$\times\left\{\exp\left(\frac{-(\alpha-1)(U^*-U)}{kT}\right)\right.$$

$$\left.-\left(1-\frac{(\alpha-1)(U^*-U)}{kT}\right)\right\}d\mathbf{r}$$

that describes this error and determine the U^* that corresponds to its minimum. We obtain,

$$\exp\left(\frac{-(\alpha-1)U^*}{kT}\right)\int\exp\left(\frac{-U}{kT}\right)d\mathbf{r}$$

$$-\int\exp\left(\frac{-U\alpha}{kT}\right)d\mathbf{r} = 0.$$

Substituting the integrals from (7) and (4) in the first and second terms, respectively, yields

$$U^* = \langle U\rangle.$$

Using this equality, Eq. (7) can be simplified to give

$$J = \exp\left(\frac{-\langle U\rangle(2-\alpha)}{kT}\right)\Omega. \tag{8}$$

Given (3), the entropy of the quasi-equilibrium state can be written as

$$S = k\frac{\langle U\rangle}{kT}(\alpha-1) + k\ln\Omega. \tag{9}$$

Given (6), (8), and (9), the change in entropy in (5) can be represented as

$$S_B - S = \frac{\langle U\rangle_B - \langle U\rangle}{T}. \tag{10}$$

It thus also follows that the free energy is the same for the equilibrium and quasi-equilibrium states. For both cases, it is defined by

$$F = \langle U\rangle + jkT/2 - ST,$$

where j is the number of degrees of freedom of the particle and the second term is its mean kinetic energy.

3. INFORMATION ON THE TIMES OF ESCAPE FROM A POTENTIAL WELL

A quasi-equilibrium system differs from an equilibrium system by the availability of information on the particle escape times (or, equivalently, on the times of collision with the wall).

To determine the amount of information, we must discretize the time, i.e., specify the characteristic time interval. This interval is the mean time τ_B between collisions with the wall in the equilibrium case. The escape probability during the ith interval does not depend on i and is

$$p = a\tau_B = \tau_B/\tau.$$

According to the Shannon formula (see, e.g., [7]), the information obtained when specifying the number i of one of the equiprobable intervals during which the particle escape occurred is

$$I = -k\ln p.$$

Taking into account the dependence of τ_B on the mean energy (2) and assuming it to be the same for the equilibrium system, we obtain

$$I = \frac{\langle U\rangle_B - \langle U\rangle}{T}.$$

This relation is identical to the expression for the entropy difference (10) and it confirms formula (5). Thus, we found the decrease in entropy in the system to be equal to the amount of information entered into it. Of greatest interest is the possibility of simulating effects that are considered to be purely quantum ones in a classical system. However, all our results are also applicable to quantum systems.

4. A QUANTUM QUASI-EQUILIBRIUM PROBABILITY DISTRIBUTION

Formula (3) in a quantum description of the distribution in ith states with energy E_i is

$$w_i = \exp\left(\frac{\langle E\rangle - E_i\alpha}{kT}\right).$$

It is a quasi-equilibrium Gibbs distribution. In this case, the integrals in system (4) are substituted with the sums

$$\sum\exp\left(\frac{-E_i\alpha}{kT}\right) = \exp\left(\frac{-\langle E\rangle}{kT}\right),$$
$$\sum E_i\exp\left(\frac{-E_i\alpha}{kT}\right) = \langle E\rangle\exp\left(\frac{-\langle E\rangle}{kT}\right). \tag{11}$$

Relation (5) for a quantum system can be derived in a similar way.

5. EXAMPLES OF THE DEPENDENCE OF THE CHANGE IN ENTROPY ON THE DEPTH AND SHAPE OF A POTENTIAL WELL

To save space, we introduce the following dimensionless variables:

$$\beta = \frac{U_{\min}}{kT} < 0, \quad 0 < \gamma = \frac{\langle U\rangle}{U_{\min}} < 1,$$

$$0 < u = \frac{U}{U_{\min}} < 1, \quad s = \frac{S}{k}.$$

Consider a parabolic potential well

$$U = U_{\min}(1 - r^2/R^2).$$

For this well, system (11) can be written as

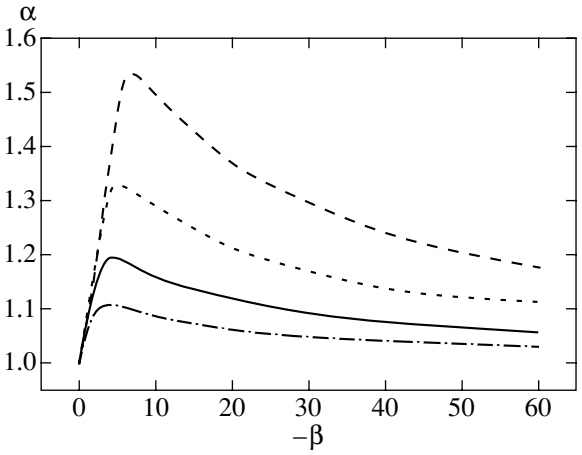

Fig. 1. The parameter of nonequilibrium α versus potential-well depth β for parabolic (solid line), cone-shaped (dotted line), and root potential wells and for a well of the form $U = U_{\min}(1 - (r/R)^4)$ (dash-dotted line).

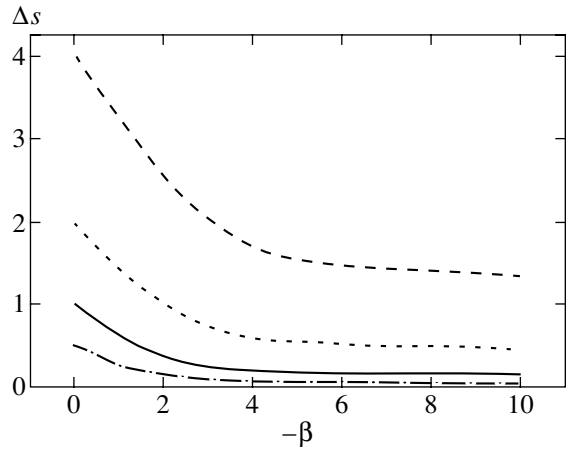

Fig. 2. The change in entropy Δ*s* versus potential-well depth β for parabolic (solid line), cone-shaped (dotted line), and root potential wells and for a well of the form $U = U_{\min}(1 - (r/R)^4)$ (dash-dotted line).

$$e^{-\beta\alpha} - 1 = -\alpha\beta e^{-\gamma\beta},$$

$$\left(\gamma\beta - \beta - \frac{1}{\alpha}\right)\alpha e^{-\gamma\beta} = -1.$$

For a cone-shaped well

$$U = U_{\min}(1 - r/R),$$

we obtain the equations

$$\beta\alpha - 1 + e^{-\beta\alpha} = \frac{1}{2}(\alpha\beta)^2 e^{-\gamma\beta},$$

$$\left(\gamma\beta - \beta - \frac{2}{\alpha}\right)\frac{\alpha}{2} e^{-\gamma\beta} = -1.$$

For a well of the form

$$U = U_{\min}(1 - \sqrt{r/R}),$$

the system takes the form

$$(6e^{-\beta\alpha} + (\beta\alpha)^3 - 3(\beta\alpha)^2 + 6\beta\alpha - 6)\frac{1}{4}(\beta\alpha)^4 = e^{-\gamma\beta},$$

$$\left(\gamma\beta - \beta - \frac{4}{\alpha}\right)\frac{\alpha}{4} e^{-\gamma\beta} = -1.$$

In Fig. 1, the calculated α is plotted against β for the parabolic (solid line), cone-shaped (dotted line), and root (dashed line) potential wells and for a well of the form

$$U = U_{\min}(1 - (r/R)^4)$$

(dash-dotted line).

Comparison of these plots leads us to conclude that the change in the distribution due to the process being a nonequilibrium one shows up most clearly for $|\beta| \sim 4$; the closer the potential well to a square shape, the smaller this change. The same dependence on the vessel shape can also be traced in the cooling of a fluid via its evaporation mentioned above.

In Fig. 2, the change in entropy is plotted against β when passing from an equilibrium system to a system with measurements for the same cases as in Fig. 1. We see a slow decrease in the entropy difference with increasing well depth and, accordingly, with decreasing escape probability.

6. DISCUSSION

We have found that the effect of measuring the times of escape from a potential well reduces to a decrease in the effective temperature, i.e., to a narrowing of the distribution in coordinates. As a result, the entropy decreases by an amount equal to the amount of information obtained. Such a measurement can be compared with the action of the so-called Maxwell demon and it can be explained by the fact that the generalized second law of thermodynamics holds.

Here, we did not discuss the technical possibilities of detecting the particles that escaped from a potential well. However, if the difficulties arising in this case were overcome, then the decrease in entropy (or, according to a different interpretation, in effective temperature) in the system could be used to produce a Bose condensate.

In general, calculating the time of system escape from a quasi-equilibrium state under the action of fluctuations is a problem that combines various fields of modern science. This problem arises, for example, in theories of phase transitions [12] and chemical reactions, in studies of the dynamics of complex biomolecules [13], in calculations of the surface diffusion coefficient in semiconductors [14], and in tracking-loss

analyses for radio and optical automatic tracking systems [15].

The quantum quasi-equilibrium Gibbs distribution can be used to take into account a low ionization of atoms in a gas laser and to calculate the corresponding corrections in the Einstein coefficients. By a low ionization we mean an ion number density that does not lead to the avalanche processes of ionization and transition to plasma but that affects the optical properties of the gas.

ACKNOWLEDGMENTS

I thank A.V. Netrebenko, whose computer experiments helped to refine and confirmed the results of the calculations; B.A. Grishanin, whose valuable advice allowed the paper to be significantly improved; and Yu.M. Romanovskiĭ, the discussion of the results with whom confirmed their applicability to biophysics. This study was supported by INTAS (grant no. 02-0450), the Russian Foundation for Basic Research (project no. 01-03-33163a), the Program "Scientific Schools of Russia" (project no. 00-15-97788843), and the Interdisciplinary Scientific Project of Moscow State University.

REFERENCES

1. R. L. Stratonovich, *Selected Problems of Fluctuation Theory in Radio Engineering* (Sov. Radio, Moscow, 1961).
2. R. L. Stratonovich, Zh. Éksp. Teor. Fiz. **108**, 1328 (1995) [JETP **81**, 729 (1995)].
3. R. L. Stratonovich and O. A. Chichigina, Zh. Éksp. Teor. Fiz. **110**, 1284 (1996) [JETP **83**, 708 (1996)].
4. O. A. Chichigina, Vestn. Mosk. Univ., Ser. 3: Fiz., Astron., No. 5, 6 (1997).
5. O. A. Chichigina, in *Collection for Memory of A.N. Malakhov*, Ed. by A. I. Saichev (TALAM, Nizni Novgorod, 2000), p. 98.
6. A. V. Netrebko and O. A. Chichigina, Izv. Vyssh. Uchebn. Zaved., Prikl. Nelineĭnaya Din. **9**, 85 (2001).
7. A. Pontryagin, A. Andronov, and A. Vitt, Zh. Éksp. Teor. Fiz. **3**, 165 (1933).
8. H. J. Kramers, Physica (Amsterdam) **7**, 284 (1940).
9. V. I. Tikhonov and M. A. Mironov, *Markov Processes* (Sov. Radio, Moscow, 1977).
10. R. L. Stratonovich, *Information Theory* (Sov. Radio, Moscow, 1975).
11. O. A. Chichigina, Zh. Éksp. Teor. Fiz. **116**, 57 (1999) [JETP **89**, 30 (1999)].
12. Yu. L. Klimontovich, *Statistical Physics* (Nauka, Moscow, 1982; Harwood Academic, New York, 1986).
13. Yu. M. Romanovskiĭ and A. V. Netrebko, Izv. Vyssh. Uchebn. Zaved., Prikl. Nelineĭnaya Din. **6**, 31 (1998).
14. B. I. Boltaks, *Diffusion in Semiconductors* (Fizmatgiz, Moscow, 1961; Academic, New York, 1963).
15. G. V. Obrezkov and V. D. Razevig, *Methods of Analysis of Tracking Loss* (Sov. Radio, Moscow, 1977).

Translated by V. Astakhov

Journal of Experimental and Theoretical Physics, Vol. 95, No. 6, 2002, pp. 981–986.
Translated from Zhurnal Éksperimental'noĭ i Teoreticheskoĭ Fiziki, Vol. 122, No. 6, 2002, pp. 1139–1145.

GRAVITATION, ASTROPHYSICS

Quantum Power Correction to the Newton Law

G. G. Kirilin[a, *] and I. B. Khriplovich[b, **]

[a]*Budker Institute of Nuclear Physics, Novosibirsk, 630090 Russia*
[b]*Novosibirsk State University, Novosibirsk, 630000 Russia*
**e-mail: g_kirilin@mail.ru*
***e-mail: khriplovich@inp.nsk.su*
Received August 19, 2002

Abstract—A graviton contribution to the one-loop quantum correction to the Newton law is found. This correction corresponds to an interaction decreasing with distance as $1/r^3$, in which the graviton contribution numerically dominates. Previous calculations of this contribution to the discussed effect are demonstrated to be incorrect. © *2002 MAIK "Nauka/Interperiodica".*

1. INTRODUCTION

The problem of corrections to the equations of motion, arising in general relativity, is far from new. The classical relativistic corrections to these equations were found long ago by Einstein, Infeld and Hoffmann [1], and by Eddington and Clark [2]. (A relatively simple derivation of these corrections is presented in textbook [3].) Later, this result was reproduced by Iwasaki by means of the Feynman diagrams [4]. Thus, the problem of the classical relativistic corrections to the Newton law has finally been solved.[1]

Let us note that the general structure of the relativistic classical correction to the potential of interaction between two bodies with masses m_1 and m_2, which would be of the second order in the Newton gravitational constant k, is *a priori* clear. Indeed, since the quantity km/c^2 (c is the velocity of light) has the dimensionality of length, the correction, with an allowance for the symmetry with respect to the interchange $m_1 \longleftrightarrow m_2$, should have the form

$$U_{\rm cl} = a_{\rm cl}\frac{k^2 m_1 m_2 (m_1 + m_2)}{c^2 r^2}. \qquad (1)$$

The dimensionless constant $a_{\rm cl}$ as found in the above works equals 1/2.

There is one more combination of constants that is linear in k and can be used for constructing a power correction to the Newton potential:

$$\frac{k\hbar}{c^3} = l_p^2,$$

where $\hbar$ is the Planck constant and $l_p = 1.6 \times 10^{-33}$ cm is the Planck length. Clearly, being of a quantum nature, such a correction should appear as follows:

$$U_{qu} = a_{qu}\frac{k^2 \hbar m_1 m_2}{c^3 r^3}. \qquad (2)$$

Then, one has to find the numerical constant a_{qu}. Although the quantum correction is extremely small, investigation of this factor has a certain methodological interest, representing a closed calculation of a high-order effect in the nonrenormalizable quantum gravity.

The reason why this problem allows for a closed solution is as follows. The Fourier transform of $1/r^3$ is

$$\int d\mathbf{r}\frac{\exp(-i\mathbf{q}\cdot\mathbf{r})}{r^3} = -2\pi \ln q^2. \qquad (3)$$

This singularity in the momentum transfer $\mathbf{q}$ means that the correction under consideration can be generated only by diagrams with two massless particles in the t-channel. The number of such diagrams of the second order in k is finite, and their parts logarithmic in q^2 can be calculated unambiguously.

The corresponding diagrams with photons and massless neutrinos in the loop (see Fig. 1) were calculated by Radkowski [6] and by Capper, Duff *et al.* [7–9]. This contribution to the numerical factor a_{qu} is

$$a_{\gamma\nu} = -\frac{4 + N_\nu}{15\pi}, \qquad (4)$$

where N_ν is the number of massless two-component neutrinos.

As for the contribution to this effect from the graviton exchange, it was considered by Donoghue [10–13], Muzinich and Vokos [14], Hamber and Liu [15], and Akhundov *et al.* [16]. However, there is no quantitative agreement between the results of these works, more-

[1] However, erroneous papers on the subject are being published up to now. We mean the articles [5], where it was claimed that the classical relativistic corrections to the equations of motion for two bodies separated by large distance depend essentially on the inner structure of these bodies. We believe that this claim does not withstand criticisms.

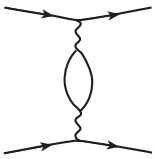

Fig. 1. Photon (neutrino) loop.

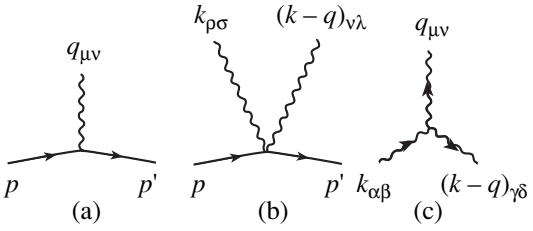

Fig. 2. Vertices.

over, even predictions for the sign of the correction are different.

We believe that the correct result for the quantum correction to the Newton law will be sufficiently interesting from the theoretical point of view. This is the aim of our investigation. Among the previous works on the subject, the most detailed presentation of the calculation is given in [11, 16]. Our approach, based on direct calculation of Feynman diagrams, choice of the field operator for the gravitational field, and selection of the gauge, is the same as that employed in [10–13, 16]. This circumstance allows for a detailed comparison of the calculations of separate contributions to the effect under consideration. This comparison has demonstrated that not all diagrams are taken into account in [10–13, 16] and the contributions considered are calculated incorrectly. Below, when discussing particular diagrams, we will return to comparison with the previous works, including [14, 15]. Here, let us only note an obvious error in [10–13, 16], where the formula for the Fourier transform of the function $1/r^3$ (see (3)) contains π^2 instead of π, and this error is retained in the final expressions as well.

Some of the diagrams considered also contribute to the classical relativistic correction. In order to check our calculations, we have computed these classical contributions in parallel and compared them with the corresponding results of [4]. For these classical corrections, we have complete agreement with [4] for each diagram taken separately.

2. PROPAGATORS AND VERTICES

Below we use the system of units in which $c = 1$ and $\hbar = 1$.

As a gravitational field operator $h_{\mu\nu}$, we choose the deviation of the metrics $g_{\mu\nu}$ from the flat one:

$$g_{\mu\nu} = \delta_{\mu\nu} + \kappa h_{\mu\nu}, \quad \delta_{\mu\nu} = \mathrm{diag}(1, -1, -1, -1), \qquad \kappa^2 = 32\pi k = 32\pi l_p^2. \tag{5}$$

We use the gauge in which the graviton propagator is

$$D_{\mu\nu,\,\alpha\beta}(q) = i\frac{P_{\mu\nu,\,\alpha\beta}}{q^2 + i0}, \qquad P_{\mu\nu,\,\alpha\beta} = \frac{1}{2}(\delta_{\mu\alpha}\delta_{\nu\beta} + \delta_{\nu\alpha}\delta_{\mu\beta} - \delta_{\mu\nu}\delta_{\alpha\beta}). \tag{6}$$

The tensor $P_{\mu\nu,\,\alpha\beta}$ is conveniently represented as [17]

$$P_{\mu\nu,\,\alpha\beta} = I_{\mu\nu,\,\alpha\beta} - \frac{1}{2}\delta_{\mu\nu}\delta_{\alpha\beta},$$

where

$$I_{\mu\nu,\,\alpha\beta} = \frac{1}{2}(\delta_{\mu\alpha}\delta_{\nu\beta} + \delta_{\nu\alpha}\delta_{\mu\beta})$$

is a kind of the unit operator such that

$$I_{\mu\nu,\,\alpha\beta}t_{\alpha\beta} = t_{\mu\nu}$$

for any symmetric tensor $t_{\alpha\beta}$. Note the following useful identity:

$$P_{\alpha\beta,\,\kappa\lambda}P_{\kappa\lambda,\,\gamma\delta} = I_{\alpha\beta,\,\gamma\delta}. \tag{7}$$

The propagator of a scalar particle has the usual form:

$$G(p) = i\frac{1}{p^2 + i0}. \tag{8}$$

The vertex of the interaction of a scalar particle with the graviton is (see Fig. 2a)

$$V_{\alpha\beta}(p, p') = -i\frac{\kappa}{2}[p_\alpha p'_\beta + p'_\alpha p_\beta - \delta_{\alpha\beta}(pp' - m^2)]. \tag{9}$$

The contact interaction of a scalar particle with two gravitons (see Fig. 2b) is

$$V_{\kappa\lambda,\,\rho\sigma} = i\kappa^2\Big[I_{\kappa\lambda,\,\alpha\delta}I_{\delta\beta,\,\rho\sigma}(p_\alpha p'_\beta + p'_\alpha p_\beta) - \frac{1}{2}(\delta_{\kappa\lambda}I_{\rho\sigma,\,\alpha\beta} + \delta_{\rho\sigma}I_{\kappa\lambda,\,\alpha\beta})p_\alpha p'_\beta + \frac{(p'-p)^2}{4}\Big(I_{\kappa\lambda,\,\rho\sigma} - \frac{1}{2}\delta_{\kappa\lambda}\delta_{\rho\sigma}\Big)\Big]. \tag{10}$$

To within the accuracy adopted, we can neglect the last term proportional to $(p' - p)^2$ in this expression.

Let us note that the vertex (10) in [11, 16] is erroneously presented (and used in the calculations) with a factor which is two times as small, $\kappa^2/2$ instead of κ^2. We will return to this factor in Sections 3 and 4.

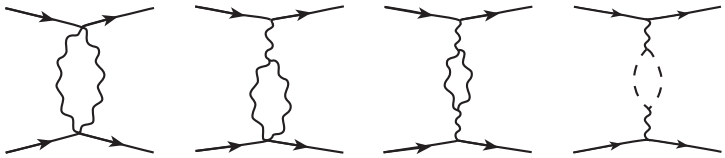

Fig. 3. Simple loops.

The following useful identities are worth mentioning here:

$$P_{\mu\nu,\alpha\beta}[p_\alpha p'_\beta + p'_\alpha p_\beta - \delta_{\alpha\beta}(pp' - m^2)] = p_\alpha p'_\beta + p'_\alpha p_\beta - \delta_{\alpha\beta}m^2, \quad (11)$$

$$P_{\alpha\beta,\kappa\lambda}P_{\gamma\delta,\rho\sigma}V_{\kappa\lambda,\rho\sigma} = V_{\alpha\beta,\gamma\delta}. \quad (12)$$

As for the three-graviton vertex (see Fig. 2c), which has the most complicated form, we will follow [11] in representing it as

$$V_{\mu\nu,\alpha\beta,\gamma\delta} = -i\frac{\kappa}{2}\sum_i {}^iV_{\mu\nu,\alpha\beta,\gamma\delta}; \quad (13)$$

$${}^1V_{\mu\nu,\alpha\beta,\gamma\delta} = P_{\alpha\beta,\gamma\delta}\left[k_\mu k_\nu + (k-q)_\mu(k-q)_\nu + q_\mu q_\nu - \frac{3}{2}\delta_{\mu\nu}q^2\right],$$

$${}^2V_{\mu\nu,\alpha\beta,\gamma\delta} = 2q_\lambda q_\sigma[I_{\lambda\sigma,\alpha\beta}I_{\mu\nu,\gamma\delta} + I_{\lambda\sigma,\gamma\delta}I_{\mu\nu,\alpha\beta} - I_{\lambda\mu,\alpha\beta}I_{\sigma\nu,\gamma\delta} - I_{\lambda\nu,\alpha\beta}I_{\sigma\mu,\gamma\delta}],$$

$${}^3V_{\mu\nu,\alpha\beta,\gamma\delta} = q_\lambda q_\mu(\delta_{\alpha\beta}I_{\lambda\nu,\gamma\delta} + \delta_{\gamma\delta}I_{\lambda\nu,\alpha\beta}) + q_\lambda q_\nu(\delta_{\alpha\beta}I_{\lambda\mu,\gamma\delta} + \delta_{\gamma\delta}I_{\lambda\mu,\alpha\beta}) - q^2(\delta_{\alpha\beta}I_{\mu\nu,\gamma\delta} + \delta_{\gamma\delta}I_{\mu\nu,\alpha\beta}) - \delta_{\mu\nu}q_\lambda q_\sigma(\delta_{\alpha\beta}I_{\gamma\delta,\lambda\sigma} + \delta_{\gamma\delta}I_{\alpha\beta,\lambda\sigma}),$$

$${}^4V_{\mu\nu,\alpha\beta,\gamma\delta} = 2q_\lambda[I_{\sigma\nu,\alpha\beta}I_{\gamma\delta,\lambda\sigma}(k-q)_\mu + I_{\sigma\mu,\alpha\beta}I_{\gamma\delta,\lambda\sigma}(k-q)_\nu - I_{\sigma\nu,\gamma\delta}I_{\alpha\beta,\lambda\sigma}k_\mu - I_{\sigma\mu,\gamma\delta}I_{\alpha\beta,\lambda\sigma}k_\nu] + q^2(I_{\sigma\mu,\alpha\beta}I_{\gamma\delta,\sigma\nu} + I_{\sigma\nu,\alpha\beta}I_{\gamma\delta,\sigma\mu}) + \delta_{\mu\nu}q_\lambda q_\sigma(I_{\alpha\beta,\lambda\rho}I_{\rho\sigma,\gamma\delta} + I_{\gamma\delta,\lambda\rho}I_{\rho\sigma,\alpha\beta}),$$

$${}^5V_{\mu\nu,\alpha\beta,\gamma\delta} = [k^2 + (k-q)^2]\times\left(I_{\sigma\mu,\alpha\beta}I_{\gamma\delta,\sigma\nu} - \frac{1}{2}\delta_{\mu\nu}P_{\alpha\beta,\gamma\delta}\right) - k^2\delta_{\gamma\delta}I_{\mu\nu,\alpha\beta} - (k-q)^2\delta_{\alpha\beta}I_{\mu\nu,\gamma\delta}.$$

In this vertex, to within the adopted accuracy, we can neglect the last structure ${}^5V_{\mu\nu,\alpha\beta,\gamma\delta}$.

Note that the vertex (13) in [11, 16] is erroneously taken with the opposite sign. Our sign is based on the following: for the physical gravitons possessing the momenta k and $k-q$, vertex (13) in the limit of $q \longrightarrow 0$ should agree with vertex (9), corresponding to the interaction of the graviton with a scalar particle.

3. SIMPLE LOOPS

It is convenient to start with the diagrams where the Feynman integrals contain two denominators only. The simplest of these (Fig. 3a) is entirely missing in [10–13, 16]. The calculation of this diagram presents no difficulties: one has only to use identity (12) and to pass to the nonrelativistic limit in both two-graviton vertices. The resulting contribution to the quantum correction is

$$U_{qu1} = -\frac{22}{\pi}\frac{k^2m_1m_2}{r^3}. \quad (14)$$

The calculation of the next diagram (Fig. 3b) and that obtained by interchanging scalar particles is also sufficiently simple and results in

$$U_{qu2} = \frac{26}{3\pi}\frac{k^2m_1m_2}{r^3}. \quad (15)$$

The result of [11] for this contribution differs from (15) only by a wrong power of π. The corresponding result of [16] is quite different.

As for the diagrams in Figs. 3c and 3d with the polarization operator of graviton, we do not have much to add to works [10–13] with respect to the method of calculation, and we have nothing at all to add to the result proper (which is also used in [14, 16]). However, for completeness, we briefly present this calculation.

The effective Lagrangian corresponding to the sum of these diagrams with gravitons and vector ghosts, as obtained by 't Hooft and Veltman [17], is

$$L = -\frac{1}{16\pi^2}\ln|q^2|\left(\frac{1}{120}R^2 + \frac{7}{20}R_{\mu\nu}R^{\mu\nu}\right). \quad (16)$$

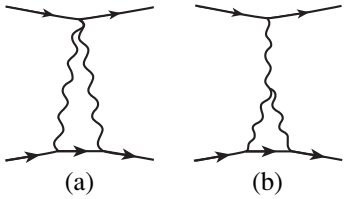

Fig. 4. Triangle diagrams.

In a linear approximation, the Ricci tensor and the scalar curvature of the external gravitational field which enter this expression are

$$R_{\mu\nu} = \frac{\kappa}{2}h_{\alpha\beta}(q^2 I_{\mu\nu,\alpha\beta} + q_\mu q_\nu \delta_{\alpha\beta} - q_\mu q_\alpha \delta_{\nu\beta} - q_\nu q_\alpha \delta_{\mu\beta}) = \frac{\kappa}{2}h_{\alpha\beta}r_{\mu\nu,\alpha\beta},$$

$$R = \kappa h_{\alpha\beta}(q^2\delta_{\alpha\beta} - q_\alpha q_\beta) = \kappa h_{\alpha\beta}r_{\alpha\beta}.$$

The corresponding contribution to the graviton polarization operator is

$$\Pi_{\alpha\beta,\gamma\delta} = -\frac{\kappa^2}{8\pi^2}\ln|q^2| \times\left(\frac{1}{120}r_{\alpha\beta}r_{\gamma\delta} + \frac{7}{80}r_{\mu\nu,\alpha\beta}r_{\mu\nu,\gamma\delta}\right). \quad (17)$$

Here, we have taken into account two possibilities of identifying $R_{\mu\nu}$ and R with the upper and lower external gravitons. The subsequent calculation is straightforward. Let us mention only that the summation over μ, ν is conveniently performed at the end. Finally, this contribution to the quantum correction is

$$U_{qu3} = -\frac{43}{30\pi}\frac{k^2 m_1 m_2}{r^3}. \quad (18)$$

Let us mention that diagrams in Figs. 3c and 3d were computed in different variables, $\psi_{\mu\nu} = h_{\mu\nu} - (1/2)\delta_{\mu\nu}h$, in [15, 18, 19] and in the Schwinger source description of gravity in [6].

4. TRIANGLE DIAGRAMS

The master formula for the triangle diagrams in Figs. 4a and 4b reads (we keep only terms singular in $|q|$)

$$i\int\frac{d^4k}{(2\pi)^4}\frac{1}{k^2(k-q)^2((p-k)^2-m^2)} = \frac{1}{32\pi^2 m^2}\left(\frac{\pi^2 m}{\sqrt{|q^2|}} + \ln|q^2|\right). \quad (19)$$

It is conveniently obtained by calculating first the imaginary part of the lhs in the t-channel and then restoring the rhs via the dispersion relation. The first term in the rhs of formula (19) generates $1/r^2$ in the coordinate representation and contributes to the classical relativistic correction. This term is retained in (19) in order to check the calculations by comparison with the corresponding results of [4].

Our result for the contribution of simpler diagrams of the type depicted in Fig. 4a is

$$U_{qu4} = \frac{28}{\pi}\frac{k^2 m_1 m_2}{r^3}. \quad (20)$$

This contribution is also missed in [11, 16]. These diagrams contribute to the classical correction as well. An extra proof of our normalization for the seagull vertex is the agreement with the corresponding classical result of [4].

Much more tedious is the calculation of diagrams of the type presented in Fig. 4b, which yields

$$U_{qu5} = -\frac{29}{3\pi}\frac{k^2 m_1 m_2}{r^3}. \quad (21)$$

The corresponding results of [16], differs from only by the sign and wrong power of π. The result of [11] for this contribution is quite different.

5. BOX DIAGRAMS

Expressions for the matrix elements corresponding to the box diagrams in Figs. 5a and 5b can be represented as

$$M_s = i\frac{\kappa^4}{16 m_1 m_2}\int\frac{d^4k}{(2\pi)^4}\frac{[a - b(D_1 + D_2)]^2}{k^2(k-q)^2 D_1 D_2}, \quad D_1 = k^2 - 2(p_1 k), \quad D_2 = k^2 + 2p_2 k, \quad a = 2(p_1 p_2)^2 - m_1^2 m_2^2, \quad b = (p_1 p_2), \quad (22)$$

$$M_u = i\frac{\kappa^4}{16 m_1 m_2}\int\frac{d^4k}{(2\pi)^4}\frac{[a' + b'(D_1 + D_2')]^2}{k^2(k-q)^2 D_1 D_2'}, \quad D_2' = k^2 - 2(p_2 + q, k), \quad b' = (p_1, p_2 + q), \quad a' = 2(p_1, p_2 + q)^2 - m_1^2 m_2^2. \quad (23)$$

It is convenient to single out in the numerators of these integrals such the structures that cancel one or both denominators D_1, D_2 (D_2'). Upon canceling a single denomina-

tor, another one is left with an effective triangle diagram of the type depicted in Fig. 4a:

$$M_{1s} = i\frac{\kappa^4}{16m_1m_2}\int\frac{d^4k}{(2\pi)^4k^2(k-q)^2} \times\left\{b^2\left(\frac{2(p_2k)}{D_1}-\frac{2(p_1k)}{D_2}\right)-2ab\left(\frac{1}{D_1}+\frac{1}{D_2}\right)\right\}, \quad (24)$$

$$M_{1u} = i\frac{\kappa^4}{16m_1m_2}\int\frac{d^4k}{(2\pi)^4k^2(k-q)^2} \times\left\{b'^2\left(-\frac{2(p_2'k)}{D_1}-\frac{2(p_1k)}{D_2'}\right)+2a'b'\left(\frac{1}{D_1}+\frac{1}{D_2'}\right)\right\}. \quad (25)$$

It can be easily demonstrated that, to within the accuracy adopted, expressions (24) and (25) are mutually canceled.

Expressions with both denominators missing,

$$M_{2s} = i\frac{\kappa^4}{16m_1m_2}\int\frac{d^4k}{(2\pi)^4}\frac{2b^2}{k^2(k-q)^2}, \quad (26)$$

$$M_{2u} = i\frac{\kappa^4}{16m_1m_2}\int\frac{d^4k}{(2\pi)^4}\frac{2b'^2}{k^2(k-q)^2}, \quad (27)$$

correspond to diagrams of the type depicted in Fig. 3a. These contributions add up to yield the following result for the effect under consideration:

$$U_{qu6} = -\frac{8}{\pi}\frac{k^2m_1m_2}{r^3}. \quad (28)$$

Now we have only to deal with the "irreducible" parts of the diagrams in Figs. 5a and 5b. These irreducible matrix elements are conveniently obtained by calculating first their imaginary parts (in the *s* and *u* channels, respectively) and then restoring the real parts through the dispersion relations. The results are as follows (we omit the terms nonsingular in $|q^2|$):

$$M_{0s} = i\frac{\kappa^4a^2}{16m_1m_2}\int\frac{d^4k}{(2\pi)^4} \times\{(k^2-\lambda^2)((k-q)^2-\lambda^2)(k^2-2p_1k)(k^2+2p_2k)\}^{-1} \quad (29)$$

$$=-\frac{\kappa^4a^2}{(16m_1m_2)^2|q^2|\pi^2}\left[-1+\frac{s-(m_1+m_2)^2}{6m_1m_2}\right]\ln\frac{|q^2|}{\lambda^2}, \quad (30)$$

$$M_{0u} = i\frac{\kappa^4a'^2}{16m_1m_2}\int\frac{d^4k}{(2\pi)^4}\{(k^2-\lambda^2) \times((k-q)^2-\lambda^2)(k^2-2p_1k)(k^2-2(p_2+q,k))\}^{-1} \quad (31)$$

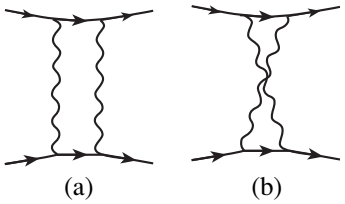

(a) (b)

Fig. 5. Box diagrams.

$$=-\frac{\kappa^4a'^2}{(16m_1m_2)^2|q^2|\pi^2}\left[1+\frac{u-(m_1-m_2)^2}{6m_1m_2}\right]\ln\frac{|q^2|}{\lambda^2}. \quad (32)$$

In these formulas, $s = (p_1 + p_2)^2$ and $u = (p_1 - p_2 - q)^2$. Expressions (29) and (31) converge in the ultraviolet sense but diverge in the infrared limit, depending logarithmically on the "graviton mass" λ. As usual, such behavior is directly related to the necessity of canceling the infrared divergence in the bremsstrahlung diagrams (of course, the gravitational bremsstrahlung in the present case). The sum of the irreducible boxes a term with $\ln|q^2|$, which generates the following quantum correction to the Newton potential:

$$U_{qu7} = -\frac{23}{3\pi}\frac{k^2m_1m_2}{r^3}. \quad (33)$$

It is worth mentioning that, in contrast to the previous contributions, where $|q^2|$ served as an infrared cutoff for ultraviolet-divergent integrals, here $|q^2|$ is the upper limit for the infrared-divergent integrals.

For the box diagrams, we have also checked that our results for thus generated classical corrections agree completely with those obtained in [4].

The box contributions to the quantum correction are missing at all in [10–13, 16], although diagrams in Figs. 5a and 5b are considered in [20] from a different point of view.

On the other hand, neither in [14] nor in [15] could we find any mention of the "infrared" contribution of type (33). In fact, the problem of classical and quantum corrections in [15] was treated in different variables, $\psi_{\mu\nu} = h_{\mu\nu} - (1/2)\delta_{\mu\nu}h$. It can be easily demonstrated that expressions for the box diagrams are exactly the same in both variables, ψ and h. However, the box contributions as calculated in [15] disagree both with the classical ones obtained in [4] (which are demonstrated explicity in [4] to be the same in both variables ψ and h) and with our results for the quantum correction presented as (28), or (33), or the sum of (28) and (33).

Finally, let us say a few more words on [14]. The approach advocated therein looks quite interesting and promising. However, the results for the quantum correction presented in [14] do not agree with ours (nor do they agree with the results of [10–13, 15, 16]). Due to the lack of details in [14], we cannot indicate with cer-

tainty what the origin of the disagreement is. Still, an impression arises that, at least, it was overlooked in [14] that the irreducible triangle diagrams generate not only classical corrections, but quantum corrections as well; that is, it seems that in [14] the second term is missing in formula (20).

6. CONCLUSIONS

Summing up all the contributions obtained, (14), (15), (18), (20), (21), (28), (33), we arrive at the following result for the quantum correction to the Newton potential due to the two-graviton exchange:

$$U(r) = -\frac{km_1m_2}{r}\left(1 + \frac{121}{10\pi}\frac{k\hbar}{c^3r^2}\right). \qquad (34)$$

Let us note that the derived overall correction enhances, but does not suppress the common Newton attraction.

ACKNOWLEDGMENTS

The authors are grateful to S. Deser and M.J. Duff for attracting our attention to [6, 9, 19].

The investigation was supported in part by the Russian Foundation for Basic Research (project no. 01-02-16898), the Program of Support for Leading Scientific Schools (project no. 00-15-96811), the Ministry of Education (project no. E00-3.3-148), and the Federal Program Integration-2002.

REFERENCES

1. A. Einstein, L. Infeld, and B. Hoffmann, Ann. Math. **39**, 65 (1938).
2. A. Eddington and G. Clark, Proc. R. Soc. London **166**, 465 (1938).
3. L. D. Landau and E. M. Lifshitz, *Course of Theoretical Physics*, Vol. 2: *The Classical Theory of Fields* (Nauka, Moscow, 1988; Pergamon, Oxford, 1975), Para. 106.
4. Y. Iwasaki, Prog. Theor. Phys. **46**, 1587 (1971).
5. K. A. Kazakov, Class. Quantum Grav. **18**, 1039 (2001); hep-th/0009073; Nucl. Phys. (Proc. Suppl.) **104**, 232 (2002); hep-th/0107080; hep-th/0111074; Class. Quantum Grav. **19**, 3017 (2002); hep-th/0201246.
6. A. F. Radkowski, Ann. Phys. **56**, 319 (1970).
7. D. M. Capper, M. J. Duff, and L. Halpern, Phys. Rev. D **10**, 461 (1974).
8. D. M. Capper and M. J. Duff, Nucl. Phys. B **44**, 146 (1974).
9. M. J. Duff and J. T. Liu, Phys. Rev. Lett. **85**, 2052 (2000); hep-th/0003237.
10. J. F. Donoghue, Phys. Rev. Lett. **72**, 2996 (1994); gr-qc/9310024.
11. J. F. Donoghue, Phys. Rev. D **50**, 3874 (1994); gr-qc/9405057.
12. J. F. Donoghue, in *Advanced School on Effective Theories*, Ed. by F. Cornet and M. J. Herrero (World Sci., Singapore, 1996); gr-qc/9512024.
13. J. F. Donoghue, in *Proceedings of Eighth Marcel Grossmann Meeting on General Relativity*, Ed. by T. Piran and R. Ruffini (World Sci., Singapore, 1999); gr-qc/9712070.
14. I. J. Muzinich and S. Vokos, Phys. Rev. D **52**, 3472 (1995); hep-th/9501083.
15. H. Hamber and S. Liu, Phys. Lett. B **357**, 51 (1995); hep-th/9505182.
16. A. Akhundov, S. Belucci, and A. Shiekh, Phys. Lett. B **395**, 19 (1998); gr-qc/9611018.
17. G. 't Hooft and M. Veltman, Ann. Inst. Henri Poincare, Sect. A **20**, 69 (1974).
18. D. M. Capper, G. Leibbrandt, and M. Ramon Medrano, Phys. Rev. D **8**, 4320 (1973).
19. M. J. Duff, Phys. Rev. D **9**, 1837 (1974).
20. J. F. Donoghue and T. Torma, Phys. Rev. D **54**, 4963 (1996); hep-th/9602121.

Translated by G. Kirilin

Journal of Experimental and Theoretical Physics, Vol. 95, No. 6, 2002, pp. 987–997.
Translated from Zhurnal Éksperimental'noĭ i Teoreticheskoĭ Fiziki, Vol. 122, No. 6, 2002, pp. 1146–1157.

NUCLEI, PARTICLES, AND THEIR INTERACTION

Collision of Rydberg Atom A** with Atom B in the Ground Electronic State. Optical Potential

G. V. Golubkov[a, *], A. Z. Devdariani[b], and M. G. Golubkov[a]

[a]*Semenov Institute of Chemical Physics, Russian Academy of Sciences, ul. Kosygina 4, Moscow, 117977 Russia*
[b]*Fock Research Institute of Physics, St. Petersburg State University, St. Petersburg, 198904 Russia*
**e-mail: golubkov@center.chph.ras.ru*

Received February 28, 2002

Abstract—A method for calculating the complex optical potential of slowly colliding Rydberg atom A** and neutral atom B in the ground electronic state is suggested. The method is based on the asymptotic approach and the theory of multichannel quantum defects, which uses the formalism of renormalized Lippmann–Schwinger equations. The potential is introduced as the $\langle q|\mathbf{V}_{\text{opt}}|q\rangle$ matrix element of the optical interaction operator, for which the integral equation is derived, and is calculated in the basis set of free particle wave functions $|q\rangle$. Fairly simple equations for the shift and broadening of the ionic term are obtained, and the principal characteristics of these equations are analyzed. By way of illustration, the optical potential of the Na**(nl) + B systems, where B is a rare gas atom, is calculated. *© 2002 MAIK "Nauka/Interperiodica".*

1. INTRODUCTION

Processes involving strongly excited (Rydberg) atoms and molecules are common in various astrophysical and plasma phenomena and are extensively studied experimentally and theoretically. Currently, a wealth of data on such processes have been collected and can be found in numerous original papers, reviews, and monographs [1–4]. Nevertheless, there are several processes that have as get been scarcely studied, for instance, diffusion of Rydberg atoms in the atmosphere of a different buffer gas. If one of the atoms is strongly excited, the "three-particle" model can most effectively be used, when the optical electron is in an orbit whose size substantially exceeds the characteristic size of the ionic core and medium atoms. The description of "elastic" scattering of Rydberg atoms by target atoms should then include not only the determination of the potential energy of their interaction, but also inelastic virtual transitions into all possible discrete and continual weakly bound electron states. A natural approach to solving this problem is the introduction of an optical potential whose imaginary part characterizes the total probability of transitions to the specified states.

The transition from a multiparticle to a two-particle description of elastic collisions of atomic particles in the optical potential representation is one of the traditional methods of the quantum theory of scattering. Usually, a $\mathbf{V}_{\text{opt}}$ nonlocal operator is introduced, and a multiparticle equation for its determination is constructed. Such a statement of the problem is formal in character, and the problem cannot be solved without additional assumptions about the interacting system [5]. To solve the problem, we must pass to the representation of noninteracting colliding particles, determine the basis set of its eigenstates $|q\rangle$, and calculate the corresponding matrix element $\langle q|\mathbf{V}_{\text{opt}}|q\rangle$. Precisely this matrix element represents the sought for optical potential V_{opt} whose imaginary part should include the complete set of quantum numbers s that describe the internal state of the interacting system and should depend on the total energy E and the orbital momentum of colliding particles. These values are integrals of motion and should be conserved.

The optical potential concept has repeatedly been applied in the theory of atomic collisions. In particular, it has been extensively used to describe processes of the type of Penning ionization [6]. In this work, we consider slow elastic collisions between Rydberg atom A** ($n \gg 1$) and atom B in the ground electronic state (n is the principal quantum number of the Rydberg level) and determine the optical potential for this system. We must distinguish between two fundamentally different physical situations, when $E < 0$ and when $E \geq 0$. In the first situation, the optical potential is formed by virtual transitions between bound electron states in a discrete spectrum, and, in the second, there is the additional possibility for the ionization of atom A**.

A weakly bound electron behaves as a free particle in the interaction with perturbing atom B, and the optical potential can therefore be constructed fairly simply and rigorously. The problem is solved in terms of asymptotic theory with the use of the integral variant of the multichannel quantum defect method [7]. By way of illustration, we calculate the interaction potentials between strongly excited Na**(nl) and rare gas atoms.

2. GENERAL EQUATIONS

Consider a slow elastic collision between strongly excited (Rydberg) atom A**(nl) and unexcited atom B. The total energy of the system E is ($\hbar = e = m_e = 1$)

$$E = -\frac{1}{2\nu_l^2} + E_k, \tag{1}$$

where $\nu_l = n - \mu_l$ is the effective principal quantum number, μ_l is the quantum defect of the level, l is the angular momentum of the electron, and E_k is the initial relative energy of the colliding particles. The U_{A^+B} interaction potential between ion A^+ and atom B is assumed to be known. To solve the eigenvalue problem, we use the integral equation for the $\boldsymbol{\tau}$-operator of the shift of levels, which, in the problem under consideration, has the form [7]

$$\boldsymbol{\tau} = \mathbf{U}_{A^+B}\mathbf{G}(E)\boldsymbol{\tau}. \tag{2}$$

The $\mathbf{U}_{A^+B}$ three-particle interaction operator, which describes the interacting pair (A^+–B) plus free electron e^-, is local and can be written as

$$\mathbf{U}_{A^+B}(\mathbf{R}, \mathbf{R}'; \boldsymbol{\rho}, \boldsymbol{\rho}') = (2\pi)^6 U_{A^+B}(R)\sum_q |q(\mathbf{R}, \boldsymbol{\rho})\rangle\langle q(\mathbf{R}', \boldsymbol{\rho}')|, \tag{3}$$

where $\mathbf{R}$ and $\boldsymbol{\rho}$ are the coordinates of the A^+ ion and the electron, respectively, counted from the center of the B atom. The basis wave function $|q\rangle$ has the form

$$|q(\mathbf{R}, \boldsymbol{\rho})\rangle = \frac{1}{(2\pi)^3}\exp[i(\mathbf{k}\cdot\mathbf{R} + \mathbf{p}_e\cdot\boldsymbol{\rho})]. \tag{4}$$

Here, $k = \sqrt{2M_cE_k}$ is the relative momentum of the A^+ and B colliding particles, M_c is their reduced mass, and p_e is the electron momentum. In essence, wave function (4), which describes the free motion of particles, corresponds to the first order of the Born approximation. Further, we will be interested in the region of fairly large ($R_{\min} \le R$) interatomic distances (for which the U_{A^+B} interaction potential is a polarization potential). For this reason, the condition of smallness of the corresponding correction to the wave function [8]

$$M_c\left|\int_{R_{\min}}^{\infty} U_{A^+B}(r)[\exp(2i\mathbf{k}\cdot\mathbf{r}) - 1]dr\right| \ll k$$

for slowly colliding particles ($kR_{\min} < 1$) imposes the requirements

$$k\sqrt{M_c\beta} \ll 1, \quad n > (M_c\beta/8)^{1/4}. \tag{5}$$

In the equations given above, β is the polarizability of atom B and $R_{\min}$ is some minimal distance between particles A^+ and B, which is defined below (see Section 3). Taking into account (4), the $\mathbf{U}_{A^+B}$ interaction operator can be written as

$$\mathbf{U}_{A^+B}(\mathbf{R}, \mathbf{R}'; \boldsymbol{\rho}, \boldsymbol{\rho}') = (2\pi)^6 U_{A^+B}(R)\delta(\mathbf{R} - \mathbf{R}')\delta(\boldsymbol{\rho} - \boldsymbol{\rho}'). \tag{6}$$

It is easy to see that the matrix element is

$$\langle q|\mathbf{U}_{A^+B}(\mathbf{R}, \mathbf{R}'; \boldsymbol{\rho}, \boldsymbol{\rho}')|q\rangle = U_{A^+B}(R).$$

The $\mathbf{G}(E)$ Green operator in (2) describes the A** + B system with U_{A^+B} interaction switched off; that is, the B atom in (2) is assumed to interact only with the weakly bound electron. To construct this operator in a regular manner, let us use the Dyson equation

$$\mathbf{G}(E) = \mathbf{G}_{A^{**}B}(E) + \mathbf{G}_{A^{**}B}(E)\mathbf{V}_{e^-B}\mathbf{G}(E), \tag{7}$$

where $\mathbf{V}_{e^-B}$ is the e^-–B interaction operator and the $\mathbf{G}_{A^{**}B}$ Green operator describes the noninteracting A** + B system with given kinetic energy E_k.

The nonlocal optical interaction operator, which depends on the total energy E of the system, is introduced as follows:

$$\boldsymbol{\tau} = \mathbf{V}_{opt}(E)\mathbf{G}_{A^{**}B}(E)\boldsymbol{\tau}.$$

This operator satisfies the integral equation

$$\mathbf{V}_{opt} = \mathbf{U}_{A^+B} + \mathbf{U}_{A^+B}\mathbf{G}_{A^{**}B}\mathbf{V}_{e^-B}\mathbf{G}\mathbf{V}_{opt}.$$

Let us use the equation known in the theory of scattering

$$\mathbf{V}_{e^-B}\mathbf{G} = \mathbf{T}_{e^-B}\mathbf{G}_{A^{**}B}.$$

The solution to (7) can then be formally represented as

$$\mathbf{G} = \mathbf{G}_{A^{**}B} + \mathbf{G}_{A^{**}B}\mathbf{T}_{e^-B}\mathbf{G}_{A^{**}B} \tag{8}$$

($\mathbf{T}_{e^-B}$ is the operator of collisions between the weakly bound electron and atom B), and the integral equation for the $\mathbf{V}_{opt}$ operator can be rewritten as

$$\mathbf{V}_{opt} = \mathbf{U}_{A^+B} + \mathbf{U}_{A^+B}\mathbf{G}_{A^{**}B}\mathbf{T}_{e^-B}\mathbf{G}_{A^{**}B}\mathbf{V}_{opt}. \tag{9}$$

This representation is exact and admits further transformations. For instance, we can conveniently pass to the real $\mathbf{K}_{e^-B}$ scattering matrix (which is known to be constructed on standing waves) using the Heitler equation [9]:

$$\mathbf{T}_{e^-B} = \mathbf{K}_{e^-B} - i\mathbf{K}_{e^-B}\mathbf{T}_{e^-B}. \tag{10}$$

Eventually, operator equation (9) takes the form

$$\mathbf{V}_{opt} = \mathbf{U}_{A^+B} + \mathbf{U}_{A^+B}\mathbf{G}_{A^{**}B}[(1 + i\mathbf{K}_{e^-B})^{-1}\mathbf{K}_{e^-B}]\mathbf{G}_{A^{**}B}\mathbf{V}_{opt}. \tag{11}$$

It is clear from the structure of (11) that the physical reason for the appearance of the imaginary part of the optical interaction operator is electron interactions with the perturbing B atom, which cause virtual transitions accompanied by changes in electron momentum and angular momentum. Additional imaginaries contained in the $\mathbf{G}_{A^{**}B}$ Green functions at $E > 0$ should only influence the shift and broadening of the U_{A^+B} potential.

3. THE GREEN FUNCTION OF THE NONINTERACTING A** + B SYSTEM

By definition, the $\mathbf{G}_{A^{**}B}$ operator is the convolution

$$\mathbf{G}_{A^{**}B}(\mathbf{R}, \mathbf{R}'; E) = \frac{1}{(2\pi)^3} \times \int \exp(i\mathbf{k}\cdot\mathbf{R})\mathbf{G}_{A^{**}}\left(E - \frac{k^2}{2M_c}\right)\exp(-i\mathbf{k}\cdot\mathbf{R}')d\mathbf{k}, \quad (12)$$

where $\mathbf{G}_{A^{**}}$ is the Green operator of the isolated Rydberg atom. Integral (12) can easily be reduced to the integral

$$\mathbf{G}_{A^{**}B}(\mathbf{R}, \mathbf{R}'; E) = \frac{1}{(2\pi)^2} \times \int_0^{k_{\max}} \mathbf{G}_{A^{**}}(E - E_k)\frac{\sin[\mathbf{k}\cdot(\mathbf{R}-\mathbf{R}')]}{|\mathbf{R}-\mathbf{R}'|}kdk, \quad (13)$$

$$E_k = k^2/2M_c.$$

Note that, if $E < 0$, this expression is strictly real, because, according to (1), the $\mathbf{G}_{A^{**}}$ Green function of the Rydberg atom is defined at negative energies and corresponds to the bound electron state in the whole range of electron and atom B coordinate variations. For a positive total energy of the system ($E > 0$), the $\mathbf{G}_{A^{**}}$ function in (13) is generally complex, because, at $E_k < E$, it describes electron motion in the continuous spectrum. This region of momentum k variations of colliding particles includes virtual transitions to the ionization continuum and transitions between continuum states. The major contribution to (13) is made by the classically allowed region of motion, and the maximum momentum value is therefore determined from the condition

$$0 \le E + \frac{1}{R} - \frac{k^2}{2M_c}$$

and equals

$$k_{\max} = \sqrt{2M_c\left(E + \frac{1}{R}\right)}, \quad R_{\min} = I_A^{-1}, \quad R_{\min} \le R \le 2\nu_l^2 \quad (14)$$

(I_A is the ionization potential of atom A). Strictly, the maximum kinetic energy value (at given R) is determined by the equation

$$E_k^{(\max)}(R) = \frac{1}{2\nu_{\min}^2(R)},$$

which corresponds to the limiting virtual momentum value

$$k_{\max} = \sqrt{M_c}/\nu_{\min}(R)$$

(here, electron motion is not classical). As integral (13) is calculated in the $kR \le 1$ region, we can assume that

$$E_k^{(\max)}(R) = 1/R$$

to obtain (14).

Let us specify the $\mathbf{G}_{A^{**}}$ Green function of the strongly excited atom. By analogy with (8), the equation for $\mathbf{G}_{A^{**}}$ can be written as

$$\mathbf{G}_{A^{**}}(E) = \mathbf{G}^{(c)}(E) + \mathbf{G}^{(c)}(E)\tilde{\mathbf{T}}(E)\mathbf{G}^{(c)}(E), \quad (15)$$

where $\mathbf{G}^{(c)}$ is the Coulomb Green function and $\tilde{\mathbf{T}}$ is the matrix of collisions between the electron and the A^+ ion. Importantly, the poles of the Coulomb Green function are here strictly compensated, and the spectrum of energy eigenvalues is determined by the poles of the $\tilde{\mathbf{T}}$ matrix, which satisfies the integral equation [10]

$$\tilde{\mathbf{T}} = \mathbf{t} + \mathbf{t}\sum_l |lm\rangle\langle lm|\cot(\pi\nu(\varepsilon))\tilde{\mathbf{T}}, \quad (16)$$

where the $\mathbf{t}$ matrix of reactions describes electron interactions with the ionic core. Its diagonal elements are related to the μ_l quantum defect of the strongly excited atom as $t_{ll} = -\tan(\pi\mu_l)$. In the one-channel case that we are interested in, the diagonal elements of the $\tilde{\mathbf{T}}$ operator are

$$\tilde{T}_{ll}(\varepsilon) = -\frac{\tan(\pi\nu(\varepsilon))\tan(\pi\mu_l)}{\tan(\pi\nu(\varepsilon)) + \tan(\pi\mu_l)}. \quad (17)$$

Of greatest interest to us is the asymptotic region of the coordinates of the weakly bound electron, that is, the region in the vicinity of the perturbing atom B (ρ, $\rho' \ll R$), where the following general representation is valid [7]:

$$\mathbf{G}_{A^{**}}(\boldsymbol{\rho}, \boldsymbol{\rho}', \mathbf{R}, \varepsilon) = \mathbf{G}_0^{(c)}(\boldsymbol{\rho}, \boldsymbol{\rho}', \varepsilon) + 2\sum_{s,s'} |s\rangle\langle s'| g_{ss'}(\mathbf{R}, \varepsilon), \quad (18)$$

$$g_{ss'}(\mathbf{R}, \varepsilon) = [p_e(\varepsilon)\cot(\pi\nu(\varepsilon))\delta_{ss'} + \alpha_{LL'}^{ll'}(\mathbf{R}, \varepsilon)\delta_{M0}\delta_{M'0}]. \quad (19)$$

Here,

$$p_e(\varepsilon) = [2(\varepsilon + 1/R)]^{1/2}$$

is the quasi-classical electron momentum in the field of a Coulomb center,

$$\nu(\varepsilon) = (-2\varepsilon)^{-1/2}$$

is the effective principal quantum number, $|s\rangle$ is the electronic wave function

$$|s\rangle = |lmLM\rangle = j_L(p_e\rho)Y_{lm}(\mathbf{R}/R)Y_{LM}(\theta, \varphi), \quad (20)$$

$j_L(x)$ is the L-order spherical Bessel function of the first kind, $Y_{LM}(\theta, \varphi)$ is the spherical function [8], θ is the angle between the vectors $\mathbf{p}_e(\varepsilon)$ and ρ, L, and M are the orbital momentum of the electron with respect to atom B and its projection onto the $\mathbf{R}$ vector, and $\mathbf{G}_0^{(c)}$ is the smooth part of the Coulomb Green function,

$$\mathbf{G}_0^{(c)}(\boldsymbol{\rho}, \boldsymbol{\rho}'; \varepsilon) = -\frac{\cos(p_e|\boldsymbol{\rho} - \boldsymbol{\rho}'|)}{2\pi|\boldsymbol{\rho} - \boldsymbol{\rho}'|}. \quad (21)$$

The $\alpha_{LL'}^{ll'}(\mathbf{R}, \varepsilon)$ matrix in (19) is defined as

$$\alpha_{LL'}^{ll'}(\mathbf{R}, \varepsilon) = 2\pi^2\sqrt{(2L+1)(2L'+1)} \times \frac{(-1)^{l+l'}(\nu(\varepsilon))^3}{\sin^2(\pi\nu(\varepsilon))}\tilde{T}_{ll'}(\varepsilon)\tilde{\varphi}_{L\varepsilon}^{(l)}(R)\tilde{\varphi}_{L'\varepsilon}^{(l')}(R)|Y_{lm}(\mathbf{R}/R)|^2\delta_{ll'}. \quad (22)$$

The corresponding radial wave functions in (22) have the form

$$\tilde{\varphi}_{L\varepsilon}^{(l)}(R) = \begin{cases} Q_{l\varepsilon}(R, \nu), & L = 2k \\ Q_{l\varepsilon}(R, \nu - 1/2), & L = 2k+1, \end{cases} \quad k = 0, 1, 2, \ldots.$$

They differ from each other by the $\pi/2$ phase shift and are expressed via the Whittaker functions

$$Q_{l\varepsilon}(r, \nu) = \frac{W_{\nu, l+1/2}(2r/\nu)}{r\nu\sqrt{\Gamma(\nu - l)\Gamma(\nu + l + 1)}}, \quad (23)$$

where $\Gamma(x)$ is the gamma function. At large $r \gg 1$, their asymptotic expansions have the form [11]

$$\tilde{\varphi}_{L\varepsilon}(r) = -\frac{2}{r}i^{L+1}[2\pi p_e(\varepsilon)\nu^3(\varepsilon)]^{-1/2} \times \begin{cases} \cos[\sqrt{8r} - \pi\nu - \pi/4], & L = 2k+1 \\ i\sin[\sqrt{8r} - \pi\nu - \pi/4], & L = 2k. \end{cases} \quad (24)$$

The optical potential can be obtained in the explicit form by expanding (16) and (18) in spherical harmonics [12]; that is,

$$\mathbf{G}_{\mathrm{A}^{**}\mathrm{B}}(E) = \frac{2}{\pi}\sum_{\tilde{L}\tilde{M}} Y_{\tilde{L}\tilde{M}}(\mathbf{R}/R)Y_{\tilde{L}\tilde{M}}^*(\mathbf{R}'/R) \times \int_0^{k_{\max}} j_{\tilde{L}}(kR)j_{\tilde{L}}(kR')\mathbf{G}_{\mathrm{A}^{**}}(E - E_k)k^2dk, \quad (25)$$

$$\frac{\cos(p_e|\boldsymbol{\rho} - \boldsymbol{\rho}'|)}{2\pi|\boldsymbol{\rho} - \boldsymbol{\rho}'|} = 2p_e\sum_{LM} n_L(p_e\rho)j_L(p_e\rho') \times Y_{LM}(\boldsymbol{\rho}/\rho)Y_{LM}^*(\boldsymbol{\rho}'/\rho'), \quad \rho > \rho', \quad (26)$$

where $\tilde{L}$ and $\tilde{M}$ are the momentum and its projection onto the direction of $\mathbf{R} - \mathbf{R}'$ vector, and $n_L(p_e\rho)$ is the L-order spherical Bessel function of the second kind, which is related to the Neumann function as [8]

$$n_L(x) = \sqrt{\frac{\pi}{2x}}N_{L+1/2}(x).$$

4. THE OPTICAL POTENTIAL

Let us find the explicit form of the optical potential. For this purpose, we will use first-order perturbation theory and replace the $\mathbf{V}_{\mathrm{opt}}$ operator in the right-hand side of (11) by local operator (5). This means that, in the range of R variations under consideration, corrections to the $U_{\mathrm{A}^+\mathrm{B}}$ potential should be small. The optical potential is then determined as the matrix element

$$V_{\mathrm{opt}} = \langle q|\mathbf{V}_{\mathrm{opt}}|q\rangle, \quad (27)$$

calculated with basis wave functions (4). Accordingly, the $\mathbf{G}_{\mathrm{A}^{**}\mathrm{B}}$ operator in (27) describes the motion of particles with given orbital momenta $\tilde{L}$, L, and l. This means that the summation with respect to the specified indices should be omitted in (16) and (25). Because of the orthogonality of the spherical Bessel functions of the first and second kinds and because the $n_L(x)$ function reduces to $j_{L+1}(x)$ at large distances, the first term in (16) makes no contribution and should be eliminated. The integration in interatomic coordinates taking into account the symmetry property of the operator

$$\langle s|\mathbf{K}_{e^-\mathrm{B}}|s'\rangle = (\mathbf{K}_{e^-\mathrm{B}})_{ss}\delta_{ss'}$$

yields

$$V_{\text{opt}}(E, n, l, \tilde{L}, R)$$
$$= U_{A^+B}(R) + 2^{14}\pi^4 U^2_{A^+B}(R)\left|Y_{\tilde{L}0}(\theta = 0)\right|^4$$
$$\times\left\{\int_0^{k_{\max}} k^2 dk k'^2 dk' j^2_L(kR) j^2_L(k'R)\left[\frac{(\mathbf{K}_{e^-B})_{LL}}{1 + i(\mathbf{K}_{e^-B})_{LL}}\right]\right. \quad (28)$$
$$\left.\times\sum_{mM} g_{ss}(R, \varepsilon_k) g^*_{ss}(R, \varepsilon_{k'})\left|Y_{lm}(\mathbf{R}/R)\right|^2\left|Y_{LM}(\boldsymbol{\rho}/\rho)\right|^2\right\},$$

where $\varepsilon_k = E - k^2/2M_c$ and $\tilde{L}$ is the initial orbital momentum of colliding particles A** and B. The $Y_{lm}(\mathbf{R}/R)$ spherical function in (28), which is also present in the $g_{ss'}(R, \varepsilon)$ matrix, should be replaced by $Y_{lm}(0)$. Indeed, the electron motion in the vicinity of atom B at $l \ll \nu_l^{3/2}$ is described by a plane wave with the momentum directed along $\mathbf{R}$.

As the Rydberg electron behaves as a free particle in the vicinity of atom B [13], the diagonal elements of the $\mathbf{K}_{e^-B}$ matrix in (28), which depend on the total energy E of the system and the kinetic energies of the incident (ε_e) and scattered (ε'_e) electrons, can be replaced by the corresponding elements of the $\mathbf{K}^{(0)}_{e^-B}$ matrix of free electron scattering calculated at

$$\varepsilon_e = E + 1/R - k^2/2M_c.$$

This is valid if the electron wavelength λ weakly changes over the effective region ρ_0 of its interaction with atom B; that is, if [4]

$$\rho_0\frac{d\lambda}{dr} \ll \lambda \quad \text{or} \quad \frac{\rho_0}{(p_e R)^2} \ll 1.$$

In addition, it is necessary that the kinetic electron energy ε_e be much larger than its binding energy; that is,

$$n \gg \frac{1}{\sqrt{2(E + 1/R)}}.$$

Equation (28) defined for a given initial energy E_k then takes the form

$$V_{\text{opt}} = U_{A^+B} + \Delta - i\frac{\Gamma}{2}, \quad (29)$$

where the shift and broadening of the ionic term are

$$\Delta(E_k, n, l, \tilde{L}, R) = \frac{\pi K^{(0)}_{LL}(n, R)}{1 + [K^{(0)}_{LL}(n, R)]^2} S_{l\tilde{L}}(E_k, R),$$
$$\Gamma(E_k, n, l, \tilde{L}, R) = \frac{2\pi[K^{(0)}_{LL}(n, R)]^2}{1 + [K^{(0)}_{LL}(n, R)]^2} S_{l\tilde{L}}(E_k, R) \quad (30)$$

and depend on the initial excitation of atom A**(n, l), orbital momentum $\tilde{L}$, and distance R between A^+ and B. The expressions for the factor in (30) are determined by the sign of the total energy E of the system and are written as

$$S_{l\tilde{L}}(E_k, R) = \left[64\pi U_{A^+B}(R) Y^2_{L0}(\theta = 0) Y_{l0}(\theta = 0)\right.$$
$$\left.\times\int_0^{k_{\max}} j^2_{\tilde{L}}(kR) g_{ss}(R, \varepsilon_k) k^2 dk\right]^2 \quad (31)$$

for $E < 0$, and

$$S_{l\tilde{L}}(E_k, R) = [64\pi U_{A^+B}(R) Y^2_{\tilde{L}0}(\theta = 0) Y_{l0}(\theta = 0)]^2$$
$$\times\left|\int_0^{k_{\max}} j^2_{\tilde{L}}(kR)\,\mathrm{Re}\, g_{ss}(R, \varepsilon_k) k^2 dk\right. \quad (32)$$
$$\left. + i\int_0^{\sqrt{2M_c E}} j^2_{\tilde{L}}(kR)\,\mathrm{Im} g_{ss}(R, \varepsilon_k) k^2 dk\right|^2$$

for $E > 0$. The integration in (31) is actually divided into two intermediate regions. In the first region (at $0 \le k \le \sqrt{2M_c E}$), the real and imaginary parts of $g_{ss}(R, \varepsilon_k)$ are obtained by substituting $\nu = i/p$ in (17), which gives

$$\mathrm{Re} g_{ss}(R, \varepsilon_k)$$
$$= -\frac{4\pi Y^2_{l0}(\theta = 0)}{R^2 p_e(\varepsilon_k)}\sin(\pi\mu_l)\sin(4\sqrt{2R} + \pi\mu_l),$$
$$\mathrm{Im} g_{ss}(R, \varepsilon_k) = -p_e(\varepsilon_k) + \frac{4\pi Y^2_{l0}(\theta = 0)}{R^2 p_e(\varepsilon_k)} \quad (33)$$
$$\times\sin(\pi\mu_l)\cos(4\sqrt{2R} + \pi\mu_l).$$

In the second region (at $k > \sqrt{2M_c E}$), the $g_{ss}(E, \varepsilon_k)$ function is real and determined by (17).

Let us analyze these results. First, note that the potential shift Δ is proportional to the $K^{(0)}_{LL}$ element and depends on its sign, and the potential width $\Gamma \sim (K^{(0)}_{LL})^2$ is always positive. The $S_{l\tilde{L}}(E, n, R)$ value is an oscillating function of distance R and total energy E. For a negative system energy ($E < 0$), it vanishes outside the classically allowed region of electron motions [that is, at $R \ge (-E)^{-1}$]. In addition, the $S_{l\tilde{L}}(E, k, R)$ region contains the centrifugal factor

$$\frac{\tilde{L}(\tilde{L} + 1)}{2M_c R^2}$$

and should increase as the $\tilde{L}$ angular momentum of colliding particles increases.

Oscillations in R appear because of the $j_{\tilde{L}}(kR)$ Bessel functions in (30) and (31). In the $R_* < R < 2n^2$ region, the characteristic size of oscillations

$$\Delta R \approx \pi \frac{R^{1/2}(RE+1)^{1/2}}{\sqrt{2M_c}(2RE+1)} \tag{34}$$

is substantially smaller than the electron wavelength $\lambda \approx n$. We can therefore perform averaging on scale λ to pass to smooth dependences of Δ and Γ on R.

Oscillations in E are more complex in character. They can be divided into three principal types. The first type are resonances corresponding to the poles of the $\tilde{\mathbf{T}}$ operator of electron collisions with ionic core A^+ in the $g_{ss}(R, \varepsilon_k)$ matrix. At a fixed initial kinetic energy E_k, they are situated in the interval

$$-I_A < E \le E_k$$

and, according to (17), are determined from the condition

$$\tan(\pi\nu(\varepsilon_k)) = -\tan(\pi\mu_l).$$

The positions of the resonances are described by the simple formula

$$E_n^{(r)} = E_k - \frac{1}{2(n-\mu_l)^2},$$

in which the principal quantum number changes in the range $n_{\min} \le n < \infty$ (with the minimum value

$$n_{\min} \ge \hat{E}(1/\sqrt{2I_A}),$$

where symbol $\hat{E}$ denotes the integer part). The scale of these oscillations is $\Delta E^{(1)} \sim 1/n^3$.

Oscillations of the second type are related to the behavior of the square of the spherical Bessel function $j_{\tilde{L}}^2(kR)$ in (31) and (32). Their scale is easy to estimate on the assumption that the $g_{ss}(R, \varepsilon_k)$ matrix can be removed from the integrand in k in the $E_n^{(r)} < E < E_{n+1}^{(r)}$ interval. The oscillations are then determined by the functions $\sin(2k_{\max}(E)R)$ (for even $\tilde{L}$) and $\cos(2k_{\max}(E)R)$ (for odd $\tilde{L}$), whose scale is

$$\Delta E^{(2)} \approx \pi^2/M_c R^2 \ll \Delta E^{(1)}.$$

This estimate is valid for small $n \ll [\Delta E^{(2)}]^{-1/3}$ values. Otherwise, a complex irregular structure should be observed.

Oscillations of the third type are "beats," which arise as a result of the disturbance of the strict compensation of the Coulomb poles in the $g_{ss}(R, \varepsilon_k)$ asymptotic function at $R \le n$ and cause splitting of resonance peaks. Naturally, for the purely Coulomb case ($\mu_l = 0$), the second term in (19) vanishes and the beats should disappear.

It follows from (30) and (31) that the $\Gamma(E)$ width at $E = 0$ has no singularities, that is, it is an analytic function. The value averaged over oscillations is larger for positive total energies than for $E < 0$. This is caused by the appearance of additional (virtual) ionization of the A** atom in passing through the $E = 0$ point.

It is also easy to see that the shift and broadening of the ionic potential are finite irrespective of the sign of total energy E in the $k \longrightarrow 0$ limit. Physically, this is a natural result, because the weakly bound electron can always exercise a virtual transition to a lower lying state (with a lower n value) when the relative motion of atoms is switched on. Note, however, that the passage to this limit requires the fulfillment of an additional condition of the smallness of scattering phase $\eta_{\tilde{L}}$ in the Born approximation. For polarization potentials, this condition is only met if $\tilde{L} \ge 1$ [5].

5. THE *K* MATRIX OF ELECTRON SCATTERING BY ATOM B

There are two mechanisms, direct and resonance, of the interaction of slow electrons with atoms [14]. The direct mechanism (potential or background scattering) is usually described as

$$K_{LL}^{(0)}(\varepsilon, R) = -\frac{1}{p_e(R)}\tan(\delta_L(\varepsilon)), \tag{35}$$

where δ_L is the phase of elastic electron scattering determined at the energy equal to the kinetic energy of the electron at the point where the B atom is situated. At low energies $\varepsilon^{1/2}|Q| \ll 1$ and $\varepsilon\beta \ll 1$ (here, Q and β are the quadrupole moment and the polarizability of atom B), the $K_{LL}^{(0)}$ value can be written in the form [15]

$$K_{LL}^{(0)} = a\delta_{L0} - \frac{L(L+1)-3M^2}{L(L+1)(2L-1)(2L+3)}Q(1-\delta_{L0}) - \frac{\pi p_e \beta}{(2L-1)(2L+1)(2L+3)} + \ldots, \tag{36}$$

where a is the scattering length. Clearly, matrix elements (36) at $L = 0$ are determined by the spherically symmetrical interaction part and largely depend on the scattering length. At $L \ne 0$, they also take into account the anisotropic interaction part, which results in a dependence on quadrupole moment Q. In the problem under consideration ($n \gg 1$), we can use the long-wave

($L = 0$) decomposition [16] for the $\mathbf{K}^{(0)}_{e^-\mathrm{B}}$ matrix elements,

$$K^{(0)}_{00}(R) = a + \frac{\pi\beta}{3}p_e(R) + \frac{4}{3}\beta p_e^2(R)a\ln p_e(R) + \gamma p_e^2(R),$$
$$p_e(R) = \left[\frac{2}{R} - \frac{1}{2\nu_l^2}\right]^{1/2}, \quad (37)$$

where γ is the coefficient whose values for rare gas atoms were calculated in [17].

For the resonance mechanism of electron interactions with the B perturbing particle, the scattering operator can be written in the form

$$\mathbf{K} = \mathbf{K}^{(0)} + \mathbf{V}\frac{|\varphi_r\rangle\langle\varphi_r|}{E - E_r + 1/R}\mathbf{V}. \quad (38)$$

Here, $|\varphi_r\rangle$ and E_r are the wave functions and the energy of the resonance state of the A^+B quasi-molecule and $\mathbf{V}$ is the corresponding interaction. The poles of the second term in (38) determine the positions of the ionic configuration terms,

$$U^{(i)}(R) = E_r - 1/R.$$

Note that the $\mathbf{K}$ operator is determined uniquely for positive and negative energies.

6. THE CROSS SECTION OF ELASTIC SCATTERING

The major contribution to optical potential (29) at small $R \sim R_{\min}$ distances is made by exchange interactions between the A^+ ion and atom B, because the δ_L phase of elastic electron scattering by atom B rapidly decreases as kinetic energy ε increases, and matrix element (35) becomes small. Taking this into account, the total cross section of elastic A**–B scattering can conveniently be written as

$$\sigma_{el} = \sum_{\tilde{L}}\sigma_{\tilde{L}} \approx 2\pi\frac{\tilde{L}_0^2}{k^2} + 4\pi\sum_{\tilde{L}_0+1}(2\tilde{L}+1)\left|f_{\tilde{L}}\right|^2. \quad (39)$$

Here, angular momentum $\tilde{L}_0$ is given by $\tilde{L}_0 = \hat{E}(kR_c(k))$ and the E symbol denotes the integer part of the $kR_c(k)$ value, where $R_c(k)$ is the turning point of the repulsive part of the $U_{\mathrm{A}^+\mathrm{B}}$ potential at a given kinetic energy E_k of the system. The Born approximation in the distorted wave method [21] can conveniently be applied to the $f_{\tilde{L}}$ partial amplitudes, which are then written as the sums of two terms,

$$f_{\tilde{L}}(k) = f^{(1)}_{\tilde{L}}(k) + f^{(2)}_{\tilde{L}}(k). \quad (40)$$

The first term corresponds to $\Delta = \Gamma = 0$ and is the elastic scattering amplitude on the polarization part of the $U_{\mathrm{A}^+\mathrm{B}}$ potential; that is,

$$f^{(1)}_{\tilde{L}}(k) = \frac{\exp(i\delta^{(1)}_{\tilde{L}}(k))\sin(\delta^{(1)}_{\tilde{L}}(k))}{k}, \quad (41)$$

where $\delta^{(1)}_{\tilde{L}}(k)$ is the corresponding phase, which, at $\tilde{L} > \tilde{L}_0$, can be described by the simple dependence [5]

$$\delta^{(1)}_{\tilde{L}}(k) = -\frac{\pi M_c\beta k^2}{8(\tilde{L}+1/2)^3}. \quad (42)$$

The cross section of scattering is then given by

$$\sigma^{(0)}_{el}(k) = \pi\left[\frac{\pi M_c\beta}{k}\right]^{2/3}. \quad (43)$$

The second term in the total amplitude [Eq. (40)] is described by the equation

$$f^{(2)}_{\tilde{L}}(k) = -\frac{2M_c}{k^2}\int_{R_0}^{2n^2} u^2_{\tilde{L}}(kR)\left[\Delta - i\frac{\Gamma}{2}\right]dR, \quad (44)$$

where the lower limit of integration is determined from the condition

$$U_{\mathrm{A}^+\mathrm{B}}(R_0) \geq \Delta(R_0).$$

The $u_{\tilde{L}}(kR)$ function is the solution to the radial Schrödinger equation with polarization interaction and is normalized by the asymptotic

$$u_{\tilde{L}}(kR) \propto \frac{1}{k}\sin\left(kR - \frac{\pi\tilde{L}}{2} + \delta^{(1)}_{\tilde{L}}\right).$$

Accordingly, the square of the modulus of the total elastic scattering amplitude is

$$\left|f_{\tilde{L}}(k)\right|^2 = (\mathrm{Re}\, f_{\tilde{L}}(k))^2 + (\mathrm{Im}\, f_{\tilde{L}}(k))^2, \quad (45)$$

where

$$\mathrm{Re}\, f_{\tilde{L}}(k) = \frac{\sin\delta^{(1)}_{\tilde{L}}\cos\delta^{(1)}_{\tilde{L}}}{k} + \mathrm{Re}\, f^{(2)}_{\tilde{L}}(k),$$

$$\mathrm{Im}\, f_{\tilde{L}}(k) = \frac{\sin^2\delta^{(1)}_{\tilde{L}}}{k} + \mathrm{Im}\, f^{(2)}_{\tilde{L}}(k).$$

7. INTERACTION OF Na(nl) ATOM WITH RARE GAS ATOMS

By way of illustration, consider slow collisions between Rydberg Na**(nl) and rare gas atoms. Of greatest interest (at given initial excitation of atoms E_{n_0} and relative energy E_k) are the dependences of the ionic term width on total energy E and interatomic distance R.

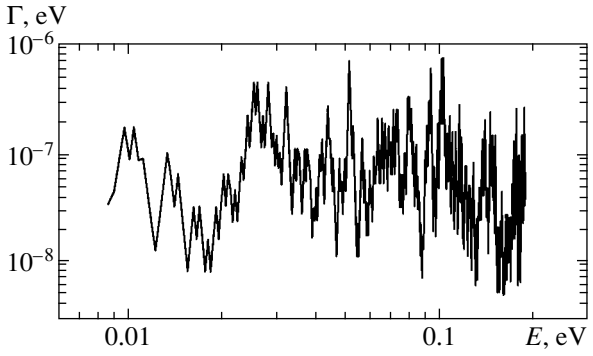

Fig. 1. Dependence of optical potential width Γ on the total energy E of the Na**(10s) + He system.

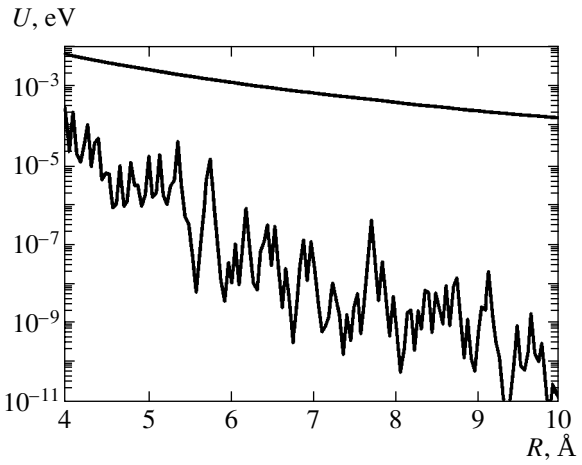

Fig. 2. Dependence of optical potential width Γ and the U_{Na^+He} ionic term taken with the opposite sign on interatomic distance R in the Na**(10d) + He system at E_k = 0.19 eV and L = 0. The smooth curve is the ionic term, and the oscillating curve is the Γ(R) width.

The dependence on the principal quantum number n of intermediate virtual states then reproduces the energy dependence at points $E_n^{(r)}$ situated in the $n_0 \le n < \infty$ interval and is of minor interest. The dependence on the electron angular momentum l is weak. Below, for the example of the Na**(10s) + He system, we restrict consideration to the dependence of Γ on energy E, and, for the example of the Na**(10d) + B systems (where B = {He, Ne, Ar, Kr, and Xe}), we analyze the dependence on R. The corresponding calculations were performed by (30)–(33) with the a, β, and γ parameters in decomposition (37) taken from [18]. These parameter values are listed in the table. The quantum defects of the s, p, and d series of the sodium atom were set equal to

$$\mu_s = 1.35, \quad \mu_p = 0.86, \quad \mu_d = 0.015.$$

These values were found based on the spectroscopic data of the National Institute for Standards and Technologies (NIST Atomic Spectra Database Data).

Parameters a, β, and γ for rare gas atoms

Atom	a	β	γ
He	1.15	1.38	6.0
Ne	0.30	2.68	6.5
Ar	–1.69	11.08	–5.0
Kr	–3.20	16.74	–40.0
Xe	–6.00	27.06	–210.0

The dependence of ionic term width Γ on the total energy E of the system shown in Fig. 1 was calculated for the following initial data:

$$E_k = 0.1904 \text{ eV}, \quad n_0 = 10, \quad l = \tilde{L} = 0, \quad R \approx 5 \text{ Å}. \tag{46}$$

As expected, the oscillations converge to the E_k limit. At small n values (in the vicinity of the $E_n^{(r)}$ Rydberg resonances, whose positions are determined by the poles of the $g_{ss}(E)$ matrix and indicated by arrows), splitting of the corresponding peaks is observed. A well-defined fine structure of oscillations of the second type is seen between the resonances. The fine structure minima are situated in the neighborhood of zeros of the $\sin[R\sqrt{2M_c(E + 1/R)}]$ function. The picture becomes noticeably more complex as n increases.

The dependences of width Γ on interatomic distance R calculated for different rare gas atoms are shown in Figs. 2–6. It follows from these figures that width Γ(R) is an oscillating function and rapidly decreases as R increases. In conformity with (34), the frequency of oscillations increases as the M_c reduced mass grows. Simultaneously, the width itself increases, which is explained by the influence of the a, β, and γ parameters (see table).

One more illustration is the dependences of the Na**(ns) + He elastic scattering cross section on kinetic energy E_k (at a fixed principal quantum number n_0 = 10) and on the level number n (at a given E_k = 10^{-3} eV energy) shown in Figs. 7 and 8; these dependences were calculated by (39)–(45). The total scattering cross section $\sigma_{el}(E_k)$ shown in Fig. 7 is a strongly oscillating function of kinetic energy. In the region of energies under consideration, its structure is determined by oscillations of the second type. The height of the peaks is one to two orders of magnitude larger than the Na^+–He scattering cross section.

The dependence of the elastic scattering cross section $\sigma_{el}(n)$ on the principal quantum number (see Fig. 8) is also a nonmonotonic function, which is, at certain points, three orders of magnitude larger than the $\sigma_{el}(0)$ value equal to 10^{-13} cm^2 at $E_k = 10^{-3}$ eV. The scale of these oscillations is $\Delta n \sim 10$, and the prospects for their

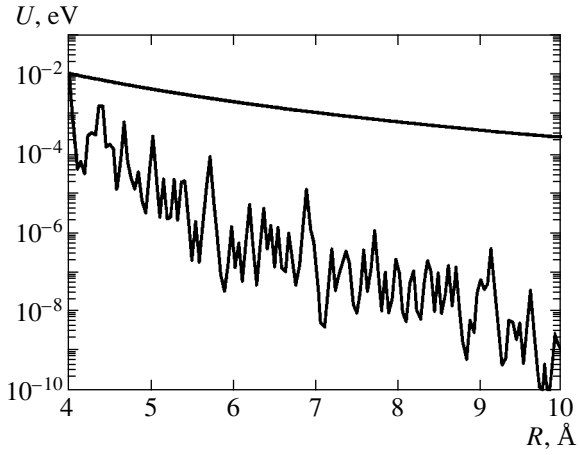

Fig. 3. The same as in Fig. 2 for the Na**(10*d*) + Ne system.

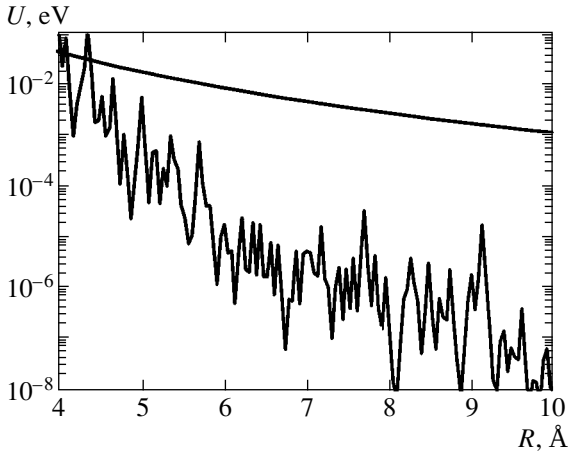

Fig. 4. The same as in Fig. 2 for the Na**(10*d*) + Ar system.

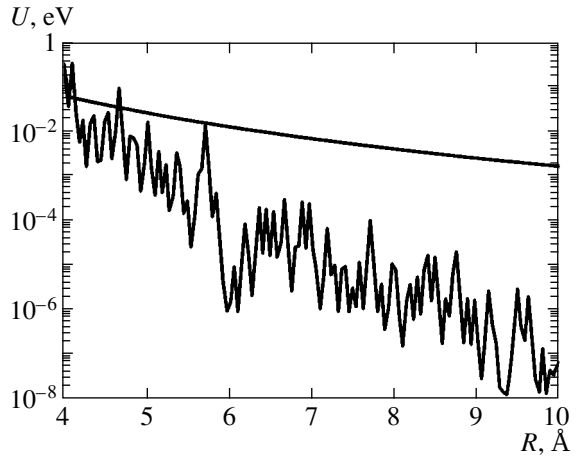

Fig. 5. The same as in Fig. 2 for the Na**(10*d*) + Kr system.

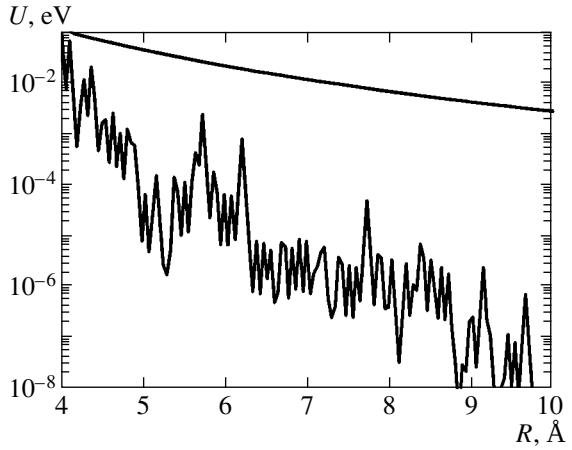

Fig. 6. The same as in Fig. 2 for the Na**(10*d*) + Xe system.

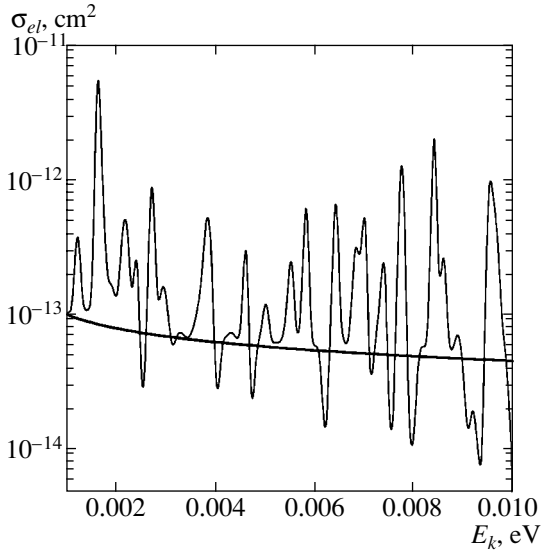

Fig. 7. Dependence of the total elastic scattering cross section for Na**(10*s*) + He on the kinetic energy of colliding particles. The thin line corresponds to calculations with the use of optical potential (29), and the thick line is the cross section of Na^+–He scattering calculated by (43).

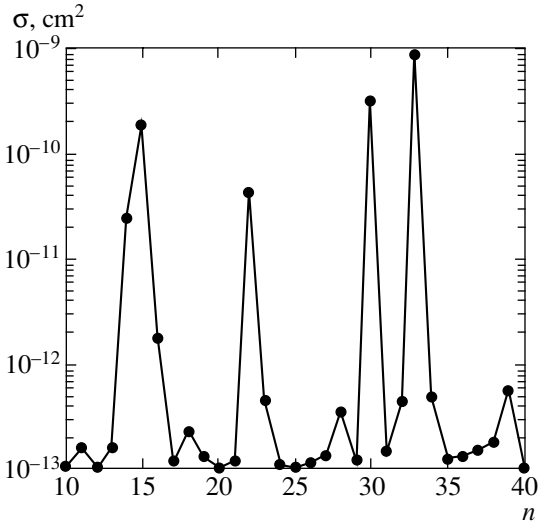

Fig. 8. Dependence of the total Na**(*ns*) + He elastic scattering cross section on principal quantum number *n*.

experimental observation therefore appear to be quite realistic. Of greatest interest is the region of superlow temperatures, which is currently being extensively studied [22–25].

A natural application of the developed theory can be calculations of inelastic and transport cross sections. One more important application is related to the use of the diffusion approach to describing the dynamics of collisions of Rydberg atoms [26], where the electronic transition in the elementary interatomic collision event is treated as diffusion over the energy states of an excited quasi-molecule. The diffusion coefficient is then determined by the probability of transitions per unit time and is directly related to the imaginary part of optical potential (29). In the absence of necessary information, only crude estimates are possible.

8. CONCLUSION

In this work, we were able to pass from the three- to the two-particle problem first and foremost because the major contribution to the broadening and shift of the U_{A^+B} ionic term was made by the region of electron motions close to the B atom, which is much smaller than interatomic distance R [7]. One more important circumstance is the weakly bound character of the electron in the A** + B system; for this reason, this electron can be treated as a free particle in interactions with the B atom. Lastly, the mass of the electron is small compared with the reduced mass of atoms, and the center of gravity of the system is therefore actually situated on the axis connecting the centers of the atoms. The introduction of the optical potential, which takes into account all possible nonadiabatic transitions, is a convenient formal technique, which allows the total and differential cross sections of processes near the ionization continuum to be calculated by the standard quantum scattering theory methods. This potential is introduced in the spectral region where the concept of the potential of nuclei makes no sense, because, in this region, the slow particle is the electron [4].

We restricted our consideration to the simplest situation when the B atom is a structureless particle. This approximation is quite justified for rare gas atoms. In considering more complex atoms, we should, however, take into account the multichannel character of electron motions [18] related to excitation of the ionic core and the possibility of electron capture with the formation of ion pairs [19]. Ion pairs are formed when the B atom has a positive electron affinity, and their formation can substantially change the resulting picture. In addition, the possibility of the decomposition of the A* + B quasi-molecule caused by predissociation, that is, a nonadiabatic transition to the dissociative electronic configuration A* + B accompanied by the acceleration of atoms [20], should be borne in mind. A study of these problems is beyond the scope of the present communication and requires additional inquiries.

ACKNOWLEDGMENTS

The authors thank Yu.N. Demkov and I.V. Komarov for discussions and valuable comments.

This work was financially supported by the Russian Foundation for Basic Research (project no. 00-03-32102) and INTAS (grant 99-00039).

REFERENCES

1. I. I. Sobelman, L. A. Vainshtein, and E. A. Yukov, *Excitation of Atoms and Broadening of Spectral Lines* (Fizmatigiz, Moscow, 1979; Springer-Verlag, Berlin, 1981).
2. *Rydberg States of Atoms and Molecules*, Ed. by R. F. Stebbings and F. B. Dunning (Cambridge Univ. Press, Cambridge, 1983; Mir, Moscow, 1985).
3. D. L. Moores and H. E. Saraph, in *Atoms in Astrophysics*, Ed. by P. G. Burke *et al.* (Plenum, New York, 1983; Mir, Moscow, 1986).
4. G. V. Golubkov and G. K. Ivanov, *Rydberg States of Atoms and Molecules and Elementary Processes with Their Participation* (URSS, Moscow, 2001).
5. N. F. Mott and H. S. W. Massey, *The Theory of Atomic Collisions* (Clarendon, Oxford, 1965; Mir, Moscow, 1969).
6. A. Z. Devdariani, V. I. Demidov, N. B. Kolokolov, and V. I. Rubtsov, Zh. Éksp. Teor. Fiz. **84**, 1648 (1983) [Sov. Phys. JETP **57**, 960 (1983)].
7. G. V. Golubkov and G. K. Ivanov, Z. Phys. A **319**, 17 (1984).
8. A. S. Davydov, *Quantum Mechanics* (Nauka, Moscow, 1973; Pergamon, Oxford, 1976).
9. M. L. Goldberger and K. M. Watson, *Collision Theory* (Wiley, New York, 1964; Mir, Moscow, 1967).
10. G. V. Golubkov and G. K. Ivanov, J. Phys. B **17**, 747 (1984).
11. E. T. Whittaker and G. N. Watson, *A Course of Modern Analysis* (Cambridge Univ. Press, Cambridge, 1952; Fizmatgiz, Moscow, 1963), Vol. II.
12. R. G. Newton, *Scattering Theory of Waves and Particles* (McGraw-Hill, New York, 1966; Mir, Moscow, 1969).
13. V. A. Alekseev and I. I. Sobel'man, Zh. Éksp. Teor. Fiz. **49**, 1274 (1965) [Sov. Phys. JETP **22**, 882 (1966)].
14. G. F. Drukarev, *Collisions of Electrons with Atoms and Molecules* (Nauka, Moscow, 1978; Plenum, New York, 1987).
15. G. K. Ivanov, Opt. Spektrosk. **43**, 1044 (1977) [Opt. Spectrosc. **43**, 617 (1977)].
16. T. O'Malley, L. Sprach, and L. Rosenberg, Phys. Rev. **125**, 130 (1962).
17. G. K. Ivanov, Opt. Spektrosk. **40**, 965 (1976) [Opt. Spectrosc. **40**, 554 (1976)].

18. E. M. Balashov, G. V. Golubkov, and G. K. Ivanov, Zh. Éksp. Teor. Fiz. **103**, 374 (1993) [JETP **76**, 200 (1993)].
19. G. K. Ivanov, G. V. Golubkov, and E. M. Balashov, Dokl. Akad. Nauk **323**, 311 (1992).
20. G. K. Ivanov and G. V. Golubkov, J. Phys. B **189**, L383 (1985).
21. J. R. Taylor, *Scattering Theory: the Quantum Theory of Nonrelativistic Colluions* (Wiley, New York, 1972; Mir, Moscow, 1975).
22. W. R. Anderson, J. R. Veale, and T. F. Gallagher, Phys. Rev. Lett. **80**, 249 (1998).
23. R. Cote and A. Dalgarno, Phys. Rev. A **58**, 498 (1998); **62**, 012709 (2000).
24. J. Weiner, V. S. Bagnato, S. Zilio, *et al.*, Rev. Mod. Phys. **71**, 1 (1999).
25. W. C. Stwalley and H. Wang, J. Mol. Spectrosc. **195**, 194 (1999).
26. A. Z. Devdariani, A. N. Klyucharev, N. P. Penkin, *et al.*, Opt. Spektrosk. **64**, 706 (1988) [Opt. Spectrosc. **64**, 425 (1988)].

Translated by V. Sipachev

Journal of Experimental and Theoretical Physics, Vol. 95, No. 6, 2002, pp. 998–1005.
Translated from Zhurnal Éksperimental'noĭ i Teoreticheskoĭ Fiziki, Vol. 122, No. 6, 2002, pp. 1158–1167.

NUCLEI, PARTICLES, AND THEIR INTERACTION

Observation of Dielectronic Satellites in the *K*-Spectrum of Argon Ions in Plasma Produced by Femtosecond Laser Pulses

A. I. Magunov[a, *], A. Ya. Faenov[b], I. Yu. Skobelev[b], T. A. Pikuz[b], E. Biémont[c, d], P. Quinet[d], F. Blasco[e], C. Bonte[e], F. Dorchies[e], T. Caillaud[e], F. Salin[e], and C. Stenz[e]

[a]*General Physics Institute, Russian Academy of Sciences, ul. Vavilova 38, Moscow, 119991 Russia*
[b]*State Research Center VNIIFTRI, Mendeleevo, Moscow oblast, 141570 Russia*
[c]*IPNE (Bat. B15), Université de Liége, Sart Tilman, B-4000, Liége 1, Belgium*
[d]*Astrophysique et Spectroscopie, Université de Mons-Hainaut, Rue de la Halle, 15, B-7000, Mons, Belgium*
[e]*CELIA, Université de Bordeaux I, 33405, Talence, France*
**e-mail: magunov@fpl.gpi.ru*

Received May 31, 2002

Abstract—The satellite structure of $1s2p^{1,\,3}P_1$–$1s^{2\,1}S_0$ lines of the He-like argon ion in plasma produced by a 45-fs laser pulse in a gas-jet cluster target is measured with a high spectral resolution. Radiation transitions $2p \longrightarrow 1s$ from autoionizing states (AISs) are detected for ions ranging from Li-like to F-like. The spectrum observed is theoretically simulated with the use of the spectroscopic data for the AISs of multicharged ions obtained within the multiconfiguration relativistic Hartree–Fock method. Good agreement with experimental data is obtained when the main population channels of these states are taken into account for typical values of cluster-target plasma parameters. © *2002 MAIK "Nauka/Interperiodica".*

1. INTRODUCTION

At present, cluster targets based on a supersonic gas jet expanding at high pressure into a vacuum chamber are widely used for producing plasma by femtosecond laser pulses; this is primarily associated with various applications of such plasma (for instance, controlled fusion, sources of monochromatic and wideband X-ray radiation, acceleration of charged particles, etc. [1–10]). Similar experiments can also be carried out for fundamental spectroscopic and diagnostic investigations of laser plasma. In particular, a promising direction is the investigation of extraordinary (from the viewpoint of conventional conditions for producing laser plasma) emission spectra of multicharged ions, such as radiation-transition lines in hollow ions [11–18] and the related transitions in inner shells, i.e., the radiation decay of autoionizing states (AISs). These lines are observed, as a rule, in plasma with high electron density, and their relative intensities are highly sensitive to the plasma parameters. It is well known that high-density plasma is created when a very short laser pulse is absorbed by a cluster target [10, 19–21].

The specific conditions implemented in the plasma produced by femtosecond laser pulses, namely, a comparatively low level of ionization and the presence of an appreciable fraction of fast electrons (see, for example, [21, 22]), should give rise to satellite lines in the emission spectrum of the plasma that are associated with the radiation decay of AISs with the number of electrons ranging from four to nine. The existence of these lines gives an additional opportunity to apply X-ray spectroscopy techniques to the diagnosis of short-lived plasma; however, this requires a preliminary investigation of the satellite lines themselves, which includes, first of all, the identification of these lines and high-precision measurements of their wavelengths.

Similar spectra were measured earlier in experiments on the interaction of slow multicharged ions with metal surfaces [12, 23]; however, the spectral resolution of these measurements was rather low. In experiments with high-voltage gas-discharge plasma (plasma focus) [24], the spectral resolution was limited by the size of the emitting region.

In the present paper, we report the results of measurements of the satellite structure of $1s2p^{1\,3}P_1$–$1s^{2\,1}S_0$ lines of the He-like argon XVII ion in the spectrum of plasma produced by a 45-fs-long laser pulse in a gas-jet argon target. The observed radiation spectrum of the satellite lines in the Ar XVI–X ions (from Li-like to F-like inclusive) is compared with the wavelengths, the radiation probabilities, and the autoinonization widths of the energy levels of appropriate ions calculated by the multiconfiguration relativistic Hartree–Fock method. A simple kinetic model that takes into account the main population channels of AISs is used for modeling the spectra. The plasma parameters are taken from detailed kinetic calculations performed earlier [9, 10].

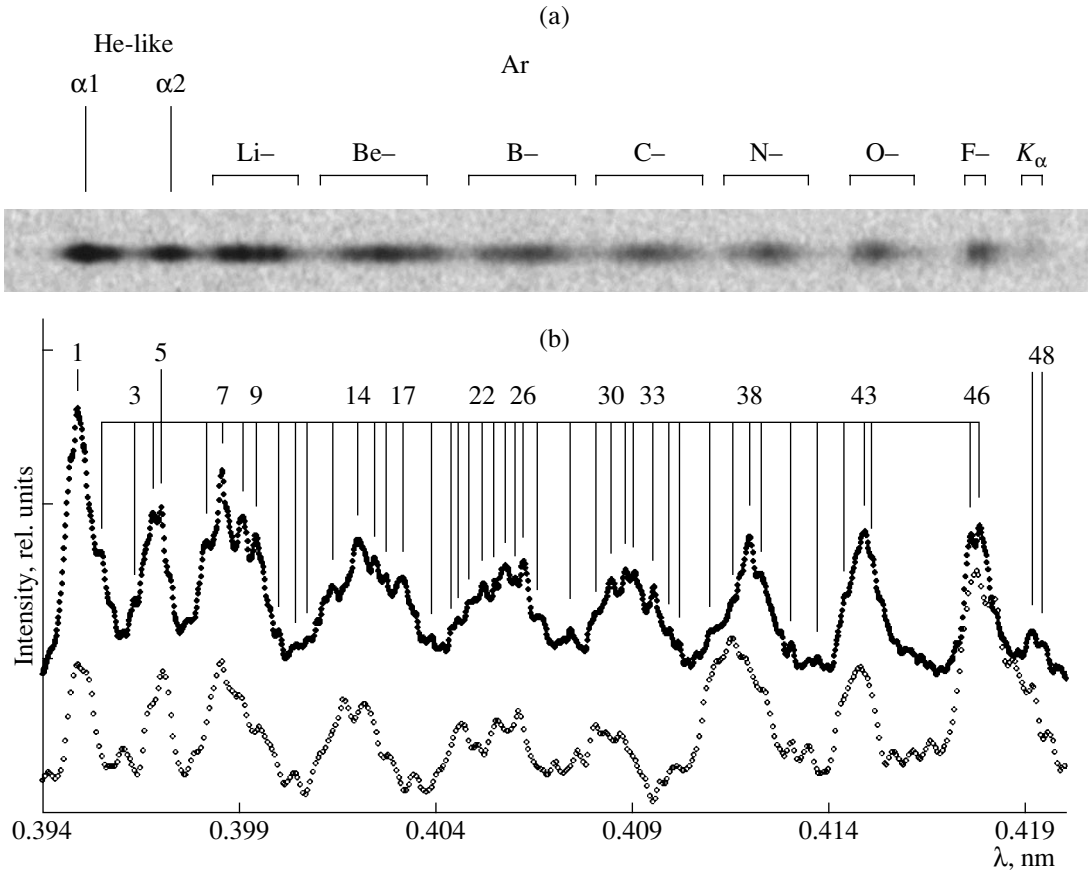

Fig. 1. (a) The spectrogram of laser-produced plasma in the argon cluster jet. (b) The spectral characteristic of the X-ray yield for the AISs of Ar X–XVII ions. Black circles correspond to femtosecond laser plasma (the present work), and light circles correspond to high-voltage gas-discharge plasma obtained in the plasma-focus equipment [24].

2. EXPERIMENTAL SETUP

Experiments were carried out on the Ti-sapphire laser system at the University of Bordeaux I; this system operates in a four-stage chirped pulse amplification mode. The details of this laser system were described in [25]. In these experiments, the energy of the main 45-fs-long pulse at the output was 15 mJ under an intensity contrast of about 10^5 with respect to a prepulse generated by a regenerative amplifier included in the system. A laser beam was focused by an off-axis parabolic mirror to give a 6-μm spot at a level of $1/e^2$ in vacuum. A pulse length of 45 fs corresponded to a peak intensity on the order of 10^{17} W/cm^2, which was sufficient for the tunneling ionization of argon ions up to F-like ions [26].

A pulsed argon jet expanding into a vacuum chamber from a supersonic conic nozzle with $M = 2.5$ was used as a target. The maximum pressure at the valve was about 60 atm, and the divergence angle of the jet was 22°. Under these conditions, atomic clusters are formed in the jet due to the Van der Waals interaction [9, 27]. Under a fast ionization of clusters, the maximum electron density in these clusters is much greater than the critical value of $N_{e,\,\mathrm{cr}} \approx 1.7 \times 10^{21}$ cm^{-3} (for $\lambda_{\mathrm{las}} = 0.8$ μm).

X-ray spectroscopic measurements were performed with the use of a focusing, spherically bent (R = 150 mm) spectrometer (a crystal-quartz spherical layer with an interplane spacing of $2d = 0.49$ nm) [28] in the range of wavelengths from 0.394 to 0.425 nm (the first reflection order) with a hardware resolution of $\lambda/\Delta\lambda \sim 10^4$. The spectrum was recorded on a DEF-2 film through a filter made of a 2-μm-thick polypropylene layer with both surfaces covered by 0.4-μm-thick aluminum film. The plasma spectrogram obtained is shown in Fig. 1a.

3. CALCULATION OF THE ATOMIC STRUCTURE

The energies and the probabilities of radiation and autoionization transitions for $1s^k2s^m2p^n(S'L')^{2S+1}L_J$ levels of the Ar X–XVII ions were calculated by a code based on the multiconfiguration Hartree–Fock method with relativistic corrections (MHFR) [29]. The mixing of the above configurations and those containing $3l$ electrons in the outer m shell was taken into consideration. To take into account the effect of other configurations, a special optimization procedure for the integrals of electrostatic and spin–orbit interactions was

applied. This procedure involves the interpolation or extrapolation of the average energy of a configuration along an isoelectronic sequence on the basis of the data for other ions available in the literature (P VII–XIV, S VIII–XV, K XI–XVIII, and Ca XII–XIX). A more detailed description of this procedure and the results can be found in [24].

4. SIMULATION OF THE SATELLITE SPECTRA

In the experiments carried out in this work, we measured the time-integrated X-ray emission from plasma. The spectral characteristic of the X-ray yield in the region of $1s2p \longrightarrow 1s^2$ transition in the He-like ion is approximately given by

$$I(\omega) \propto \omega \sum_{Z,\,i,\,f} A_{if}^Z S_{if}^z(\omega - \omega_{if}^Z, N_e, T_e) \times N_i^Z(N_e, T_e, f, T_h), \quad (1)$$

where A_{if}^Z is the rate of the radiation transition $i \longrightarrow f$ ($1s2s^n2p^m \longrightarrow 1s^22s^n2p^{m-1}$) in the Ar^{Z+} ion and N_i^Z is the population of the upper level for electron temperature T_e and density N_e, averaged over time plasma volume, and the fraction $f \ll 1$ of hot electrons with temperature T_h. The spectral function, normalized to unity in frequency, is given by

$$S_{if}^Z(\omega - \omega_{if}^Z, N_e, T_e, \gamma) = \frac{1}{\sqrt{\pi}\gamma} \times \int \exp[-(\omega - \omega')^2/\gamma^2] L(\omega' - \omega_{if}^Z, \Gamma_{if}^Z) d\omega', \quad (2)$$

which corresponds to the averaging of the line spectrum of radiation over the normal distribution width γ defined by the hardware resolution and the inhomogeneous Doppler broadening of lines. Homogeneous line broadening for a small Stark shift is described by the Lorentz profile $L(\Delta\omega, \Gamma)$ with the total width

$$\Gamma_{if}^Z = A_i^Z + A_f^Z + \Gamma_i^Z + \gamma_{if}^Z$$

determined by the radiation decay rates

$$A_j^Z = \sum_k A_{jk}^Z$$

of the upper and lower levels, by the autoionization rate Γ_i^Z of the upper level, and by the collisional width γ_{if}^Z.

In a quasistationary approximation under the condition that the temperature T_e of the main fraction of electrons is much less than the excitation energy of AISs, the populations of these states are defined by the relation

$$\frac{1}{\tau_i^Z} N_i^Z = C_i^{Z+1}(T_e) N_e N_1^{Z+1} + f R_{1i}^Z(T_h) N_e N_1^Z, \quad (3)$$

which takes into account the channels of population during the dielectronic capture,

$$A_1^{Z+1} + e \longrightarrow A_i^Z,$$

from the ground state of an ion of the next ionization state with a rate of C_i^{Z+1} and during the excitation $A_1^Z + e \longrightarrow A_i^Z + e'$ by the hot electron impact from the ground state of an ion of the same ionization state with a rate of $R_{1i}^Z(T_h)$, as well as the relaxation of AISs with the lifetimes

$$\tau_i^Z = \frac{1}{A_i^Z + \Gamma_i^Z + R_i^Z(T_e) N_e}, \quad (4)$$

where $R_i^Z(T_e)$ is the total rate of collisional depletion of a level.

Using the detailed balance relation for the dielectronic-capture and the autoionization rates, we obtain

$$N_i^Z = \frac{g_i^Z \Gamma_i^Z N_1^Z / g_1^Z}{A_i^Z + \Gamma_i^Z + R_i^Z(T_e) N_e} \times \left[f \frac{R_{i1}^Z(T_h) N_e}{\Gamma_i^Z} \exp(-E_i^Z/T_h) + \alpha^Z \exp(-E_i^Z/T_e) \right], \quad (5)$$

where E_i^Z is the excitation energy of the AISs of an ion with respect to the ground state; g_i^Z and g_1^Z are the statistical weights of the AISs and the ground state of ion Z, respectively; R_{i1}^Z are the collisional deexcitation rates of the AISs; and α^Z is determined by the distribution of ions in plasma:

$$\alpha^Z = \frac{N_1^{Z+1}/N_1^Z}{(N_1^{Z+1}/N_1^Z)_{\text{Saha}}}.$$

Under real-life conditions for the argon plasma ($T_e \approx 200$ eV, $N_e \approx 2 \times 10^{22}$ cm^{-3}, $T_h \approx 5$ keV, and $f \sim 10^{-4}$), the Mewe and Lotz approximate formulas yield the following estimates for the rates: $R_i^Z(T_e) N_e \ll 10^{13}$ s^{-1}; thus, formula (1) is rewritten as

$$I(\omega) \propto \omega \sum_Z \frac{N_1^Z}{g_1^Z} \times \sum_{i,\,f} \left[f \frac{R_{i1}^Z(T_h) N_e}{\Gamma_i^Z} \exp(-E_i^Z/T_h) + \alpha^Z \exp(-E_i^Z/T_e) \right] \times Q_d^Z(if) S_{if}^Z(\omega - \omega_{if}^Z, \Gamma_{if}^Z, \gamma), \quad (6)$$

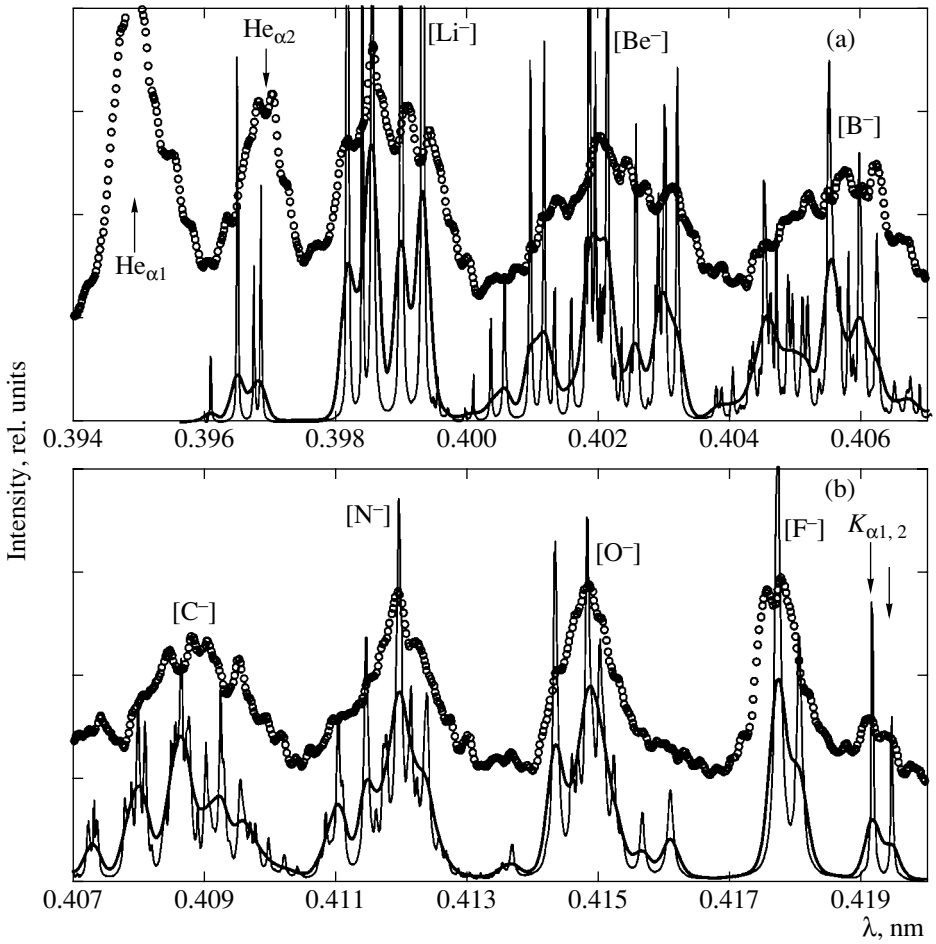

Fig. 2. Comparison of the measured spectrum for the Ar X–XVII ions in femtosecond laser plasma with the spectrum calculated by (6). The parameters of the plasma are as follows: $N_e = 2 \times 10^{22}$ cm^{-3}, $T_e = 200$ eV, $T_h = 5000$ eV, and $f = 10^{-4}$ [9]; the spectroscopic data are borrowed from [24]. The thin curves are obtained by taking into account solely the homogeneous line broadening, and the thick curves are obtained by averaging over an effective hardware width of $\Delta\lambda = 2.6$ mÅ.

where

$$Q_d^Z(if) = \frac{g_i^Z A_{if}^Z \Gamma_i^Z}{A_i^Z + \Gamma_i^Z}$$

are independent of the plasma parameters.

Formula (6) shows that, for narrow AISs at a sufficiently low bulk electron temperature ($T_e \ll E_i^Z$), the excitation from the ground state (or from a low-lying excited state) may become a more efficient population channel even in the presence of a small fraction of hot electrons ($T_h > E_i^Z$). It should be noted that another possible population channel of AISs with the filled $2s^2$ subshell is the ejection of an electron from the $1s$ subshell of a lower ionized ion by hot electrons. However, according to estimations, the efficiency of this population channel is low for real-life plasma parameters.

5. RESULTS AND DISCUSSION

Figure 1 shows the measurement results for the soft X-ray emission spectra in a plasma produced in a gas-cluster argon jet in the range of wavelengths 0.394–0.420 nm containing the resonance $1s2p^1P_1$–$1s^2{}^1S_0$ ($He_{\alpha 1}$) and intercombination $1s2p^3P_1$–$1s^2{}^1S_0$ ($He_{\alpha 2}$) lines of the He-like ion, their dielectronic satellites (from Li-like to F-like ions), and the characteristic $K_{\alpha 1,2}$ lines. To determine the dispersion curve, we used the $He_{\alpha 1,2}$ and $K_{\alpha 1,2}$ lines as reference ones. For comparison, Fig. 1b presents, together with the spectrum obtained in the present experiment, the results of measurements carried out in high-voltage gas-discharge plasma [24] with lower spectral resolution. The measurements of the spectrum of femtosecond laser plasma yield a more detailed satellite structure. In particular, F-like satellites are not blended with the K_α doublet. This fact can be attributed, in particular, to the higher temperature of ions, which results in an increase in the Doppler width. Moreover, the considerable size of the

Measured wavelength of satellite lines in the Ar X–XVII ions. The numbers of the lines correspond to the notations of Fig. 1b. Theoretical data are borrowed from [24]

Line	Experiment	Theory			Ion	Transition
	λ, nm	λ, nm	A_{if}, 10^{13} s^{-1}	Γ_i, 10^{13} s^{-1}		
1	0.39489	0.39491	–	–	XVII	$1s2p\,^1P_1$–$1s^2\,^1S_0$
2	0.39552	–	–	–	–	–
3	0.39633	0.39647	4.14	6.39	XVI	$1s2p^2(^1S)^2S_{1/2}$–$1s^22p^2P_{3/2}$
4	0.39680	0.39683	2.07	8.66	XVI	$1s2s2p(^3S)^2P_{1/2}$–$1s^22s^2S_{1/2}$
5	0.39702	0.39694	–	–	XVII	$1s2p\,^3P_1$–$1s^2\,^1S_0$
6	0.39816	0.39816	10.35	0.37	XVI	$1s2s2p(^3S)^2P_{3/2}$–$1s^22s^2S_{1/2}$
		039838	8.91	1.47	XVI	$1s2s2p(^1S)^2P_{1/2}$–$1s^22s^2S_{1/2}$
7	0.39855	0.39854	14.59	1.10	XVI	$1s2p^2(^3P)^2P_{3/2}$–$1s^22p^2P_{3/2}$
8	0.39910	0.39898	6.09	14.47	XVI	$1s2p^2(^1D)^2D_{3/2}$–$1s^22p^2P_{1/2}$
9	0.39943	0.39931	5.29	15.40	XVI	$1s2p^2(^1D)^2D_{5/2}$–$1s^22p^2P_{3/2}$
10	0.40000	0.40008	1.50	8.62	XV	$1s2s2p^2(^1S)^3S_1$–$1s^22s2p\,^3P_1$
11	0.40044	0.40035	3.09	8.62	XV	$1s2s2p^2(^1S)^3S_1$–$1s^22s2p\,^3P_2$
12	0.40071	0.40056	8.58	15.85	XV	$1s2p^3(^2P)^1P_1$–$1s^22p^2\,^1D_2$
		0.40096	10.20	5.69	XV	$1s2s^22p\,^1P_1$–$1s^22s^2\,^1S_0$
		0.40117	15.76	5.69	XV	$1s2s2p^2(^3P)^1P_1$–$1s^22s2p\,^1P_1$
13	0.40137	0.40133	4.03	14.54	XV	$1s2p^3(^2P)^3P_1$–$1s^22p^2\,^3P_2$
		0.40195	6.82	13.42	XV	$1s2s2p^2(^1D)^3D_2$–$1s^22s2p\,^3P_1$
14	0.40201	0.40214	7.08	16.85	XV	$1s2p^3(^2P)^3P_2$–$1s^22p^2\,^1D_2$
		0.40214	5.16	16.49	XV	$1s2s2p^2(^1D)^3D_3$–$1s^22s2p\,^3P_2$
15	0.40244	0.40249	0.81	17.74	XV	$1s2s2p^2(^3P)^3P_2$–$1s^22s2p\,^1P_1$
		0.40257	8.39	20.87	XV	$1s2p^3(^2D)^1D_2$–$1s^22p^2\,^1D_2$
16	0.40272	0.40286	3.54	21.30	XV	$1s2p^3(^2D)^3D_1$–$1s^22p^2\,^3P_0$
		0.40291	4.37	25.51	XV	$1s2s2p^2(^1D)^1D_2$–$1s^22s2p\,^1P_1$
17	0.40317	0.40320	4.97	21.57	XV	$1s2p^3(^2D)^3D_3$–$1s^22p^2\,^3P_2$
18	0.40389	0.40387	1.42	27.13	XIV	$1s2s2p^3(^2D)^2D_{5/2}$–$1s^22s2p^2\,^2D_{5/2}$
19	0.40439	0.40435	4.49	18.05	XIV	$1s2s2p^3(^2P)^2P_{3/2}$–$1s^22s2p^2\,^2D_{5/2}$
20	0.40456	0.40452	13.11	12.50	XIV	$1s2s^22p^2(^3P)^2P_{3/2}$–$1s^22s2p^2P_{3/2}$
21	0.40483	0.40488	5.53	29.05	XIV	$1s2s^22p^2(^1D)^2D_{3/2}$–$1s^22s^22p^2P_{1/2}$
22	0.40518	0.40518	4.75	30.49	XIV	$1s2s^22p^2(^1D)^2D_{5/2}$–$1s^22s^22p^2P_{3/2}$
23	0.40549	0.40550	12.70	20.80	XIV	$1s2s2p^3(^2D)^2D_{5/2}$–$1s^22s2p^2\,^2D_{5/2}$
24	0.40575	0.40580	4.18	16.49	XIV	$1s2s2p^3(^2D)^4D_{5/2}$–$1s^22s2p^2\,^4P_{3/2}$
25	0.40601	0.40596	4.90	16.61	XIV	$1s2s2p^3(^2D)^4D_{7/2}$–$1s^22s2p^2\,^4P_{5/2}$
26	0.40624	0.40622	4.72	24.10	XIV	$1s2s2p^3(^2D)^2D_{5/2}$–$1s^22s2p^2\,^2P_{3/2}$
27	0.40659	0.40668	2.39	25.69	XIV	$1s2p^4(^3P)^2P_{3/2}$–$1s^22p^3\,^2P_{1/2}$
	–	0.40721	2.72	37.15	XIV	$1s2p^4(^1D)^2D_{5/2}$–$1s^22p^3\,^2P_{3/2}$
28	0.40741	0.40735	8.16	29.71	XIII	$1s2s^22p^3(^2P)^1P_1$–$1s^22s^22p^2\,^1D_2$
29	0.40806	0.40808	13.53	34.85	XIII	$1s2s^22p^3(^2D)^1D_2$–$1s^22s^22p^2\,^1D_2$
30	0.40847	0.40848	6.29	37.03	XIII	$1s2s2p^4(^1D)^3D_2$–$1s^22s2p^3(^2D)^3D_3$
31	0.40880	0.40876	4.41	40.27	XIII	$1s2s^22p^3(^2D)^3D_3$–$1s^22s^22p^2\,^3P_2$
32	0.40903	0.40901	4.71	24.03	XIII	$1s2s2p^4(^3P)^5P_2$–$1s^22s2p^3(^4S)^5S_2$
33	0.40953	0.40952	5.83	54.52	XIII	$1s2s2p^4(^1D)^1D_2$–$1s^22s2p^3\,^1D_2$
34	0.40994	0.40996	3.89	32.68	XIII	$1s2s2p^4(^3P)^3P_2$–$1s^22s2p^3(^2P)^3P_2$
35	0.41019	0.41040	0.93	45.72	XIII	$1s2s2p^4(^3P)^3P_2$–$1s^22s2p^3\,^1P_1$

Table (Contd.)

Line	Experiment	Theory			Ion	Transition
	λ, nm	λ, nm	A_{if}, 10^{13} s^{-1}	Γ_i, 10^{13} s^{-1}		
36	0.41096	0.41103	10.72	40.85	XII	$1s2s^22p^4(^3P)^2P_{3/2}$–$1s^22s^22p^3{}^2D_{5/2}$
37	0.41154	0.41147	8.61	52.59	XII	$1s2s^22p^4(^1D)^2D_{3/2}$–$1s^22s^22p^3{}^2D_{3/2}$
38	0.41197	0.41198	11.71	56.50	XII	$1s2s2p^5{}^2P_{3/2}$–$1s^22s2p^4(^1D)^2D_{5/2}$
39	0.41225	0.41215	6.08	43.84	XII	$1s2s2p^5{}^4P_{5/2}$–$1s^22s2p^4{}^4P_{5/2}$
		0.41240	6.48	58.22	XII	$1s2s2p^5{}^2P_{3/2}$–$1s^22s2p^4{}^4P_{3/2}$
40	0.41304	0.41258	4.82	61.78	XII	$1s2s2p^5{}^2P_{1/2}$–$1s^22s2p^4(^3P)^2P_{1/2}$
41	0.41369	0.41369	1.55	56.50	XII	$1s2s2p^5{}^2P_{3/2}$–$1s^22s2p^4(^1S)^2S_{1/2}$
42	0.41439	0.41436	14.06	59.20	XI	$1s2s^22p^5{}^1P_1$–$1s^22s^22p^4{}^1D_2$
43	0.41491	0.41485	6.13	63.92	XI	$1s2s^22p^5{}^3P_2$–$1s^22s^22p^4{}^3P_2$
44	0.41507	0.41504	6.92	60.11	XI	$1s2s2p^6{}^3S_1$–$1s^22s2p^5{}^3P_2$
45	0.41759	–	–	–	–	–
46	0.41781	0.41775	7.93	78.19	X	$1s2s^22p^6{}^2S_{1/2}$–$1s^22s^22p^5{}^2P_{3/2}$
		0.41807	3.95	78.19	X	$1s2s^22p^6{}^2S_{1/2}$–$1s^22s^22p^5{}^2P_{1/2}$
47	0.41916	0.41918	–	25[1)]	II	$K_{\alpha1}$
48	0.41942	0.41947	–	25[1)]	II	$K_{\alpha2}$

Note: [1)] Data from [30].

emitting plasma limits the spectral resolution of the measurements carried out by the Johann scheme.

Figure 2 presents the results of the numerical simulation of the satellite spectrum by formula (6). The simulation was carried out with the use of the wavelengths and the radiation and autoionization rates obtained by the MHFR method; the details of this method are described in [24]. In the present calculations, we used the following plasma parameters: $N_e = 2 \times 10^{22}$ cm^{-3}, $T_e = 200$ eV, $T_h = 5$ keV, and $f = 10^{-4}$. These parameters were obtained earlier in [9, 10] by fitting the results of calculations in a stationary radiative–collisional kinetic model to the spectra of Li- and Be-satellites measured under the same experimental conditions. The relative concentrations of ions of different states of ionization in (6) were used to normalize the spectra by the maximum intensity in the groups of satellite lines of different ions. The obtained parameters $\alpha^{Li} = 0.9$, $\alpha^{Be} = 0.2$, $\alpha^{B} = 0.04$, $\alpha^{C} = 0.008$, $\alpha^{N} = 0.005$, and $\alpha^{O} = 0.003$ show that the difference of the plasma charge distribution from the equilibrium one increases as the ion charge decreases. For the K_α doublet, we used the value $\Gamma_K = 2.5 \times 10^{14}$ s^{-1} and a radiation rate ratio of 0.5 from [30].

When calculating the line profiles, we took into account that the collisional broadening has a significant effect only on the lines with small radiation and autoionization widths whose contribution to the total intensity is small. An approximate expression for the collisional width [31] is given by $\gamma_{if}^Z \approx 10^{14}$ s^{-1}. The estimate for the quadratic Stark shift in the average ion microfield made with regard to the Debye screening gives a still lesser value of $\Delta\omega^{St} \approx 3 \times 10^{13}$ s^{-1} for the chosen plasma parameters. For simplicity, we took into account the Stark broadening by assigning an appropriate width to the Lorentz line shape.

The results of calculations show a strong variation in the relative intensities of certain lines of the Li-like (lines *6–8* in Fig. 1b) and Be-like (lines *13* and *14*) ions due to the population of AISs by hot-electron excitation. For other lines, this population channel is less efficient. The results of calculations also show that the spectral resolution of lines is determined by the Doppler broadening in expanding plasma and is given by $\lambda/\Delta\lambda = 1500$ ($\Delta\lambda = 2.6$ mÅ). This fact significantly changes the structure of satellite lines (the thin curve in Fig. 2b). The data presented in the table show that the maximal value of the autoionization width (attained for the F-like ion) corresponds to $\Delta\lambda_A = 0.8$ mÅ, which is less than the spectral resolution approximately by a factor of three. The autoionization width can be determined experimentally when these values are approximately equal.

Another example that demonstrates the possibility of using the results of our measurements for verifying various atomic calculations is the comparison (see Fig. 3a) of the model spectra obtained with the use of two sets of spectroscopic constants for argon ions that are borrowed from [24, 32]. A comparison with experimental data allows one to assess the accuracy of various theo-

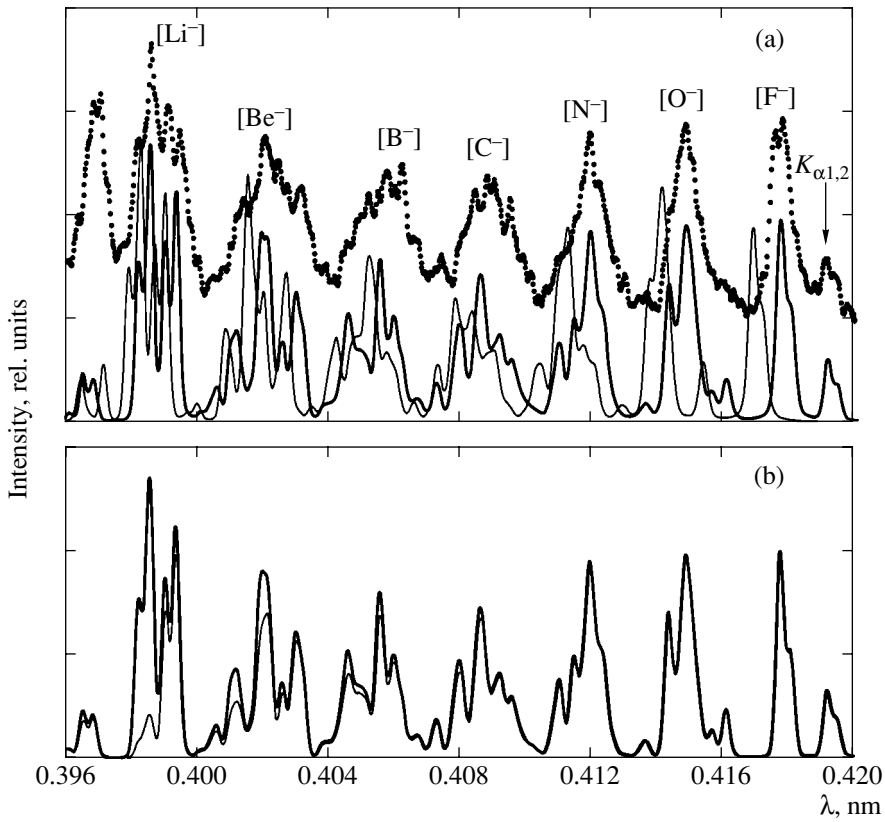

Fig. 3. (a) Simulated satellite spectrum of argon ions with different sets of atomic data; the thick curve is obtained using the atomic data of [24], the thin curve corresponds to the data of [32], and the dots represent experimental data. (b) Calculations performed with the use of solely the Doppler width $\Delta\lambda = 3$ mÅ, without taking into account (thick curve) homogeneous broadening and (thin curve) hot electrons.

retical approaches. In [32], a similar method of calculation was used; however, the authors did not apply the improvement procedure for the contribution of the electron–electron interaction to the total energy of levels on the basis of the experimental data available (see [24] for more details). This explains a substantial line shift and an appreciable variation in the shape of blended lines and indicates that the results of calculations are more reliable [24]. Finally, Fig. 3b demonstrates the effect of the natural width on the shape of the spectrum and the influence of hot electrons on the intensity of certain lines of the Li-, Be-, and B-like ions.

The table presents the wavelengths of the most distinct lines in the observed spectrum and the results of calculations for the most intense transitions close to these lines. More comprehensive theoretical information is given in [24]. On the whole, the measured wavelengths agree well with the results of calculations. The satellite lines of multicharged ions of Ar XVI–XIV exhibit the greatest difference in the structure of the spectrum. Probably, this fact is attributed to the specific features of the kinetics of level population that are not included in the simple model considered, as well as to the contribution of satellite lines from higher levels. These questions require an additional investigation.

6. CONCLUSION

The emission *K*-spectra of satellite lines of multicharged argon ions from Li-like to F-like have been measured for the first time in plasma produced by the interaction of femtosecond laser pulses with a cluster target. High-precision measurements have allowed us to determine the fine structure of the spectrum of satellite lines and to identify them by calculating the characteristics of the AISs $1s2s^n2p^m$ of multicharged argon ions for $n + m \le 8$.

The experimental data have been obtained for the wavelengths of radiation transitions from autoionizing levels of ions. These data can be used for verifying the accuracy of calculations and the effect of various types of configuration mixing on this accuracy.

The results of calculations obtained in a simple kinetic model with typical plasma parameters are in qualitative agreement with the spectrum observed. A direct comparison with the observed intensities of certain lines of the Li-like argon ion confirms the dominant role of hot electrons in the population of appropriate AISs in plasma.

The spectral resolution achieved in the present experiments is limited by the Doppler shift in moving

ions. This fact has not allowed us to carry out the direct measurement of dominant autoionization widths by the observed profiles of spectral lines. However, estimations show that such a measurement becomes possible when the spectral resolution and the autoionizing width increases by a factor of two. These conditions can be satisfied in the plasma produced in the clusters of heavier atoms. The verification of such a possibility is of undoubted interest.

ACKNOWLEDGMENTS

This work was supported in part by the Fond Europeen de Development Economique Regional and Counceil Regional d'Aquitaine, France, and by the NATO grant PST.CLG.977637. The research described in this publication was made possible in part by Award no. RP1-2328-ME-02 of the US Civilian Research & Development Foundation for the Independent States of the Former Soviet Union (CRDF).

REFERENCES

1. A. McPherson, T. S. Luk, B. D. Thompson, *et al.*, Phys. Rev. Lett. **72**, 1810 (1994).
2. T. Ditmire, T. Donnelly, A. M. Rubenchik, *et al.*, Phys. Rev. A **53**, 3379 (1996).
3. M. Lezius, S. Dobosz, D. Normand, and M. Schmidt, Phys. Rev. Lett. **80**, 261 (1998).
4. T. Ditmire, J. Zwelback, V. P. Yanovsky, *et al.*, Nature **398**, 489 (1999).
5. S. Dobosz, M. Schmidt, M. Perdrix, *et al.*, Zh. Éksp. Teor. Fiz. **115**, 2051 (1999) [JETP **88**, 1122 (1999)].
6. T. Auguste, P. D'Oliveira, S. Hulin, *et al.*, Pis'ma Zh. Éksp. Teor. Fiz. **72**, 54 (2000) [JETP Lett. **72**, 38 (2000)].
7. E. Parra, T. Alexeev, J. Fan, *et al.*, Phys. Rev. E **62**, R5 931 (2000).
8. H. M. Milchberg, S. J. McNaught, and E. Parra, Phys. Rev. E **64**, 056402 (2001).
9. G. C. Junkel-Vives, J. Abdallah, Jr., F. Blasco, *et al.*, Phys. Rev. A **64**, 021201 (2001).
10. J. Abdallah, Jr., A. Ya. Faenov, I. Yu. Skobelev, *et al.*, Phys. Rev. A **63**, 032706 (2001).
11. I. W. Armour, B. C. Fawcett, J. D. Silver, and E. Trabert, J. Phys. B **13**, 2701 (1980).
12. J. P. Briand, J. P. L. Billy, P. Charles, *et al.*, Phys. Rev. Lett. **65**, 159 (1990); Phys. Rev. A **43**, 565 (1991).
13. H. Winter and F. Aumay, J. Phys. B **32**, R39 (1999).
14. A. Ya. Faenov, J. Abdallah, Jr., R. E. H. Clark, *et al.*, Proc. SPIE **3157**, 10 (1997).
15. A. M. Urnov, J. Dubau, A. Ya. Faenov, *et al.*, Pis'ma Zh. Éksp. Teor. Fiz. **67**, 513 (1998) [JETP Lett. **67**, 489 (1998)].
16. A. Ya. Faenov, A. I. Magunov, T. A. Pikuz, *et al.*, Phys. Scr. T **80**, 536 (1999).
17. F. Rosmei, A. Ya. Faenov, T. A. Pikuz, *et al.*, J. Phys. B **32**, L107 (1999).
18. J. Abdallah, Jr., I. Yu. Skobelev, A. Ya. Faenov, *et al.*, Quantum Electron. **30**, 694 (2000).
19. A. I. Magunov, T. A. Pikuz, I. Yu. Skobelev, *et al.*, Pis'ma Zh. Éksp. Teor. Fiz. **74**, 412 (2001) [JETP Lett. **74**, 375 (2001)].
20. G. C. Junkel-Vives, J. Abdallah, Jr., F. Blasco, *et al.*, Phys. Rev. A **66**, 033204 (2002).
21. I. Yu. Skobelev, A. Ya. Faenov, A. I. Magunov, *et al.*, Zh. Éksp. Teor. Fiz. **121**, 88 (2002) [JETP **94**, 73 (2002)].
22. I. Yu. Skobelev, A. Ya. Faenov, A. I. Magunov, *et al.*, Zh. Éksp. Teor. Fiz. **121**, 1124 (2002) [JETP **94**, 966 (2002)].
23. Y. Zou, Y. Awaya, C. P. Bhalla, *et al.*, Phys. Rev. A **51**, 3790 (1995).
24. E. Biemont, P. Quinet, A. Ya. Faenov, *et al.*, Phys. Scr. **61**, 555 (2000).
25. C. Stenz, V. Bagnoud, F. Blasco, *et al.*, Quantum Electron. **30**, 721 (2000).
26. M. V. Ammosov, N. B. Delone, and V. P. Kraĭnov, Zh. Éksp. Teor. Fiz. **91**, 2008 (1986) [Sov. Phys. JETP **64**, 1191 (1986)].
27. A. S. Boldarev, V. A. Gasilov, F. Blasco, *et al.*, Pis'ma Zh. Éksp. Teor. Fiz. **73**, 583 (2001) [JETP Lett. **73**, 514 (2001)].
28. I. Yu. Skobelev, A. Ya. Faenov, B. A. Bryunetkin, *et al.*, Zh. Éksp. Teor. Fiz. **108**, 1263 (1995) [JETP **81**, 692 (1995)].
29. R. D. Cowan, *The Theory of Atomic Structure and Spectra* (Univ. of California Press, Berkeley, 1981).
30. M. A. Blokhin and I. G. Shveĭtser, *X-ray Spectrum Handbook* (Nauka, Moscow, 1982).
31. H. R. Griem, *Spectral Line Broadening by Plasmas* (Academic, New York, 1974; Mir, Moscow, 1978).
32. K. R. Karim, B. Vancleave, and C. P. Bhalla, J. Quant. Spectrosc. Radiat. Transf. **61**, 227 (1999).

Translated by I. Nikitin